Wave-based Finite Element Method applied to thick, in-vacuo, cylindrical shells with keel or bulkhead plate attachments at middle to high frequency.

by

Mark A. Hayner

B.S., Mechanical Engineering Cornell University (1982)
M.S., Ocean Engineering M.I.T. (1994)

Submitted to the Department of Ocean Engineering
in partial fulfillment of the requirements for the degree of

Doctor of Philosophy in Ocean Engineering

at the

MASSACHUSETTS INSTITUTE OF TECHNOLOGY

June 1998

Signature of Author... .....
Department of Ocean Engineering
15 May 1998

Certified by..... .....
J. Kim Vandiver
Professor of Ocean Engineering
Thesis Supervisor

Accepted by..... ...
J. Kim Vandiver
Chairman, Department Committee on Graduate Students

Wave-based Finite Element Method applied to thick, in-vacuo, cylindrical shells with keel or bulkhead plate attachments at middle to high frequency.

by

Mark A. Hayner

Submitted to the Department of Ocean Engineering
on 15 May 1998, in partial fulfillment of the
requirements for the degree of
Doctor of Philosophy in Ocean Engineering

Abstract

The Wave-based Finite Element Method or WFEM is applied to in-vacuo cylindrical shells to study structure-borne wave interaction with bulkhead and keel-type plate attachments. The frequency range considered is from one to ten times the shell "ring" frequency. The goal is to better understand the shell-plate interaction, which plays an important role in the acoustic scattering and radiation processes from submarine hulls.

Two formulations of a WFEM stiffness matrix for in-vacuo cylindrical shell are derived. I refer to them as the axial wave formulation and the circumferential wave formulation. Both are based on the Herrmann-Mirsky theory for *thick* 2D shells, which supports five wave types: compressional, shear, flexural, evanescent, and through-thickness shear. The WFEM method is shown to be exact to within the underlying assumptions of the governing equation. The method is numerically efficient by effectively eliminating an integration over wavenumber in the direction of the propagating wave. I show that an ordered formulation of the stiffness matrix allows one to decompose the solution in post-processing by wave-type without wavenumber processing. The wave-sorting is also exact, numerically efficient, and can be done in the near-field of structural discontinuites and in the presence of heavy material damping.

In addition, I apply the WFEM method to a 3D solid cylinder that is infinitely extended in the axial direction. The stiffness matrix relates displacements at the inner and outer radii to corresponding surface stresses. Wavenumber integration is used in the other two directions to find the total solution. The 3D model may also be used for cylindrical shells with multiple layers. The global stiffness matrix for the WFEM formulation is less than one sixth the size of a global matrix as derived by Ricks using the Direct Global Matrix method (DGM) [10] due to symmetry about the main diagonal and fewer degrees of freedom. I use the 3D WFEM model to establish the limits of the Herrmann-Mirsky theory versus frequency and shell thickness.

The 2D WFEM shell model is hybridized with a conventional FEM model of the shell-plate T-junction to provide an accurate model of the junction from middle to high frequencies. I also use it to evaluate the typical boundary matching condition when a FEM T-junction model is not used. This evaluation is carried out by comparing wave power scattering coefficients. I show that the hybrid model is needed at all frequencies when the shell thickness is relatively thick (10% of the shell radius). I show that T-junction details are even important for relatively thin shells (2%-4%) especially when the bulkhead is thicker than the shell. In any case, the hybrid model may be used without sacrificing the good numerical efficiency of the WFEM method because the number of required conventional FEM elements is minimal.

To demonstrate the use of the 2D shell model, I compare the predicted response of a cylindrical shell due to an array of piezoelectric volume sources embedded in the shell wall with available experimental data collected by Lin [24]. I show that the agreement between the experimental data and the model is very good down to the ring frequency of the shell. I provide a detailed analysis of the source-shell interaction.

Appended to the above research is a compact formulation of the acoustic scattering from an infinitely long cylindrical shell with heavy fluid loading and both (at the same time) an internal bulkhead and deck-type attachment. The problem is formulated strictly in terms of wavenumber integration methods applied to the Herrmann-Mirsky thick shell theory. Although, I don't actually solve the problem due to the high computational cost, it provides an interesting context within which I may discuss the limitations of the WFEM method.

Also appended to the above research is the application of the WFEM method to tensioned beams with rigid body attachments. Specifically, I formulate a beam/rigid link/beam element for both pinned and welded boundary conditions. I use the element to study wave propagation past a rigid body and wave reflection at a *fixed-end absorber*. This work has application to marine risers and cable systems.

Thesis Supervisor: J. Kim Vandiver
Title: Professor of Ocean Engineering

Acknowledgments

I would like to acknowledge not only those people who have had an influence on this thesis but also on my life. I want to first remember my Mom who died of cancer. She loved life and had a great compassion for people. Thanks to Hon and Dad for their unwavering support. Thanks to everyone in my extended family, especially my brothers and sisters: Maryhelen, Paul, Ann, Jim, Tom, Marge, Awe, Chris, George, and Den (The names should be run-off at the cadence that Mom used.). A special thanks to Maryhelen and Paul Pellini for meticulously proofing the chapters. Also, thanks to Nana and Grandpa Carbonneau and their very hospitable neighbors Jane and Jeff Ferketic.

Thanks to my first advisor, Rob Fricke, for getting me into MIT and coming to my defense at the end. Thanks to my final advisor, Kim Vandiver, for getting me out of MIT! I enjoyed our weekly meetings. Your clear thinking, confidence, and steady guidance got me through the tough times. Thanks to Eduardo Kausel for being on my committee and taking the time to talk things through in detail. Thanks to Rama Rao for being on my committee and helping me prepare for my final defense. That was huge! I hope I have the opportunity to work again with all of you in the future.

In addition, I appreciate the long-distance advice of Yue Ping Guo. Thanks to Ira Dyer for the financial support through the years. I'm inspired by your unrelenting standard of excellence. Thanks to Joe Bondaryk for his constructive criticism. I always knew that you wanted me to succeed. Thanks to Shiela and Sabina for the administrative help.

Good luck to all my fellow graduate students: Enrique Gonzalez, Ching-Yu Lin, and Patty Manning. Also, past and present residents of Room 5-435 especially, Mike Klausbruckner, Peter Daly, Pierre Elisseeff, Vince Lupien, and Brian Sperry. I regret that I didn't share the office experience with you more. I know that you all have very bright futures and I'll enjoy seeing your names appear again and again in the journals.

When I began at MIT six years ago, little did I know that doctoral degrees came with a wife and two kids!!! To my new daughter Tess, I look forward to our years together. You feel good when I hold you and I hear your little breaths. To my daughter, Michelle, you helped too Pumpkin. You helped me to forget about work by taking me into your world. What makes the lamb love Mary so? Can I hold the Balmex? How many cookies did the dragon eat? Like my mother used to say to me, "May God bless you and keep you safe through the night and always, my dearest Michelle".

Finally, how do I begin to say thanks to my wife, Kathy. You were my first and best friend through it all. You kept me grounded through all the ups and downs. You took such good care of Michelle, Tess, and me too! You were patient and understanding while another year slipped by because you knew how much this meant to me. You listened to all my big plans. You asked those tough schedule and "why?"

questions. This is our achievement together. It is ours to remember and ours to forget. We can at last think about our future together. For these reasons and more, I dedicate this thesis to you with all my love.

Contents

List of Figures

Chapter 1

Introduction

1.1 Motivation

The study of wave propagation on cylindrical shells with discontinuities is primarily motivated by, but not limited to, the desire to better understand the acoustic scattering process from submarine hulls. Near the shell ring frequency, at which the wavelength of the compressional wave is equal to the shell perimeter, the important wave types are the compressional, shear, flexural, and evanescent waves. All have been shown to play important and inter-dependent roles in the scattering process. The membrane waves (compressional and shear) are, somewhat surprisingly, good absorbers and emitters of acoustic energy for two reasons: they are coupled to the fluid due to shell curvature and they have supersonic wave speeds relative to the acoustic medium (water), which allows them to trace match to the incident acoustic wave. For membrane waves that encounter structural discontinuites, there is wave conversion between all wave types. Converted evanescent waves radiate into the fluid. Converted flexural waves are subsonic and act as an energy storage mechanism until they either viscously dissipate their energy or convert back to radiating waves due to an encounter with another discontinuity.

While in water testing is closer to reality, it is expensive and time consuming because of the difficulty of sealing test specimens and instrumentation from hydrostatic pressure. For this reason, M.I.T.'s department of Ocean Engineering is currently being funded by the U.S. Navy (contract number tbd) to conduct in-air tests to study structure-borne wave scattering on cylindrical shells due to discontinuities, such as, bulkheads and keels. This program is referred to as the Membrane Wave Program. The program goals are to:

- Develop procedures and techniques for exciting and measuring waves on cylinders.
- Provide accurate measurements of wave conversion and dissipation due to typical discontinuites in

real structures. These discontinuities may be neckdown sections, conical end caps, bulkheads, or keels.

- Provide numerical models to guide experiments and analyze test results.

In addition to reduced cost, the in-air experiments are generally more accurate because of the unencumbered access to the test specimen, a more controlled environment, and larger physical scale. Another advantage is faster turnaround of results. My own research and personal interest is focused on the numerical modeling aspects in support of the Membrane Wave Program.

1.2 Overview of this thesis

In this thesis, I use a general method that I refer to as a wave based finite element method (WFEM). The WFEM method is a frequency domain method. All displacements and forces have an assumed time dependence of $e^{-i\omega t}$, where ω is some fixed frequency. The method is very efficient and suitable for analyzing shells at the middle to high frequency ranges, where conventional FEM is very inefficient due to wavelength sampling requirements. Like conventional FEM methods, a stiffness matrix is formulated that relates nodal or end displacement to nodal or end forces. In contrast to conventional FEM methods, the WFEM stiffness matrix is formulated in terms of free waves on the shell and represents an exact solution to within the assumptions of the underlying shell theory.

Using the WFEM method, I develope three different numerical models of a cylindrical shell. The first model may be used to analyze finite length cylindrical shells with one or more axial discontinuities, such as, a bulkhead plate attachment. The second may be used to analyze infinitely long cylindrical shells with one or more circumferential discontinuities, such as, a deck-type or keel attachment. Both these models are based on the *thick* shell theory by Herrmann and Mirsky [11]. I use the adjective *thick* to refer to a shell theory that includes shear deformation and rotary inertia, as opposed to a thin shell theory that does not. The third shell model is based on the Navier equations for a three dimensional elastic solid. This model may be used to analyze through-thickness discontinuities introduced by shell layering. The way these models are formulated and how they may be used separately or together to study shell dynamics is the subject of this thesis.

The outline of the thesis is as follows. The WFEM shell models are developed in Chapter 2 through Chapter 4. To introduce the WFEM method and establish the mathematical basis of the method without undue complication, I analyze the simplest of all wave-bearing system, a one-dimensional rod, in Chapter 2. For the rod, each of the waves have the form $Ae^{+ikx}e^{-i\omega t}$, where A is some complex wave amplitude, k is wavenumber, and x is the axial rod dimension. In Chapter 3, I extend the WFEM method to a two dimensional shell. For the 2D shell, each of the waves have an additional circumferential dependence

of $e^{+\imath n\theta}$ and the waves are travelling in a helical pattern down the axis of the shell. Continuing my progression in dimensional space, in Chapter 4, I formulate the stiffness matrix for a three dimensional shell. For the 3D shell, each of the waves have an additional radial dependence of $H_n^{(1)}\left(\sqrt{k_o^2 - k^2}r\right)$, where $H_n^{(1)}$ is a Hankel function and k_o is the material wavenumber of either a dilational or shear wave. In the 3D shell, the waves are spiralling radially outward and down the shell axis.

In Chapter 5, I use one of the two 2D shell models to consider a shell-bulkhead T-junction connection in detail. Specifically, I compare several different ways to model the connection including a hybrid WFEM-FEM technique. The use of the hybrid model allows me to study the effects of shear deformation at the T-junction and interpret these effects in terms of shell wave scattering.

In Chapter 6, I compare the 2D model to experimental data collected by Lin and provide a detailed analysis of the source-shell interaction. The comparison serves to validate the WFEM model and demonstrate it's usefulness.

In Appendix G, I attach a compact formulation of the acoustic scattering from an infinitely long cylindrical shell with heavy fluid loading and both (at the same time) an internal bulkhead and deck-type attachment. The problem is also based the Herrmann-Mirsky thick shell theory and formulated strictly in terms of wavenumber integration methods (WI). Although, I don't actually solve the problem due to the high computational cost, this problem provides an interesting context within which I may discuss the limitations of the WFEM method.

In Appendix D and Appendix E, I apply the WFEM method to tensioned beams with rigid body attachments. Specifically, I formulate a beam/rigid link/beam element for both pinned and welded boundary conditions. I use the element to study wave propagation past a rigid body and wave reflection at a *fixed-end absorber*. This work has application to marine risers and cable systems.

1.3 Definition of terms

There are a number of terms that I frequently use throughout this thesis and it is useful to define them here. I've already referred to several numerical methods: FEM, WFEM, WI, and DGM. Yet another related numerical method is the thin layer method or TLM.

Other terms frequently used are the *shell ring frequency,* that is, the frequency ω at which a compressional wave fits into the circumference of the shell. When frequency is normalized by the shell radius a and shell compressional speed c_p as

$$\Omega = \frac{\omega a}{c_p},$$

the ring frequency occurs at $\Omega = 1$ and the normalized frequency is defined in terms of multiples of the ring frequency. The frequency range considered throughout this thesis ranges from an order below to an

order above the ring frequency.

I define the *middle frequency range* or the *mid-frequency range* generally as those frequencies on the order of the ring frequency of the shell and the *high frequency range* on the order of one order above the ring frequency.

I often refer to three different types of shell theories: *thin, thick,* and *full.* In Chapter 3, I use the Herrmann-Mirsky shell theory to describe the motions of the shell. I refer to this theory as a *thick* shell theory because it includes shear deformation and rotary inertia effects. This is in contrast to *thin* shell theory, which does not. I use the adjective *full* to refer to the three dimensional shell theory. Of course, there are also corresponding : *thin, thick,* and *full* flat plate theories. I'll show that depending on the shell thickness, the shell begins to behave like a flat plate somewhere between $\Omega = 1$ and $\Omega = 10$. Also, that the frequency range considered here is not so high and the shell is not so thick that *thick* shell theory is still applicable.

Chapter 2

Wave-based FEM analysis of a 1-D rod

In this chapter, I apply the wave-based finite element method (WFEM) to the simplest of all wave bearing systems, the one-dimensional rod. By presenting the method for the rod, the essence of WFEM is brought out without undue complication. Moreover, it allows me to establish the mathematical basis for WFEM by relating it to the wavenumber integration method (WI), which is essentially Fourier analysis. In a funny sense, WFEM is WI without the integration. It also allows me to discuss the advantages and disadvantages of the method compared to WI and conventional FEM. In Appendix D and Appendix E, I apply the method to a higher order 1-D problem (a beam with a rigid body attachment) and in subsequent chapters, I extend the method to higher order problems in 2D and 3D cylindrical shells.

2.1 Governing equation

To begin, I consider the dynamic response of a one-dimensional rod to an externally applied sinusoidal point force. The rod is infinitely long with a circular cross section, whose axis is aligned with the x axis. The rod is assumed to be made of a linear visco-elastic material with complex Young's modulus E, linear density ρ_c, and cross-sectional area S. I am interested in finding the axial displacement of the rod, $u(x)$, caused by the concentrated force

$$f_o(x) = F_o \delta(x - x_o) e^{-i\omega t}$$

located at x_o. Because the system is linear, the displacement has the same time dependance as the driving force and the factor $e^{-i\omega t}$ is hereafter implied.

The momentum balance on a differential element dx may be expressed as

$$F_o\delta\left(x-x_o\right)dx+df\left(x\right)=\rho_c u_{,tt}dx,$$

where $f\left(x\right)$ is the internal force within the rod and $u_{,tt}$ is the second derivative of u with respect to time. This force is related to the displacement by the constitutive relation

$$f=\rho_c c_L^2 u_{,x}, \tag{2.1}$$

where

$$c_L=\sqrt{\frac{E}{\rho_c/S}}. \tag{2.2}$$

The constitutive equation for the rod is just Hooke's law. I may substitute the constitutive relation into the momentum balance and rearrange to obtain the displacement-based momentum equation

$$-\rho_c c_L^2 u_{,xx}+\rho_c u_{,tt}=F_o\delta\left(x-x_o\right). \tag{2.3}$$

The dynamics of the rod, as expected, are governed by the wave equation.

2.2 Free-wave solution

To study the behavior of waves on the rod, I begin by looking at the free wave solution to Eq.(2.3). To find the free waves, I transform the displacement-based momentum equation into the wavenumber domain using the Fourier transform pair,

$$u(x)=\frac{1}{2\pi}\int_{k=-\infty}^{\infty}U\left(k\right)e^{+ikx}dk \quad\Leftrightarrow\quad U\left(k\right)=\int_{x=-\infty}^{\infty}u\left(x\right)e^{-ikx}dx, \tag{2.4}$$

where k is the wavenumber. The result is

$$K\left(k\right)U\left(k\right)=F_o e^{-ikx_o}, \tag{2.5}$$

where the rod stiffness is

$$K\left(k\right)=\rho_c c_L^2\left(k^2-\left(\frac{\omega}{c_L}\right)^2\right). \tag{2.6}$$

To study the free wave behavior in a rod, I consider the unforced solution by setting $F_o = 0$ in Eq.(2.5), which means that

$$K(k)\,U(k) = 0.$$

This equation has a form that is similar to a standard eigenvalue problem (this is discussed in more detail in Chapter 3). For a non-trivial solution to exist,

$$K(k) = 0$$

which means that

$$k = \pm k_L = \pm\frac{\omega}{c_L} \tag{2.7}$$

where k_L is the *free* wavenumber. There are, therefore, two wave solutions representing right-going and left-going waves and the general solution must be some linear combination of the two, that is,

$$u(x) = A_1 e^{+ik_L x} + A_2 e^{-ik_L x}.$$

I consider this form of solution later in this chapter.

Equation (2.7) relating the driving frequency to the wavenumber of the free waves is known as the dispersion relation. Because it is derived without mention of the boundary conditions, it is not a function of the boundary conditions. This concept, a rather simple one for the rod, is powerful. Rather than thinking in terms of an infinite number of modes, one can think more simply in terms of just two waves.

For an elastic material, E is a pure real number, which means that c_L and k_L are also pure real numbers. For a viscoelastic, material E is a complex number that may be expressed in terms of its real and imaginary parts as

$$E = E' - iE'' = E'(1 - i\eta), \tag{2.8}$$

where the loss factor is fundamentally defined as

$$\eta = \frac{E''}{E'}.$$

The loss factor is a positive real number. The reason for the negative sign for the imaginary part of E will become clear presently. If I assume that $\eta \ll 1$, then I may use Eq.(2.2), Eq.(2.7), and Eq.(2.8) to write

$$c_L \simeq c_L'(1 - i\eta/2),$$

and

$$k_L \simeq \frac{\omega}{c'_L}\left(1 + i\eta/2\right)$$

Note that the sign of the imaginary part of the sound speed leads to a positive imaginary part of the wavenumber.

To interpret the complex wavenumber, consider a right-going wave having the form

$$e^{+ik_L x}e^{-i\omega t}.$$

If I expand the complex wavenumber into its real and imaginary parts, then

$$e^{+\imath k_L x}e^{-i\omega t} = e^{+\imath k'_L x}e^{-\left(k'_L \eta/2\right)x}e^{-\imath\omega t},$$

and it is clear that as the wave travels there is a decay in its amplitude related to the magnitude of the imaginary part of the wavenumber. Similarly, if I consider a left-going wave, then it decays as it travels to the left. Physically, the complex E indicates that the material is lossy and propagating waves continuously dissipate energy. I choose a negative sign for the imaginary part of E to ensure that the wave decays with distance travelled, which is what we expect to happen physically.

2.3 Wavenumber Integration

There are several ways to solve Eq.(2.3). One common method is by WI, which is an application of Cauchy's integral theorem [5]. The transform defined by Eq.(2.4) expresses the solution for $u(x)$ in terms of a sum of waves having the form

$$e^{+\imath kx}e^{-i\omega t}.$$

Since k takes on all possible real values, the solution is a sum over contributions from all possible propagating (non-decaying) waves travelling either to the right or left. In some sense, this is a solution by mode superposition, only for an infinite length rod the mode spacing is zero.

It is clear from Eq.(2.5) that the displacement has two poles in the complex wavenumber plane, which for an elastic rod are located on the real wavenumber axis at $k = \pm k_L$. If the rod material has a finite but extremely small amount of dissipation, the poles move off the real wavenumber axis and I need not deform the contour around the poles. Both poles rotate counter-clockwise by an angle $\eta/2$. The pole at $k = +k_L$ moves into the upper half complex k-plane, while the other pole moves into the lower half plane.

I may evaluate the inverse transform by Cauchy's residue theorem but I need to consider two spacial

domains. The first domain is when $x \geq x_o$. I complete the contour with a semi-circle enclosing the upper half plane (see Hildebrand [5]). Because the contribution due to the semi-circle is zero, the only contribution is due to the single root in the upper half complex plane and the inverse transform is given by

$$\frac{1}{2\pi}\int_{k=-\infty}^{k=\infty} U(k)\, e^{+\imath kx} dk = \text{Res}\left[iU(k)\, e^{+ikx}; k = +k_L\right] = \lim_{k\to+k_L}\left[U(k)\,(k-k_L)\, e^{+\imath kx}\right].$$

The solution to rod velocity due to point force for $x \geq x_o$ has the form of a right-going wave with the form

$$u(x) = Ae^{+ik_L(x-x_o)},$$

where the wave amplitude is

$$A = \frac{F_o}{-i\omega 2\rho_c c_L}.$$

It physically makes sense that to the right of the point force there only exists a right-going wave that is propagating and/or decaying away from its source.

For the second domain $x \leq x_o$, following a similar procedure (only now I enclose the lower half complex plane and the pole at $k = -k_L$. There is also a change in sign to change the direction of the contour so that is progresses clock-wise from negative infinity to positive infinity.), the solution is a left-going wave with the form

$$u(x) = Ae^{-ik_L(x-x_o)}$$

with the same amplitude as before. Note that the two solutions agree at $x = x_o$, therefore satisfying continuity of displacement.

I may also use Eq.(2.1) to show that the force in the rod for $x \geq x_o$ and $x \leq x_o$ is

$$f(x) = -\frac{1}{2}F_o e^{+ik_L(x-x_o)}$$

and

$$f(x) = +\frac{1}{2}F_o e^{-\imath k_L(x-x_o)},$$

respectively. The discontinuity in the internal rod forces at $x = x_o$ is equal to the applied force, that is,

$$-f\left(x_o^+\right) + f\left(x_o^-\right) = F_o. \tag{2.9}$$

Another way to look at the balance of the applied force with the internal force is to integrate the momentum equation, Eq.(2.3), over a small interval surrounding the concentrated external force. I

express this as

$$\int_{x=x_o^-}^{x=x_o^+} -\rho_c c_L^2 u_{,xx}\, dx + \int_{x=x_o^-}^{x=x_o^+} -\rho_c \omega^2 u\, dx = \int_{x=x_o^-}^{x=x_o^+} F_o \delta(x - x_o)\, dx, \tag{2.10}$$

where the "+" and "−" superscripts denote "just above" and "just below", respectively. If I assume that the displacement is continuous everywhere in the rod, then the inertia term on the left hand side goes to zero as the integration interval go to zero. I may carry out the integration to arrive at

$$-\rho_c c_L^2 u\left(x_o^+\right)_{,x} + \rho_c c_L^2 u\left(x_o^-\right)_{,x} = F_o,$$

which is simply the force balance equation, Eq.(2.9). If I remove the section of rod to the left of the applied force then the force balance simplifies to

$$-f\left(x_o^+\right) = F_o. \tag{2.11}$$

For a positive applied force, the internal force on the section of rod to the right is in the opposite direction of the applied force. Similarly, if I remove the right section of rod, the internal force is equal to the applied force, that is,

$$+f\left(x_o^-\right) = F_o. \tag{2.12}$$

These later two equations are useful when considering rods of finite length. Even if there were additional external point forces at locations other than x_o, they would not be included in the integral in Eq.(2.10), and Eq.(2.11) and Eq.(2.12) are still valid.

Before proceeding, let's consider a rod with multiple, say two, point forces with amplitudes F_1 and F_2. The first force is located at $x = 0$ and the other at $x = L$. The solution for multiple point forces is just the sum of the solutions to the individual point forces. Although, the solution would have three spatial domains rather than two. The solution to the left of the F_1 would be a sum of two left-going waves travelling at the same wave speed; one generated by F_1 and the other by F_2. Similarly, to the right of F_2, the solution would be a sum of two right-going waves. Between the two forces, the solution would be a sum of a right-going wave generated by F_1 and a left-going wave generated by F_2.

2.4 Wave-based FEM solution

I now consider the solution of a finite length rod subject to an applied point force

$$f_1 = F_1 \delta(x)$$

at its left end located at $x = 0$ and an applied point force

$$f_2 = F_2 \delta (x - L)$$

at its right end located at $x = L$. Both forces are acting in the positive x direction. My goal in this section is to find the stiffness matrix $\mathbf{K}$, which relates the applied forces at the ends of the rod to the displacements at the ends. If I define $U_1 = U(0)$ and $U_2 = U(L)$, then the relationship I am looking for is

$$\mathbf{KU} = \mathbf{F},$$

where the applied force vector is

$$\mathbf{F} = \{F_1, F_2\}^T$$

and the element (end) displacement vector is

$$\mathbf{U} = \{U_1, U_2\}^T.$$

The discussions in the previous section suggest that the vibration of a finite length rod may be constructed from a linear combination of the free wave solutions for an infinite length rod having the form

$$u(x) = A_1 e^{+\imath k_L x} + A_2 e^{+ik_L L} e^{-ik_L x}. \tag{2.13}$$

The amplitudes, A_1 and A_2, are determined from the boundary conditions which must ensure force balance at both ends. To find $\mathbf{K}$, I first solve for the relationship between the element displacements and the wave amplitudes. I write this relationship symbolically as

$$\mathbf{DA} = \mathbf{U} \tag{2.14}$$

where

$$\mathbf{A} = \left\{ \begin{array}{cc} A_1, & A_2 \end{array} \right\}^T$$

is the vector containing the right and left-going wave amplitudes, and I refer to $\mathbf{D}$ as the displacement-amplitude matrix. I can easily evaluate $\mathbf{D}$ by evaluating Eq.(2.13) at $x = 0$ and $x = L$ to find

$$\mathbf{D} = \left[\begin{array}{cc} 1 & e^{+\imath k_L L} \\ e^{+ik_L L} & 1 \end{array} \right].$$

The displacement matrix is a function of the beam material, geometric properties, and frequency.

In a similar fashion, I may solve for the relationship between the applied forces and the wave amplitudes. I may use the constitutive relation, Eq.(2.1), to evaluate the internal stress force in the rod at any position as

$$f(x) = +ik_L\rho_c c_L^2 A_1 e^{+ik_L x} - ik_L\rho_c c_L^2 A_2 e^{+ik_L L} e^{-ik_L x}. \tag{2.15}$$

I want to find the relationship

$$\mathbf{CA} = \mathbf{F}, \tag{2.16}$$

where I refer to $\mathbf{C}$ as the force-amplitude matrix. I know from Eq.(2.11) that a positive force applied to the left side of the rod is equal in magnitude to the internal rod force f but opposite in sign. I also know from Eq.(2.12) that a positive force applied to the right side is equal in magnitude and sign to the internal force. I may then use these relations to evaluate f at $x = 0$ and $x = L$ to find

$$\mathbf{C} = ik_L\rho_c c_L^2 \begin{bmatrix} -1 & e^{+ik_L L} \\ e^{+ik_L L} & -1 \end{bmatrix}.$$

The force matrix is also a function of the beam material, geometric properties, and frequency. For the simple case of the rod, the $\mathbf{D}$ and $\mathbf{C}$ matrices are symmetric. It turns out, however, that this is not a general property. I'll show that neither is symmetric for higher order problems.

I can now solve for the dynamic stiffness matrix, defined by simply eliminating the wave amplitudes from Eq.(4.12) and Eq.(4.14). The stiffness matrix is

$$\mathbf{K} = \mathbf{CD}^{-1} = \frac{k_L\rho_c c_L^2}{\sin(k_L L)} \begin{bmatrix} \cos(k_L L) & -1 \\ -1 & \cos(k_L L) \end{bmatrix}. \tag{2.17}$$

The stiffness matrix for a rod is always symmetric due to reciprocity. For finite length beams, the stiffness matrix elements are pure real numbers. Positive and negative real values denote spring-like and mass-like characteristics respectively. As discussed earlier, dissipative effects may be included by letting the Young's modulus be complex, which results in complex stiffness matrix elements with negative imaginary parts.

2.5 Summary

In this chapter, I have derived two forms of the rod stiffness matrix, which I refer to as the WI stiffness matrix and the WFEM stiffness matrix. The former is given by Eq.(2.6) and the latter by Eq.(2.17). In subsequent appendices, I will make use of both forms for a infinite rectangular plate and a circular plate. To derive higher order elements, I will follow many of the basic steps taken here for the simple rod

element. The steps are summarized as follows in terms that apply as well to more complex problems:

- The displacement-based momentum equations are solved for and transformed from the spatial domain to the wavenumber domain using the Fourier integral transform pair defined by Eq.(2.4). The transformed momentum equation produces Eq.(2.5), and defines the WI stiffness matrix, which relates the external force amplitudes to the displacement amplitudes. For the simple rod equation the dimension of the stiffness matrix is $1x1$. For more complex problems the dimensions will grow.

- To find the free wavenumbers the roots of the determinant of the WI stiffness matrix are found. For the rod the determinant of K is just K. The number of wavenumber roots is two times the dimension of the WI stiffness matrix. The roots appear in $\pm$ pairs, representing right and left-going waves.

- A step that is nearly transparent for the rod is that the *free-wave vectors* were found. (If the free wavenumbers are considered eigenvalues of the problem, then the free wave vectors are the associated eigenvectors. For the rod, the free wave vectors are just unity for both the right and left-going wave. The displacement anywhere in the rod is then given by a linear combination of the free wave solutions. The wavenumber of these waves are shown to be independent of the boundary conditions.

- The internal rod forces associated with each wave is calculated using the constitutive relation, Eq.(2.1).

- The WFEM stiffness matrix for a finite length rod is formed by first constructing the displacement-amplitude matrix and the force-amplitude matrix. The stiffness matrix is found by eliminating the unknown wave amplitudes as described.

To complete this section I make a few comments about the advantages, limitations, and restrictions of the method:

- An advantage of the wave-based formulation of the stiffness matrix over conventional FEM is that it is exact over the entire spatial domain to within the assumptions of the governing equations. There is no sampling error and the solution is known over the entire spatial domain.

- The dynamics may be separated by wave type. For the rod this means that the contribution due to the left and right-going waves may be separated. For more complex systems, such as a beam or shell, where there may be more than one wave type, this feature becomes more important.

- The stiffness matrix for semi-infinite length elements may be formulated using the same procedure used above. For a element that extends to positive infinity, only the right-going waves are retained. For an element extending to negative infinity, only the left-going waves are retained.

- Dissipation is added by letting the Young's modulus be complex and there is no restriction as to how heavy the damping may be.

- It is clear from Eq.(2.17), that the stiffness matrix is frequency dependent and therefore must be formulated at each frequency. For conventional FEM, the dynamic stiffness matrix may be written as

$$\mathbf{K} = \mathbf{K}_0 - \omega^2 \mathbf{M}_0,$$

  where $\mathbf{K}_0$ and $\mathbf{M}_0$ are the static stiffness and mass matrices. Both $\mathbf{K}_0$ and $\mathbf{M}_0$ are frequency independent and need to calculated only once. The dynamic stiffness matrix is formed simply by addition of the two static matrices.

- Thinking in terms of a small number of waves rather than an infinite number of modes is easier and provides greater insight into the problem being studied.

- The method may be applied to one, two, or three-dimensional problems provided they are separable. This is discussed more in the following appendices. The external forces must be at discrete points and the material properties must be constant between these forces.

- The use of the Fourier transform requires that the system is a linear system.

Chapter 3

Stiffness matrices for a thick 2D shell

3.1 Introduction

In this chapter, I present the numerical methods that may be used to analyze the shell shown in Figures 2.1. The shell is referred to a cylindrical coordinate system $\{x, \theta, r\}$, where x is the axial direction, θ is the circumferential direction, and r is the radial direction. It is made from a linear elastic solid with Young's modulus E, density ρ, and Poisson's ratio ν. It is surrounded on all sides by a vacuum. It has an average radius a, thickness h, and length L_x in the axial direction, and length L_θ in the circumferential direction.

I analyze the shell based on the Hermann-Mirsky theory [11]. The Hermann-Mirsky theory is to thick shells as the Timoshenko theory is to thick beams, although there is no unique thick shell theory due to finite series approximation of logarithmic terms in the radial direction. It turns out that the use of a thick shell theory is necessary for a good comparison with the experimental data.

I discuss two different methods to analyze the shell motions. I refer to them as the wavenumber integration method (WI) and the wave-based FEM method (WFEM). I discuss their relationship in Appendix-A for a simple rod problem and show that they are close cousins. The two methods impose different restrictions on L_x and L_θ. In all, three different shell configurations may be analyzed. The WI method is suitable to analyze an infinitely long cylinder with a complete cross-section, while the WFEM is suitable to analyze either a shell with a complete cross-section and a finite axial extent or a shell with a partial cross-section and an infinite axial length. In this chapter, a separate section is devoted to the analysis of each shell configuration.

Figure 3-1: Cylindrical shell element in coordinate system $\{x, \theta, r\}$.

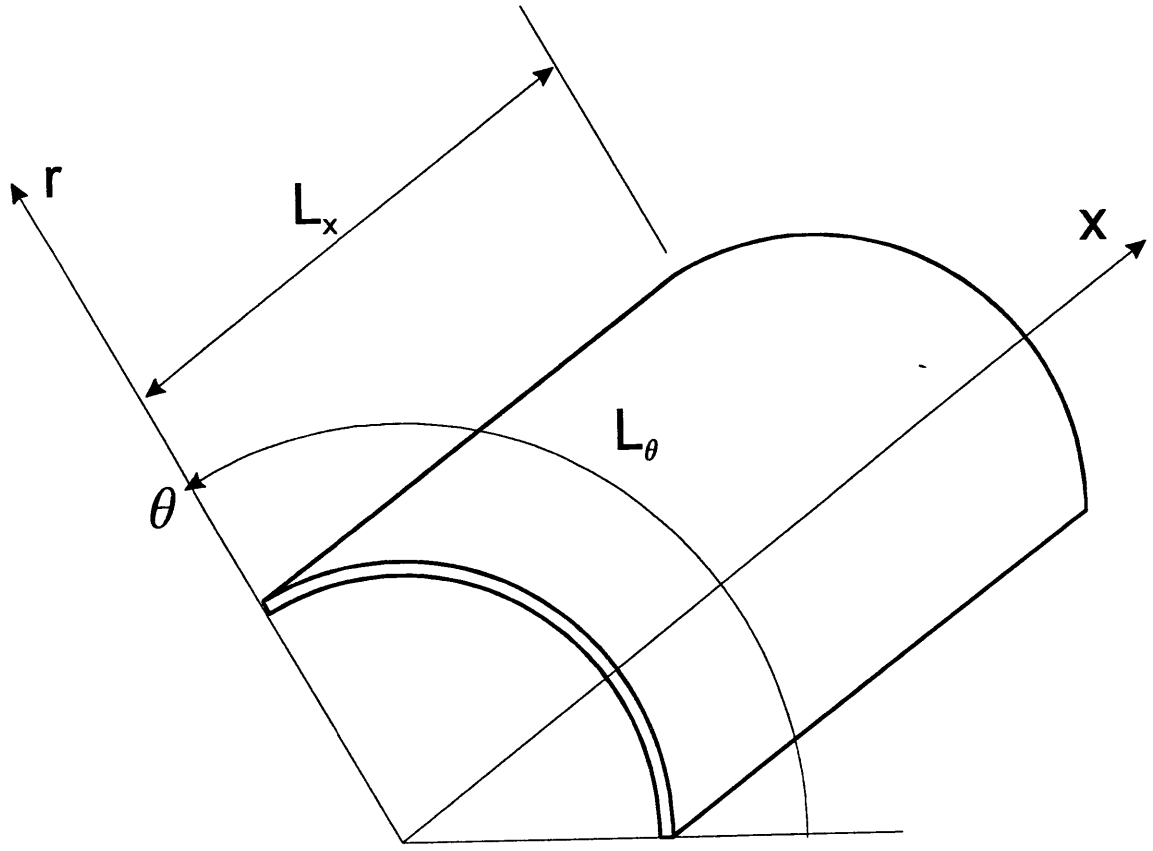

3.2 Original contributions

The development of numerical models of elastic media has been on-going for decades. My contributions may be generally described as extending existing methods so they may applied to the experiments described in Chapter 1. Specifically, my contributions are:

- Formulated WFEM element for a thick, finite length, cylindrical shell in terms of axial wave amplitudes. The formulation is expressed in terms of a stiffness matrix, which relates ring forces applied to the ends of the shell element to their respective end displacements. The forces and displacements have an implied circumferential dependence of $e^{+\imath n\theta}$ and a time dependence of $e^{-\imath\omega t}$. The element is used in Chapter 4 to analyze wave scattering at a shell/bulkhead connection.

- Formulated WFEM element for a thick, infinite length, cylindrical shell in terms of circumferential wave amplitudes. In contrast to the axial wave formulation, the circumferential length of the shell is finite. The formulation is expressed in terms of a stiffness matrix, which relates axial line forces applied to the ends of the shell element to their respective end displacements. The forces and displacements have an implied axial dependence of $e^{+ik_x x}$ and a time dependence of $e^{-i\omega t}$. This formulation is useful when analyzing shells with one or more discontinuities in the circumferential direction.

- Both shell models include wave sorting technique, which allows the motions of the shell to be decomposed by wave direction and also wave type. The shell theory used includes five different wave types: compressional, shear, flexural, evanescent, and through thickness shear. There is no error associated with the wave decomposition from either wave amplitude decay caused by heavy viscoelastic dissipation or spatial sampling. Because the sorting includes the decaying waves (at most frequencies the evanescent and through-thickness shear are rapidly decaying waves), the technique works in the near-field as well as the far-field.

3.3 Previous work

The WFEM method has been used by Kausel et al [33] to analyze wave propagation in horizontally layered solid media. They also implemented a wave sorting technique that is similar to the one described here. The WFEM element for a finite length, thin shell formulated in terms of axial waves was done by Harari [7]. Borgiotti and Rosen [4] extended Harari's work to to an infinitely long thick shell. Langley calculated circumferential wave reflection coefficients in thin shells due to beam and plate discontinuities [45].

3.4 Infinitely long, thin cylindrical shell with circular cross-section

In this section, I consider an infinitely long shell with a complete circular cross-section. To save writing, I present the governing equations using the Herrmann-Mirsky theory only after they have been transformed from the spatial and time domain to what I'll call the helical wave domain. Therefore, I first assume that all variables have a time dependence of $e^{-i\omega t}$, and then define the helical wave transform for some

general variable f as

$$f(x,\theta) = \frac{1}{(2\pi)^2} \sum_{n=-\infty}^{\infty} \int_{k_x=-\infty}^{\infty} F(k_x,n)\, e^{+ik_x x} e^{+in\theta} dk_x \quad \Leftrightarrow \quad F(k_x,n) = \int_{\theta=0}^{2\pi} \int_{x=-\infty}^{\infty} f(x,\theta)\, e^{-ik_x x} e^{-in\theta} dx d\theta, \tag{3.1}$$

where my convention is to use capital letters for transformed quantities. This transform describes a steady-state solution as a summation of helical waves with axial wavenumber component k_x and circumferential wavenumber component n. The circumferential wavenumber component is discrete due to the cyclic nature of the shell in the circumferential direction.

The transform of the displacement-based momentum equations for the Hermann-Mirsky theory may then be written as

$$\mathbf{K}(k_x,n)\,\mathbf{U}(k_x,n) = \mathbf{F}_o(k_x,n), \tag{3.2}$$

where $\mathbf{K}$ is a $5x5$ stiffness matrix, $\mathbf{U}$ is a $5x1$ displacement vector, and $\mathbf{F}_o$ is a $5x1$ external force vector. The elements of the displacement vector are

$$\mathbf{U}(k_x,n) = \{U,V,W,\Psi_\theta,\Psi_x\}^T,$$

where U, V, and W are translations of the mid-surface displacements in the $\{x,\theta,r\}$ directions, Ψ_θ is the mid-surface rotation about the *negative* x-axis, and Ψ_x is the mid-surface rotation about the positive θ-axis. The shell displacements above and below the mid-plane displacements have a linear dependence with the radial coordinate. The corresponding elements of the applied force vector are ordered in the same manner as the displacement vector. Their directions are also the same. The stiffness matrix may be written as

$$\mathbf{K}(k_x,n) = \rho c_p^2 h \begin{bmatrix} k_{11} & k_{12} & k_{13} & 0 & k_{15} \\ k_{12} & k_{22} & k_{23} & k_{24} & 0 \\ -k_{13} & -k_{23} & k_{33} & k_{34} & k_{35} \\ 0 & k_{24} & -k_{34} & k_{44} & k_{45} \\ k_{15} & 0 & -k_{35} & k_{45} & k_{55} \end{bmatrix}, \tag{3.3}$$

where the thirteen unique, non-zero elements of $\mathbf{K}$ are:

$$\begin{aligned} k_{11} &= -k_p^2 + k_x^2 + \left(1 + Ia^{-2}\right)\sigma_m k_s^2, \\ k_{12} &= \sigma_p k_x k_s, \\ k_{13} &= a^{-1}\left(-i\nu k_x\right), \\ k_{15} &= a^{-1} I\left(-k_p^2 + k_x^2 - \sigma_m k_s^2\right), \end{aligned}$$

$$
\begin{aligned}
k_{22} &= -k_p^2 + \sigma_m k_x^2 + \left(1 + Ia^{-2}\right) k_s^2 + a^{-2}\left(1 + Ia^{-2}\right)\left(\kappa^2 \sigma_m\right), \\
k_{23} &= a^{-1}\left(1 + Ia^{-2}\right)\left(-ik_s\right)\left(1 + \kappa^2 \sigma_m\right), \\
k_{24} &= a^{-1}\left\{I\left(-k_p^2 + \sigma_m k_x^2 - k_s^2\right) - \left(1 + Ia^{-2}\right)\kappa^2 \sigma_m\right\}, \\
k_{33} &= -k_p^2 + \kappa^2 \sigma_m k_x^2 + \left(1 + Ia^{-2}\right)\kappa^2 \sigma_m k_s^2 + a^{-2}\left(1 + Ia^{-2}\right), \\
k_{34} &= -ik_s\left(\left(1 + Ia^{-2}\right)\kappa^2 \sigma_m + Ia^{-2}\right), \\
k_{35} &= -i\kappa^2 \sigma_m k_x, \\
k_{44} &= I\left(-k_p^2 + \sigma_m k_x^2 + k_s^2\right) + \left(1 + Ia^{-2}\right)\kappa^2 \sigma_m, \\
k_{45} &= I\sigma_p k_x k_s, \\
k_{55} &= I\left(-k_p^2 + k_x^2 + \sigma_m k_s^2\right) + \kappa^2 \sigma_m,
\end{aligned}
$$

defined in terms of the material wavenumber,

$$k_p = \frac{\omega}{c_p},$$

the circumferential wavenumber,

$$k_s = \frac{n}{a},$$

the thickness parameter,

$$I = \frac{h^2}{12},$$

the shear correction factor

$$\kappa^2 = \frac{\pi^2}{12},$$

and the material parameters

$$\sigma_{p,m} = \frac{1 \pm \nu}{2}.$$

The stiffness matrix quantifies the opposition of the shell to helical surface waves with wavenumber components k_x and n. Notice that when c_p is pure real, $\mathbf{K}$ is Hermitian.

To complete the mathematical description of the theory, the mid-surface displacements are related to the constant-x surface forces by

$$\mathbf{M}_x \mathbf{U}\left(k_x, n\right) = \mathbf{F}_x\left(k_x, n\right), \tag{3.4}$$

where $\mathbf{F}_x$ is defined in a consistent manner with $\mathbf{U}$ and the auxiliary matrix is

$$\mathbf{M}_x = \rho c_p^2 h \begin{bmatrix} ik_x & i\nu k_s & \nu\frac{1}{a} & 0 & \frac{1}{a}iIk_x \\ i\sigma_m k_s & i\sigma_m k_x & 0 & \frac{1}{a}i\sigma_m Ik_x & 0 \\ 0 & 0 & i\kappa^2\sigma_m k_x & 0 & \kappa^2\sigma_m \\ 0 & \frac{1}{a}i\sigma_m Ik_x & 0 & i\sigma_m Ik_x & i\sigma_m Ik_s \\ \frac{1}{a}iIk_x & 0 & 0 & i\nu Ik_s & iIk_x \end{bmatrix}.$$

Similarly, the mid-surface displacements are related to the constant-θ surface forces by

$$\mathbf{M}_\theta \mathbf{U}(k_x, n) = \mathbf{F}_\theta(k_x, n),$$

where $\mathbf{F}_\theta$ is defined in a consistent manner with $\mathbf{U}$ and the auxiliary matrix is

$$\mathbf{M}_s = \rho c_p^2 h \begin{bmatrix} i\sigma_m k_s\left(1+Ia^{-2}\right) & i\sigma_m k_x & 0 & 0 & \frac{1}{a}\left(-i\sigma_m Ik_s\right) \\ i\nu k_x & ik_s\left(1+Ia^{-2}\right) & \frac{1}{a}\left(1+Ia^{-2}\right) & \frac{1}{a}\left(-iIk_s\right) & 0 \\ 0 & -\kappa^2\sigma_m\left(1+Ia^{-2}\right)\frac{1}{a} & i\kappa^2\sigma_m k_s\left(1+Ia^{-2}\right) & \kappa^2\sigma_m\left(1+Ia^{-2}\right) & 0 \\ 0 & \frac{1}{a}\left(-iIk_s\right) & -\frac{1}{a}I & iIk_s & i\nu Ik_x \\ \frac{1}{a}i\sigma_m Ik_s & 0 & 0 & i\sigma_m Ik_x & i\sigma_m Ik_s \end{bmatrix}. \tag{3.5}$$

These two relations may be thought of as the constitutive relations for the shell.

3.5 Finite length shell with circular cross-section

In this section, I find the WFEM solution to the finite length shell with the complete circular annulus. The origin of the coordinate system is positioned on the centerline at the left end so that $x = x_1 = 0$, while the right end of the shell is located at $x = x_2$. I am looking for the relationship between externally applied ring forces at the ends of the shell to the resulting end disagreements. The ring forces have an implied circumferential phase shift of $e^{+\imath n\theta}$. By symmetry arguments the shell displacements also have the same dependence.

The WFEM formulation is based on the free wave solution of an infinite shell. For this reason, I derive and discuss the free wave solution in the following two subsections.

3.5.1 Wave dispersion

In this section, I find two forms of the dispersion relation for a thick cylindrical shell. I will show mathematically that for one form of the dispersion relation, the motions of the shell may be decomposed

by circumferential waves of integer order n, where the order $n = k_\theta/a$ is the non-dimensional wavenumber in the circumferential direction and k_θ is the dimensional wavenumber. Furthermore, using thick shell theory, for each order n there are five different wave types that either propagate, decay, or propagate and decay. This description is beneficial when the shell has an attachment that breaks the continuity of the shell in the axial direction, such as a bulkhead. An alternative description of waves on a cylindrical shell is found by considering the axial wavenumber k_x as fixed, and then solving for the wavenumbers of the five propagating or decaying wave types in the circumferential direction. The circumferential wave description is beneficial when the shell has an attachment that breaks the continuity of the shell in the circumferential direction, such as a keel.

A procedure for finding the free axial wavenumbers on a shell for a given circumferential order is given by Borgiotti and Rosen. They manipulate the equations so that there are no off diagonal axial wavenumbers. This step is not necessary. The procedure here eliminates this step and may be generally applied to either the circumferential wave or axial wave.

To solve for the free-wave solution on the shell, I am very nearly solving a standard eigenvalue problem of the form

$$[\mathbf{A} - \lambda_j \mathbf{I}]\, \mathbf{U}(k_x, n) = \mathbf{B}(\lambda_j)\, \mathbf{U}(k_x, n) = 0, \tag{3.6}$$

where $\mathbf{A}$ is some 5x5 matrix, $\mathbf{I}$ is the identity matrix, $\mathbf{U}$ is some vector, and λ_j is the j'th eigenvalue of $\mathbf{A}$. The eigenvalues are the roots of the characteristic polynomial of $\mathbf{A}$, which is found by setting the determinant of matrix $\mathbf{B}$ to zero. There are five eigenvalues λ_j, $j = 1$ to 5, each with an associated eigenvector $\mathbf{U}_j$. The eigenvectors are found by setting one of the elements in $\mathbf{U}_j$ equal to unity and using any four of the remaining five available equations in Eq.(3.6), with $\mathbf{B}$ evaluated at λ_j, to determine the remaining values of $\mathbf{U}_j$.

How does the standard eigenvalue problem compare with the free-wave problem? By definition the free-wave solutions for the shell are those that satisfy the homogeneous or unforced governing equation. Therefore, if I set the forcing term in Eq.(4.16) to zero, then

$$\mathbf{K}(k_x, n)\, \mathbf{U}(k_x, n) = 0$$

and for non-trivial solutions to exist

$$\det(\mathbf{K}(k_x, n)) = 0. \tag{3.7}$$

It is evident that the matrix $\mathbf{K}$ takes the place of $\mathbf{B}$ in Eq.(3.6) and I may refer to the k_x's that satisfy Eq.(3.7) as eigenvalues. However, the matrix $\mathbf{K}$ is different than $\mathbf{B}$ in two ways. The first is that eigenvalues appear in off-diagonal terms and the second is that the characteristic polynomial is 10th

order in k_x (this is evident by considering the trace of $\mathbf{K}$), which is twice the dimension of the stiffness matrix.

The first difference is easily resolved because it can be shown that the characteristic polynomial is fifth order in $\gamma = k_x^2$ and although there are a total of ten free waves, only five are unique free. Physically, this is because for every right going wave there is a corresponding left going wave that travels at the same speed.

The second difference is resolved by first rewriting the stiffness matrix as

$$\mathbf{K}(k_x, n) = \begin{bmatrix} c_1 + c_2 k_x^2 & c_3 k_x & c_4 k_x & 0 & c_5 + c_6 k_x^2 \\ c_3 k_x & c_7 + c_8 k_x^2 & c_9 & c_{10} + c_{11} k_x^2 & 0 \\ -c_4 k_x & -c_9 & c_{12} + c_{13} k_x^2 & c_{14} & c_{15} k_x \\ 0 & c_{10} + c_{11} k_x^2 & -c_{14} & c_{16} + c_{17} k_x^2 & c_{18} k_x \\ c_5 + c_6 k_x^2 & 0 & -c_{15} k_x & c_{18} k_x & c_{19} + c_{20} k_x^2 \end{bmatrix}, \tag{3.8}$$

where I consider the axial wavenumber as an unknown quantity and all other variables as known quantities. To limit the size of the resulting expressions, I group the known quantities together into coefficients c_m, $m = 1$ to 20. The values of these coefficients may be found by comparing Eq.(A.1) with Eq.(3.8). I may then use a symbolic solver to find the six coefficients of the fifth order polynomial in k_x^2 (the coefficients of γ). I don't write them here because they are still very long expressions. I then use a polynomial root finder to solve for its roots. I find the first five free wavenumbers using

$$k_j = i\sqrt{-\gamma}$$

and the remaining five wavenumbers using

$$k_{j+5} = -k_j,$$

where $j = 1$ to 5. By calculating the wavenumbers in this manner, I am guaranteed that the five free waves exist in the upper half complex k_x-plane [10] and, therefore, represent helical waves travelling in the positive x direction. The remaining five wavenumbers are in the lower half plane and represent left going waves. The five unique values of wavenumber are associated with the five wave types mentioned earlier. Because there is no closed form solution for the roots of a fifth order polynomial, the root finding technique must be numerical and the ordering of the five roots of γ is never guaranteed. I discuss how to sort them by wave type in the next section.

Having solved for the free wavenumbers or eigenvalues, I may immediately solve for their associated

free wave shell displacements or eigenvectors. I've found that the conditioning on the $4x4$ matrix that must be inverted to find the eigenvectors is best when I normalize to the bending rotation Ψ_x (After the inversion has been carried out, I may renormalize to any displacement).

A special case exists when $n \neq 0$, when the in-plane and through thickness shear waves are decoupled from the compressional, flexural, and evanescent waves. The former are associated with the displacements V and Ψ_θ, the latter with the displacements U, W, and Ψ_x. This is clear from examination of Eq.(A.1) when $n = 0$. In effect, the decoupling creates two eigenvalue problems: one for a submatrix with dimension $2x2$ and the other for a submatrix with dimension $3x3$. The solution of each follows the standard solution, but the choice of the displacement used to normalize the eigenvector must be associated with that particular eigenvalue.

3.5.2 Sorted free-wave solutions

As mentioned in the previous section,the wavenumbers are not found in any particular order and I need to sort them. I do this by first sorting the wavenumbers at the high frequency at which their identities are clear because they approach those for a flat plate. For example, if I designate the compressional, shear, flexural, evanescent, and thickness-shear wavenumbers as k_1 through k_5, respectively, then k_1 at high frequency ($\Omega = 5$ is considered high frequency) is approximately given by

$$k_1 = i\sqrt{-k_p^2 + \left(\frac{n}{a}\right)^2}. \tag{3.9}$$

Because the trajectories of the wavenumbers in $\Omega - ka$ space are continuous when there is finite damping, I am able to track these trajectories down to the lowest frequency of interest. For elastic shells, an extremely small amount of damping may be added without incurring significant error. As an example, the real and imaginary parts of the sorted $n = 2$ mode wavenumbers are plotted in Figure 2.2, where I have used the material properties and cross-section geometry of the 16" PVC shell. To make the graph a little clearer, I omit the k_5 through-thickness shear wavenumber.

Having sorted the wavenumbers, I may also find their associated eigenvectors. The eigenvectors are plotted in Figure 2.3 and Figure 2.4 for the first four wave types. I describe in later in this chapter how the sorted wavenumber and their associated eigenvectors are used to decompose the shell response in terms of particular wave types. This decomposition technique is a powerful tool to understand what is happening to the shell.

It is interesting to compare the wavenumber trajectories for a shell with those for a thick flat plate. I can use Eq.(3.9) to approximate the dispersion for the compressional wave and similar expressions for the shear and flexural waves. I compare them in $\Omega - k_x a$ space for the $n = 2$ wave in Figure 2.5. The

Figure 3-2: Sorted frequency-wavenumber dispersion curves for $n = 2$ mode for a cylindrical shell with $h/a = 2\%$, $\nu = .2$, and $\eta = .05$. Legend: comp.(solid), shear(dashed), flexural wave (dash-dot), evanescent(dash-dash).

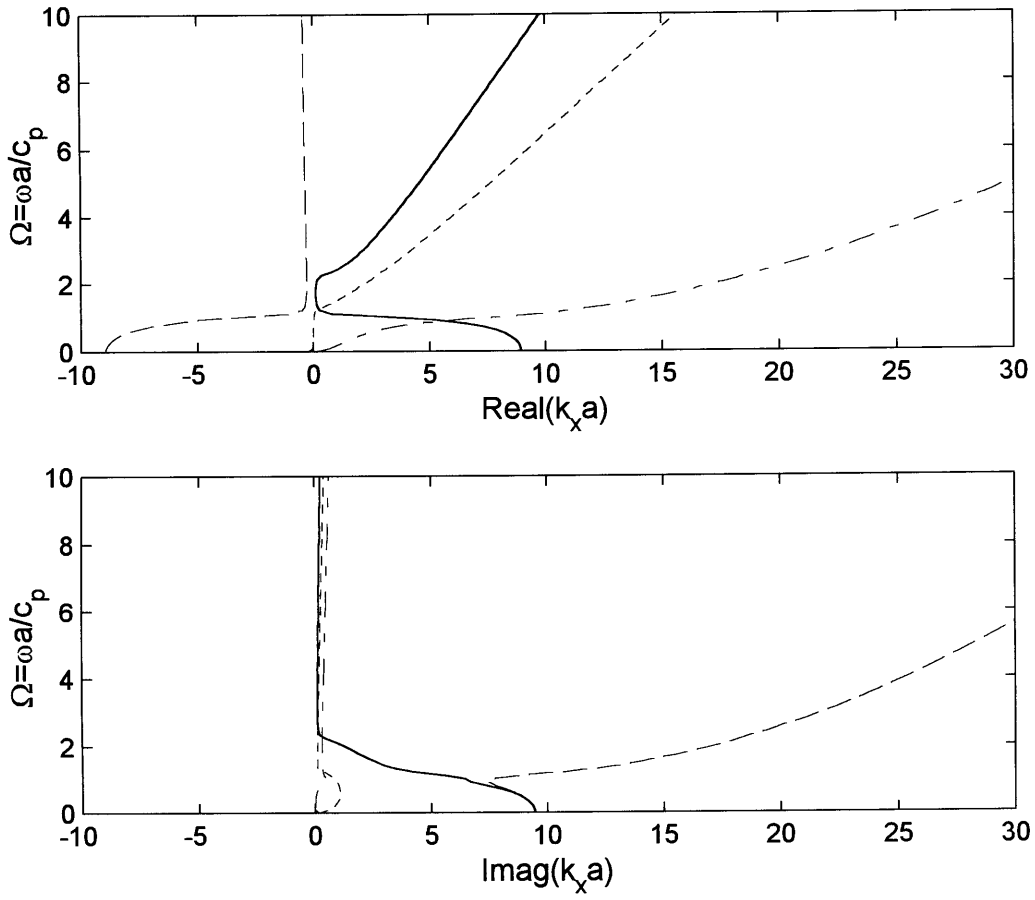

damping in this case is set to zero and I plot only the propagating compressional, shear, and flexural waves above their cut-off frequency. The error is small at $\Omega = 5$ and increases with decreasing frequency. The actual shell waves have faster phase speeds than those estimated using plate theory. The error is largest for the flexural wave. This makes sense because the effect of shell curvature is to couple in-plane and out-of-plane displacements for all waves (see eigenvector plots). Because the out-of-plane stiffness is much less than the in-plane stiffness, I expect that the in-plane compressional and shear wave speed would not change much but the out-of-plane flexural wave would be affected to a much greater extent.

Another way to compare a flat plate with a shell is to fix frequency and look at the loci of wavenumbers in wavenumber space, that is, $k_x a - n$ space. The loci for the propagating compressional, shear, and flexural wavenumbers are plotted in Figure 2.6 for $\Omega = 2$. Because I have assumed that the plate is

Figure 3-3: Absolute values of $n = 2$ compressional and shear wave eigenvectors normalized by radial displacment for a cylindrical shell with $h/a = 2\%$, $\nu = .2$, and $\eta = .05$. Legend: axial(solid), circumferential(dash).

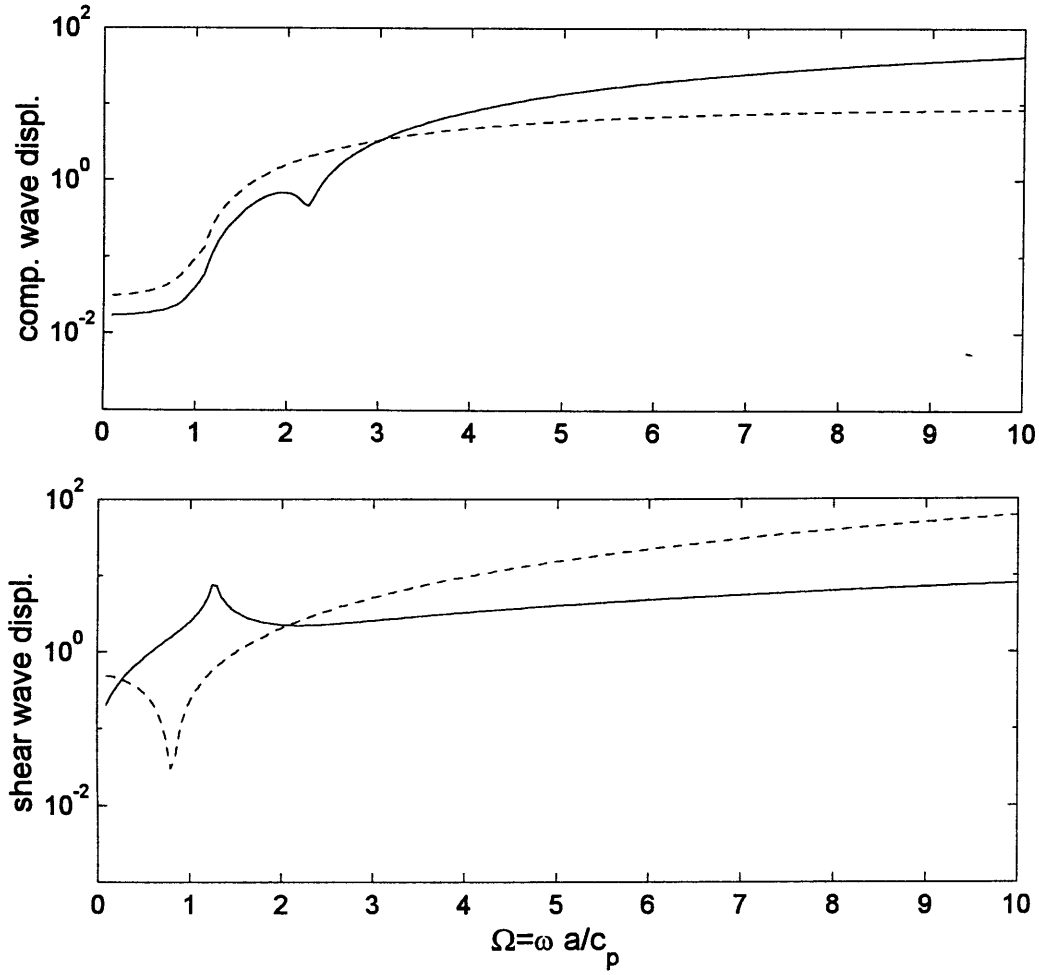

infinitely extended, its trajectories are continuous. The shell model trajectories are plotted for all real n that are not cutoff. The plate loci are perfect circles. The flexural wave is the largest circle because it has the slowest wave speed and the figure shows that the wave speed for each wave is the same in all directions. The shell model shows that the flexural wave in the axial direction is faster than in the circumferential direction. The flexural wave speed in circumferential direction is about that of the plate model.

Figure 3-4: Absolute values of $n = 2$ flexural and evanescent wave eigenvectors normalized by radial displacment for a cylindrical shell with $h/a = 2\%$, $\nu = .2$, and $\eta = .05$. Legend: axial(solid), circumferential(dash).

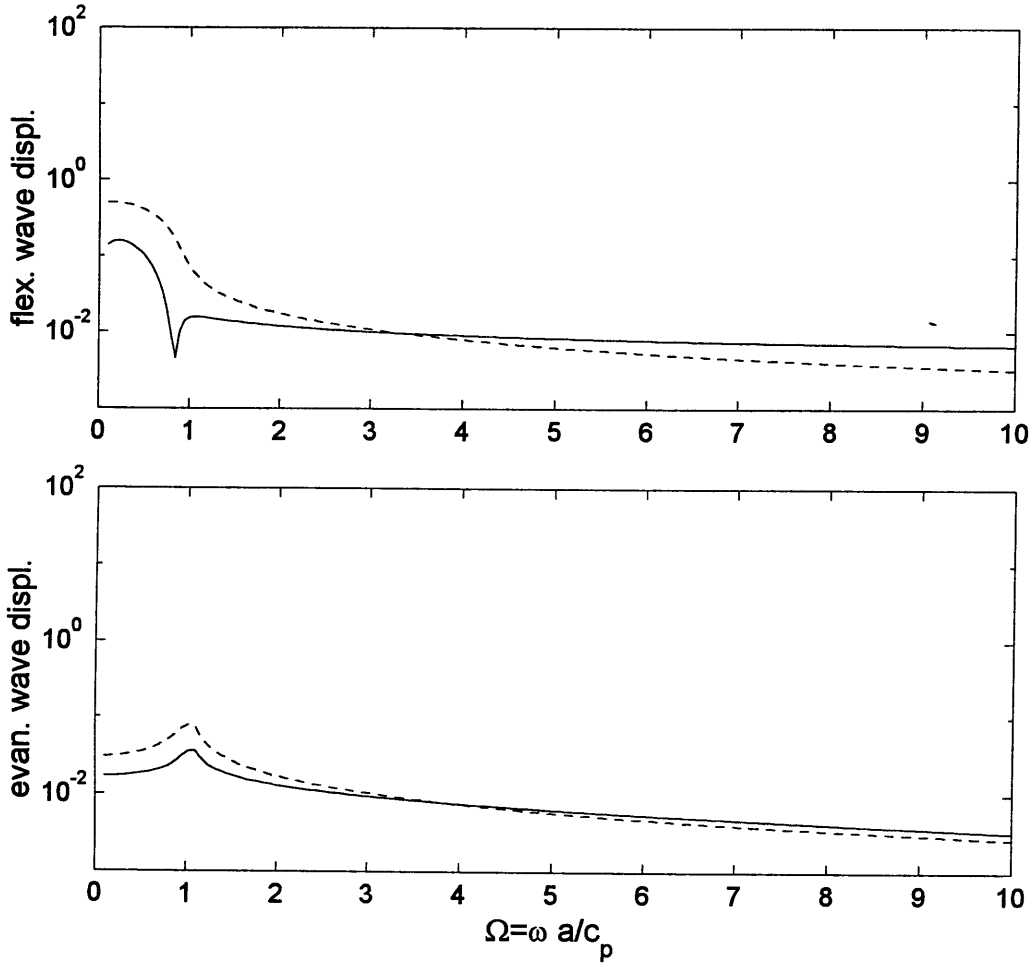

3.5.3 Free wave solution

If I denote the free wave vector associated with k_j as $\mathbf{E}_j$, then the shell displacements anywhere on the shell are some linear combination of these ten solutions. This may be written as

$$\mathbf{U}(x) = \mathbf{D}_1(x)\,\mathbf{A}_1 + \mathbf{D}_2(x)\,\mathbf{A}_2, \tag{3.10}$$

where the two $5x5$ matrices are

$$\mathbf{D}_1(x) = \left[\ \mathbf{E}_1 e^{+\imath k_1 x},\ \ \mathbf{E}_2 e^{+\imath k_2 x},\ \ \ldots\ \ \mathbf{E}_5 e^{+\imath k_5 x}\ \right] \tag{3.11}$$

Figure 3-5: Comparison of $n = 2$ mode shell and flat plate dispersion relation for $h/a = 2\%$ and $\nu = .2$. Legend: shell(solid), plate(dashed).

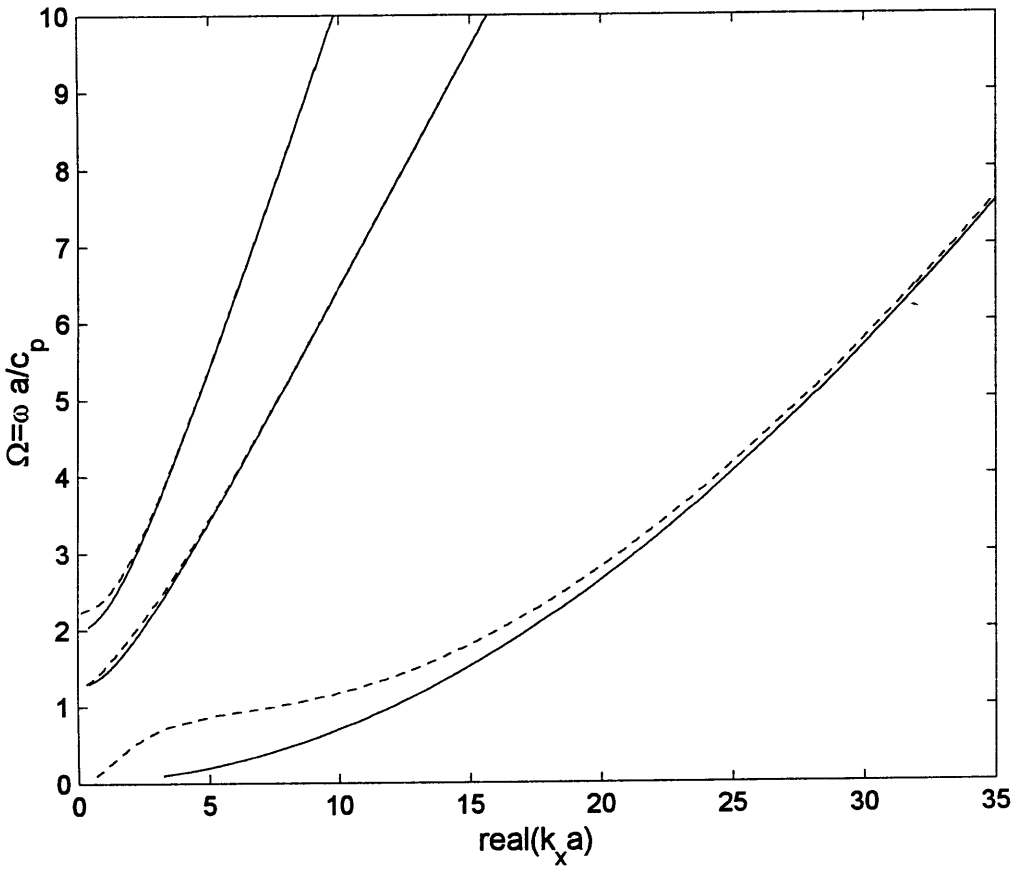

and

$$\mathbf{D}_2(x) = \left[\begin{array}{cccc} \mathbf{E}_6 e^{-\imath k_1 x}, & \mathbf{E}_7 e^{-\imath k_2 x}, & \ldots & \mathbf{E}_{10} e^{-\imath k_5 x} \end{array} \right] \tag{3.12}$$

and the unknown amplitudes of the right and left going waves are contained in vectors

$$\mathbf{A}_1 = \left\{ \begin{array}{ccccc} A_1, & A_2, & A_3, & A_4, & A_5 \end{array} \right\}^T$$

and

$$\mathbf{A}_2 = \left\{ \begin{array}{ccccc} A_6, & A_7, & A_8, & A_9, & A_{10} \end{array} \right\}^T,$$

respectively. Note that $\mathbf{U}(x) \neq \mathbf{U}(k_x, n)$ and also that $\mathbf{U}$, $\mathbf{E}_j$, $\mathbf{D}_1$, $\mathbf{D}_2$, $\mathbf{A}_1$, and $\mathbf{A}_2$ all have an implied n dependence.

Figure 3-6: Shell (dotted) and flat plate (see legend) dispersion relation in wavenumber space at $\Omega = 2$ for $h/a = 2\%$ and $\nu = .2$. Legend: shell compressional(solid), shell shear(dashed), and shell flexural(dash-dot).

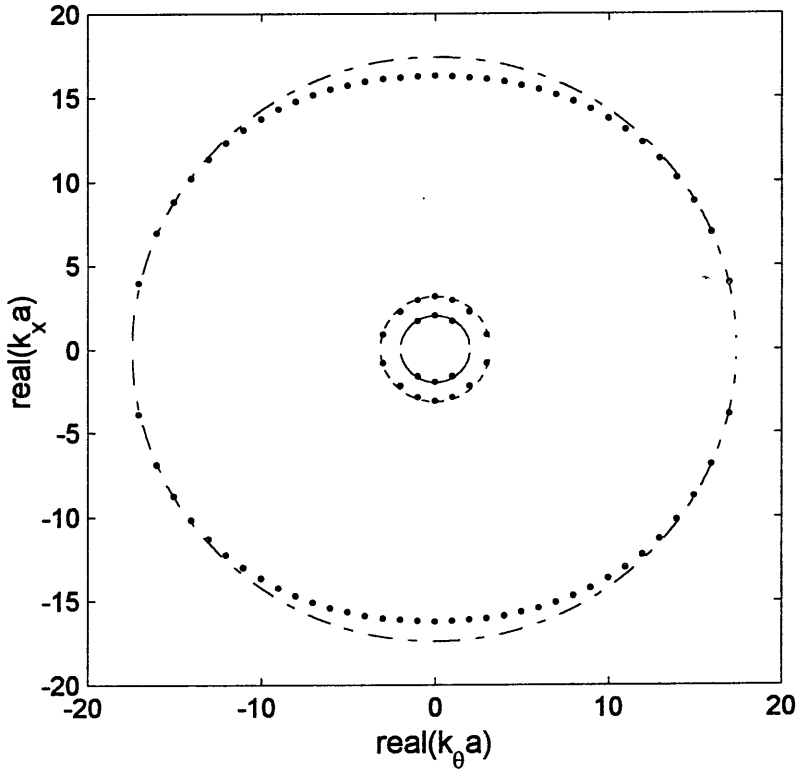

In a similar fashion, I may use Eq.(3.4) to calculate the associated free-wave forces (on the constant-x surface of the shell for reasons that will become clear when I formulate the WFEM stiffness matrix) and express the shell forces anywhere on the shell as

$$\mathbf{F}(x) = \mathbf{C}_1(x)\,\mathbf{A}_1 + \mathbf{C}_2(x)\,\mathbf{A}_2, \tag{3.13}$$

where the auxiliary matrices are

$$\mathbf{C}_1(x) = \left[\; \mathbf{M}_x(k_1)\,\mathbf{E}_1 e^{+ik_1 x},\quad \mathbf{M}_x(k_2)\,\mathbf{E}_2 e^{+ik_2 x},\quad \ldots\quad \mathbf{M}_x(k_5)\,\mathbf{E}_5 e^{+ik_5 x} \;\right] \tag{3.14}$$

and

$$\mathbf{C}_2(x) = \left[\mathbf{M}_x(-k_1)\mathbf{E}_6 e^{-ik_1 x}, \quad \mathbf{M}_x(-k_2)\mathbf{E}_7 e^{-ik_2 x}, \quad \ldots \quad \mathbf{M}_x(-k_5)\mathbf{E}_{10} e^{-ik_5 x} \right]. \tag{3.15}$$

I'll make use of Eq.(3.10) and Eq.(3.13) in the following section.

3.5.4 WFEM stiffness matrix

The WFEM solution is expressed in terms of a stiffness matrix, which relates the ring forces applied at the ends of the shell to the resulting displacements. Mathematically, the solution I am looking for is

$$\mathbf{K}\{\mathbf{U}(x_1), \mathbf{U}(x_2)\}^T = \{\mathbf{F}_1, \mathbf{F}_2\}^T, \tag{3.16}$$

where $\mathbf{K}$ is the WFEM stiffness matrix (not to be confused with the WI stiffness matrix $\mathbf{K}(k_x, n)$ given in Eq.(3.16)), $\mathbf{U}_1$ and $\mathbf{U}_2$ are the left and right end displacements, and $\mathbf{F}_1$ and $\mathbf{F}_2$ are the left and right end external forces.

I may easily solve for the stiffness matrix using some of the above relations. The procedure is to first use Eq.(3.10) to relate the unknown wave amplitudes to the displacements as

$$\mathbf{D}\{\mathbf{A}_1, \mathbf{A}_2\}^T = \{\mathbf{U}_1, \mathbf{U}_2\}^T, \tag{3.17}$$

where

$$\mathbf{D} = \begin{bmatrix} \mathbf{D}_1(x_1) & \mathbf{D}_2(x_1) \\ \mathbf{D}_1(x_2) & \mathbf{D}_2(x_2) \end{bmatrix} \tag{3.18}$$

and then use Eq.(3.13) to relate the wave amplitudes to the internal forces as

$$\mathbf{C}\{\mathbf{A}_1, \mathbf{A}_2\}^T = \{-\mathbf{F}(x_1), \mathbf{F}(x_2)\}^T,$$

where

$$\mathbf{C} = \begin{bmatrix} -\mathbf{C}_1(x_1) & -\mathbf{C}_2(x_1) \\ \mathbf{C}_1(x_2) & \mathbf{C}_2(x_2) \end{bmatrix}. \tag{3.19}$$

The external forces must balance with the internal forces, I may eliminate the wave amplitudes from Eq.(4.13) and Eq.(4.15) to directly relate the forces to the displacements in Eq.(3.16). Therefore, the stiffness matrix may is

$$\mathbf{K} = \mathbf{C}\mathbf{D}^{-1}, \tag{3.20}$$

which represents the solution of the shell to externally applied ring forces at each end. When the

compressional and shear wave speeds are both pure real, $\mathbf{K}$ is Hermitian. Notice that to calculate $\mathbf{K}$ or its inverse (the compliance matrix) I need to invert either $\mathbf{D}$ or $\mathbf{C}$. To improve the conditioning of this inversion, I first redefine

$$\mathbf{D}_2(x) = \left[\begin{array}{cccc} \mathbf{E}_6 e^{ik_1 x_2} e^{-ik_1 x}, & \mathbf{E}_7 e^{ik_2 x_2} e^{-ik_2 x}, & \ldots & \mathbf{E}_{10} e^{ik_5 x_2} e^{-ik_5 x} \end{array} \right]$$

and

$$\mathbf{C}_2(x) = \left[\begin{array}{cccc} \mathbf{M}_x(-k_1)\,\mathbf{E}_6 e^{ik_1 x_2} e^{-ik_1 x}, & \mathbf{M}_x(-k_2)\,\mathbf{E}_7 e^{ik_2 x_2} e^{-ik_2 x}, & \ldots & \mathbf{M}_x(-k_5)\,\mathbf{E}_{10} e^{ik_5 x_2} e^{-ik_5 x} \end{array} \right],$$

where I have referenced the left-going waves (propagating, decaying, or both) to the right end of the shell element.

The stiffness matrix given by Eq.(4.17) may be used in the same way as any conventional FEM stiffness matrix [1]. In general, an element is part of some global system of elements subjected to a combination of external forces. A global stiffness matrix made up of the individual element stiffness matrices is assembled and inverted to solve for the element displacements. Having solved for these displacments, the sorted wave amplitudes are found in post-processing simply by solving Eq.(4.12). The first five wave amplitudes correspond to the right-going compressional, shear, flexural, evanescent, and through-thickness shear wave amplitudes, respectively. The remaining five are the sorted left-going wave amplitudes. The wave amplitudes are sorted because the eigenvalues and their associated eigenvectors were sorted when forming $\mathbf{D}_1$, $\mathbf{D}_2$, $\mathbf{C}_1$, and $\mathbf{C}_2$ given by Eq.(3.11), Eq.(3.12), Eq.(3.14), and Eq.(3.15).

3.5.5 Shell response by wave type

Having solved for the wave amplitudes, the contribution to the total displacement at some position x due to a right-going wave of a particular wave type is

$$\mathbf{U}_j(x) = A_j \mathbf{E}_j e^{+ik_j x},$$

while the internal force is

$$\mathbf{F}_j(x) = A_j \mathbf{M}_x(-k_j)\,\mathbf{E}_j e^{+ik_j x}.$$

These two equations may also be used to calculate the associated time averaged power flow

$$\mathbf{\Pi}_j(x) = \frac{1}{2}\,\mathrm{Re}\left\{ [\mathbf{F}_j(x)]^{\dagger}\,\mathbf{U}_j(x) \right\}.$$

This expression is useful when calculating reflection and transmission coefficients. Similar expression are used to find the displacements, forces, and power flow for the left-going wave amplitudes.

3.5.6 Semi-infinite and infinite shells

Before moving on to some examples, I derive some additional results for shells with semi-infinite and infinite axial length.

Let's first consider a shell formulated that is semi-infinite in length with left end located at the origin. To satisfy the radiation condition at $x = \infty$, I set the left-going wave amplitudes to zero. The stiffness matrix at the left end of the shell is then

$$\mathbf{K} = \mathbf{C}_{11} \left[\mathbf{D}_{11}\right]^{-1}, \tag{3.21}$$

where the subscripts refer to the second quadrant submatrices of the $\mathbf{D}$ and $\mathbf{C}$ matrices defined by Eq.(3.18) and Eq.(3.19).

Similarly, the stiffness matrix for a semi-infinite shell extending to the left is

$$\mathbf{K} = \mathbf{C}_{22} \left[\mathbf{D}_{22}\right]^{-1}, \tag{3.22}$$

where the subscripts refer to the fourth quadrant submatrices of the $\mathbf{D}$ and $\mathbf{C}$ matrices.

Following standard FEM procedures for assembling collection of elements, the stiffness of an infinitely long shell is

$$\mathbf{K} = \mathbf{C}_{11} \left[\mathbf{D}_{11}\right]^{-1} + \mathbf{C}_{22} \left[\mathbf{D}_{22}\right]^{-1}, \tag{3.23}$$

which is just the sum of the two previous results. The motions of the infinite shell to sums of ring forces of different circumferential order is

$$\mathbf{u}(x,\theta) = \frac{1}{2\pi} \sum_{n=-\infty}^{\infty} \left[\mathbf{K}(n)\right]^{-1} \mathbf{F}(n)\, e^{+in\theta},$$

where $\mathbf{K}(n)$ is given by Eq.(3.23). The above equation clearly shows how the use of the WFEM approach eliminates the integration over axial wavenumber k_x.

3.6 Shell with an infinite axial length and incomplete circular cross-section

As mentioned earlier, when there is an axial line of discontinuity on the surface of the shell due to some internal attachment, such as a keel, it is advantageous to formulate a stiffness matrix in terms of circumferential waves. The formulation follows closely that outlined for the axial wave formulation. I assume that the shell extends from $\theta = \theta_1 = 0$ to $\theta = \theta_2 = L_\theta/a$. I will consider the $\theta = 0$ position as the left end of the shell. Throughout this section, there is an implied dependence of k_x for all variables.

3.6.1 Wave dispersion

To find the dispersion relation for circumferential waves, I follow the same general procedure with the following differences. In order to think about waves in the circumferential direction, I need to extend the angular domain of the shell to infinity. This technique is used by Felsen, among others [32]. I discussed its' justification in Chapter 2 in terms of a simple rod problem. The same arguments apply to the consideration of the circumferential waves. The complication of the added dimension does not change the arguments. This means that the helical wave transform is now redefined in terms of a double integral as

$$f(x,\theta) = \frac{1}{(2\pi)^2} \int_{n=-\infty}^{\infty} \int_{k_x=-\infty}^{\infty} F(k_x,n)\, e^{+\imath k_x x} e^{+in\theta} dk_x dn \quad \Leftrightarrow \quad F(k_x,n) = \int_{\theta=-\infty}^{\infty} \int_{x=-\infty}^{\infty} f(\theta,z)\, e^{-\imath k_x x} e^{-\imath n\theta} dx d\theta, \tag{3.24}$$

where n is now the non-dimensional, non-integer wavenumber in the circumferential direction and k_x is the real wavenumber component in the axial direction. The spectrum of n in the frequency-circumferential wavenumber domain is now continuous.

Another difference, is that in order to find the circumferential wavenumbers, I redefine the c_m coefficients in Eq.(A.1), such that

$$\mathbf{K}(k_x,n) = \begin{bmatrix} c_1 + c_2 n^2 & c_3 n & c_4 & 0 & c_5 + c_6 n^2 \\ c_3 n & c_7 + c_8 n^2 & c_9 n & c_{10} + c_{11} n^2 & 0 \\ -c_4 & -c_9 n & c_{12} + c_{13} n^2 & c_{14} n & c_{15} \\ 0 & c_{10} + c_{11} n^2 & -c_{14} n & c_{16} + c_{17} n^2 & c_{18} n \\ c_5 + c_6 n^2 & 0 & -c_{15} & c_{18} n & c_{19} + c_{20} n^2 \end{bmatrix} \tag{3.25}$$

and consider the characteristic polynomial of $\mathbf{K}$ in terms of n^2. The final difference relates to finding

the eigenvectors for the special case of $k_x = 0$. In this case, the V, W, and Ψ_θ, are decoupled from U, W, and Ψ_x. Other than these differences, the eigenvalues are found in the same manner as above.

I should note that Borgiotti and Rosen also solved the dispersion for the axial waves. Their shell theory was based on the Hermann-Mirsky theory with some modifications. Their technique was to manipulate the governing equations (including the internal force-displacement equations) so that their eigenvalue problem associated with some matrix, call it $\mathbf{A}$, does not have k_x appearing in the off-diagonal terms. However, the matrix $\mathbf{A}$ is not in the form suitable for solving for the free waves in the circumferential direction. I have shown here that their manipulation is not necessary in any case and that the off-diagonal terms are easily handled. Furthermore, I detected an error in their formulation that results in a stiffness matrix $\mathbf{K}$ that is non-Hermitian when c_p is pure real indicating a theory that does not adhere to reciprocity.

3.6.2 Circumferential wave formulation

If the five n_j roots are ordered by wave-type as before and $\mathbf{E}_j$ are the corresponding eigenvectors, then the displacements anywhere on the shell are

$$\mathbf{U}(\theta) = \mathbf{D}_1(\theta)\,\mathbf{A}_1 + \mathbf{D}_2(\theta)\,\mathbf{A}_2,$$

where

$$\mathbf{D}_1(\theta) = \left[\begin{array}{cccc} \mathbf{E}_1 e^{in_1\theta}, & \mathbf{E}_2 e^{in_2\theta}, & \ldots & \mathbf{E}_5 e^{in_5\theta} \end{array}\right]$$

and

$$\mathbf{D}_2(\theta) = \left[\begin{array}{cccc} \mathbf{E}_1 e^{in_1\theta_2} e^{-in_1\theta}, & \mathbf{E}_2 e^{in_2\theta_2} e^{-in_2\theta}, & \ldots & \mathbf{E}_5 e^{in_5\theta_2} e^{-in_5\theta} \end{array}\right].$$

Similarly, the forces on the constant-θ surface are

$$\mathbf{F}(\theta) = \mathbf{C}_1(\theta)\,\mathbf{A}_1 + \mathbf{C}_2(\theta)\,\mathbf{A}_2,$$

where

$$\mathbf{C}_1(\theta) = \left[\begin{array}{cccc} \mathbf{M}_s(n_1)\,\mathbf{E}_1 e^{in_1\theta}, & \mathbf{M}_s(n_2)\,\mathbf{E}_2 e^{in_2\theta}, & \ldots & \mathbf{M}_s(n_5)\,\mathbf{E}_5 e^{in_5\theta} \end{array}\right]$$

and

$$\mathbf{C}_2(\theta) = \left[\begin{array}{cccc} \mathbf{M}_s(-n_1)\,\mathbf{E}_6 e^{in_1\theta_2} e^{-in_1\theta}, & \mathbf{M}_s(-n_2)\,\mathbf{E}_7 e^{in_2\theta_2} e^{-in_2\theta}, & \ldots & \mathbf{M}_s(-n_5)\,\mathbf{E}_{10} e^{in_5\theta_2} e^{-in_5\theta} \end{array}\right]$$

is defined in terms of the constitutive relation given by Eq.(3.5). The zero phase reference for $\mathbf{D}_2(\theta)$, and $\mathbf{C}_2(\theta)$ is at θ_2.

Using the same procedure as for the axial wave formulation, the stiffness matrix is given by Eq.(4.17) provided I redefine

$$\mathbf{D} = \begin{bmatrix} \mathbf{D}_1(\theta_1) & \mathbf{D}_2(\theta_1) \\ \mathbf{D}_1(\theta_2) & \mathbf{D}_2(\theta_2) \end{bmatrix} \tag{3.26}$$

and

$$\mathbf{C} = \begin{bmatrix} -\mathbf{C}_1(\theta_1) & -\mathbf{C}_2(\theta_1) \\ \mathbf{C}_1(\theta_2) & \mathbf{C}_2(\theta_2) \end{bmatrix}. \tag{3.27}$$

In addition, the sorted wave amplitudes are found in the same manner as previously described.

3.6.3 Semi-infinite and infinite shells

The concept of a shell with semi-infinite or infinite length in the circumferential direction is somewhat strange. I'll discuss why it may be useful at the end of this chapter and in Chapter 6.

The stiffness matrix relations derived here follow in a completely analogous manner to those derived in Section 3.5.6. The stiffness matrix for a semi-infinite long circumferential length with its' end located at $\theta = 0$ and extending out towards $\theta = \infty$ is given by

$$\mathbf{K} = \mathbf{C}_{11}\left[\mathbf{D}_{11}\right]^{-1},$$

where $\mathbf{D}$ and $\mathbf{C}$ matrices defined by Eq.(3.26) and Eq.(3.27).

Similarly, the stiffness matrix for a semi-infinite shell extending to $\theta = -\infty$ is

$$\mathbf{K} = \mathbf{C}_{22}\left[\mathbf{D}_{22}\right]^{-1},$$

where the subscripts refer to the fourth quadrant submatrices of the $\mathbf{D}$ and $\mathbf{C}$ matrices.

Following standard FEM procedures for assembling collection of elements, the stiffness of an infinitely long shell is

$$\mathbf{K} = \mathbf{C}_{11}\left[\mathbf{D}_{11}\right]^{-1} + \mathbf{C}_{22}\left[\mathbf{D}_{22}\right]^{-1}, \tag{3.28}$$

which is just the sum of the two previous results. The motions of the infinite shell to sums of ring forces of different circumferential order is

$$\mathbf{u}(x,\theta) = \frac{1}{2\pi}\int_{k_x=-\infty}^{\infty} \left[\mathbf{K}(k_x)\right]^{-1}\mathbf{F}(k_x)\, e^{+\imath k_x x} e^{+\imath n\theta} dk_x,$$

where $\mathbf{K}(k_x)$ is given by Eq.(3.23). The above equation clearly shows how the use of the WFEM approach eliminates the summation over n.

3.7 Examples

In Chapter 6, I compare some experimental results for a finite length shell excited by an array of piezoelectric sources to WFEM model predictions. In this section, I consider two examples that are related to the problem considered in Chapter 6. These examples serve to demonstrate the usefulness of both the axial and circumferential wave formulations discussed in this Chapter by emphasizing the numerical efficiency of the WFEM method compared to the WI method.

In the first example, I calculate the drive point displacement of an infinitely extended shell to an axial force. In the second example, I consider the same problem, only this time, the force is applied in the circumferential direction. I want to emphasize that the dimensions of the shell are infinite in both the axial and circumferential directions. This removes the effects of virtual image sources and the drive point displacement is a true measure of the local shell compliance. It also means that the appropriate transform is that given by Eq.(3.24), where the summation over circumferential index becomes an integral over all real values of n. The comparison of the two examples is a measure of the local shell isotropy. I'll discuss this further in Chapter 6.

For both examples, the shell material and geometric properties are the same. The shell has $\rho = c_p = a = 1$, $h = .02$, $\nu = .3$, and $\eta = .05$.

3.7.1 Concentrated axial force

For the first example, I drive the shell in the axial direction with the distributed force

$$\mathbf{f}(x,\theta) = \delta(x)\, g(\theta)\, \{1,0,0,0,0\}^T,$$

where $\delta(x)$ is the Dirac delta function and $g(\theta)$ is some force distribution in the θ direction. The shell displacement response at the drive point at the center of the applied force distribution is

$$\mathbf{u}(x,\theta)|_{x=\theta=0} = \{u,v,w,\psi_\theta,\psi_x\}^T\Big|_{x=\theta=0} = \frac{1}{2\pi}\int_{n=-\infty}^{\infty} [\mathbf{K}(n)]^{-1}\,\mathbf{G}(n)\,dn, \tag{3.29}$$

where $\mathbf{K}(n)$ is given by Eq.(3.23) and $\mathbf{G}(n)$ is the transform of $g(\theta)$.

One might be tempted to set

$$g(\theta) = \delta(\theta),$$

which means that

$$\mathbf{G}(n) = 1.$$

Figure 3-7: Absolute value of the real and imaginary parts of integrand $U(n)$ versus n (without Gaussian weighting).

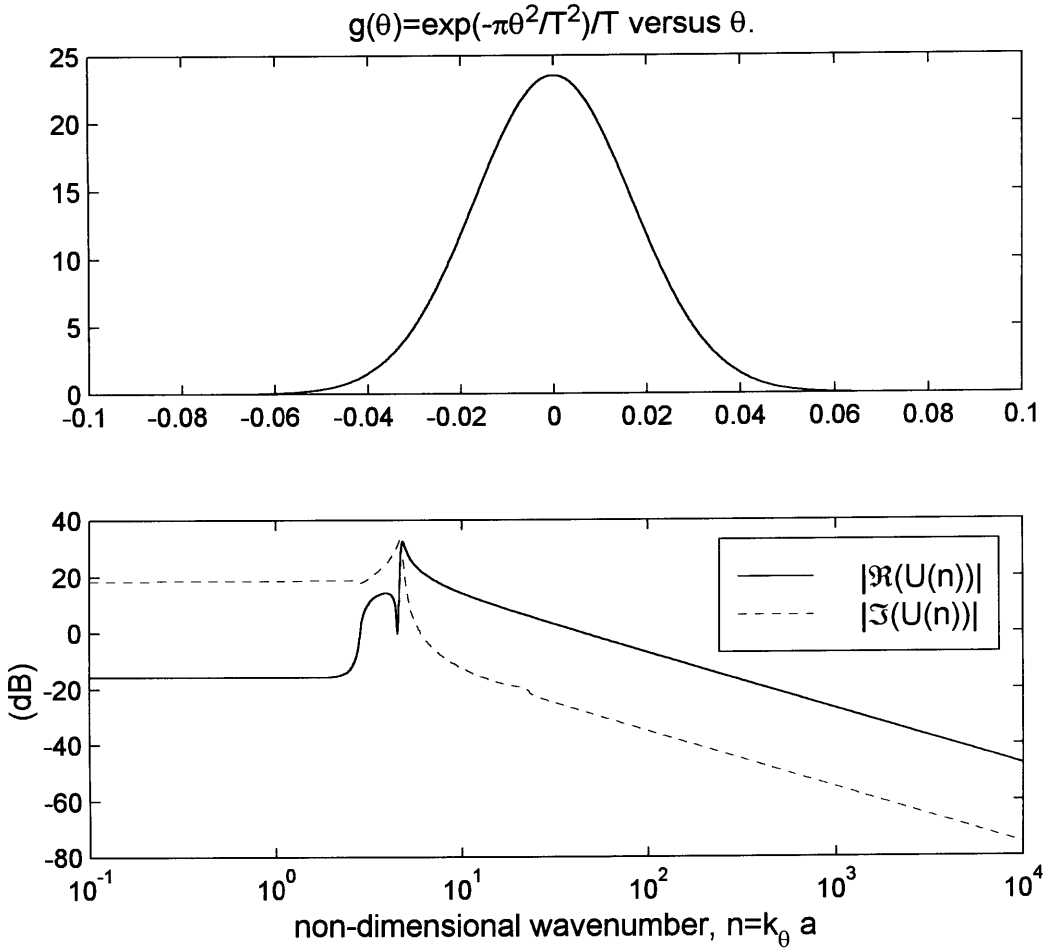

The problem with this approach is that the integrand in Eq.(3.29) approaches $1/n$ for large n and, therefore, does not converge. To illustrate this, I plot the $U(n)$ versus n when $\Omega = 3$ in Figure 3.7.

Therefore, to make Eq.(3.29) converge, I set

$$g(\theta) = \frac{1}{T} \exp\left(\frac{-\pi\theta^2}{T^2}\right), \tag{3.30}$$

which is a Gaussian function defined by the spatial constant T. I select T so that the Gaussian decays to half its' peak value at $\theta = .02$, which corresponds to the thickness dimension of the shell. The transform of $g(\theta)$ is given by

$$\mathbf{G}(n) = \exp\left(\frac{-T^2 n^2}{4\pi}\right).$$

Both $g(\theta)$ and $\mathbf{G}(n)$ are plotted in Figure 3.8. To solve for the drive point displacement due to the

Figure 3-8: Gaussian forcing function spatial and circumferential wavenumber distributions. a.) $g(\theta)$ versus θ b.) $\mathbf{G}(n)$ versus n

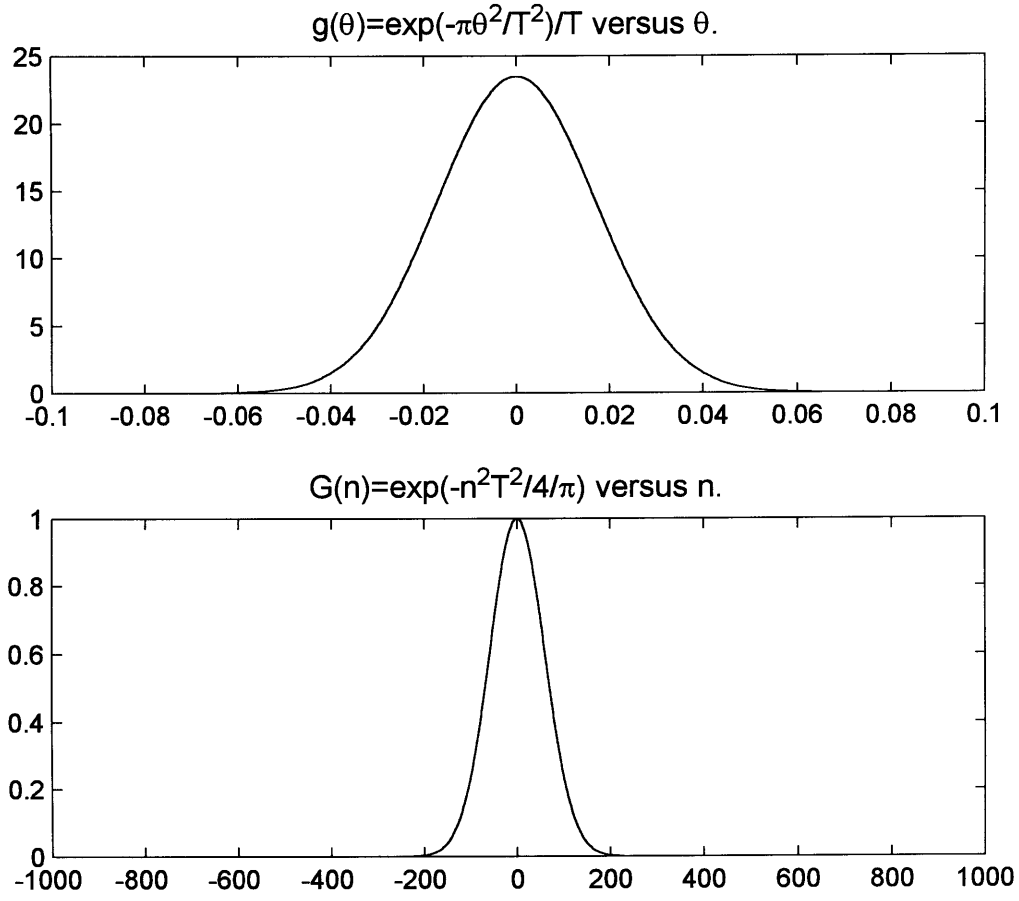

Gaussian force distribution, I use an adaptive recursive Newton-Cotes 8 panel rule to integrate Eq.(3.29) over n for the frequency range from $\Omega = .5$ to $\Omega = 3$. I'll withhold presenting the results till the next section.

3.7.2 Concentrated circumferential force

For the second example, I drive the shell in the circumferential direction with the distributed force

$$\mathbf{f}(x,\theta) = \delta(\theta)\, g(x)\, \{0,1,0,0,0\}^T,$$

where I use the Gaussian force distribution $g(x)$ defined by Eq.(3.30). The shell displacement response at the drive point at the center of the applied force distribution is

$$\mathbf{u}(x,\theta)|_{x=\theta=0} = \{u,v,w,\psi_\theta,\psi_x\}^T\Big|_{x=\theta=0} = \frac{1}{2\pi}\int_{k_x=-\infty}^{\infty} [\mathbf{K}(k_x)]^{-1}\,\mathbf{G}(k_x)\,dk_x,$$

where $\mathbf{K}(k_x)$ is defined by Eq.(3.28). The integral over k_x is evaluated using the Newton-Cotes method.

I present the results for the drive point displacment $u(0,0)$ from the first example compared to $v(0,0)$ from the second example in Figure 3.9. The real part of the displacments are presented in Figure 3.9a, while the imaginary parts are presented in Figure 3.9b. It is reassuring to see that the imaginary parts are always greater than zero because postive imaginary parts represent systems that dissipate energy. It is also reassuring that at the higher frequencies, the displacements are nearly equal. This is also expected because the shell curvature is getting small compared to the shell wavelengths. The results also show that below the ring frequency, the shell is no longer isotropic to in-plane forcing.

Figure 3-9: Real and imaginary parts of shell drive point response to Gaussian forcing in axial (solid) and circumferential (dashed) directions versus frequency. a.) real part of $u(0,0)$ and $v(0,0)$ b.) imaginary part of $u(0,0)$ and $v(0,0)$

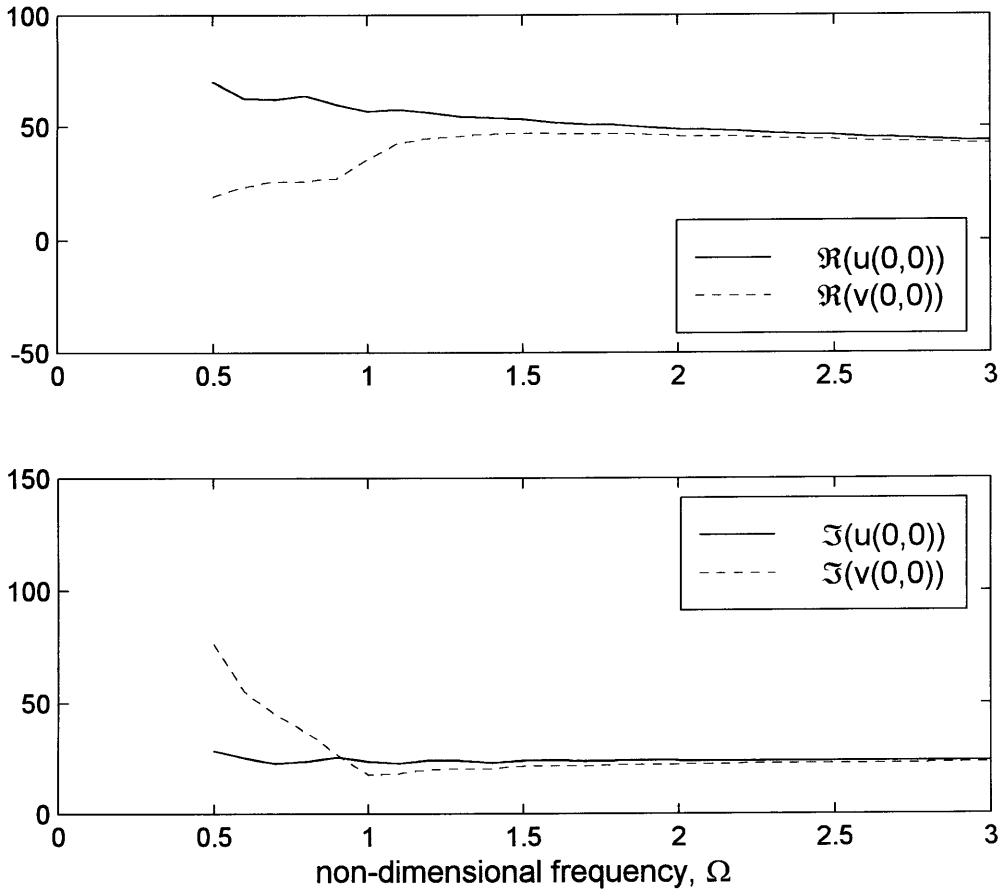

Chapter 4

Wave FEM analysis of a 3D cylindrical shell

4.1 Introduction

I have shown in Chapter 2 that for the 1D rod that the WFEM method may be used to effectively eliminate the wavenumber integration in the axial direction. I have also shown in Chapter 3 for the 2D shell that WFEM may be applied to eliminate the wavenumber integration in either the axial or circumferential directions. Finally, in this chapter, I show how I apply WFEM to the Navier equations for a 3D cylindrical shell to eliminate the wavenumber integration in the radial or thickness direction. I use the 3D shell in the following chapter to test the limits of my 2D shell model.

In this chapter, I demonstrate the use of the 3D model by solving the four layer cylindrical shell system shown in Figure 1. This four layer system is really a quite general representation of multi-layered systems. I consider both a distributed traction force and a point volume source. I conclude the chapter with discussion of the relative merits of the WFEM approach versus two other methods referenced in the following section.

I use the 3D shell model in the following chapter to test the limits of the Herrmann-Mirsky 2D shell theory versus thickness and frequency.

4.2 Previous work

In related work, Schmidt and Jensen developed the Direct Global Matrix approach (DGM) for infinitely extended, horizontally layered media [34]. The feature of this method is numerical stability in the

presence of through-thickness evanescence. Using the DGM method, a global matrix is formed, which relates the wave amplitudes in each layer to both stress and displacement boundary conditions at the interfaces between each layer. For the DGM method, the wave amplitudes are the unknown degrees of freedom of the problem.

Pathak and Stepanishen solved for the acoustic scattering from a single layer cylindrical shell using the 3D Navier equations [23]. Their shell solution is generalized by Ricks [10] using Schmidt and Jensen's DGM approach. Ricks used two scaling procedures to prevent overflow and underflow of the Bessel function solutions. The first is the usual exponential scaling for arguments with large imaginary parts, which occurs when the wave solution is evanescent in the through-thickness or radial direction. The second scaling is for small arguments, which occurs when the axial wavenumber approaches the material wavenumber. The sensitivity of the Bessel functions to small argument increases with increasing circumferential order.

The WFEM stiffness matrix approach was applied to horizontally layered media by Kausel and Roësset [33]. Although they did not use the acronym WFEM but referred to it as the stiffness matrix approach (Remember that I use the WFEM method to distinguish the exact wave-based method from conventional FEM methods.). Another related method is the Thin Layer Method (TLM) used by Kausel [36] and Tassoulas [35] to analyze horizontally layered media. Using TLM, each layer is essentially a conventional FEM element. By using linear shape functions the characteristic equation of the global stiffness matrix is algebraic in axial wavenumber rather than transcendental. This allows the integration over horizontal wavenumber to be done analytically. Thus TLM eliminates integration in both the radial and axial directions. The disadvantage is that many elements must be used for acoustically thick layers.

4.3 Original contributions

My own contribution is a WFEM formulation for multi-layered cylindrical shells. Both DGM and WFEM are wave-based methods and exact to within underlying equations. The key difference between the methods is that the WFEM global matrix is a global *stiffness* matrix, where the unknowns of the problem are the layer interface *displacements* rather than *wave amplitude*. The size of the global stiffness matrix is about $4x$ smaller than the global DGM matrix due to the fact that the total number of *displacement* degrees of freedom at the layer interfaces is half the number of *wave amplitude* degree of freedom within a layer. The global stiffness matrix is also symmetric about the main diagonal, which further reduces the size of the global matrix. The good numerical stability of the DGM method is retained and wave amplitudes may still be found in post-processing for any or all shell layers if desired. Also, because the stiffness matrix relates displacements directly to interface surface stresses, unidirectional

point forces may be applied directly to the layer interfaces.

In this chapter, I show how to formulate a stiffness matrix for a layer with finite inner and outer radii, a core layer with zero inner radius, an infinitely extended layer with infinite outer radius, and a infinitely extended medium. All layers may be either solids or fluids. The format in which I present the layer equations is such that these special cases precipitate out with little additional effort. As I show at the end of this chapter, this makes for some very compact programming. Formulating in terms of a stiffness matrix brings to bear all the well known conventional FEM procedures for solving assemblages of multiple elements [1], which in this case is multiple shell layers.

In addition to the force excitation, I derive the point volume source excitation to round out the WFEM formulation for cylindrically layered media. The point volume source is a fundamental method of excitation and was not considered by either Pathak or Ricks. The solution is given for both an elastic and fluid layer.

4.4 Governing Equations

Here I consider the dynamics of an individual cylindrical shell layer. The cylinder is referred to the cylindrical coordinate system $\{r, \theta, z\}$, where r is the radial direction, θ is the circumferential direction, and z is the axial direction with the corresponding shell displacement vector

$$\mathbf{u}(r, \theta, z) = \{u, v, w\}^T .$$

Note that this cylindrical coordinate system is different than that used for the 2D shell. The cylinder is made out of a linear-elastic solid with density ρ, and Lame' constants λ and μ. The inner radius of the shell is at $r = r_1$ and the outer radius is at $r = r_2$. Throughout this chapter, I assume a steady state time dependence of $e^{-i\omega t}$ for all variables, which is hereafter implied.

The homogeneous displacement-based momentum equations for the shell are given by Achenbach [22] as

$$\mu \nabla^2 \mathbf{u} + (\lambda + \mu) \boldsymbol{\nabla} (\boldsymbol{\nabla} \cdot \mathbf{u}) + \omega^2 \rho \mathbf{u} = 0,$$

where I have used the assumed time dependence to carry out the derivatives on the inertial term. Using the Helmholtz decomposition of the displacement vector, Pathak and Stepanishen show that the displacements may be written as

$$\mathbf{u} = \boldsymbol{\nabla}\phi + \boldsymbol{\nabla} \times \psi \mathbf{a}_z + \boldsymbol{\nabla} \times \boldsymbol{\nabla} \times (\chi \mathbf{a}_z), \tag{4.1}$$

where ϕ is the dilational potential function, and ψ, and χ are two shear potential functions. The three potentials satisfy the uncoupled wave equations:

$$\begin{aligned} \left(\nabla^2 + h^2\right)\phi &= 0 \\ \left(\nabla^2 + k^2\right)\psi &= 0 \\ \left(\nabla^2 + k^2\right)\chi &= 0, \end{aligned} \tag{4.2}$$

where the dilational wavenumber is

$$h = \omega/c_d = \omega/\sqrt{(\lambda + 2\mu)/\rho}, \tag{4.3}$$

the shear wavenumber is

$$k = \omega/c_s = \omega/\sqrt{\mu/\rho}, \tag{4.4}$$

and the Laplacian scalar operator in cylindrical coordinates is

$$\nabla^2 = \left(\frac{\partial^2}{\partial r^2} + \frac{1}{r}\frac{\partial}{\partial r}\right) + \frac{1}{r^2}\frac{\partial^2}{\partial^2\theta} + \frac{\partial^2}{\partial^2 z}.$$

Using Eq.(4.1), Ricks shows that the displacements may be written in terms of the potential functions as:

$$\begin{aligned} u &= \phi_{,r} + \frac{1}{r}\psi_{,\theta} + \chi_{,rz} \\ v &= \frac{1}{r}\phi_{,\theta} - \psi_{,r} + \frac{1}{r}\chi_{,\theta z} \\ w &= \phi_{,z} + \chi_{,rr} + \frac{1}{r}\chi_{,r} + \frac{1}{r^2}\chi_{,\theta\theta}, \end{aligned} \tag{4.5}$$

and the stresses on the constant-r surface, defined in terms of the displacements, are:

$$\begin{aligned} \sigma_{rr} &= \lambda\left(u_{,r} + \frac{1}{r}u + \frac{1}{r}v_{,\theta} + w_{,z}\right) + 2\mu u_{,r} \\ \sigma_{r\theta} &= \mu\left(v_{,r} - \frac{1}{r}v + \frac{1}{r}u_{,\theta}\right) \\ \sigma_{rz} &= \mu\left(u_{,z} + w_{,r}\right). \end{aligned} \tag{4.6}$$

4.5 Transformed equations

To solve for the dynamics of the shell, I use wavenumber integration in the axial direction, modal summation in the circumferential direction, and the *WFEM* technique in the radial direction. I define

the axial and circumferential transforms as

$$u(r,\theta,z) = \frac{1}{(2\pi)^2} \sum_{n=-\infty}^{\infty} \int_{s=-\infty}^{\infty} \hat{u}(r,n,s)\, e^{+\imath sz} e^{+in\theta} ds \quad \Leftrightarrow \quad \hat{u}(r,n,s) = \int_{\theta=0}^{2\pi} \int_{z=-\infty}^{\infty} u(r,\theta,z)\, e^{-\imath sz} e^{-\imath n\theta} dz d\theta, \tag{4.7}$$

where s is the axial wavenumber and n is the circumferential index. Using this transform, it may be shown that the set of wave equations in Eq.(4.2) transform to Bessel's equations with Bessel function solutions. The potential functions may then be written in terms of six unknown wave amplitudes as:

$$\begin{aligned}
\hat{\phi} &= A_1 H_n^{(1)}(h_r r)\left(H_n^{(1)}(h_r r_1)\right)^{-1} + A_2 J_n(h_r r) H_n^{(1)}(h_r r_2) = A_1 F_1 + A_2 F_2 \\
\hat{\psi} &= B_1 H_n^{(1)}(k_r r)\left(H_n^{(1)}(k_r r_1)\right)^{-1} + B_2 J_n(k_r r) H_n^{(1)}(k_r r_2) = B_1 G_1 + B_2 G_2 \\
\hat{\chi} &= C_1 H_n^{(1)}(k_r r)\left(H_n^{(1)}(k_r r_1)\right)^{-1} + C_2 J_n(k_r r) H_n^{(1)}(k_r r_2) = C_1 G_1 + C_2 G_2,
\end{aligned} \tag{4.8}$$

where the radial dependance for a particular wave is given by a linear combination of two independent Bessel functions, corresponding in some manner to the sum of an outgoing and an incoming wave. The arguments for the Bessel functions are written in terms of the radial component of the dilational and shear wavenumbers at infinite radius defined as

$$h_r^2 = h^2 - s^2$$

and

$$k_r^2 = k^2 - s^2,$$

respectively. The normalization of the Bessel functions is that given by Ricks [10] and I introduce the shorthand notation, F_j and G_j, for the various normalized functions.

It is useful to define the wave amplitude vector

$$\mathbf{A} = \{\mathbf{A_1}, \mathbf{A_2}\}^T$$

in terms of two additional wave amplitude vectors

$$\mathbf{A}_j = \{A_j, B_j, C_j\}^T.$$

I may evaluate the derivatives in Eq.(4.5) through Eq.(4.6) to relate the potential functions to the displacements as

$$\mathbf{D}_1(r)\,\mathbf{A}_1 + \mathbf{D}_2(r)\,\mathbf{A}_2 = \{\hat{u}(r), \hat{v}(r), \hat{w}(r)\}^T, \tag{4.9}$$

where the auxiliary matrices are defined by

$$\mathbf{D}_j(r) = \begin{bmatrix} F_{j,r} & i\frac{n}{r}G_j & isG_{j,r} \\ i\frac{n}{r}F_j & -G_{j,r} & -s\frac{n}{r}G_j \\ isF_j & 0 & k_r^2 G_j \end{bmatrix}.$$

The first and second derivatives for either the Bessel or Hankel functions of the first kind are given by

$$\begin{aligned} y_n(\alpha r)_{,r} &= -\alpha y_{n+1}(\alpha r) + \left(\frac{n}{r}\right) y_n(\alpha r) \\ y_n(\alpha r)_{,rr} &= \alpha\left(\frac{1}{r}\right) y_{n+1}(\alpha r) + \left(-\alpha^2 - \left(\frac{1}{r}\right)\left(\frac{n}{r}\right) + \left(\frac{n}{r}\right)^2\right) y_n(\alpha r). \end{aligned}$$

Similarly, using Eq.(4.6) through Eq.(4.7), I may relate the wave amplitudes to the stresses as

$$\mathbf{C}_1(r)\,\mathbf{A}_1 + \mathbf{C}_2(r)\,\mathbf{A}_2 = \{\hat{\sigma}_{rr}(r), \hat{\sigma}_{r\theta}(r), \hat{\sigma}_{rz}(r)\}^T, \tag{4.10}$$

where

$$\mathbf{C}_j(r) = \begin{bmatrix} -\lambda h^2 F_j + 2\mu F_{j,rr} & i2\mu\frac{n}{r}\left(-\frac{1}{r}G_j + G_{j,r}\right) & i2\mu s G_{j,rr} \\ i2\mu\frac{n}{r}\left(-\frac{1}{r}F_j + F_{j,r}\right) & \mu\left(-\left(\frac{n}{r}\right)^2 G_j + \frac{1}{r}G_{j,r} - G_{j,rr}\right) & 2\mu s\frac{n}{r}\left(\frac{1}{r}G_j - G_{j,r}\right) \\ i2\mu s F_{j,r} & -\mu s\frac{n}{r}G_j & \mu\left(k_r^2 - s^2\right)G_{j,r} \end{bmatrix}.$$

4.6 Stiffness matrix formulation

In this section, I formulate the stiffness matrix $\mathbf{K}(n,s)$ for a solid layer, a fluid layer, a complete cylinder that is either solid or fluid, and an infinitely extended layer (a layer with an infinite outer radius) that is either solid or fluid. Formulating in terms of a stiffness matrix brings to bear all the well developed conventional FEM procedures for solving assemblages of multiple elements [1], which may be used to analyze multiple layers of shell elements.

4.6.1 Solid layer

For a solid layer, the stiffness matrix $\mathbf{K}(n,s)$ relates the shell stresses at the inner and outer surfaces to their corresponding displacements. The displacements are defined as

$$\mathbf{U} = \{\mathbf{U}_1, \mathbf{U}_2\}^T,$$

where

$$\mathbf{U}_j = \left\{\hat{u}\left(r_j\right), \hat{v}\left(r_j\right), \hat{w}\left(r_j\right)\right\}^T.$$

The stresses are defined as

$$\mathbf{F} = \left\{\mathbf{F}_1, \mathbf{F}_2\right\}^T,$$

where

$$\mathbf{F}_j = \left\{\hat{\sigma}_{rr}\left(r_j\right), \hat{\sigma}_{r\theta}\left(r_j\right), \hat{\sigma}_{rz}\left(r_j\right)\right\}^T. \tag{4.11}$$

To formulate the stiffness matrix, I may use Eq.(4.9) to relate the wave amplitudes to the displacements as

$$\mathbf{DA} = \mathbf{U}, \tag{4.12}$$

where

$$\mathbf{D} = \begin{bmatrix} \mathbf{D}_{11} & \mathbf{D}_{12} \\ \mathbf{D}_{11} & \mathbf{D}_{22} \end{bmatrix} = \begin{bmatrix} \mathbf{D}_1\left(r_1\right) & \mathbf{D}_2\left(r_1\right) \\ \mathbf{D}_1\left(r_2\right) & \mathbf{D}_2\left(r_2\right) \end{bmatrix}. \tag{4.13}$$

Similarly, I may use Eq.(4.10) to relate the wave amplitudes to the forces as

$$\mathbf{CA} = \mathbf{F}, \tag{4.14}$$

where

$$\mathbf{C} = \begin{bmatrix} \mathbf{C}_{11} & \mathbf{C}_{12} \\ \mathbf{C}_{11} & \mathbf{C}_{22} \end{bmatrix} = \begin{bmatrix} -\mathbf{C}_1\left(r_1\right) & -\mathbf{C}_2\left(r_1\right) \\ \mathbf{C}_1\left(r_2\right) & \mathbf{C}_2\left(r_2\right) \end{bmatrix}. \tag{4.15}$$

Note that I define the "force" at the inner radius in terms of negative stress, which is consistent with conventional FEM procedures. I may eliminate the wave amplitudes from Eq.(4.12) and Eq.(4.14) to relate the forces to the displacements as

$$\mathbf{KU} = \mathbf{F}, \tag{4.16}$$

where

$$\mathbf{K} = \mathbf{CD}^{-1} \tag{4.17}$$

is the $6x6$ stiffness matrix.

4.6.2 Symmetry properties of K

The layer stiffness matrix $\mathbf{K}$ defined by Eq.(4.17) is not symmetric with respect to its' main diagonal. To make it symmetric takes two steps. I first redefine Eq.(4.11) as

$$\mathbf{F}_j = \left\{ r_j \hat{\sigma}_{rr}\left(r_j\right), r_j \hat{\sigma}_{r\theta}\left(r_j\right), r_j \hat{\sigma}_{rz}\left(r_j\right) \right\}^T,$$

where the $\mathbf{F}_j$ is now force per axial length per radian. If I then redefine $\mathbf{C}_j\left(r\right)$, $\mathbf{C}$, and $\mathbf{K}$ consistent with the redefined $\mathbf{F}_j$, then $\mathbf{K}$ becomes Hermitian provided the Lame' constants are pure real numbers.

The second step is more involved. The layer stiffness matrix $\mathbf{K}$ is derived in terms of a helical wave solution to the governing equation. The spatial dependence of that wave is

$$\hat{\mathbf{u}}\left(r,n,s\right) = \left\{ \hat{u}, \hat{v}, \hat{w} \right\}^T = \mathbf{A} J_n\left(k_r r\right) e^{+\imath s z} e^{+in\theta},$$

where $\mathbf{A}$ is some amplitude vector and $\hat{\mathbf{u}}$ satisfies the governing equation. It is also possible to show that

$$\hat{\mathbf{u}}\left(r,\theta,z\right) = \mathbf{A} J_n\left(k_r r\right) \left\{ \cos\left(n\theta\right)\cos\left(sz\right), \sin\left(n\theta\right)\sin\left(sz\right), \cos\left(n\theta\right)\sin\left(sz\right) \right\}^T \tag{4.18}$$

also satisfies the governing equations. This solution given is really a superposition of four waves of equal magnitude and a phase relationships that creates a two-dimensional standing wave (a mode) in the axial and circumferential directions. Therefore, the wave is travelling in only one dimension (the radial direction). If I had started my derivation with $\hat{\mathbf{u}}$ given by Eq.(4.18), the resulting stiffness matrix $\bar{\mathbf{K}}$ expressed in terms of $\mathbf{K}$ (redefined as described above in terms of force per length) is

$$\bar{\mathbf{K}} = \left[\mathbf{T}''\right]^{-1} \left[\mathbf{T}'\right]^{-1} \mathbf{K} \mathbf{T}' \mathbf{T}'',$$

where the two transform matrices are

$$\mathbf{T}' = \frac{1}{2}\mathrm{diag}\left\{ \begin{array}{cccccc} 1, & -i, & 1, & 1, & -i, & 1 \end{array} \right\}$$

and

$$\mathbf{T}'' = \frac{1}{2}\mathrm{diag}\left\{ \begin{array}{cccccc} 1, & 1, & -i, & 1, & 1, & -i \end{array} \right\}.$$

The matrix $\bar{\mathbf{K}}$ is symmetric even when the layer Lame' constants are complex. In addition to symmetry, the components of $\bar{\mathbf{K}}$ are pure real numbers when the layer is elastic and complex when it is not, which is the same symmetry property of the 1D rod stiffness matrix derived in Chapter 2. The symmetry of $\bar{\mathbf{K}}$ is a good way to see that the implementation of the model is correct. One final observation is for the

rod

$$\mathbf{K}_{11} = \mathbf{K}_{22},$$

which is not generally true for the shell. It is true only as the radius goes to infinity. Physically, it is possible to interchange the two nodes of the rod, while it is not possible to do this for the shell.

4.6.3 Fluid layer

The stiffness matrix for a fluid, which supports only dilational waves and normal stress, is found by redefining

$$\mathbf{D}_j(r) = F_{j,r}$$

and

$$\mathbf{C}_j(r) = -\lambda h^2 F_j.$$

If these expressions are used to recalculate **D** and **C** given by Eq.(4.13) and Eq.(4.15), then Eq.(4.17) may be used to calculate the $2x2$ fluid stiffness matrix.

4.6.4 Inner core layer, infinite outer layer, and infinite layer

For an inner core with radii $r = r_2$, fluid or solid, its' stiffness matrix is given by

$$\mathbf{K} = \mathbf{C}_{22}\left[\mathbf{D}_{22}\right]^{-1}.$$

For an infinite outer layer with radius $r = r_1$, its' stiffness matrix is

$$\mathbf{K} = \mathbf{C}_{11}\left[\mathbf{D}_{11}\right]^{-1}.$$

For a solid, these stiffness matrices have dimension $3x3$. For a fluid, they have dimension $1x1$. The stiffness matrix for an infinite homogeneous medium (without any cavities) is just the sum of that for the core layer and an infinitely extended layer.

The use of the outer radius for the core insures that its' motions are governed by the Bessel function of the first kind and has finite solutions at $r = 0$. The use of the inner radius for the infinitely extended medium insures that its' motions are governed by the Hankel function of the first kind and there is no energy coming in from infinity (Remember that my convention is to assume a time dependence of $e^{-i\omega t}$ and the Hankel function of the first kind represents a wave that is propagating outward).

Figure 4-1: Cylindrical shell with 4 layers and 3 interfaces excited by a source at $r = r_2$.

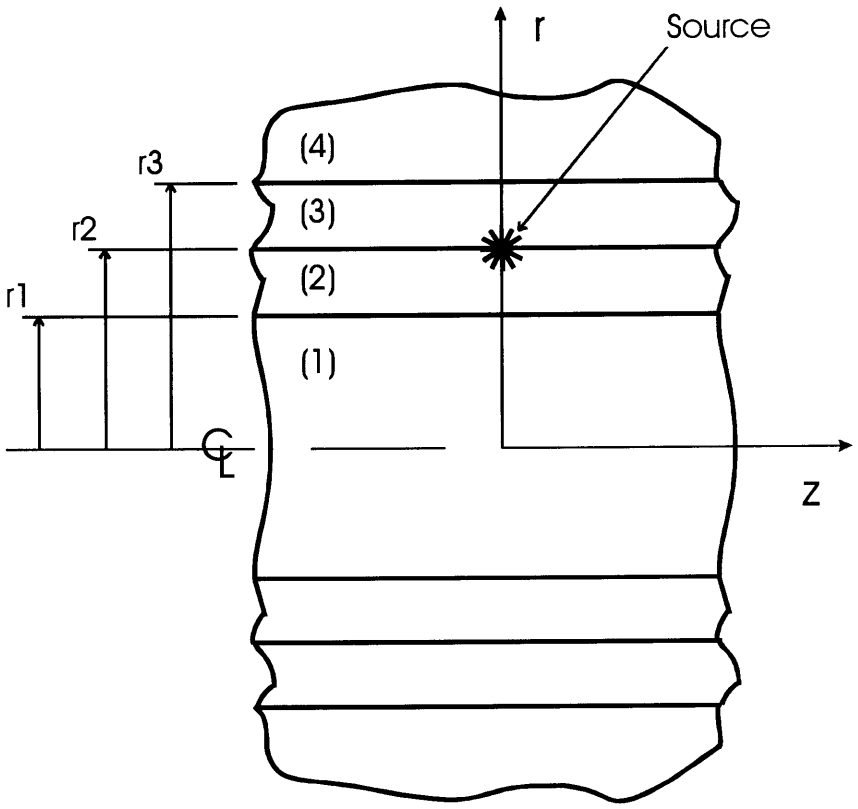

4.7 Source modeling

Here I consider the excitation of a system of finite elements (shell layers) excited by a single source. The system is shown in Figure 4-1. To model this system only four finite elements need to be used. The first element, designated $\mathbf{K}^{(1)}$, is a cylindrical core with outer radius r_1 (superscripts in braces are used to denote element variables). The second element, designated $\mathbf{K}^{(2)}$, extends from r_1 to r_2. The third element, designated $\mathbf{K}^{(3)}$, extends from r_2 to r_3. The fourth element, designated $\mathbf{K}^{(4)}$, extends from r_3 to infinity. All elements are solid elements that are welded together at their connecting interfaces. Because the first and fourth elements have only one surface, their stiffness matrices have dimension $3x3$. The stiffness matrix for all elements are calculated as described in the previous section. In this section, I consider three different types of forcing at the $r = r_2$ interface.

The system of elements considered here is really quite general when the stiffness of the inner core

layer and the surrounding foundation layer, that is, $\mathbf{K}^{(1)}$ and $\mathbf{K}^{(4)}$, are considered the input stiffness matrices for subsystems. Each subsystem may themselves be made up of multiple layers that are external to the two middle layers surrounding the source.

4.7.1 Spatial distribution of stress

Modeling a stress distribution on the shell is the most straight forward of the three types of excitation that I consider. The reason is that the boundary conditions at the three interfaces are either continuity of displacement, dynamic balance of stress, or an impedance boundary condition (actually stiffness), where the impedance is defined in terms of displacement and stress. Because the stiffness matrix is formulated in terms of stress and displacement, the solution of the system follows standard FEM procedures found in Bathe [1]. The only non-standard FEM procedure is to first decompose the spatial stress distribution by its circumferential and axial wave components before applying them to the finite element system using the transform defined in Eq.(4.7). Any combination of surface tractions described by Eq.(4.6) may be applied to the shell including point forces.

4.7.2 Point volume source

In this section, I model the excitation of the shell at r_2 due to a volume source with source strength S_ϕ, which is equal to the total displaced volume. To simplify the problem, I require that the two middle elements have identical material properties. Because, as I'll show shortly, the source strength is defined in terms of the dilational wave potential function ϕ, the boundary conditions at the source are defined in terms of the wave amplitudes of the two middle elements, that is, $\mathbf{A}^{(2)}$ and $\mathbf{A}^{(3)}$. Therefore, it is easiest to consider these wave amplitudes as the unknowns of the problem and then satisfy all boundary conditions in terms of these unknowns. This may be considered a DGM approach to the problem. This contrasts with the FEM approach where the wave amplitudes are eliminated from the problem, although, they may be found in post-processing if desired.

There are a total of 12 boundary conditions that need to be satisfied: the stiffness boundary conditions at r_1 and r_3 (that's a total of 6 conditions); continuity of displacement at r_2 (that's another 3); and the strength of the source at r_2 must be matched by contributions from the two elements (that's the final 3). Thankfully, there are 12 unknowns for the element system, the six wave amplitudes in the second element contained in $\mathbf{A}^{(2)}$ and the six wave amplitudes in the third element contained in $\mathbf{A}^{(3)}$. Because matching the impedance boundary conditions at r_1 and r_3 and the continuity of displacement boundary conditions at r_2 is straight-forward, I present that part of the solution without detailed formulation. I do, however, consider the source matching boundary conditions in detail.

To see how the elements respond to a point volume source, I consider the non-homogenous wave equations, Eq.(4.2), which I rewrite here as:

$$\begin{aligned}\nabla^2\phi + h^2\phi &= S_\phi \delta(r - r_s)\,\delta(\theta)\,\delta(z) \\ \left(\nabla^2 + k^2\right)\psi &= 0 \\ \left(\nabla^2 + k^2\right)\chi &= 0.\end{aligned}$$

I may use Eq.(4.7) to write them as:

$$\begin{aligned}\hat{\phi}_{,rr} + \frac{1}{r}\hat{\phi}_{,r} + \left(h^2 - \frac{n^2}{r^2}\right)\hat{\phi} &= S_\phi \delta(r - r_s) \\ \hat{\psi}_{,rr} + \frac{1}{r}\hat{\psi}_{,r} + \left(h^2 - \frac{n^2}{r^2}\right)\hat{\psi} &= 0 \\ \hat{\chi}_{,rr} + \frac{1}{r}\hat{\phi}_{,r} + \left(h^2 - \frac{n^2}{r^2}\right)\hat{\chi} &= 0.\end{aligned}$$

If integrate this equation about a thin shell layer surrounding the source at $r = r_2$ to find the relations between the source strength and the potential function. For an arbitrarily small area around the source, it must hold that:

$$\begin{aligned}-\hat{\phi}_{,r}\left(r_2^+\right) + \hat{\phi}_{,r}\left(r_2^-\right) &= S_\phi \\ -\hat{\psi}\left(r_2^+\right) + \hat{\psi}\left(r_2^-\right) &= 0 \\ -\hat{\chi}\left(r_2^+\right) + \hat{\chi}\left(r_2^-\right) &= 0,\end{aligned} \tag{4.19}$$

where I use the superscripted r_2 to denote "just above" or "just below" $r = r_2$. Note that because the shear forcing terms are zero, the shear wave equations impose continuity of the shear potential functions at the source radius. Also, as expected, if the source potential goes to zero, all three potential functions are continuous across the source location.

I can use Eq.(4.8) to write Eq.(4.19) in terms of the unknown wave amplitudes as

$$\mathbf{G}_{21}^{(2)}\mathbf{A}_1^{(2)} + \mathbf{G}_{21}^{(2)}\mathbf{A}_2^{(2)} + \mathbf{G}_{11}^{(3)}\mathbf{A}_1^{(3)} + \mathbf{G}_{12}^{(3)}\mathbf{A}_2^{(3)} = \{S_\phi, 0, 0\}^T, \tag{4.20}$$

where I have defined the auxiliary matrix

$$\mathbf{G} = \begin{bmatrix} \mathbf{G}_{11} & \mathbf{G}_{12} \\ \mathbf{G}_{21} & \mathbf{G}_{22} \end{bmatrix} = \begin{bmatrix} -\mathbf{G}_1(r_1) & -\mathbf{G}_2(r_1) \\ \mathbf{G}_1(r_2) & \mathbf{G}_2(r_2) \end{bmatrix} \tag{4.21}$$

from submatrices

$$\mathbf{G}_j(r) = \begin{bmatrix} F_{j,r} & 0 & 0 \\ 0 & G_{j,r} & 0 \\ 0 & 0 & G_{j,r} \end{bmatrix}.$$

Note that the sign conventions for $\mathbf{G}$ is the same as for $\mathbf{C}$.

Enforcement of the boundary conditions on all three interfaces results in the matrix relation

$$\mathbf{M}\left\{\mathbf{A}_1^{(2)}, \mathbf{A}_2^{(2)}, \mathbf{A}_1^{(3)}, \mathbf{A}_2^{(3)}\right\}^T = \mathbf{N}, \tag{4.22}$$

where

$$\mathbf{M} = \begin{bmatrix} \mathbf{K}^{(1)}\mathbf{D}_{11}^{(2)} - \mathbf{C}_{11}^{(2)} & \mathbf{K}^{(1)}\mathbf{D}_{12}^{(2)} - \mathbf{C}_{12}^{(2)} & 0 & 0 \\ \mathbf{D}_{21}^{(2)} & \mathbf{D}_{22}^{(2)} & -\mathbf{D}_{11}^{(3)} & -\mathbf{D}_{12}^{(3)} \\ \mathbf{G}_{21}^{(2)} & \mathbf{G}_{22}^{(2)} & \mathbf{G}_{11}^{(3)} & \mathbf{G}_{12}^{(3)} \\ 0 & 0 & \mathbf{K}^{(4)}\mathbf{D}_{21}^{(3)} - \mathbf{C}_{21}^{(3)} & \mathbf{K}^{(4)}\mathbf{D}_{22}^{(3)} - \mathbf{C}_{22}^{(3)} \end{bmatrix} \tag{4.23}$$

and the forcing term is

$$\mathbf{N} = \{0,0,0,0,0,0,S_\phi,0,0,0,0,0\}^T,$$

The first and last rows in Eq.(4.22) satisfy the boundary conditions at r_1 and r_3. The second row satisfies the continuity of displacement condition at r_2 and the third row is just Eq.(4.20).

The point force solutions given by Eq.(4.22) is in some sense a hybrid WFEM-DGM method. It is DGM-like because the degrees of freedom are wave amplitudes. This is necessary because the response to the forcing depends on derivatives of displacements (evaluated at the source radius), which in turn depend on the wave amplitudes directly. It is FEM-like when $\mathbf{K}^{(1)}$ and $\mathbf{K}^{(4)}$ are considered subsystems of multiple layers as already discussed.

The matrix $\mathbf{M}$ in Eq.(4.22) is defined to maintain good numerical conditioning. It can be shown that at high wavenumber, all off diagonal submatrices in $\mathbf{M}$ approach zero, that is,

$$\lim_{s\to\infty} \mathbf{M} = \begin{bmatrix} \mathbf{K}^{(1)}\mathbf{D}_{11}^{(2)} - \mathbf{C}_{11}^{(2)} & 0 & 0 & 0 \\ 0 & \mathbf{D}_{22}^{(2)} & -\mathbf{D}_{11}^{(3)} & 0 \\ 0 & \mathbf{G}_{22}^{(2)} & \mathbf{G}_{11}^{(3)} & 0 \\ 0 & 0 & 0 & \mathbf{K}^{(4)}\mathbf{D}_{22}^{(3)} - \mathbf{C}_{22}^{(3)} \end{bmatrix}$$

and there is a natural decoupling between layers. Physically, the high wavenumber components are evanescent in the thickness direction. This is the basic feature in the DGM method as described by

Schmidt and Jensen. I also define **D** in Eq.(4.13) and **C** in Eq.(4.15) to have this same feature. This is important because **D** must be inverted to calculate **K** for each layer.

4.7.3 Zero forcing

Another use of the model is to study wave dispersion or wavenumber-frequency relations in layered media. Dispersion relations are powerful tools used to understand the behavior of waves in solids. The dispersion relation for such systems may be found by assembling the global matrix and searching for the wavenumber roots of its' determinant. Muller's method is a common root finding method based on a quadratic polynomial interpolation for the next best guess [48]. Because the determinant of a shell layer is transcendental, the root finding procedure is inherently iterative and the efficiency of the WFEM formulation becomes important. Having found the wavenumber roots, group velocities and wave attenuation may be predicted. It is also possible to examine the free-wave vectors.

4.8 Matlab program for a solid shell layer

To close this chapter, I include a listing of three Matlab m-files: *shell.m*, *dc.m*, and *bfcn.m*. The m-file *shell.m* calls the other two m-files to calculate the matrices **K**, **D**, **C**, and **G** for a 3D solid cylindrical shell layer. These may be used as described in this chapter along with a few conventional FEM techniques to solve for shells with multiple layers driven by either a point force or a volume source. The input/output for this routine is defined in Table I. The program uses the Matlab defined exponential scaling for Bessel functions calculations. I include the listing here because the program is extremely powerful, compact, and easy to use. Using the relationships derived in Section 4.3, *shell.m* may also be used to calculate the stiffness matrix for a core layer, an infinitely extended layer, and an infinite homogeneous layer, all

of which may be either solid or fluid. All from 31 lines of Matlab code!

Table I: Input/output for Matlab *shell.m* program.

Layer variable	Symbol	Matlab I/O	Size	Units	Type of I/O	Defined by
density	ρ	`rho`	$1x1$	M/L^3	positive real	-
dilational speed	c_d	`cd`	$1x1$	L/T	complex	Eq.(4.3)
shear speed	c_s	`cs`	$1x1$	L/T	complex	Eq.(D.16)
radial frequency	ω	`w`	$1x1$	$1/T$	positive real	-
axial wavenumber	s	`s`	$1x1$	$1/L$	real	-
circumferential order	n	`n`	$1x1$	–	real	-
inner radius	r_1	`r1`	$1x1$	L	positive real	-
outer radius	r_2	`r2`	$1x1$	L	positive real	-
stiffness matrix	$\mathbf{K}$	`K`	$6x6$	F/L^2	complex	Eq.(4.16)
displacement matrix	$\mathbf{D}$	`D`	$6x6$	–	complex	Eq.(4.12)
force matrix	$\mathbf{C}$	`C`	$6x6$	F/L	complex	Eq.(4.14)
volume source matrix	$\mathbf{G}$	`G`	$6x6$	F/L	complex	Eq.(4.21)

The only additional restriction on the input is that $-1e-4 < \mathrm{Im}\,(c_d)\,, \mathrm{Im}\,(c_s) < 0$. I do this for two reasons. First to insure that waves decay in the direction that they propagate. Second, to insure that the Matlab Bessel function routines do not underflow or overflow due to small argument when either h_r or k_r approach zero.

To check that the program is correctly implemented, execute the command:

```
K=shell(1.1,1.3-i*.1,.62*(1.3-i*.1),3,7,2,.7,.9);det(K)
```

The response should be:

```
ans=3.7693e+002-8.0079e+003i.
```

Listing of Matlab m-file: shell.m

```
function[K,D,C,G]=shell(rho,cd,cs,w,s,n,r1,r2)
[D11,C11,G11]=dc(rho,cd,cs,w,s,n,r1,r1,r2,1);
[D12,C12,G12]=dc(rho,cd,cs,w,s,n,r1,r1,r2,2);
[D21,C21,G21]=dc(rho,cd,cs,w,s,n,r2,r1,r2,1);
[D22,C22,G22]=dc(rho,cd,cs,w,s,n,r2,r1,r2,2);
D=[+D11,+D12;D21,D22];
C=[-C11,-C12;C21,C22];
G=[-G11,-G12;G21,G22];
K=C/D;

function[DD,CC,GG]=dc(rho,cd,cs,w,s,n,r,r1,r2,ind)
h=w/cd;
hr=i*sqrt(-h^2+s^2);
kr=i*sqrt(-(w/cs)^2+s^2);
[F0,F1,F2]=bfcn(hr,r,r1,r2,n,ind);
[G0,G1,G2]=bfcn(kr,r,r1,r2,n,ind);
DD=[F1, i*(n/r)*G0, i*s*G1;
    i*(n/r)*F0, -G1, -s*(n/r)*G0;
    i*s*F0, 0, kr^2*G0];
CC=rho*cs^2*[-((cd/cs)^2-2)*h^2*F0+2*F2, ...
   i*2*(n/r)*(-G0/r+G1), i*2*s*G2;
   i*2*(n/r)*(-F0/r+F1), -(n/r)^2*G0+G1/r-G2, ...
   2*s*(n/r)*(G0/r-G1);
   i*2*s*F1, -s*(n/r)*G0, (kr^2-s^2)*G1];
GG=[F1,0,0;0,G1,0;0,0,G1];

function[Fp0,Fp1,Fp2]=bfcn(a,x,x1,x2,n,ind);
if ind==1
   temp=besselh(n+0,1,a*x1,1);
   B0=besselh(n+0,1,a*x,1)/temp*exp(+i*a*(x-x1));
   B1=besselh(n+1,1,a*x,1)/temp*exp(+i*a*(x-x1));
elseif ind==2
   temp=besselh(n+0,1,a*x2,1);
   B0=besselj(n+0,a*x,1)*temp*exp(abs(imag(a*x))+i*a*x2);
   B1=besselj(n+1,a*x,1)*temp*exp(abs(imag(a*x))+i*a*x2);
end
Fp0=B0;
Fp1=-a*B1+n*B0/x;
Fp2=(a/x)*B1+(-a^2-n/x^2+n^2/x^2)*B0;
```

Chapter 5

Hybrid FEM model of a shell-bulkhead connection

5.1 Introduction

In this chapter, I consider the scattering of propagating shell waves due to a complete circular plate, a bulkhead, that is welded to the shell as shown schematically in Figure 5-1. What is of particular interest is how to properly model the T-junction connection between the shell and the bulkhead.

For the sake of discussion, let's first consider how a T-junction is modeled when both the shell and the bulkhead are formulated using classical shell and plate theory. The approach that is usually used to join the shell and the bulkhead is shown in Figure 5-2. A three-element system is used (I'll refer to this technique as the three-element method), which is composed of two shell elements (numbered element 1 and element 2) and a single bulkhead element, as shown in Figure 5-2a. The elements are joined together at a node located at the mid-surface of the shell. For a welded boundary condition, the usual continuity of displacement and rotation and force and moment balance is imposed. This approach is possible because for each shell degree of freedom (either displacement or force) there is a corresponding bulkhead degree of freedom as shown in Figure 5-2b. The obvious errors introduced by this technique is that the bulkhead is not attached at the mean radius but at the inner shell radius and that the connection is not along a circular line but along a two dimensional surface area.

Now let's consider how a thick shell and bulkhead are joined. By *thick* I mean that rotary inertia and shear deformation are included in the formulation of the elements. By including shear deformation, the shell and plate formulations have an additional degree of freedom, the twist degree of freedom. One technique to join the shell and bulkhead is to use the same three-element method discussed above. This

Figure 5-1: Schematic of shell-bulkhead T-junction.

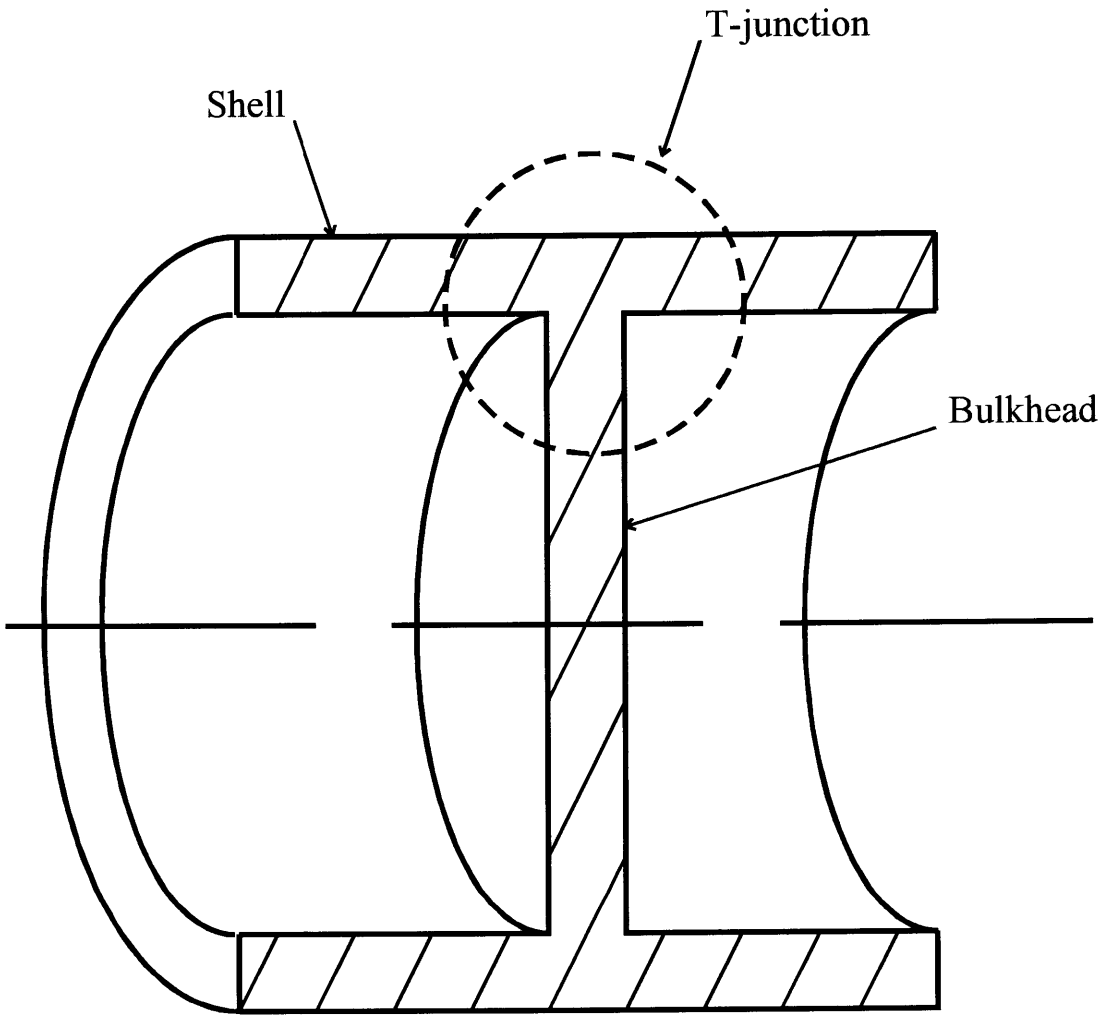

Figure 5-2: Schematic of shell-bulkhead T-junction model using thin shell and plate theory.

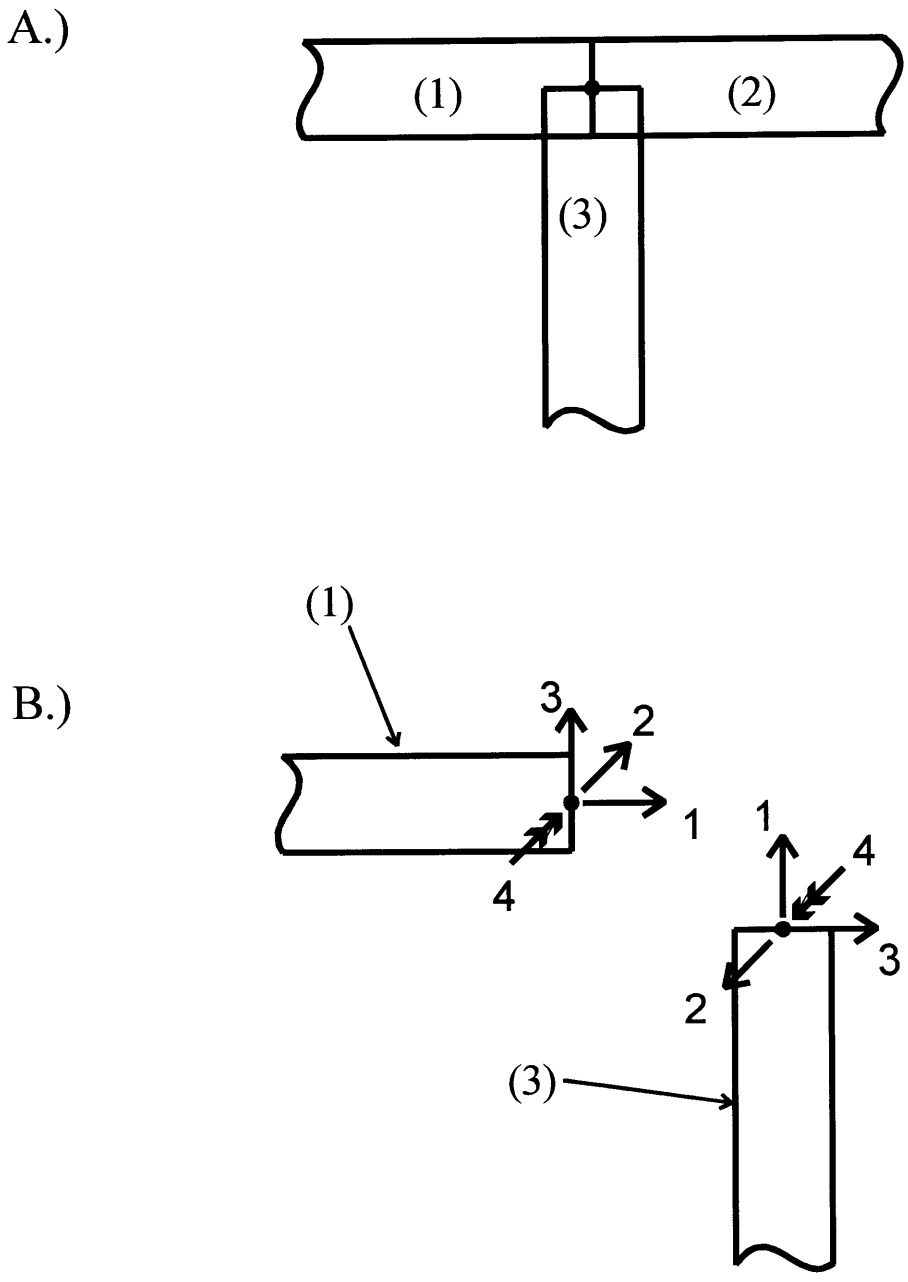

is shown schematically in Figure 5-3. The problem is that the additional (twist) degree of freedom of the shell does not correspond with the twist degree of freedom of the bulkhead. The shell twist is about the axial direction, the bulkhead twist is about the radial direction. To circumvent this problem, it is assumed that the twist moment applied to the bulkhead is zero and that the twist moment on the shell due to the bulkhead is also zero. Details of how to connect the bulkhead are contained in Appendix-A. For a welded boundary condition, these twist moments are not zero and some additional error is introduced.

To more accurately model the T-junction, I use the four-element method as shown in Figure 5-4. I still use the two shell elements and the bulkhead element as before (elements 1 through 3). These elements are all formulated using thick shell and plate theory. But now I introduce a fourth element, the T-junction element, which is formulated using conventional finite elements. The T-junction element has three nodes, each with five degrees of freedom. The first two nodes (the left and right nodes) have degrees of freedom that correspond to the shell degrees of freedom. The third (bottom) node has degrees of freedom that correspond to the bulkhead degrees of freedom. Therefore, it is not necessary to assume that the twist moments are zero. In addition, the bulkhead element is effectively joined along a two dimensional surface area at the inner radius of the shell. More details of the T-junction element formulation are given later in this chapter.

To evaluate these different T-junction modeling techniques, I compare the scattering of shell waves at the T-junction connection. The incident wave is one of three types of propagating waves supported by the shell (compressional, shear, and flexural) with an assumed circumferential dependence of $e^{+\imath n\theta}$ and assumed time dependence of $e^{-i\omega t}$. The incident wave scatters at the T-junction connection between the shell and the bulkhead into both reflected and transmitted waves of all types including non-propagating evanescent and through-thickness shear waves. To help analyze the effects of the bulkhead, I sort all scattered waves by wave type and express the scattering in terms of power flow. I also calculate the amplitudes of the waves in the bulkhead by wave type to study the energy storage mechanisms of the bulkhead.

5.2 Comparison of various shell theories

To provide some insight into the wave scattering process, it is useful to compare the dispersion relations for a cylindrical shell based on thin, thick, and full elastic shell theories. For the thin shell theory, I use the Donnell-Mushtari theory, which is the simplest thin shell theory that includes both flexural and membrane waves. The equations for the Donnell-Mushtari theory are given in Leissa's monograph [3]. For the thick shell theory, I use the Herrmann-Mirsky theory as described in Chapter 2 and I use the

Figure 5-3: Schematic of non-compatible shell-bulkhead T-junction model.

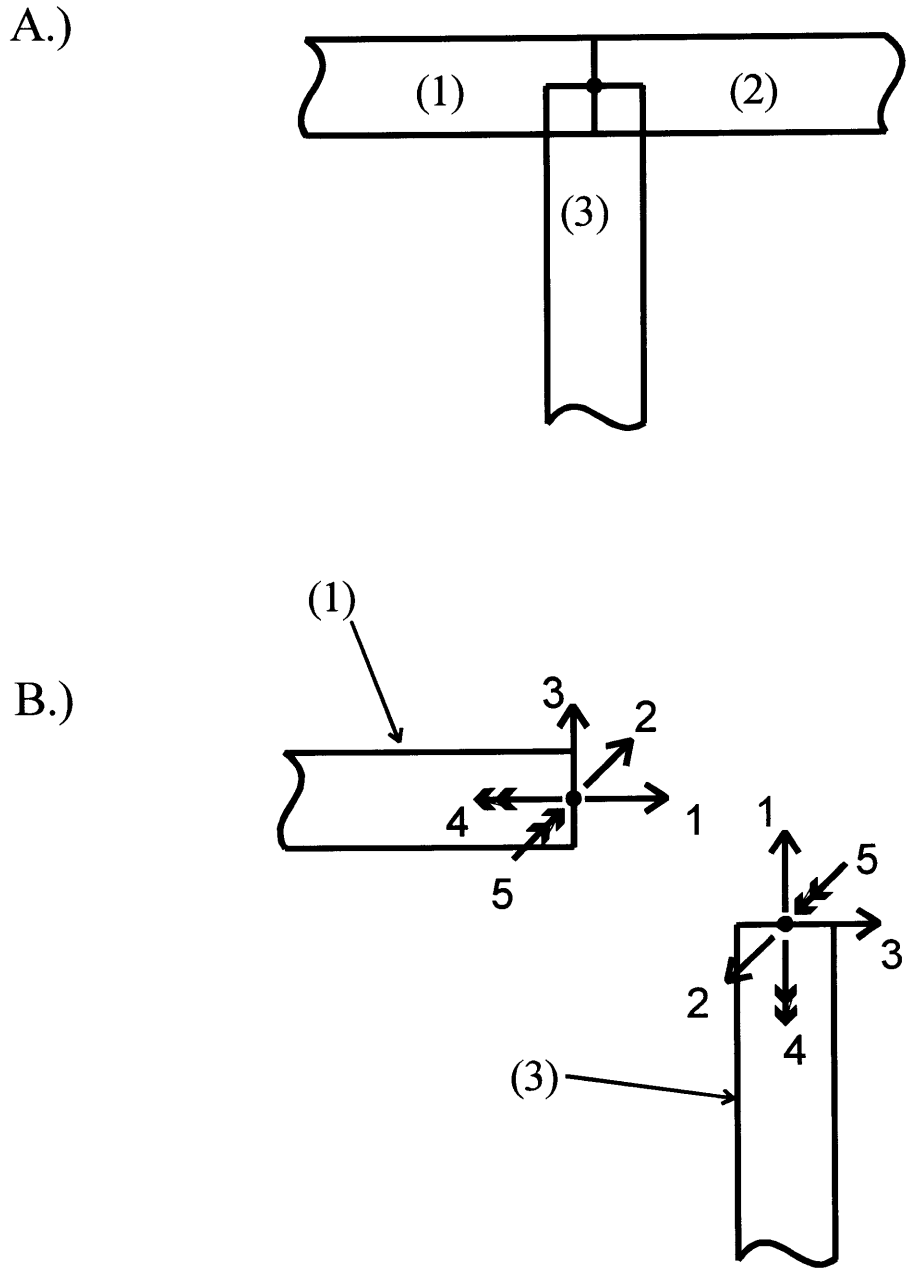

Figure 5-4: Schematic of compatible shell-bulkhead T-junction model.

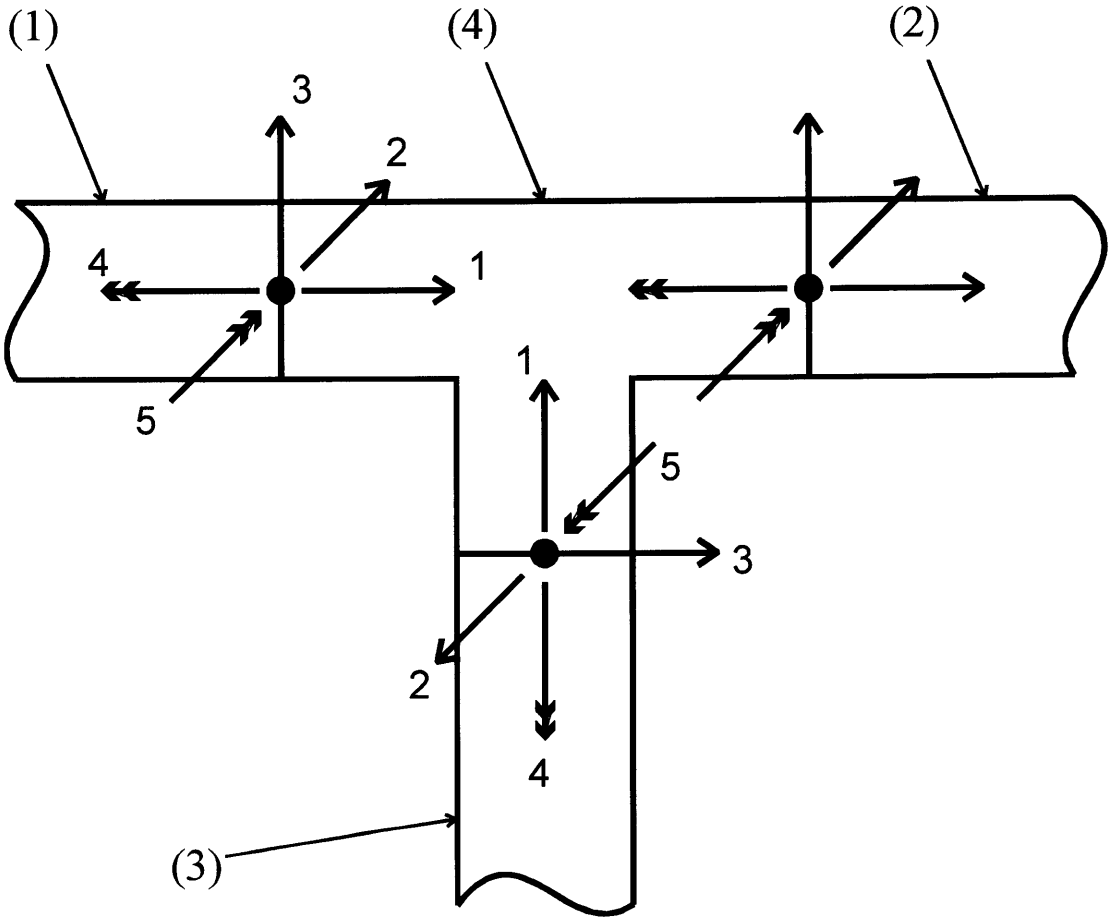

full elastic shell theory as described in Chapter 3.

Differences may be quantified by comparing the dispersion relations (frequency versus axial wavenumber) for the three shell theories. When the differences in the dispersion relations are small, the theories may be considered to be in agreement. It is natural to assume that when the differences in the wavenumbers are small, then differences in the free-wave vectors are also small.

I choose to compare two cases. For the first case, I consider a shell with 2% thickness (the ratio of thickness to mean radius) and for the second case I consider a shell with 10% thickness. For both cases, I consider a shell with Poisson's ratio $\nu = .3$ and one that is effectively lossless, $\eta = 0$. For both cases, I consider the $n = 2$ shell mode. I choose this mode because all wave types are coupled and there are propagating compressional, shear, and flexural waves at the mid-frequency range of the shell (below $\Omega < 5$).

The comparison for the 2% shell is shown in Figure 5-5 and Figure 5-6 for the $.1 < \Omega = \omega a/c_p < 10$. In Figure 5-5, frequency is plotted versus the real part of the axial component of the wavenumber. In Figure 5-6, frequency is plotted versus the imaginary part of axial wavenumber. To make the figure clearer, I have only plotted the results for the Donnell-Mushtari theory and the Herrmann-Mirsky theory. There is very little difference between the exact theory and the Herrmann-Mirsky theory for the frequency and thickness considered here. The figures show that there are three propagating waves and an evanescent wave as discussed in Chapter 2. The thickness wave for the Herrmann-Mirsky theory is essentially a constant at $k_x = 157i$ and is outside the range of the plot axes. There is no thickness wave type supported by the Donnell-Mushtari theory. The figures show that there is no difference in the two theories for the compressional and shear waves. The two theories predict significant differences for the flexural and evanescent waves beginning at about $\Omega = 5$.

The comparison for the 10% thick shell is shown in Figure 5-7 and Figure 5-8 for the same frequency range. The format is the same as Figure 5-5 and Figure 5-6, except that I have plotted all three shell theories. The main effect of the thicker shell is to increase the speed of the flexural wave and increase the influence of the evanescent and thickness waves by moving them closer to the real axis (in the complex wavenumber plane). The influence of these waves is now increasing with frequency. Even for this thicker shell, there is very little difference between the exact theory and the Herrmann-Mirsky theory for any of the wave types. There is still no difference between the Donnell-Mushtari and the Herrmann-Mirsky theories for the compressional and shear waves. The two theories predict significant differences for the flexural and evanescent waves beginning at about $\Omega = 2$ (lower than that for the 2% thick shell).

The Herrmann-Mirsky theory is a more accurate representation of the shell because it includes through-thickness shear deformation and rotary inertia effects that are important at higher frequencies because the inertial terms are increasingly dominant and the wavelengths are comparable to the thickness

Figure 5-5: Comparison of $\Omega - \mathrm{Re}\,(k_x)$ for thin and thick shell theory for $n = 2$, $h/a = 2\%$, $\nu = .3$, and $\eta = 1e - 3$.

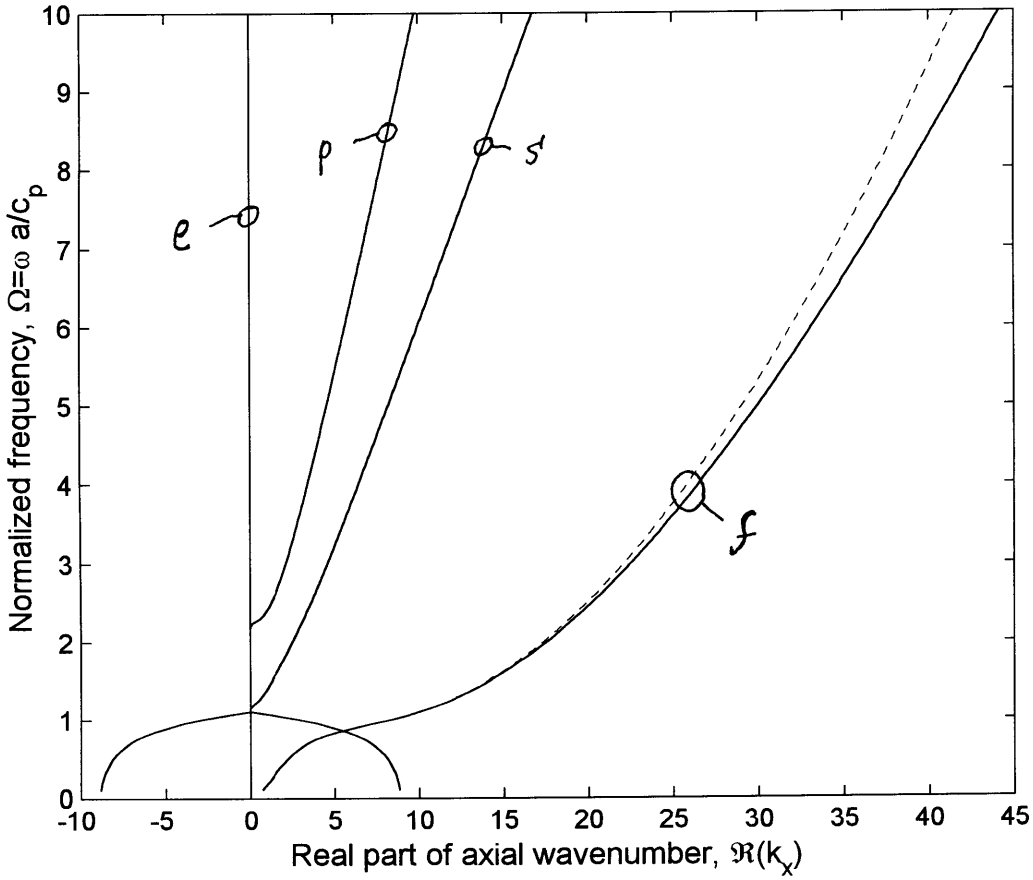

Figure 5-6: Comparison of $\Omega - \mathrm{Im}\,(k_x)$ for thin and thick shell theory for $n = 2$, $h/a = 2\%$, $\nu = .3$, and $\eta = 1e - 3$.

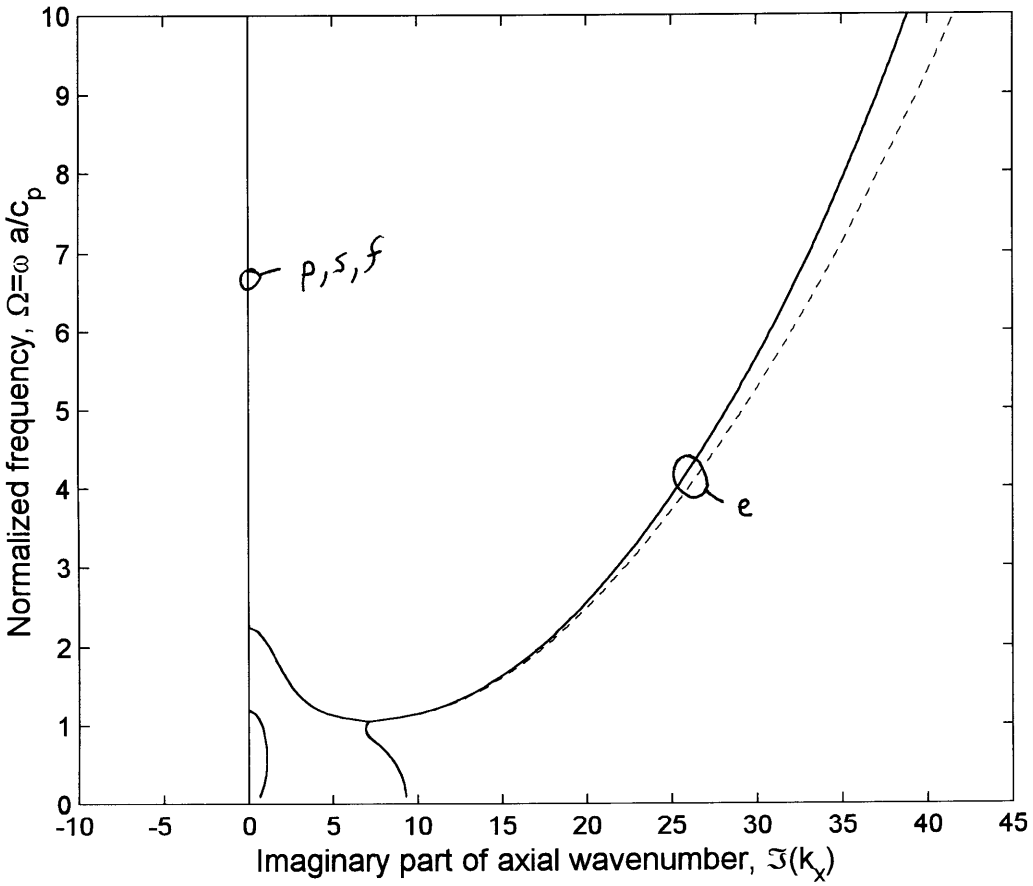

Figure 5-7: Comparison of $\Omega - \mathrm{Re}\,(k_x)$ for thin and thick shell theory for $n = 2$, $h/a = 10\%$, $\nu = .3$, and $\eta = 1e-3$.

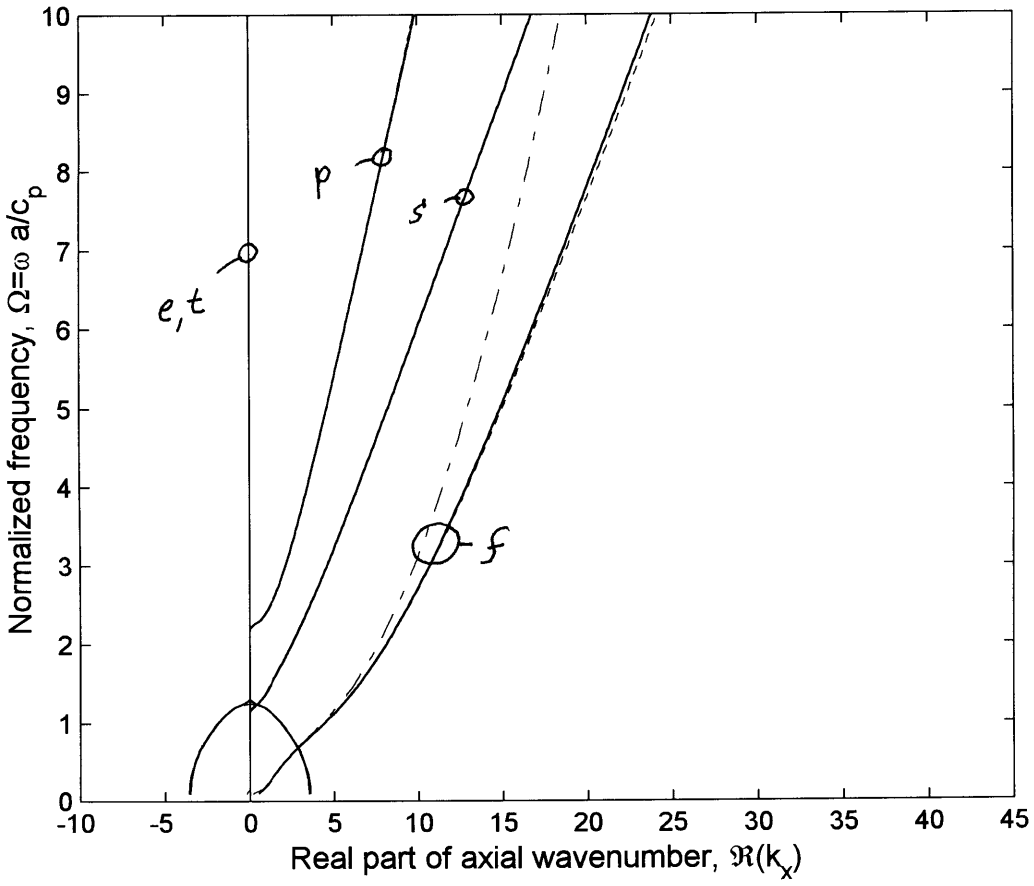

Figure 5-8: Comparison of $\Omega - \mathrm{Im}\,(k_x)$ for thin, thick, and full shell theory for $n = 2$, $h/a = 10\%$, $\nu = .3$, and $\eta = 1e - 3$.

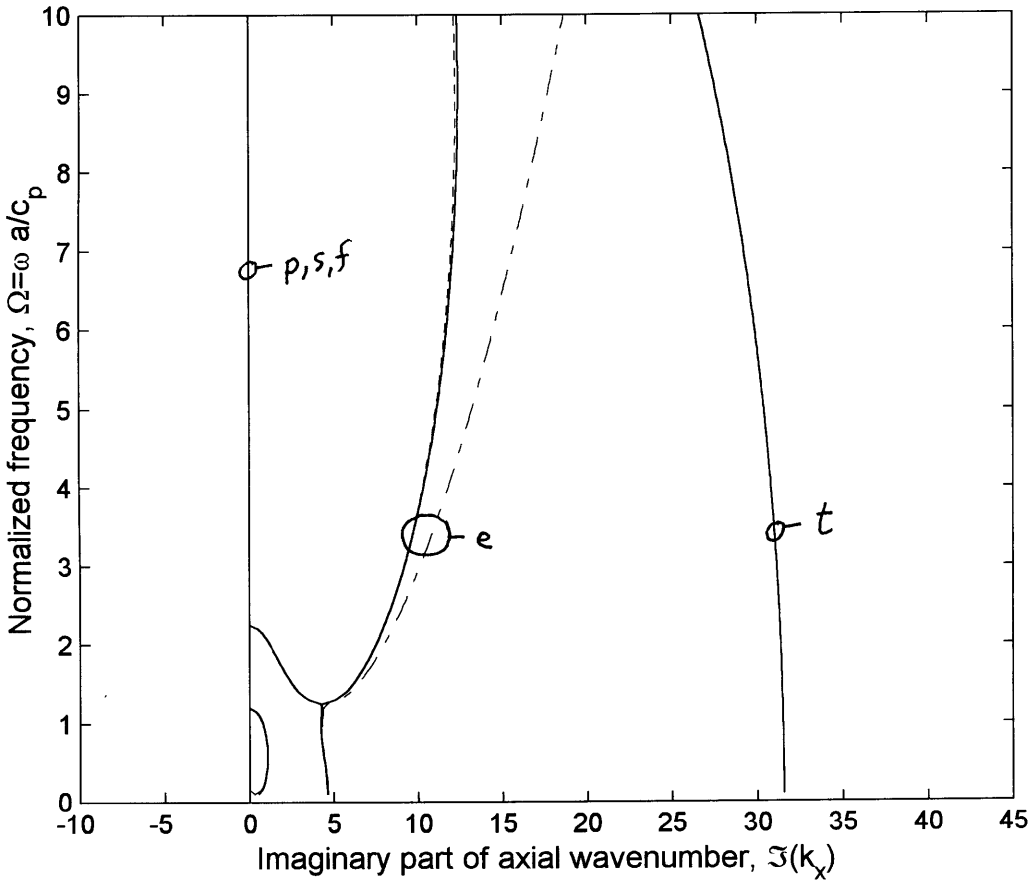

dimension. The new through-thickness wave type gives rise to the additional twist degree of freedom. I refer to this comparison throughout this chapter.

5.3 T-junction element formulation

There are several steps to formulating the T-junction element to make it compatible with the shell and bulkhead elements. I use Figure 5-9 to help explain each step, which I enumerate here:

1. The first step is to model the T-junction using a mesh or assembly of ring elements. For the present analysis, I use two mesh sizes, which I refer to as the coarse mesh and the fine mesh. The fine mesh doubles the number of ring elements used in both the radial and axial directions. The coarse mesh is shown in Figure 5-9a. Each ring element is a conventional FEM element. They are formulated as described in Appendix-B based on the piecewise application of variational principals applied to a 3D, linear, elastic, solid. The ring element is a four-noded rectangular element with linear interpolation functions. Each node has three displacements acting in the three coordinate directions. The coordinate system is the same used for the WFEM shell elements. The static stiffness and mass matrices are formulated separately and then combined to form the dynamic stiffness matrix, which relates the nodal displacements to the dynamic nodal forces. Throughout, I assume the same circumferential and time dependence as the WFEM shell formulation. The numerical integration required to calculate the static stiffness and mass matrix is done using two point Gauss quadrature in both the axial and radial directions.

2. I then remove all internal degrees of freedom from the T-junction stiffness matrix. Internal degrees of freedom are those that do not interact directly with any externally applied forces. This process, referred to as condensation, is a standard FEM procedure described by Bathe [1]. Condensation leaves only the external degrees of freedom that interact with the shell and plate elements as shown in Figure 5-9b.

3. I constrain the motions of the external nodal displacements so that they are compatible with the shell and bulkhead displacements. This means that the three surfaces between the T-junction and the shell and bulkhead remain flat at all times. I also require that at these same three surfaces there is no through-thickness stretch. Note that because I use linear shape (or interpolation) functions, the displacements are compatible across the entire interface between the shell and T-junction (or the bulkhead and T-junction), that is, they are compatible between the nodes as well as at the nodes. The procedure to constrain an FEM assembly is detailed in Appendix-B. After imposing

these constraints, the resulting stiffness matrix may be written as

$$\mathbf{K}^{(4')}\mathbf{U}^{(4')} = \mathbf{F}^{(4')}, \tag{5.1}$$

where the 15 translational displacement degrees of freedom at the six nodes are grouped in $\mathbf{U}^{(4')}$and the corresponding external forces are grouped in $\mathbf{F}^{(4')}$. I use the slash superscript to refer to the T-junction element as shown in Figure 5-9c. The expanded displacement vector is

$$\mathbf{U}^{(4')} = \{U_1, V_1, W_1, U_2, V_3, U_3, V_3, W_3, U_4, V_4, U_5, V_5, W_5, V_6, W_6\}, \tag{5.2}$$

where the displacements $\{U, V, W\}$ are in the $\{x, \theta, r\}$ cylindrical coordinate directions and the subscripts refer to one of the six node numbers as shown in Figure 5-9c.

4. The final step is to transform $\mathbf{U}^{(4')}$ and $\mathbf{F}^{(4')}$ in Eq.(5.1) so that they are consistent with the mid-surface displacements and forces of the shell and bulkhead as shown in Figure 5-4. The transform for the displacements are based on geometry, while the transform for the forces is based on a dynamic force balance. The T-junction stiffness matrix relation may then be expressed as

$$\mathbf{K}^{(4)} \begin{Bmatrix} \mathbf{U}_1^{(4)} \\ \mathbf{U}_2^{(4)} \\ \mathbf{U}_3^{(4)} \end{Bmatrix} = \begin{Bmatrix} \mathbf{F}_1^{(4)} \\ \mathbf{F}_2^{(4)} \\ \mathbf{F}_3^{(4)} \end{Bmatrix} = \begin{Bmatrix} -\mathbf{F}^{(1)} \\ -\mathbf{F}^{(2)} \\ -\mathbf{F}^{(3)} \end{Bmatrix}, \tag{5.3}$$

where $\mathbf{U}_j^{(4)}$ and $\mathbf{F}_j^{(4)}$ ($j = 1$, 2, or 3) are the T-junction displacements and forces at the left, right, and bottom nodes, respectively (see Figure 5-9d). Also, the T-junction stiffness matrix is

$$\mathbf{K}^{(4)} = \begin{bmatrix} \mathbf{T}_F^{(1)} & 0 & 0 \\ 0 & \mathbf{T}_F^{(1)} & 0 \\ 0 & 0 & \mathbf{T}_F^{(3)} \end{bmatrix} \mathbf{K}^{(4')} \begin{bmatrix} \mathbf{T}_U^{(1)} & 0 & 0 \\ 0 & \mathbf{T}_U^{(1)} & 0 \\ 0 & 0 & \mathbf{T}_U^{(3)} \end{bmatrix}^{-1},$$

which is defined in terms of the submatrices:

$$\mathbf{T}_U^{(1)} = \begin{bmatrix} 1/2 & 0 & 0 & 1/2 & 0 \\ 0 & 1/2 & 0 & 0 & 1/2 \\ 0 & 0 & 1 & 0 & 0 \\ 0 & 1/h & 0 & 0 & -1/h \\ 1/h & 0 & 0 & -1/h & 0 \end{bmatrix}, \mathbf{T}_F^{(1)} = \begin{bmatrix} 1 & 0 & 0 & 1 & 0 \\ 0 & 1 & 0 & 0 & 1 \\ 0 & 0 & 1 & 0 & 0 \\ 0 & h/2 & 0 & 0 & -h/2 \\ h/2 & 0 & 0 & -h/2 & 0 \end{bmatrix},$$

$$\mathbf{T}_U^{(3)} = \begin{bmatrix} 0 & 0 & 1/2 & 0 & 1/2 \\ 0 & -1/2 & 0 & -1/2 & 0 \\ 1 & 0 & 0 & 0 & 0 \\ 0 & 1/h_b & 0 & -1/h_b & 0 \\ 0 & 0 & -1/h_b & 0 & 1/h_b \end{bmatrix}, \text{ and } \mathbf{T}_F^{(3)} = \begin{bmatrix} 0 & 0 & 1 & 0 & 1 \\ 0 & -1 & 0 & -1 & 0 \\ 1 & 0 & 0 & 0 & 0 \\ 0 & h_b/2 & 0 & -h_b/2 & 0 \\ 0 & 0 & -h_b/2 & 0 & h_b/2 \end{bmatrix}.$$

The subscript on the submatrices denotes whether the submatrix represents a force or a displacement transform and the superscript refers to the T-junction node G_j at which it applies. The transforms for the G_2 node are identical to those at G_1. This completes the description of the T-junction element formulation.

5.3.1 Verifying T-junction element formulation

While it is not possible to check the implementation of the bulkhead directly, I can make an indirect check by first formulating a shell and bulkhead element using conventional FEM or CFEM in the same manner as the T-junction and then comparing them to a shell and bulkhead element using WFEM (as described in Chapter 2 and Appendix-A).

The coarse meshes used to formulate a shell and bulkhead using conventional FEM are shown in Figure 5-10a and Figure 5-10b, respectively. The steps outlined above are applied to these meshes to formulate a shell and bulkhead element that is compatible (the same number of degrees of freedom, which are defined in the same manner) with the WFEM elements. The resulting elements are shown to the right of the arrows in Figure 5-10.

For the shell, I set the $\rho = 1.3$, $c_p = 1.2 - .05i$, $\nu = .3$, $a = 1.2$, $h = .01$, and $n = 2$. All elements have a square cross-section, which sets the axial length at $L = .05$. All units are consistent units. The left node is driven with a unit force in each of its five degrees of freedom. The resulting displacement (taken in the same direction as the driving force) is plotted in Figure 5-11. The subplots from top to bottom correspond to the axial, circumferential, radial, twist, and bending drive point displacements. The left column is the absolute value versus frequency normalized by the ring frequency. The right column is the phase angle divided by π versus normalized frequency. In each subplot, three curves are plotted: the solid curve is the WFEM result; the dashed curve is the fine mesh result (twice as many elements as the coarse mesh); and the dash-dot curve is the coarse mesh result. The CFEM element is shown to converge on the exact WFEM result for both the magnitude and phase for all five degrees of freedom.

For the bulkhead, all input variables are the same as for the shell except the outer radius is $r_o = a$, the inner radius is $r_i = a - L$, and the coarse mesh is a $10x2$ as opposed to a $2x10$. The results for the bulkhead are presented in Figure 5-12 using the same format as Figure 5-11. Again, the CFEM element

Figure 5-9: Compatible T-junction FEM element.

A.)

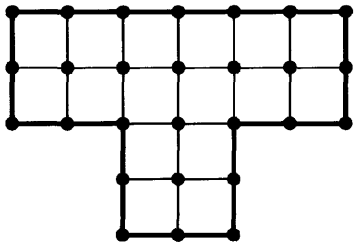

B.)

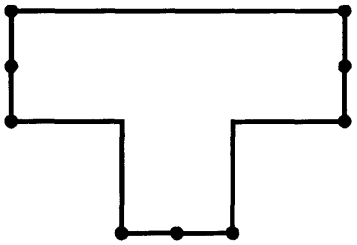

C.)

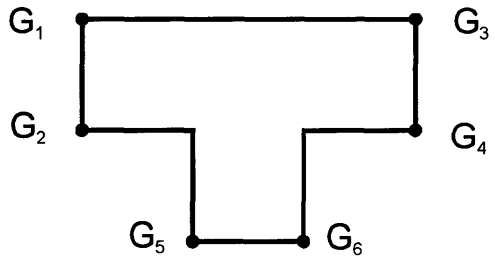

D.)

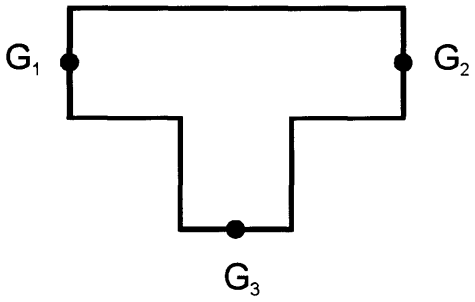

Figure 5-10: Shell (A.) and bulkhead (B.) course FEM meshes used to verify T-junction element formulation. Note: not drawn to scale.

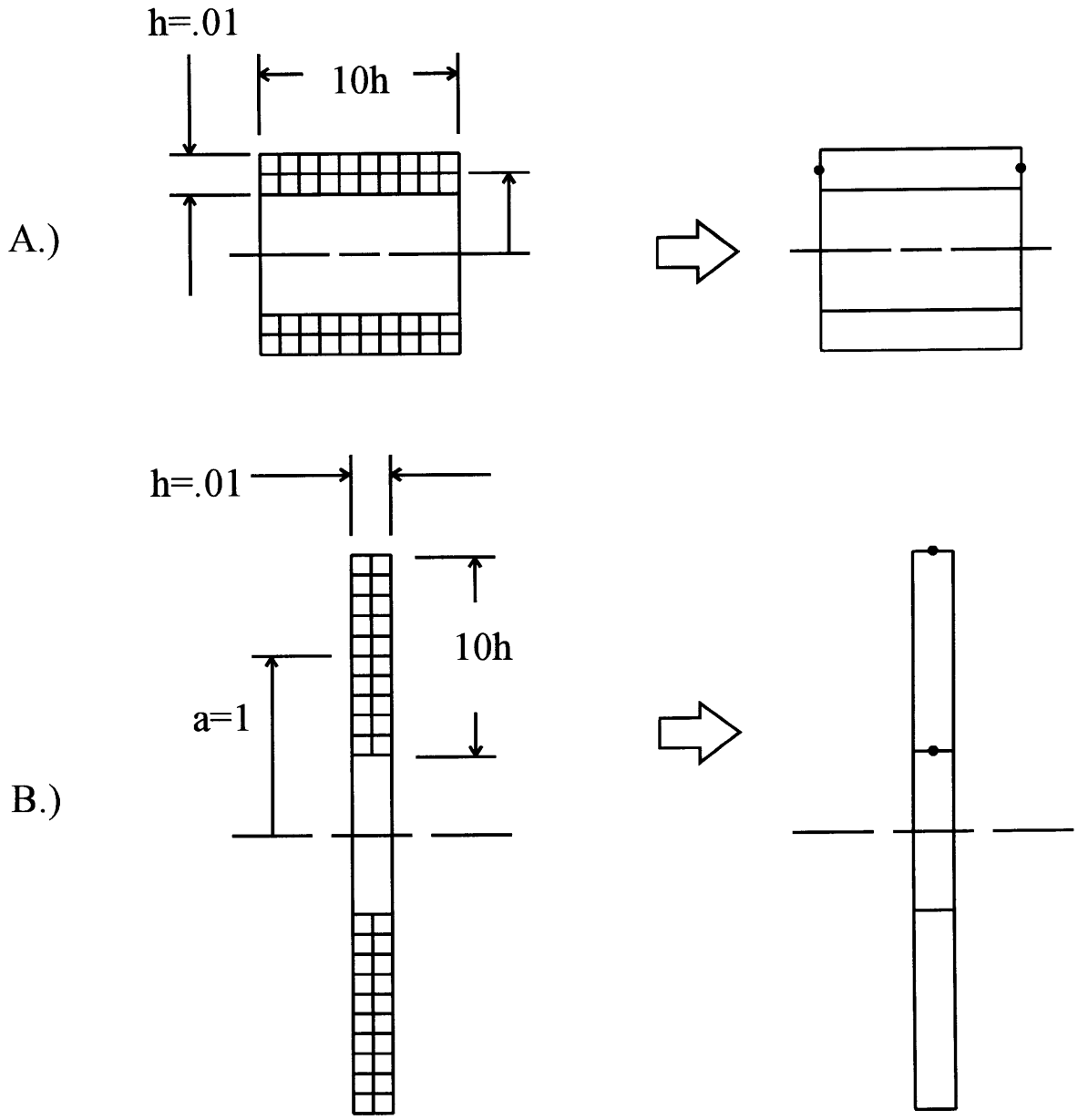

is shown to converge on the exact WFEM result for both the magnitude and the phase and for all five degrees of freedom.

These results are satisfactory and offer assurance that both the WFEM and CFEM formulations are correctly implemented.

5.4 Numerical results

In this section, I compare the T-junction modeled as shown in Figure 5-3 and Figure 5-4. I refer to these two models as the 3-element model and the 4-element model. The comparison is based on the scattering of propagating waves on an infinite shell that encounter the T-junction. I examine the scattering process in the frequency range of $1/10 < \Omega < 10$, where Ω is frequency normalized by the shell ring frequency. The incident wave is assumed to have a particular circumferential order n. Due to the symmetry of the problem, the incident wave scatters into reflected and transmitted waves of all wave types but of the same order n.

I express the shell wave scattering in terms of the reflection coefficient R_{ij} or the transmission coefficient T_{ij}, where R and T are the ratios of the time-averaged reflected and transmitted power to the time averaged incident power. Also, the subscript j refers to the incident wave type and the subscript i refers to the reflected or transmitted wave type. Because there are three propagating shell waves, there are a total of nine reflection and nine transmission coefficients. But $R_{ij} = R_{ji}$ and $T_{ij} = T_{ji}$ due to reciprocity and only six of the R_{ij}'s and six of the T_{ij}'s are unique. The non-propagating waves, that is, the evanescent and the through-thickness wave do not transmit any time-averaged power but still indirectly influence the partitioning of the reflected and transmitted power.

To compare the two models, I select seven different test cases, which are summarized in Table 1. For all cases, the plate speed, radius, and density are unity and the Poisson's ratio is $\nu = .3$. I consider Case #1 as the baseline case. The remaining cases are the same as this case except either n is changed, both h and h_b are changed (to the same value), or just h_b is changed. Notice that the $h/a = 2\%$ and the

Figure 5-11: Comparison of WFEM and FEM models shown in Figure 5-10a. From top to bottom is drive point stiffness to applied forces in x, θ, r and to applied moments about θ and r directions versus normalized frequency, $\Omega = \omega a/c_p$. Left column is magnitude and right column is phase angle divided by π. Legend: WFEM(solid), FEM(dashed).

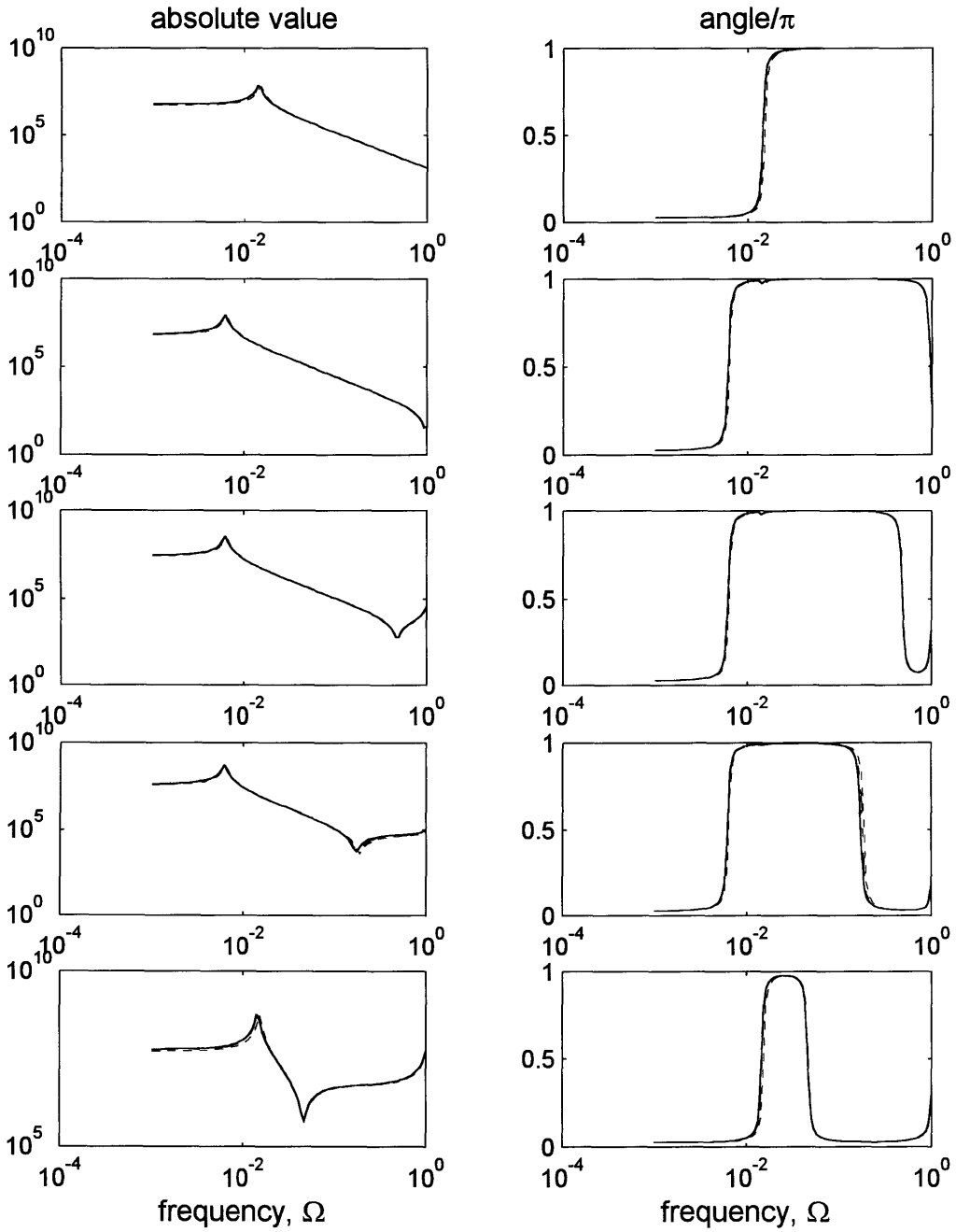

Figure 5-12: Comparison of WFEM and FEM models shown in Figure 5-10b. From top to bottom is drive point stiffness to applied forces in x, θ, r and to applied moments about θ and r directions versus normalized frequency, $\Omega = \omega a/c_p$. Left column is magnitude and right column is phase angle divided by π. Legend: WFEM(solid), FEM(dashed). Conclusion: mutual verification of WFEM and FEM element implementation.

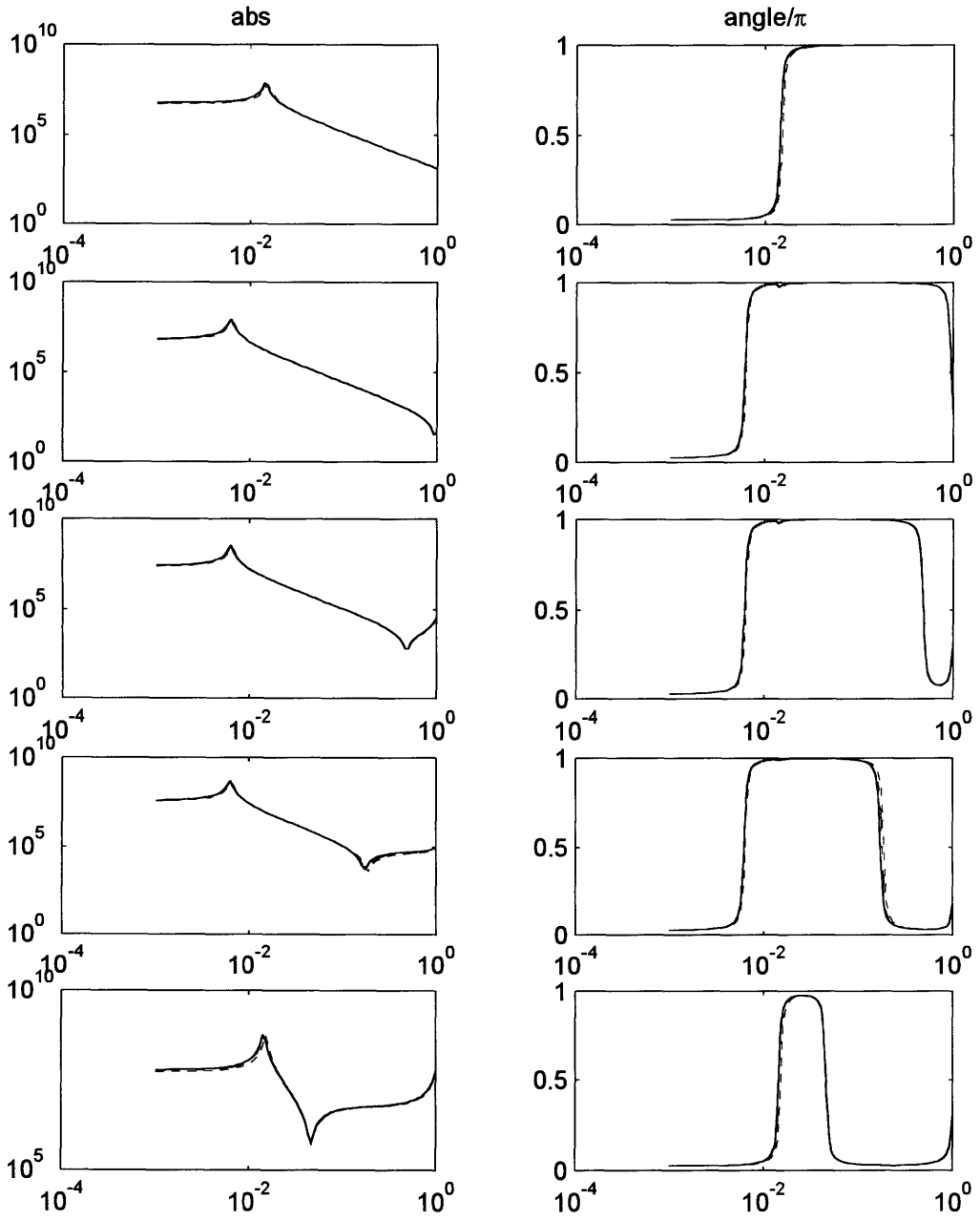

$h/a = 10\%$ thick shells are those considered earlier in Section 5.2.

Table 1: Summary of test cases.

Case	n	$h/a(\%)$	$h_b/a(\%)$
1	2	2	2
2	0	2	2
3	2	2	4
4	2	10	10

5.4.1 Checking calculation of scattering coefficients

Because I specify that the shell, bulkhead, and T-junction elements have no dissipation ($\eta = 0$), I may use conservation of power flow to check that the model is correctly implemented. In Figure 5-13, I plot the total power deficit versus frequency for the Case #1 using the four-element model. The power deficit is the difference between the incident power and the total scattered power (the sum of the reflected and transmitted powers) divided by the incident power in decibels. Three curves are shown corresponding to an incident compressional, shear, and flexural wave. The error is plotted for each wave type above its cutoff frequency. The flexural wave cutoff is below the lowest frequency considered. The shear wave cutoff is near $\Omega = 1.2$. The compressional wave cutoff is near $\Omega = 2.1$. For all three incident waves, the error is very small, about -100 dB, and probably incurred during several matrix inversion operations.

To check convergence of the scattering coefficients with refinement in the T-junction element mesh size, I compare the six unique R_{ij}'s for the coarse mesh and the fine mesh in Figure 5-14. The fine mesh has four times as many elements. The differences in the results for the coarse and fine mesh sizes is negligible proving that the solution has converged.

To check reciprocity of the scattering coefficients, I compare the reflection coefficients R_{12} and R_{21} in Figure 5-15a and the transmission coefficients T_{12} and T_{21} in Figure 5-15b for Case #1. The figures show that the scattering coefficients are equal as expected.

These checks on the implementation are satisfactory and give me confidence that the scattering coefficients are properly calculated.

Figure 5-13: Error (dB) in wave power scattering coefficients versus normalized frequency, $\Omega = \omega a/c_p$, for $n = 2$, $h/a = h_b/a = 2\%$. Legend: incident compressional wave(solid), incident shear wave(dash), incident flexural wave(dash-dot). Conclusion: error is negligible.

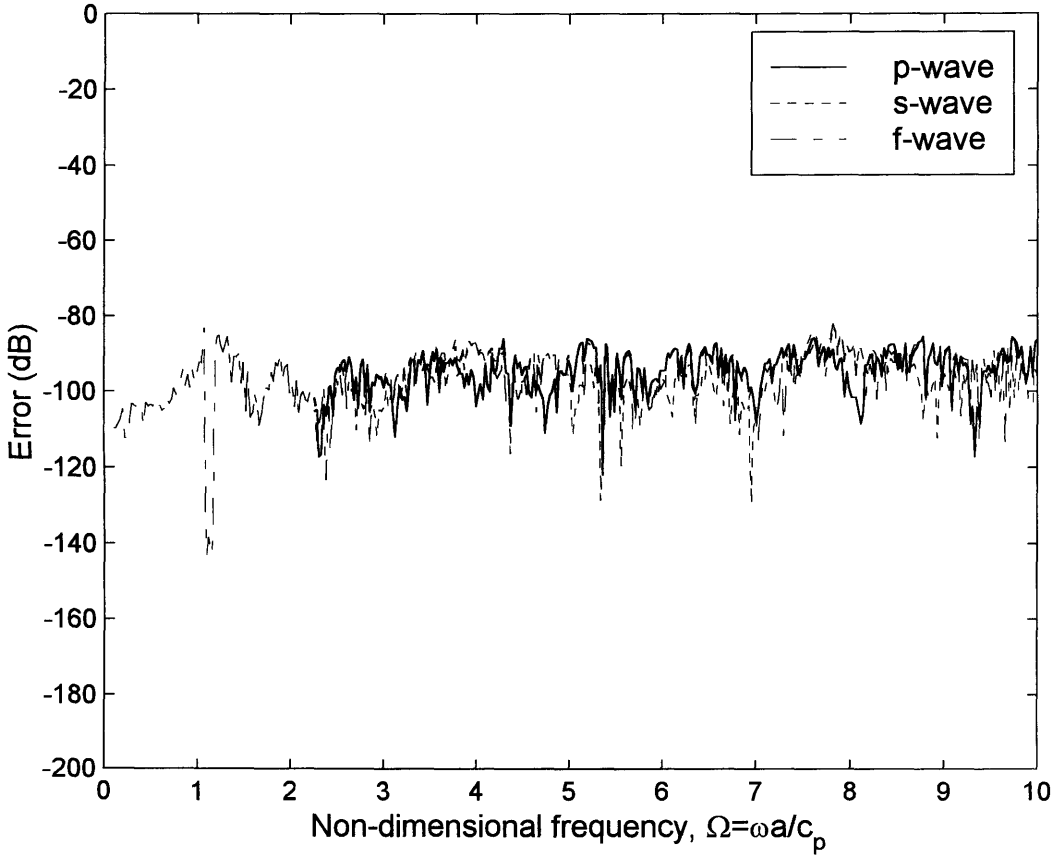

Figure 5-14: Comparison of wave scattering coefficients using fine (solid) and coarse mesh (dashed) versus normalized frequency, $\Omega = \omega a/c_p$, for $n = 2$, $h/a = h_b = 2\%$. Conclusion: FEM solution has converged.

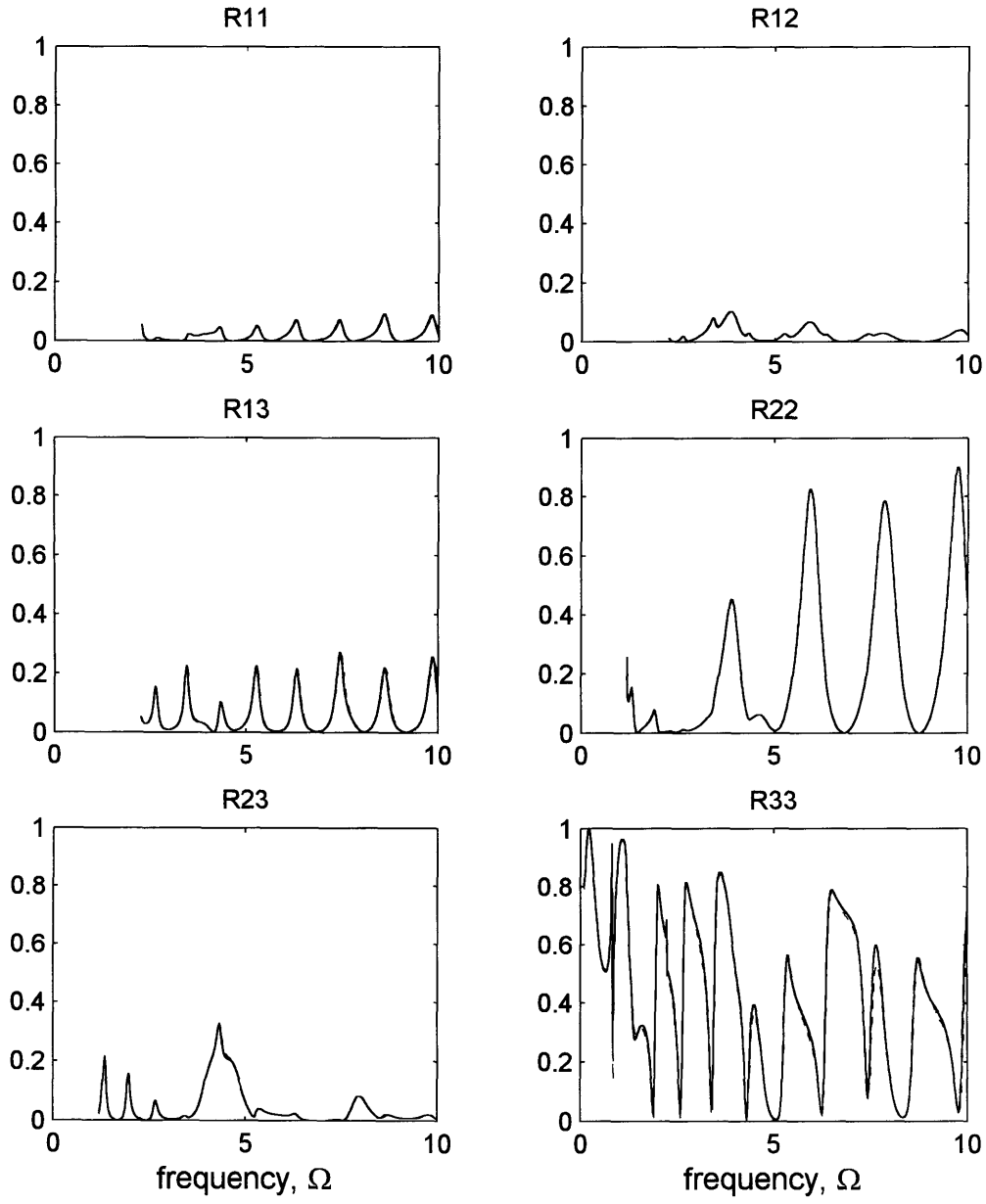

Figure 5-15: Comparison of a.) R_{13} and R_{31} and b.) T_{13} and T_{31} versus normalized frequency, $\Omega = \omega a/c_p$, for $n = 2$, $h/a = h_b = 2\%$. Conclusion: reciprocity is maintained.

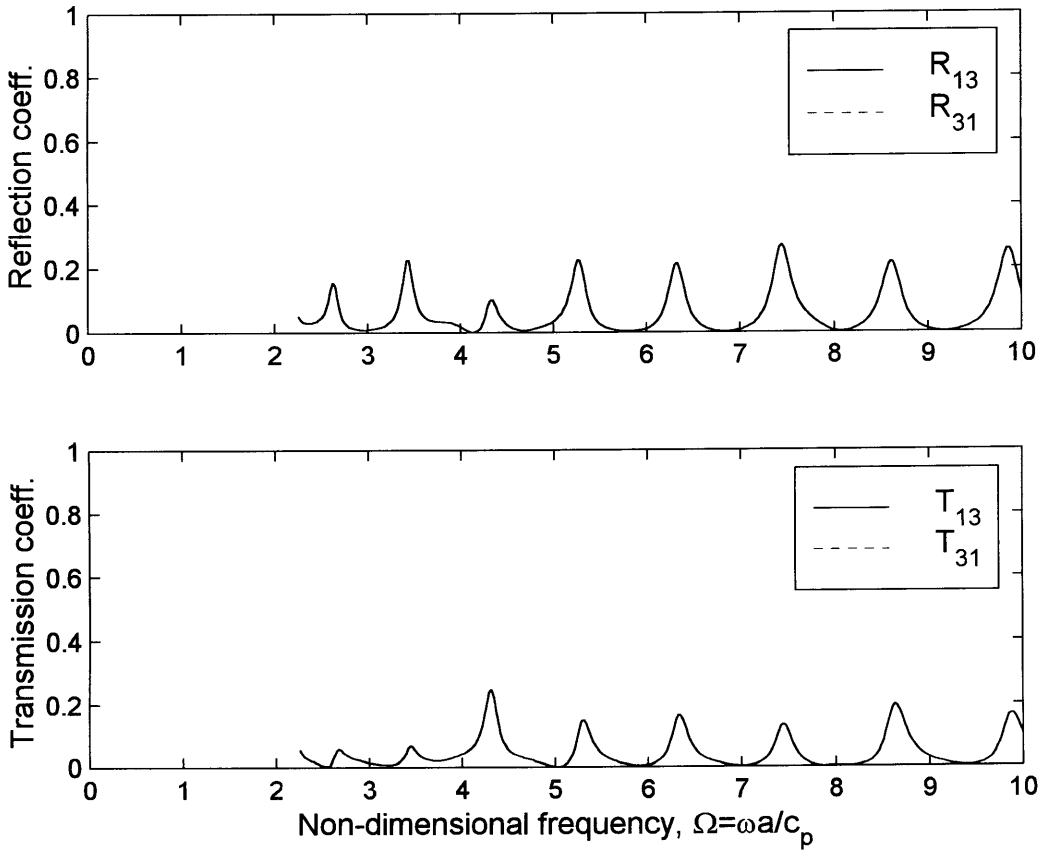

5.4.2 Four-element model results for Case #1

To get our bearing, I first present the results for Case #1 using the four-element model only. Scattering at a bulkhead connection has been studied by a number of researchers including Guo [15][20] and Tso[47] but were limited to thin shells and bulkheads.

The scattering coefficients for the incident compressional wave are shown in Figure 5-16. The top three subplots are the compressional, shear, and flexural reflection and transmission coefficients versus frequency, respectively. The bulkhead wave amplitudes versus frequency are plotted in the bottom subplot. The bulkhead flexural wave is the propagating bulkhead flexural wave. The non-propagating flexural wave amplitudes are not plotted because they don't store much energy. For the most part, the incident compressional wave is transmitted past the bulkhead. This is because the compressional wave shell displacements are mostly axial and primarily couple with the low impedance flexural waves (also mostly axial) of the bulkhead. The T_{11} curve goes through regions of alternating high and low transmission. This scalloping is due to the alternating resonance/anti-resonance flexural response of the bulkhead. This is evidenced by the correlation between the scalloping in T_{11} with the scalloping in the bulkhead flexural wave amplitude (although the maximum and minimum values are not quite aligned). The increase in spacing between maximum and minimum values of T_{11} is due to the dispersive nature of the bulkhead flexural waves. At low values of T_{11}, most of the power is scattered into a flexural wave power. The transmitted flexural wave has roughly the same magnitude as the reflected flexural wave. There is also some scattering into reflected compressional wave. There are additional low points in T_{11} that are correlated with the bulkhead shear wave resonances and peaks in the R_{12} and T_{12} coefficients. At these low values of T_{11}, the R_{12} and T_{12} coefficients are roughly equal.

The scattering coefficients for the incident shear wave is shown in Figure 5-17 in the same format as Figure 5-16. The character of the R_{22} and T_{22} coefficients above $\Omega = 5$ is quite regular. Most of the power flows away from the junction carried by either the reflected or transmitted shear wave. The scalloping pattern of the T_{22} is correlated with the amplitude shear waves in the plate. When the shear wave amplitude peaks, T_{22} is at a minimum. This is opposite that for the bulkhead flexural wave and T_{11}. It is interesting that the minimum values of T_{22} and R_{22} are nearly zero, while the maximum of T_{22} is nearly unity but R_{22} is about .9.

The character of the R_{22} and T_{22} coefficients below $\Omega = 5$ is quite different from that above. This is because the shear wave is travelling in a more tightly wound helix. At the shear wave cutoff, in fact, the shear wave has no axial component at all. The shear wave shell displacement is primarily transverse to its direction of propagation. Therefore, when it is travelling in a tight helix, it has a significant axial displacement and therefore is coupled to the flexural bulkhead wave. Again, it is observed that the off-diagonal transmission and reflection coefficients for a given wave type are roughly equal.

Figure 5-16: Incident compressional wave scattering coefficients and bulkhead wave amplitudes versus frequency for Case #1: $n = 2$, $h/a = 2\%$, $h_b = 2\%$. Legend for a.), b.), and c.): R_{ij}(solid), T_{ij}(dashed). Legend for d.): $|A_p|$(solid), $|A_s|$(dashed), $|A_f|$(dash-dot).

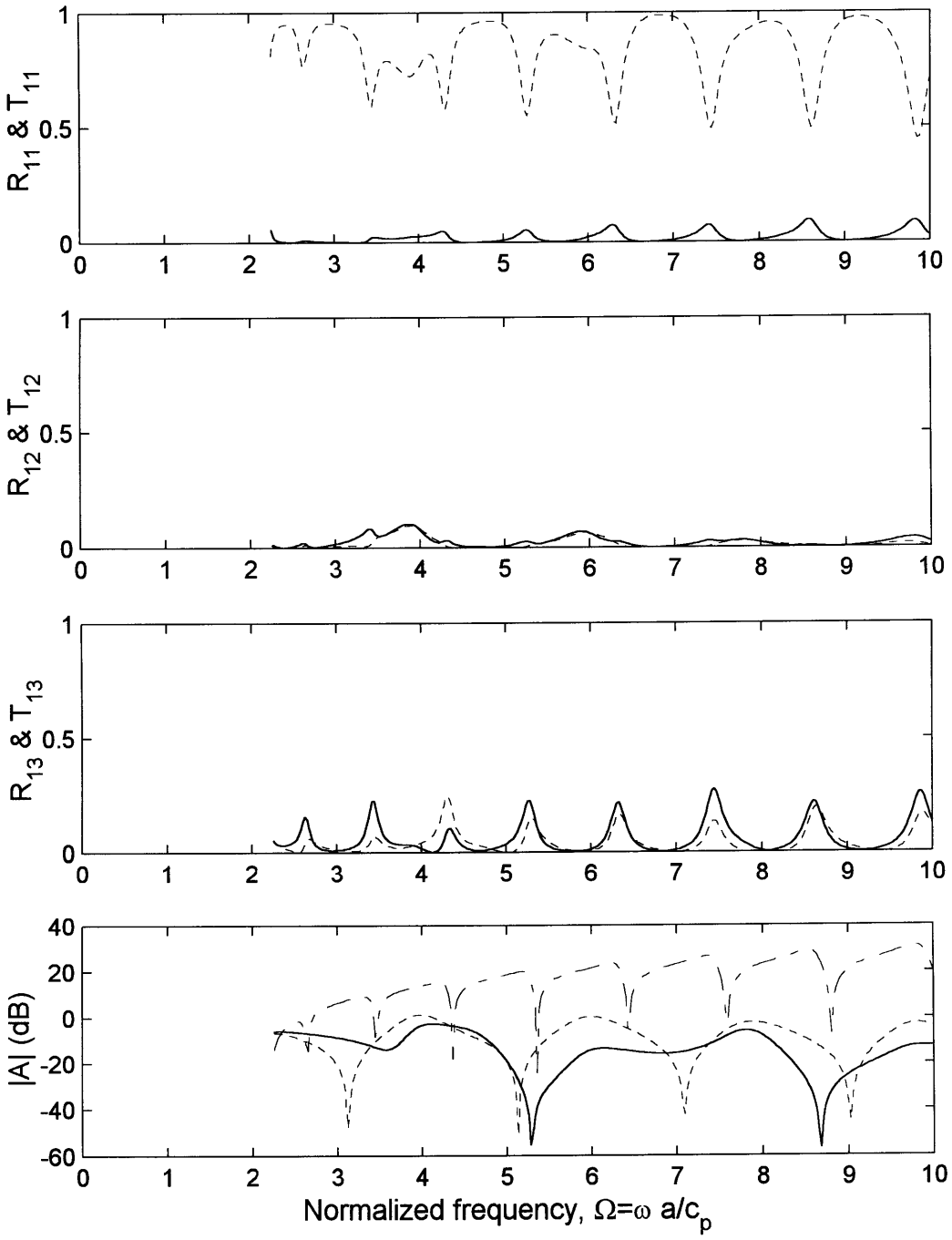

Figure 5-17: Incident shear wave scattering coefficients and bulkhead wave amplitudes versus frequency for Case #1: $n = 2$, $h/a = 2\%$, $h_b = 2\%$. Legend for a.), b.), and c.): R_{ij}(solid), T_{ij}(dashed). Legend for d.): $|A_p|$(solid), $|A_s|$(dashed), $|A_f|$(dash-dot).

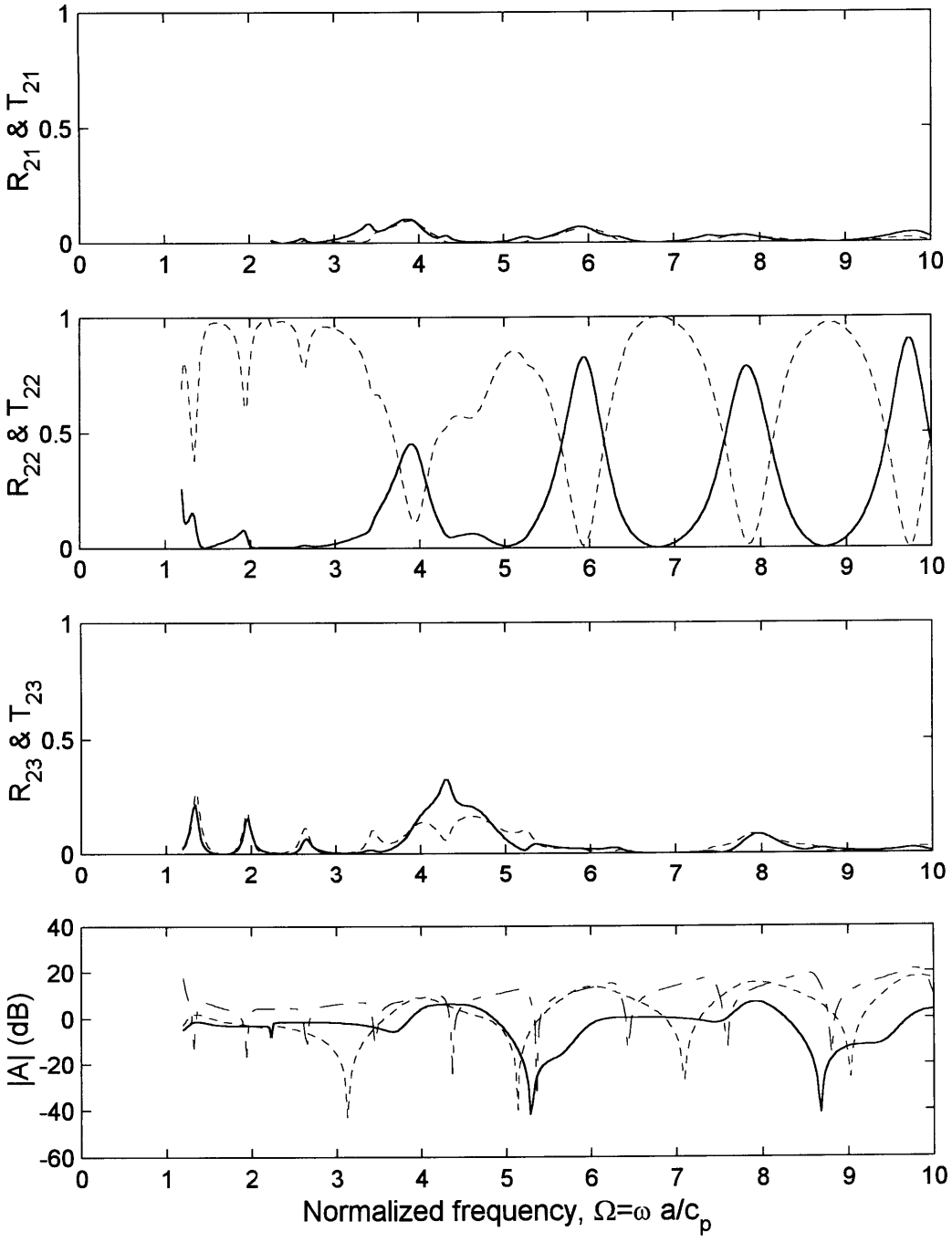

The scattering coefficients for the incident flexural wave is shown in Figure 5-18 in the same format as Figure 5-16. Obviously, the incident shell flexural wave couples with the bulkhead flexural wave even though the flexural shell wave is prominently radial and the flexural bulkhead wave is axial. The reason is that the waves couple through the rotation caused by the flexural wave. In addition, there is some correlation between the flexural shell wave and the bulkhead compressional wave. The T_{33} coefficient seems to be generally greater at the peaks in the bulkhead compressional wave amplitude.

5.4.3 Comparison of three and four-element model results

I now compare the three and four-element model results. I define error as the difference between the respective scattering coefficients for the three-element model and the more accurate four-element model.

The results for Case #1 (see Table I) are presented in Figure 5-19 and Figure 5-20, where the six unique reflection and transmission coefficients are plotted versus normalized frequency. The solid curve is the four-element model result, while the dashed curve is the three-element model result. Generally, the agreement is pretty good. There is about a 10% to 30% difference between the minimum points in the R_{11} and T_{11} coefficients above $\Omega = 5$. The three-element model predicts a higher R_{11}. For the most part, the difference is made up by a lower T_{11}. The frequencies at which the peaks in R_{11} occur are slightly higher for the four-element model indicating that it is the stiffer model. There are similar differences in the R_{33} and T_{33} coefficients.

To check sensitivity of the results to circumferential order, I present the Case #2 results in Figure 5-21 and Figure 5-22. The compressional and flexural $n = 0$ waves have no circumferential component, while the $n = 0$ shear wave has no axial component. They are, therefore, uncoupled and thus the R_{12}, T_{12}, R_{23}, and the T_{23} coefficients are all zero. There is essentially no difference between the two models for the shear wave scattering coefficients. The differences for the R_{11} and T_{11} and R_{33} and T_{33} coefficients is only slightly higher than for Case #1.

To check sensitivity to changes in bulkhead thickness with no change in shell thickness, I present the Case #3 results in Figure 5-23 and Figure 5-24. The error for all shear wave coefficients is small. The error for the R_{11} and T_{11} and R_{33} and T_{33} coefficients is not, where the error is progressively worse at the higher frequencies.

As I showed in Section 5.2, the thick shell model is an accurate representation of the shell for thicknesses at least up to 10%. To test the limits of the applicability of the three-element model, I present the Case #4 results in Figure 5-25 and Figure 5-26. The error for all shear wave coefficients is no longer small but the three-element model captures the character of R_{22} and T_{22}. It's clear that the three-element model fails to capture much of the character of the R_{11}, T_{11}, R_{33}, T_{33}, R_{13}, and T_{13}. It fails at the middle frequencies (below $\Omega = 5$) as well as at the higher frequencies (above $\Omega = 5$).

Figure 5-18: Incident flexural wave scattering coefficients and bulkhead wave amplitudes versus frequency for Case #1: $n = 2$, $h/a = 2\%$, $h_b = 2\%$. Legend for a.), b.), and c.): R_{ij}(solid), T_{ij}(dashed). Legend for d.): $|A_p|$(solid), $|A_s|$(dashed), $|A_f|$(dash-dot).

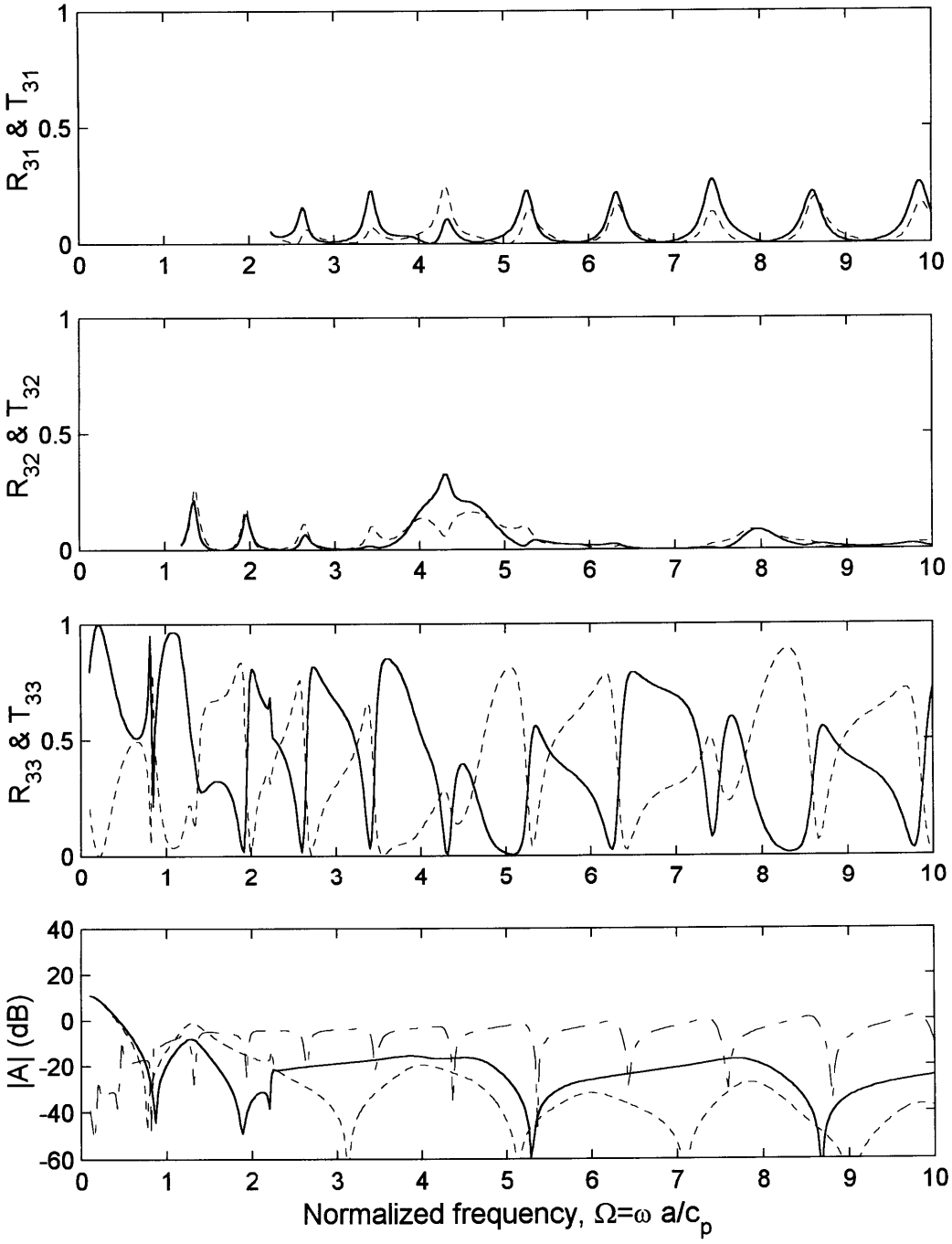

Figure 5-19: Unique wave reflection coefficients versus frequency, $\Omega = \omega a/c_p$, for Case #1. Legend: 4-element model(solid), 3-element model(dashed).

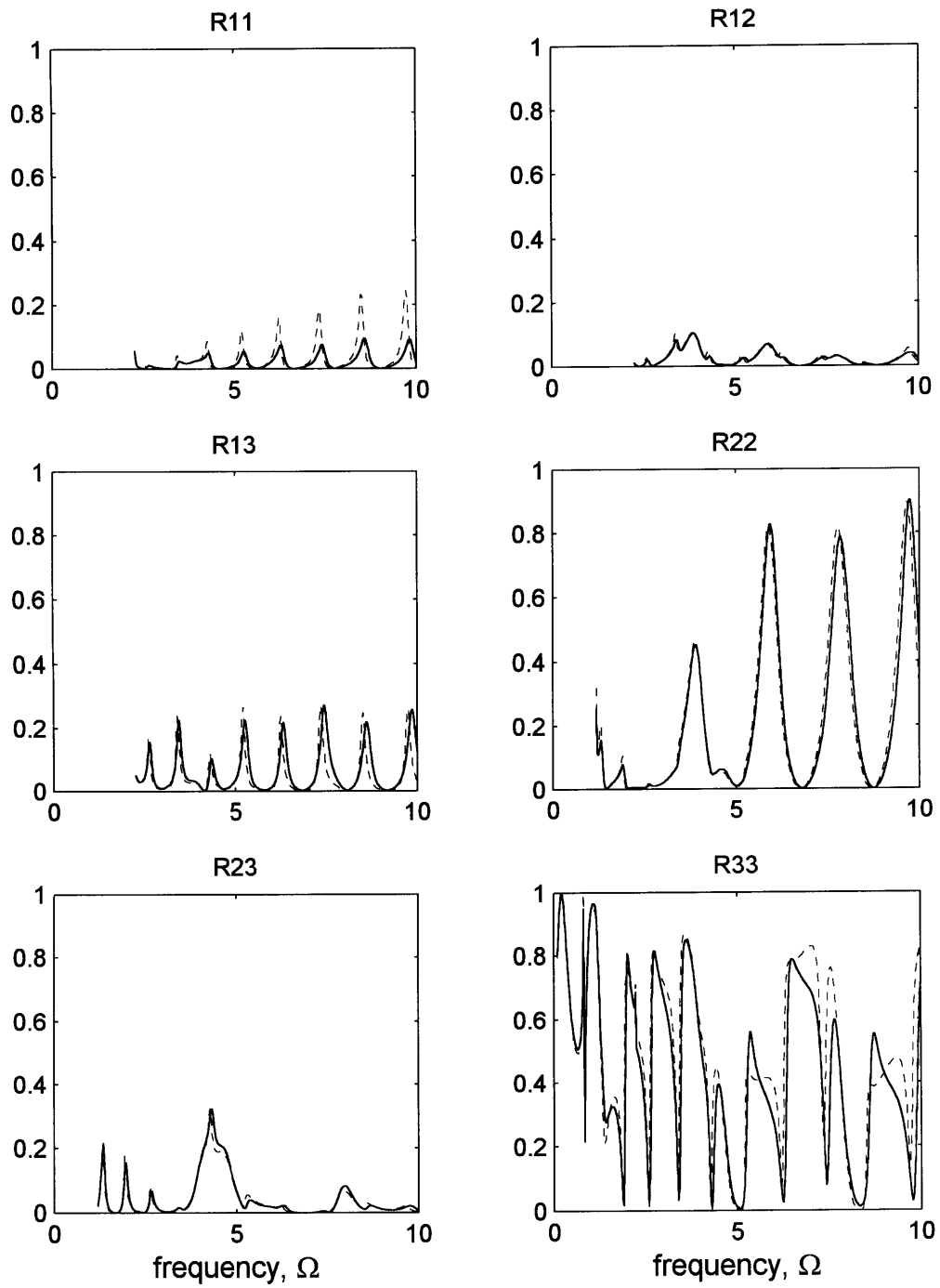

Figure 5-20: Unique wave transmission coefficients versus frequency, $\Omega = \omega a/c_p$, for Case #1. Legend: 4-element model(solid), 3-element model(dashed).

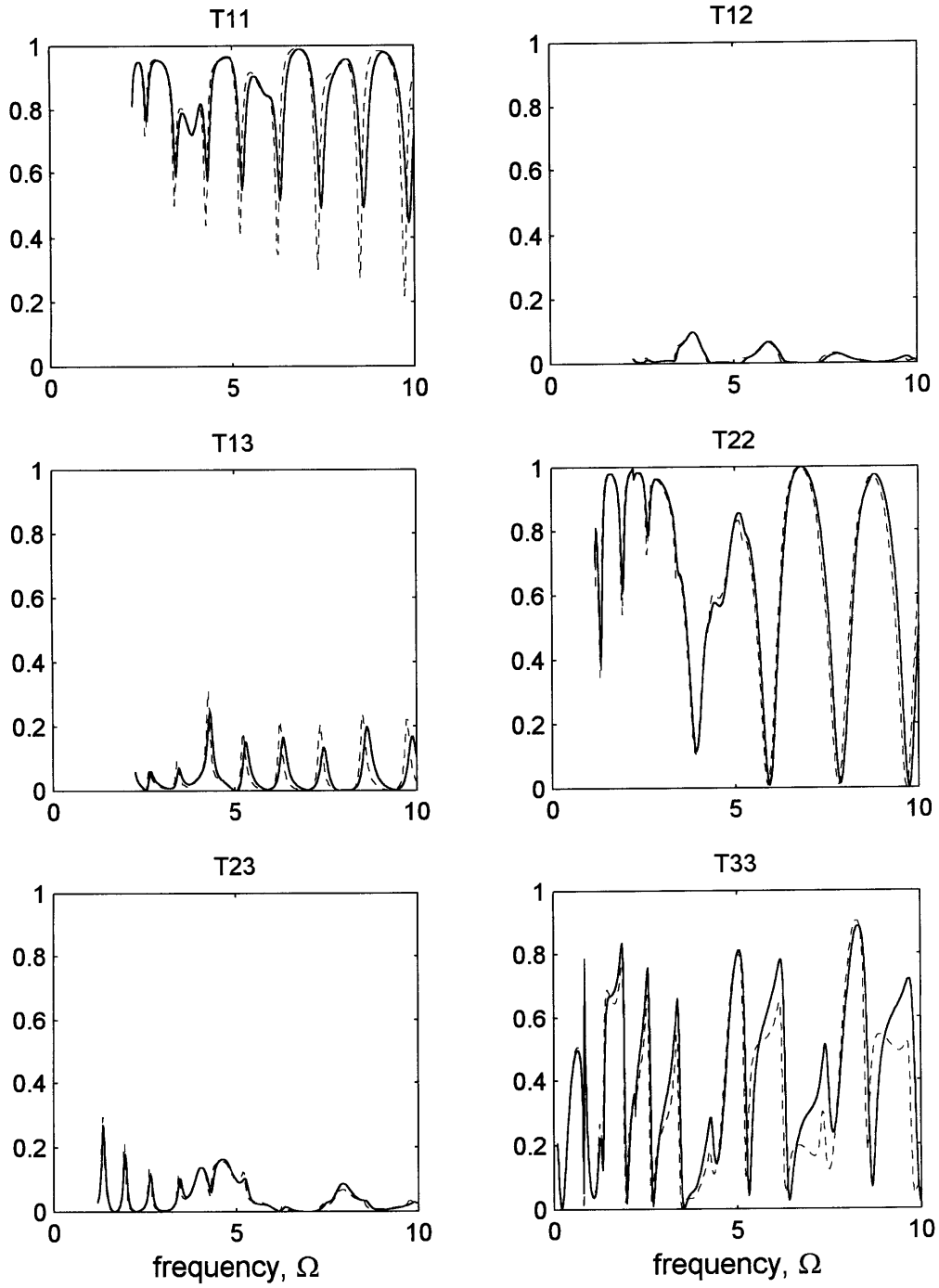

Figure 5-21: Unique wave reflection coefficients versus frequency, $\Omega = \omega a/c_p$, for Case #2. Legend: 4-element model(solid), 3-element model(dashed).

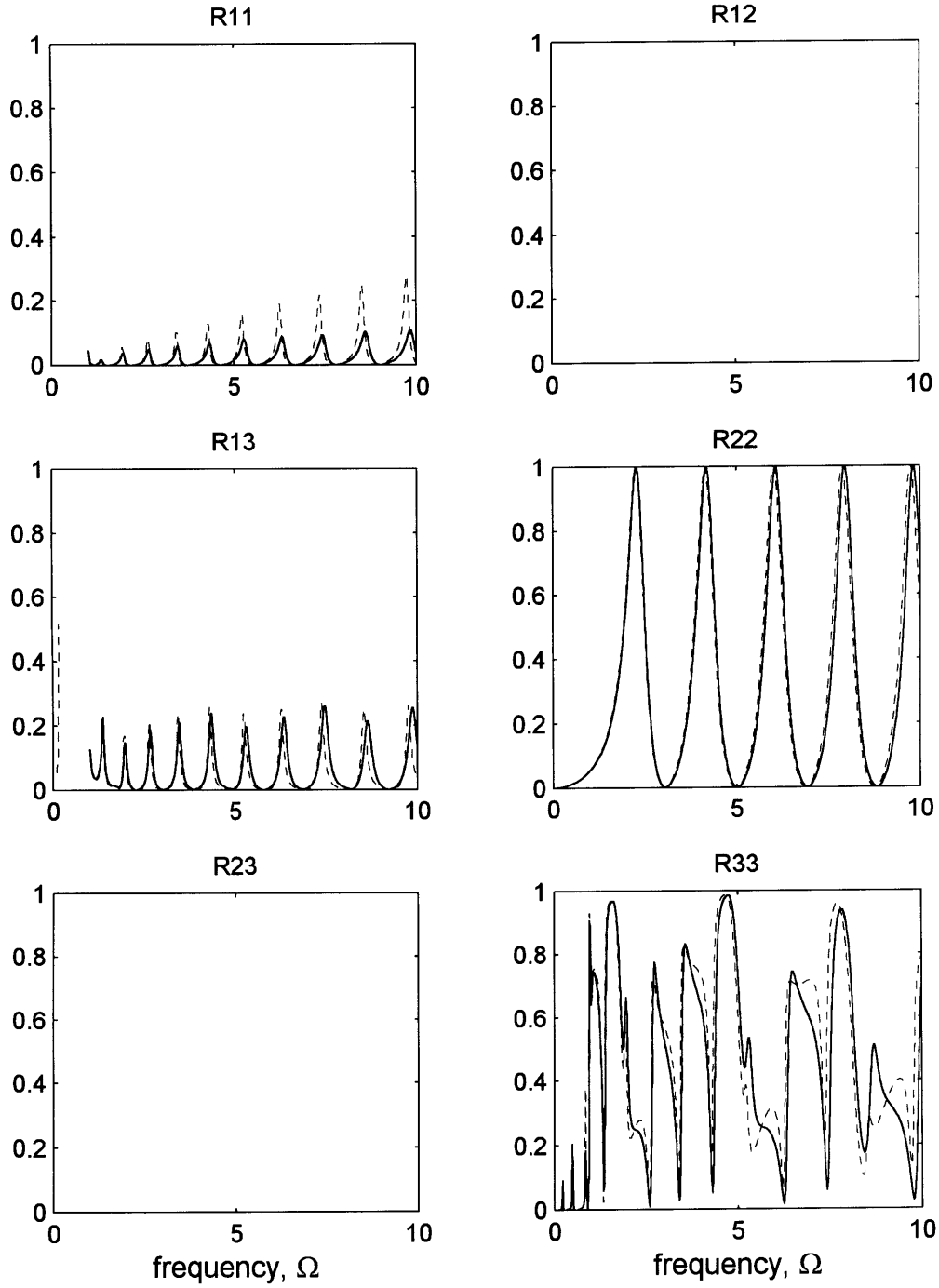

Figure 5-22: Unique wave transmission coefficients versus frequency, $\Omega = \omega a/c_p$, for Case #2. Legend: 4-element model(solid), 3-element model(dashed).

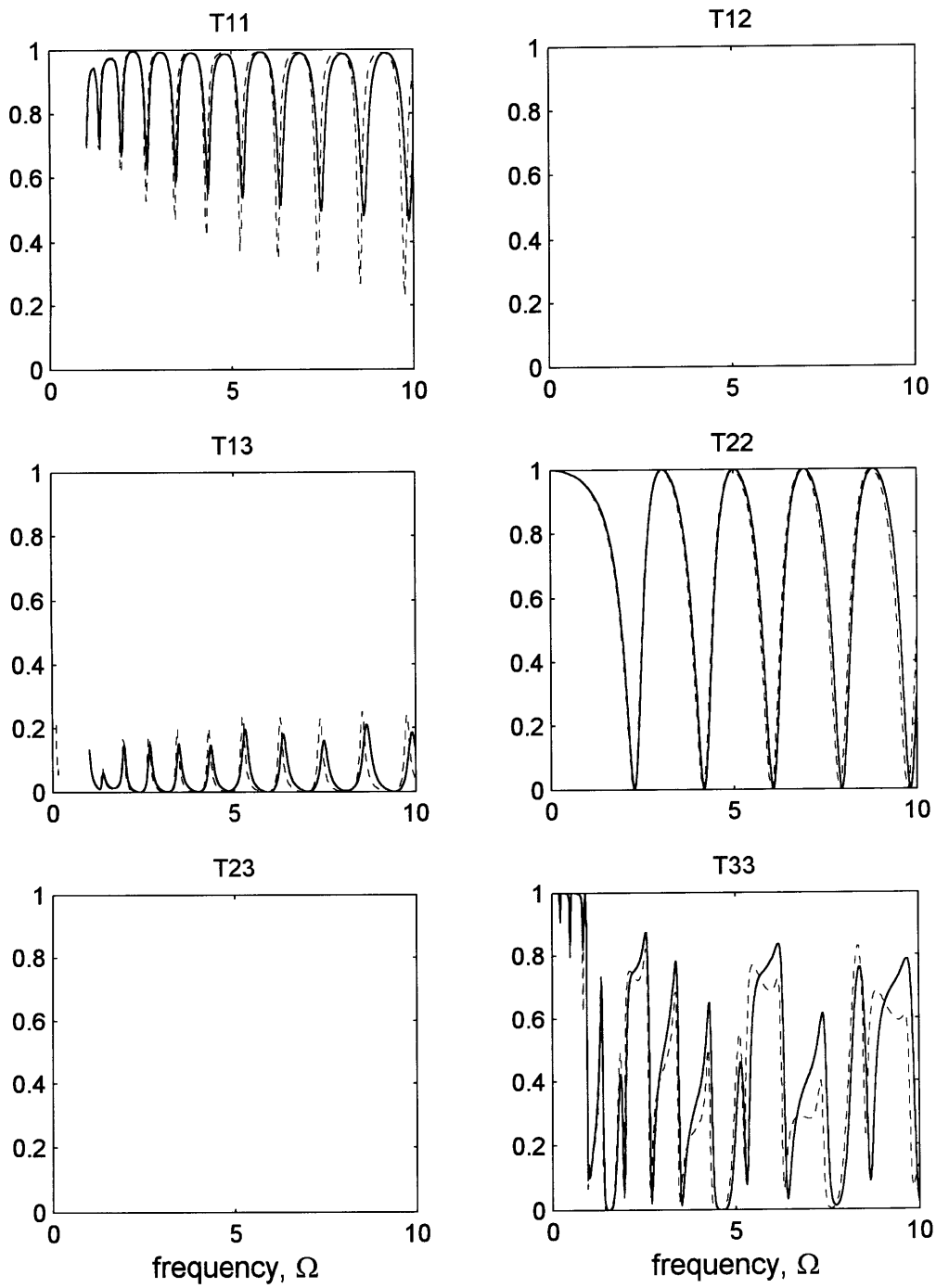

Figure 5-23: Unique wave reflection coefficients versus frequency, $\Omega = \omega a/c_p$, for Case #3. Legend: 4-element model(solid), 3-element model(dashed).

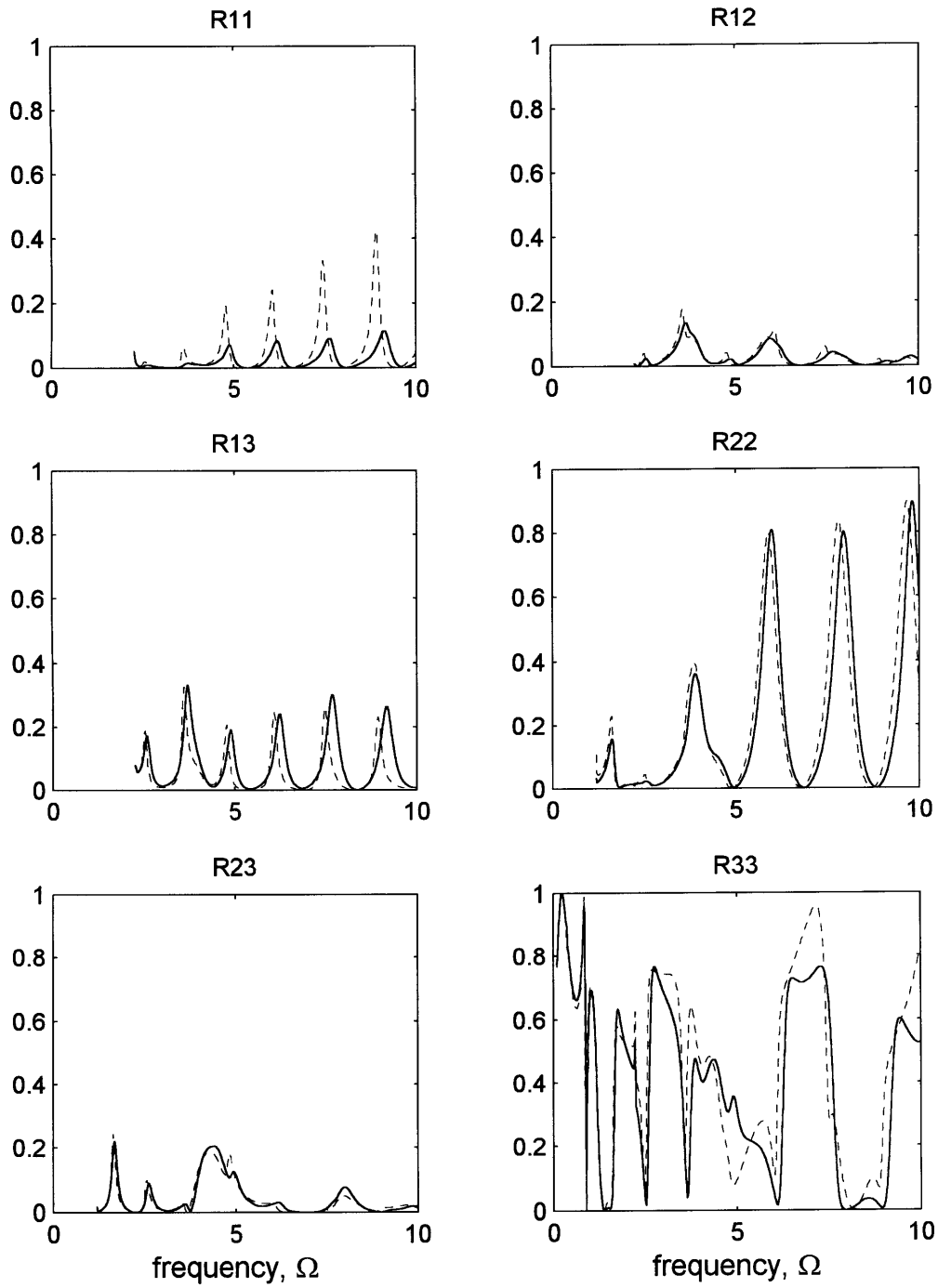

Figure 5-24: Unique wave transmission coefficients versus frequency, $\Omega = \omega a/c_p$, for Case #3. Legend: 4-element model(solid), 3-element model(dashed).

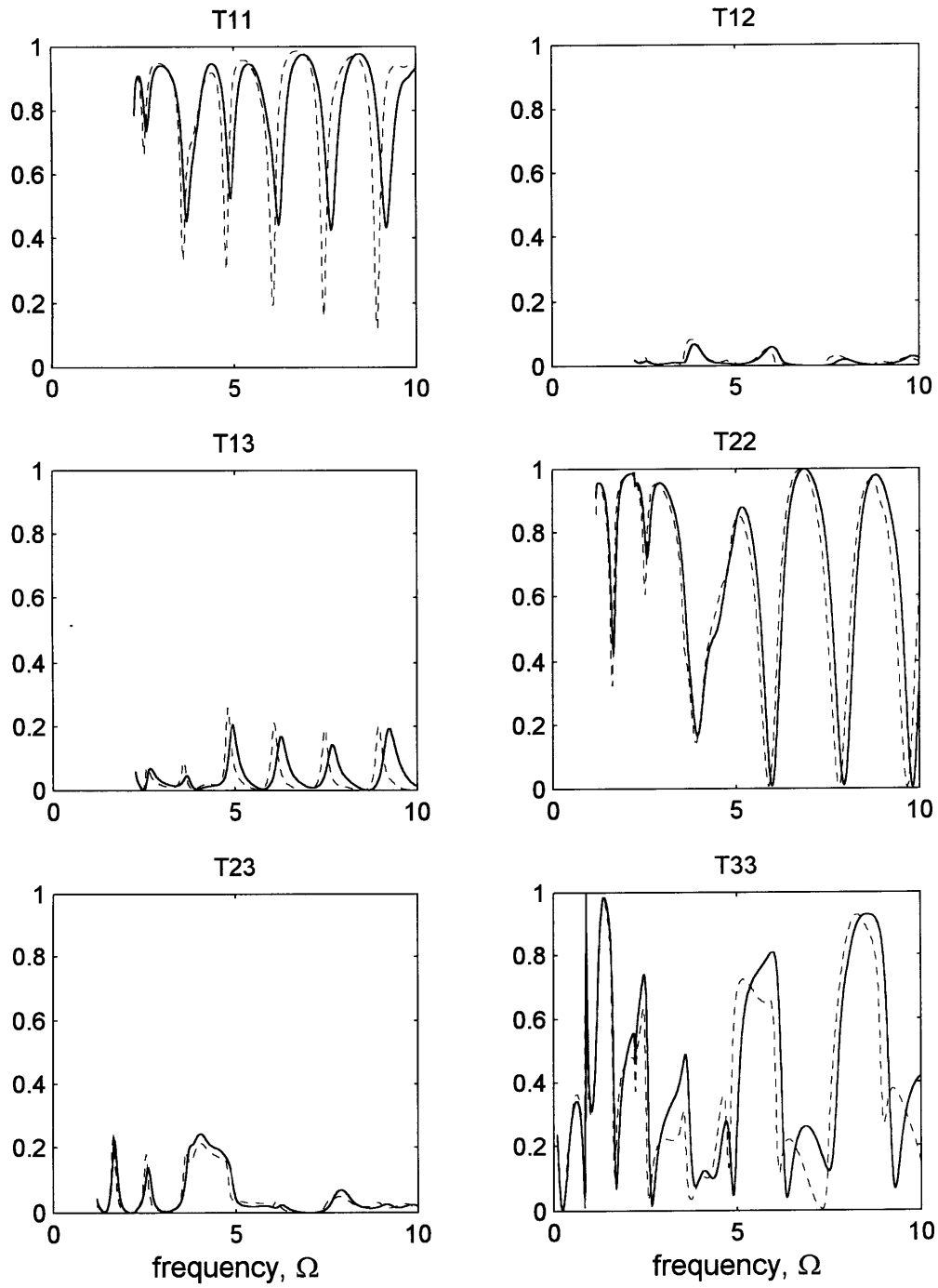

Figure 5-25: Unique wave reflection coefficients versus frequency, $\Omega = \omega a/c_p$, for Case #4. Legend: 4-element model(solid), 3-element model(dashed).

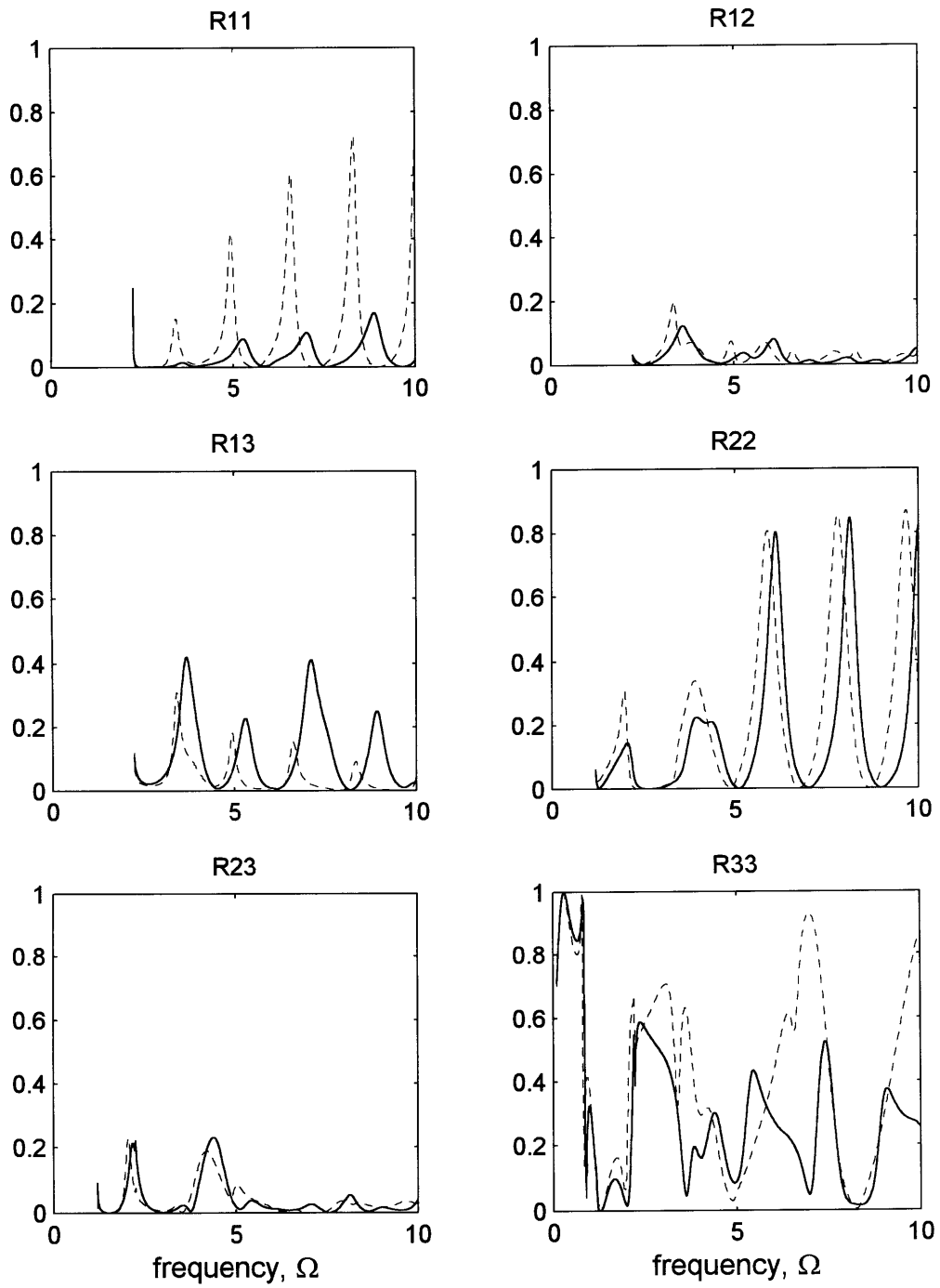

Figure 5-26: Unique wave transmission coefficients versus frequency, $\Omega = \omega a/c_p$, for Case #4. Legend: 4-element model(solid), 3-element model(dashed).

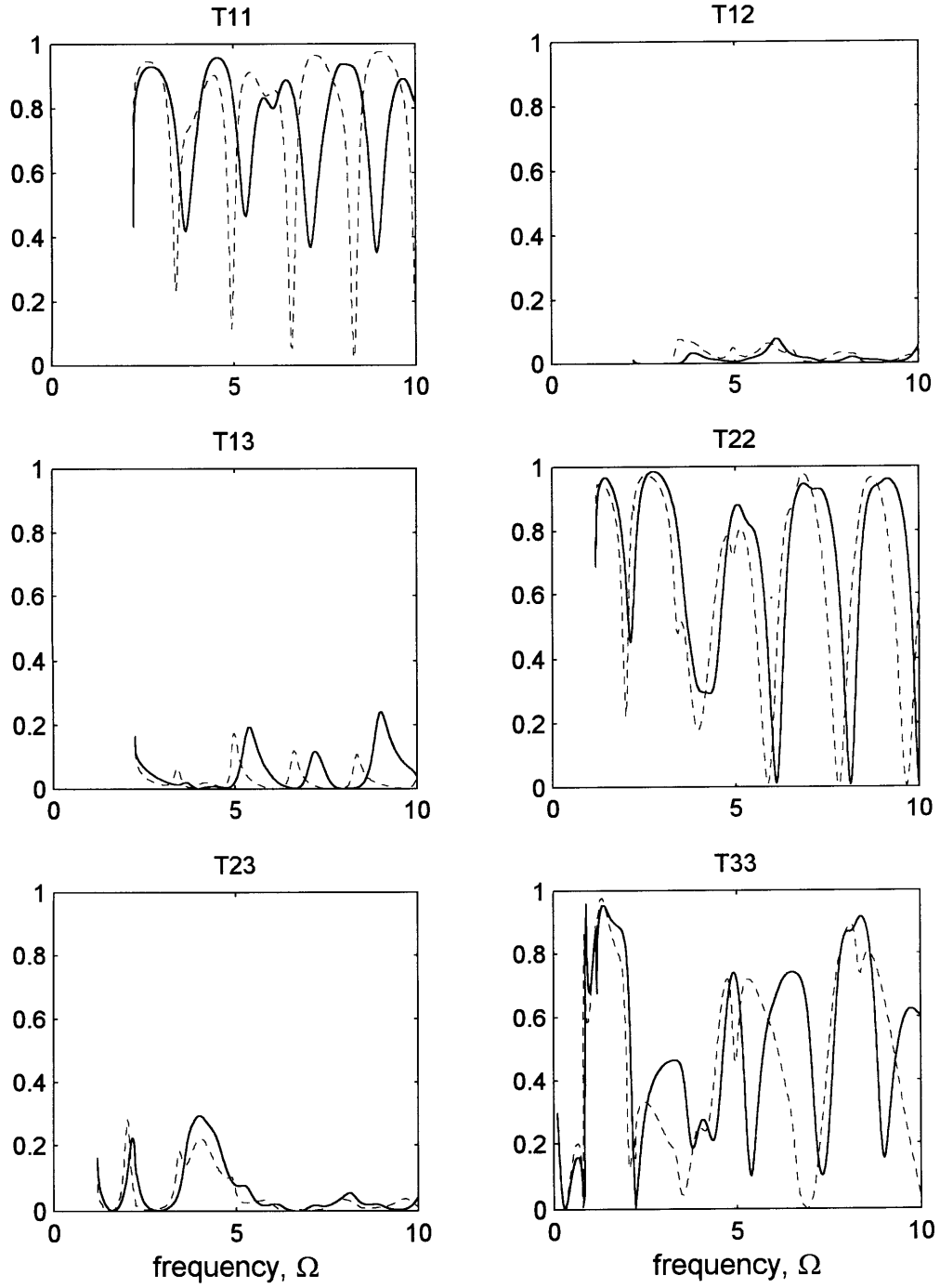

5.5 Summary

I have shown that the thick shell model provides an accurate description of the shell waves at middle to high frequencies for thin to moderately thick shells (10%). For plate connections, such as the bulkhead example used here, the details of the T-junction are important when the bulkhead and plate are moderately thick. The T-junction details are even important for relatively thin shells (2%-4%) when the bulkhead is thicker than the shell. In addition, I have shown that the T-junction may be modeled with conventional FEM and combined in a manner that is consistent with the thick shell theory. Because the wavelengths are large compared to the dimensions of the T-junction, the number of required ring elements used to form the T-junction element is small and that the good numerical efficiency of the WFEM approach is maintained.

Chapter 6

Comparison with experiment

6.1 Introduction

My objective in this chapter is to model the response of a cylindrical shell due to one or more piezoelectric sources embedded in the shell wall and then compare the results with available experimental data. I use experimental data collected by Lin [24]. I compare his data with two separate models of the shell, which I refer to as simply the *flat plate* or *plate model* and the *shell model.* The shell model is the WFEM model formulated in terms of axial waves and circumferential modes as described in Chapter 2 . I'll show that the agreement between the experimental data and both models is very good. This comparison serves to validate the WFEM model.

Lin also compared experimental data using both a flat plate model and a shell model. He used a flat plate model to estimate the near-field response of the shell and a WFEM shell model (which I provided for him) to model the far-field $n = 0$ mode excitation of the shell. In this chapter, I generalize his plate model so that it may also be used in the far-field for any excitation mode. I also generalize the use of the shell model so that it may be used in the near-field for any excitation mode. In addition, I consider data that Lin collected but not presented in his thesis.

6.2 Test specimen and set-up

A schematic of the test set-up is shown in Figure 6.1. The basic elements of the test set-up are a long, thin cylindrical PVC (polyvinyl-chloride) shell surrounded by air, a PVC keel (a flat plate) attached to the left end of the shell, a circumferential ring array of 12 piezoelectric sources located towards the middle of the shell, and a laser doppler velocimeter or LDV measurement system that samples at a rate

of about $64kHz$.. The LDV allows non-contact measurement of the shell velocity at one point on the shell surface at a time. The shell is suspended by bungee cords at each end. The drive system of the source array allows the individual sources to be phased to drive shell modes $n = 0$ to $n = 6$, although all experimental data considered here is for the $n = 0$ drive.

As shown in Figure 6.1, the shell is in coordinate system $\{x, \theta, r\}$ with corresponding displacments $\{u, v, w\}$. These are consistent with the shell model developed in Chapter 2. The material and geometric properties of the shell and keel are shown in Table I. The keel is attached at the left end of the shell on the outside surface. It is radially oriented and bonded in place with epoxy. Ideally the shell would not have a keel during these experiments and is a possible source of error as discussed later. The test data is taken on the right end of the shell without the keel to try and minimize its' influence.

Table 1: Material and geometric properties of PVC shell and keel.

Plate speed	$c_p = 1.70 \times 10^3\ m/\sec$
Density	$\rho = 1.39 \times 10^3\ kg/m^3$
Poisson's ratio	$\nu = .20$
Thickness	$h = 4.70 \times 10^{-3}\ m$
Loss factor	$\eta = .05$
Shell outer radius	$a = 2.05 \times 10^{-1}\ m$
Shell total length	$L = 6.09\ m$
Length from left end of shell to source array	$L_1 = 2.33\ m$
Length from source array to right end of shell	$L_2 = L - L_1$
Keel axial length	$L_k = 1.5\ m$
Keel thickness	$h_k = 4.70 \times 10^{-3}\ m$

The shell is driven by an equi-spaced 12 element circumferential piezo-electric ring array. Each source is itself a small cylinder. To insert the source, a radial hole is drilled in the shell. The source is then centered in the hole and bonded in place with epoxy. The axis of the source is therefore along the radial coordinate of the shell. The source is a "31-mode" piezoelectric ceramic with material and geometric properties given in Table 2. A 31-mode source is poled in the "3" direction (the radial direction of the source) and expands in the "1" (the circumferential direction of the source). Due to curvature there is a corresponding radial displacement (in the radial direction of the source). I assume throughout that the source-shell interaction is only through a *uniform* radial displacement of the source. I discuss the validity of this assumption at the end of this chapter. I'll define the individual or local coordinate systems for

Figure 6-1: Schematic of 16 inch PVC shell with embedded array of piezoelectric sources.

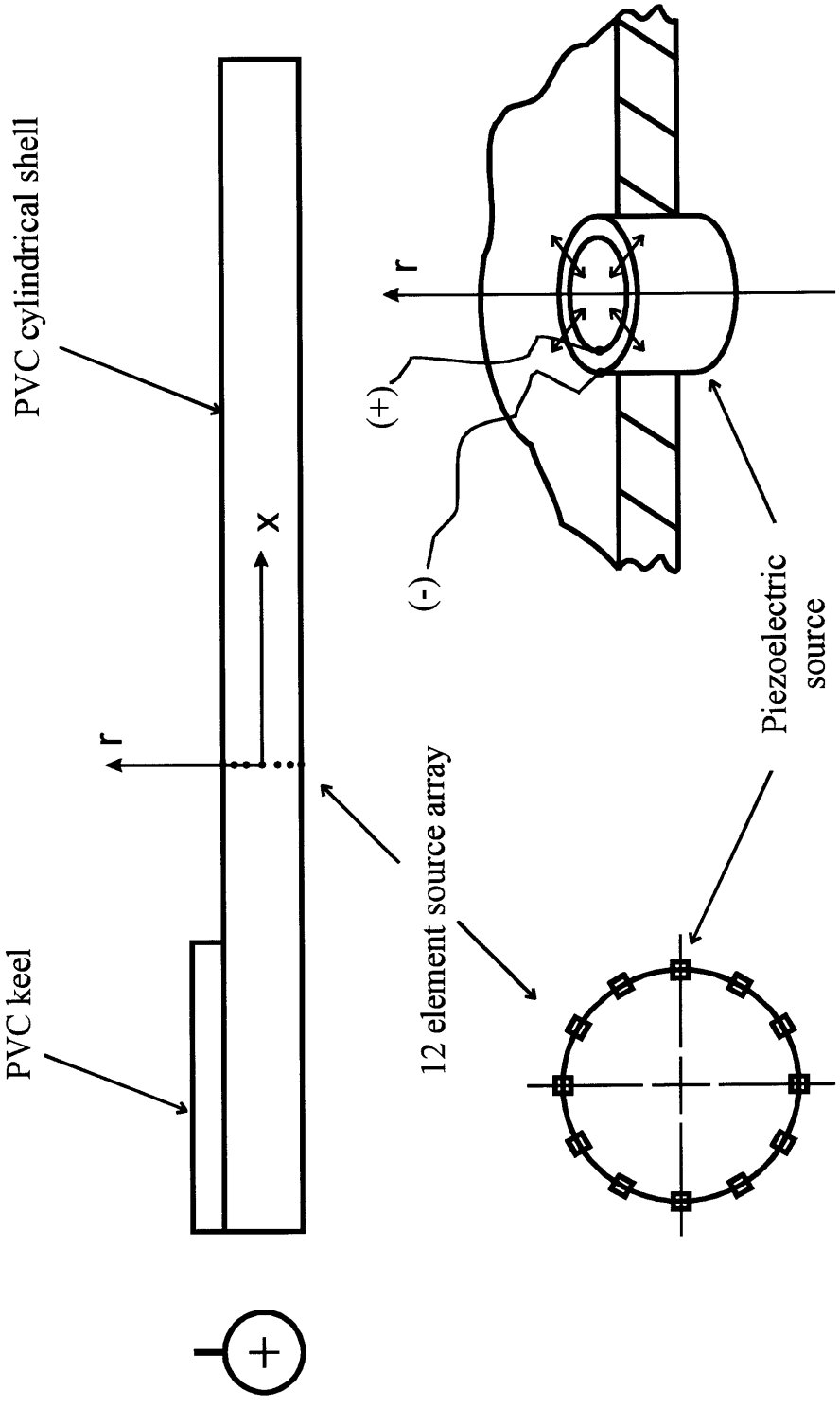

all the sources in the following section.

Table 2: Material properties and geometric properties of piezo-electric source

Material	Channel 5700 (Navy Type VI)
Piezoelectric constant	$d_{31} = -2.5 \times 10^{-10}\ m/V$
Dielectric constant	$\epsilon_{33}^{T} = 3400\left(8.85 \times 10^{-12}\right)\ F/m$
Young's modulus	$1/s_{11}^{E} = 6.2 \times 10^{10}\ N/m^2$
Density	$\rho_x = 7400\ kg/m^3$
Outer radius	$a_x = 4.0 \times 10^{-3}\ m$
Thickness	$h_x = 7.0 \times 10^{-4}\ m$
Length	$L_x = 8.0 \times 10^{-3}\ m$

The source input is swept sine from 50 Hz. to 20 kHz with 50 Hz spacing. The data is presented in terms of non-dimensional frequency that is normalized by the shell ring frequency, which occurs at about 1.35 kHz. In terms of the non-dimensional frequency, the data extends from about $\Omega = .05$ to $\Omega = 15$.

Shell velocities were measured at $x = .008$ and 3.5 m using the LDV. Both receiver locations at the same circumferential position as one of the sources. Two laser measurements were taken at each receiver location. The first directly records radial velocity. The second records the velocity at 45° from the radial direction in the $x - r$ plane. The two measurements are combined in the time domain to solve for the axial velocity. The circumferential component was not measured.

6.3 Flat plate model

The *flat plate model* developed in this section is based on a high frequency approximation of the shell equations and the method if images [6][21]. I develope this model for three reasons. First, a good portion of the available experimental results is at high frequency and it is, therefore, the appropriate model to use. Second, it provides additional verification of the shell model. Third, the ray interpretation of the source-shell interaction is insightful and roughly applies at the at lower frequencies.

To implement the model, I make the following assumptions:

- The response of the shell due to an individual source is that of an infinite flat plate due to an individual source.
- The cyclic boundary condition in the circumferential direction and the free edge boundary conditions may be satisfied by a grid of image sources.

- There is no source interaction.
- The source is compact (small compared to wavelength).
- The source dimensions are small compared to the shell radius.

The validity of these assumptions are discussed at the end of this chapter. The details of the model are developed by progression in the following subsections.

6.3.1 Coordinate systems

I discussed in Chapter 2, how the effects of curvature become negligible at high frequency and the shell behaves as if it were a flat plate. In that same sense, the shell cylindrical coordinate system $\{x, \theta, r\}$ may also be considered as approaching a cartesian coordiante system $\{x, y, z\}$, where I define $y = a\theta$ and $z = r - a$ (x doesn't change). It is as if I am able take the cartesian coordinate system and wrap it around the shell an infinite number of times. Therefore, in this section only, *the* shell coordinate system is the cartesian coordinate system $\{x, y, z\}$. I'll continue to use the same variables, $\{u, v, w\}$, for the shell displacements.

I define two coordinate systems for each source. These systems are local relative to the global coordinate system $\{x, y, z\}$. For the the m'th source with global coordinates $\{x, y, z\} = \{x_m, y_m, 0\}$, the local cartesian coordinate system is $\{X_m, Y_m, Z_m\}$ and the local cylindrical coordinate system is $\{R_m, \Phi_m, Z_m\}$. The origin of both local systems are centered between the ends of the source located at $Z_m = \pm L_x/2$. In addition, the polar angle Φ_m is defined such that at $\Phi_m = 0$, R_m is aligned with X_m, which is parallel with x. This allows me to relate the global shell coordinates to local source coordinates as

$$R_m = \sqrt{X_m^2 + Y_m^2} = \sqrt{(x - x_m)^2 + (y - y_m)^2} \tag{6.1}$$

and

$$\Phi_m = \arctan\left(\frac{Y_m}{X_m}\right) = \arctan\left(\frac{y - y_m}{x - x_m}\right). \tag{6.2}$$

These relationships are shown graphically for a source located at $\{x, y, z\} = \{x_m, y_m, 0\}$ in Figure 6.2.

6.3.2 Piezoelectric ring source in an infinite flat plate

I derive the response of an infinite flat plate to a single piezoelectric source in Appendix C. I show that the transfer function between the radial plate displacement at radius R and the source input voltage V_o is

$$\frac{U_R(R)}{V_o} = \frac{N_{em}}{K_p + K_x} \frac{H_1(k_p R)}{H_1(k_p a_x)}, \tag{6.3}$$

Figure 6-2: Receiver response due to a volume source.

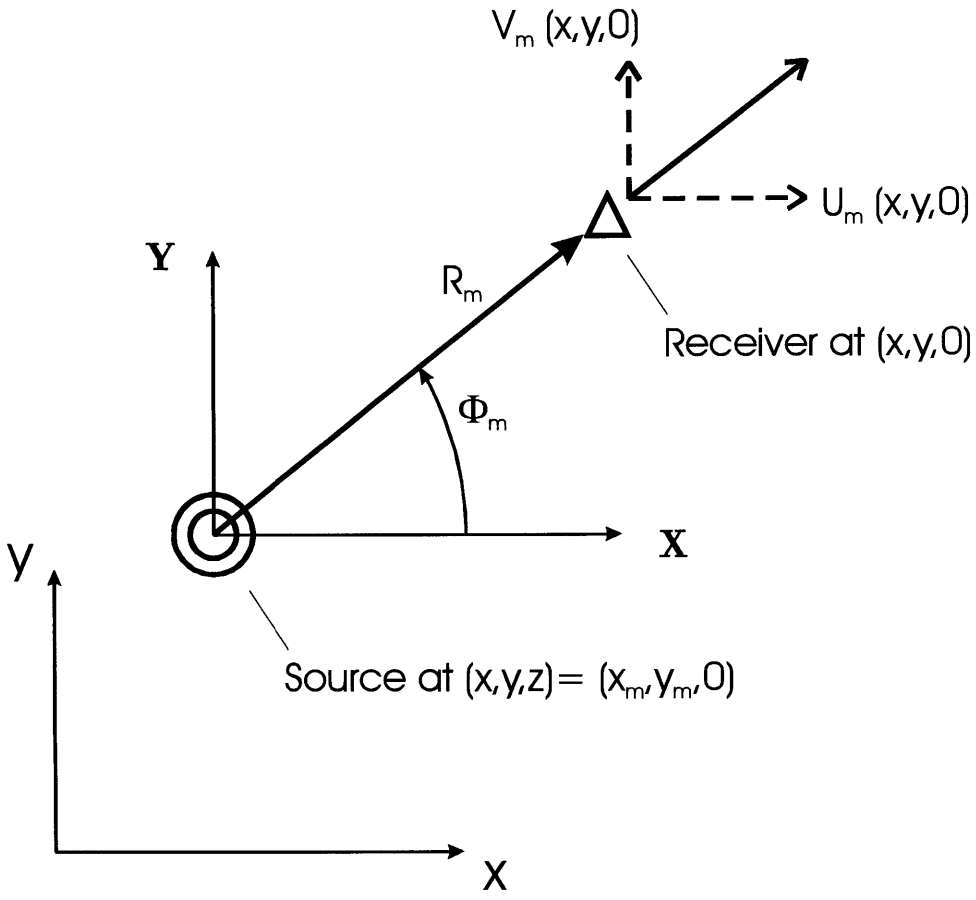

where

$$N_{em} = \frac{2\pi L_x d_{31}}{s_{11}^E} \tag{6.4}$$

is the electro-mechanical turns ratio (the total radial force produced by the source per volt),

$$K_x = \left[\frac{s_{11}^E a_x}{2\pi L_x h_x}\right]^{-1} \tag{6.5}$$

is the source internal mechanical compliance, and

$$K_p = 2\pi h \rho c_p^2 \left[(1-\nu) - k_p r \frac{H_0(k_p a_x)}{H_1(k_p a_x)}\right] \tag{6.6}$$

Figure 6-3: Comparison of plate and source stiffness at source radius as predicted by plate model.

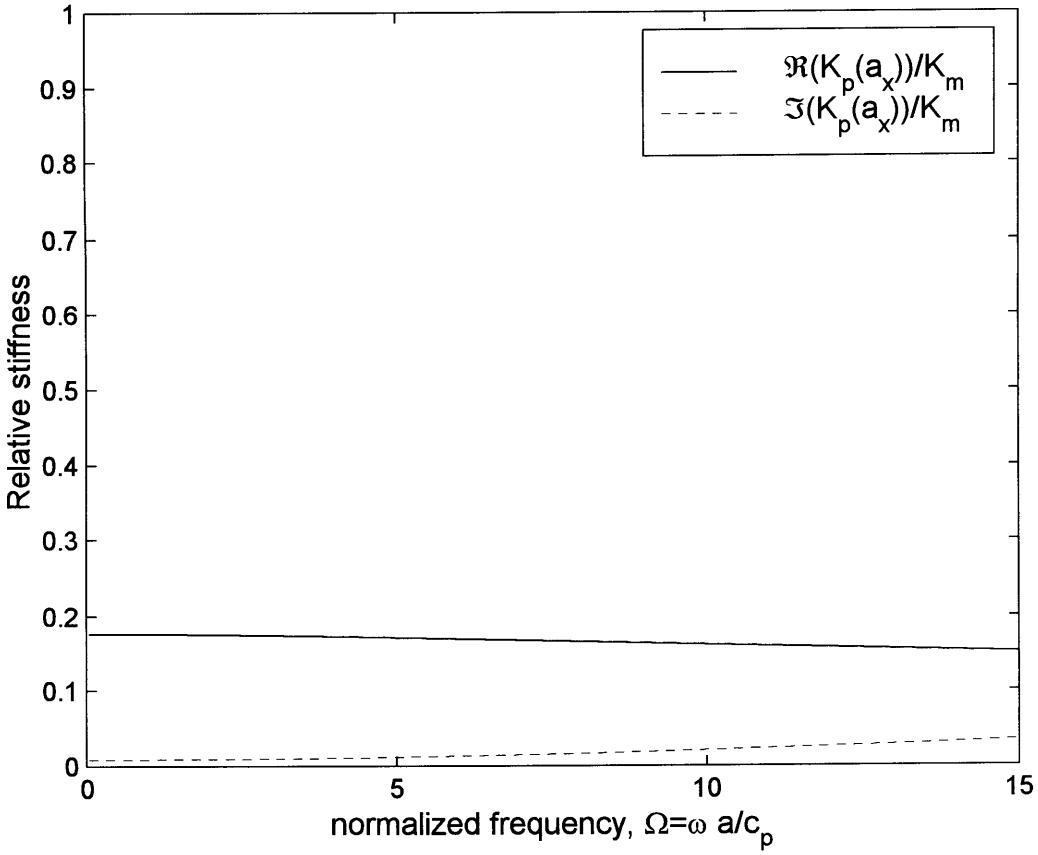

is the plate stiffness as seen by the source. I use Eq.(6.3) in the following subsection as a building block for the shell model. The first term on the right of Eq.(6.3) is the source displacment per unit input volt, while the second term on the right is the ratio of the displacment at R to that at a_x.

Using the source and plate (shell) properties specified earlier, I compare the plate stiffness to the source stiffness in Figure 6.3. As modeled in Appendix C, the source stiffness is a pure real constant and as shown in the figure is about $5x$ greater than the real part of the plate stiffness from zero frequency up to 15 times the shell ring frequency. The figure also shows that the magnitude of the imaginary part of K_p is negligible compared to the source stiffness. I'll discuss the implications of this at the end of this chapter.

6.3.3 Shell response using flat plate model

For the moment, let's consider an infinitely long cylindrical shell with a source at the origin. If I model the shell by its high frequency relations, then the only difference between its response and that of an infinite flat plate is the presence of an infinitely long line array of image sources at $\{x_m, \theta_m\} = \{0, \pm m2\pi a\}$, where m takes on all non-zero integer values. The $m = 0$ value represents the actual source. The image sources have the same phase as the actual source at the origin because the cyclic boundary condition imposes continuity of displacement over the entire θ domain.

I can use Eq.(6.3) to write the shell axial and circumferential response (in the shell global coordinate system) as

$$\left\{ \begin{array}{c} U(x,\theta) \\ V(x,\theta) \end{array} \right\} = \frac{N_{em} V_o}{K + K_x} \sum_m \frac{H_1(k_p R_m)}{H_1(k_p a_x)} \left\{ \begin{array}{c} \cos(\Phi_m) \\ \sin(\Phi_m) \end{array} \right\}, \tag{6.7}$$

where R_m and Φ_m are defined by Eq.(6.1) and Eq.(6.2). I have done nothing more than write a vector sum of the shell response due to all the image sources.

Now, if I consider a finite length shell with the left end at $x = -L_1$ and the right end at $x = L_2$, then the infinite number of image sources at $x = 0$ create additional line arrays at $x = -2L_1$ and $x = -2L_2$. The phase of these sources must be negative to match the free-edge condition at the ends of the shell. These line arrays create their own image arrays at $x = \pm 2(L_1 + L_2)$. However, the phase of these sources is positive (opposite the phase of the previously imaged line array). This process of successive images with alternating phase continues out to $x = \pm\infty$ forming a virtual source grid. The resulting grid pattern due to this imaging process is shown graphically in Figure 6.4 for the real source located at $\theta = 0$. Note that the spacing in the axial direction is not uniform when $L_1 \neq L_2$. The shell axial response is the vector sum of the responses due to each image source and Eq.(6.7) still applies provided that the m subscript is now used to refer to the positions of a particular source in the virtual source grid.

The model may be used to predict either axial or circumferential shell response and will, of course, falsely predict that the out-of-plane displacement is exactly zero. This model also predicts that only compressional waves are injected into the shell. The response to a multiple real sources is easily accomplished by adding the response due to each real source and its grid of image sources.

6.3.4 Equivalent point forcing

To complete this section, I consider what set of unidirectional point forces are equivalent to the force distribution that a single source exerts on the plate. I show here that this distribution is equivalent to a pair of orthogonally oriented force-dipoles of equal strength. Kausel solved the closely related problem

Figure 6-4: Schematic of flat plate model showing locations and phase of virtual sources due to a single source at the origin.

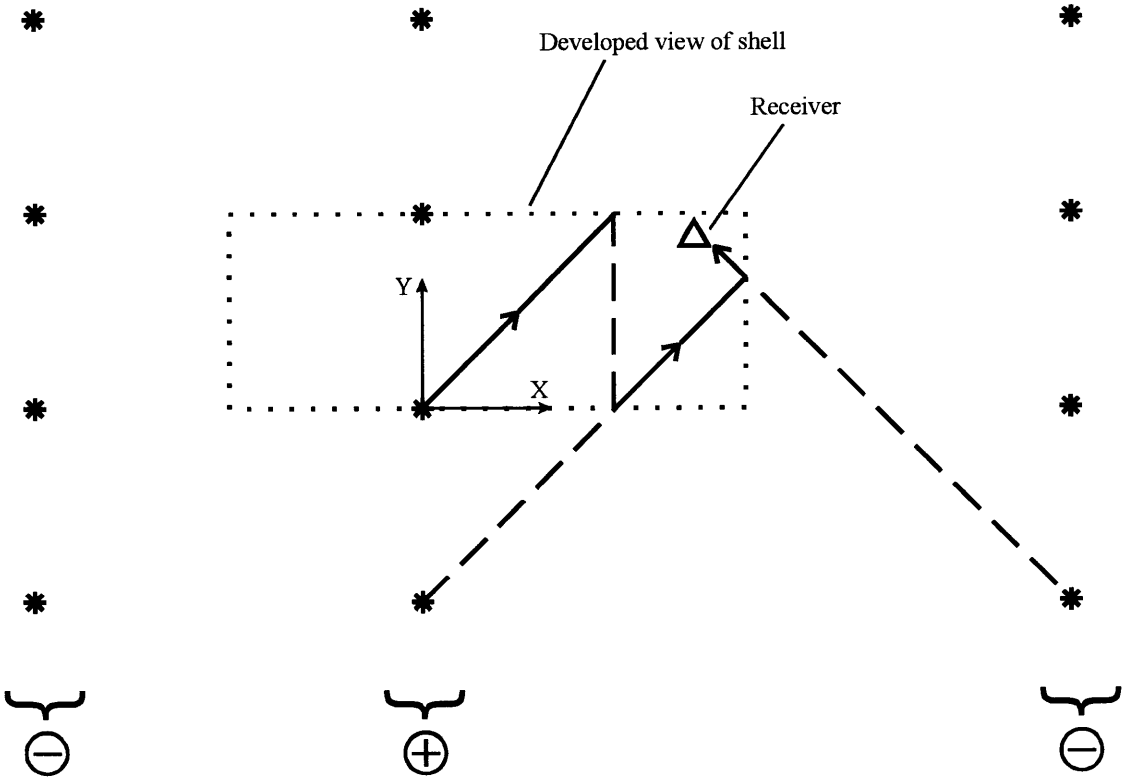

of an infinitely thick plate [29][28] and I follow his solution nearly verbatim. The equivalent point forcing is used in the following section to approximate the source-shell interaction. For reasons that will become clear, I find the equivalent forcing by first considering a plate without a hole and then a plate with a hole (the same hole that is drilled to embed the source in the shell).

Plate without hole

A uniform radial force F_r centered at the origin is applied at radius a_x to a flat plate as shown in Figure 6.5. The plate is infinitely extended in all directions with no holes. It is convenient to use both a cartesian coordinate system $\{x, y\}$ and a polar coordinate system $\{r, \phi\}$ as shown in the figure (This are the same coordinate systems described in Section 6.3.1, only I use lower case letters without the m-subscript). The plate has compressional speed c_p, density ρ, Poisson's ratio ν and has thickness h.

Figure 6-5: Continuous ring force distribution acting on an infinite flat plate.

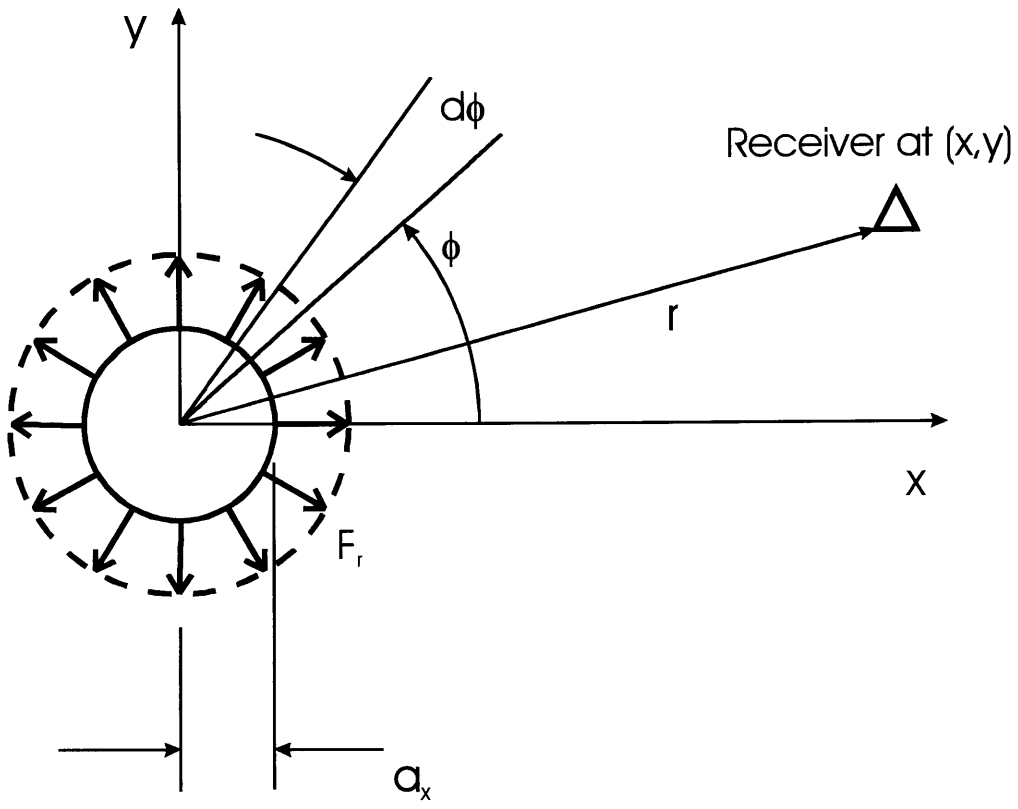

The response of the plate may be expressed in terms of its' Green's function solution. If a unidirectional point force

$$\mathbf{f}(x_s, y_s) = \{F_x, F_y\}^T \delta(x - x_s)\, \delta(y - y_s) \tag{6.8}$$

is applied at $\{x_s, y_s, 0\}$, then the displacement response is

$$\mathbf{u}(x, y) = [\mathbf{g}_x(x - x_s, y - y_s), \mathbf{g}_y(x - x_s, y - y_s)]\, \{F_x, F_y\}^T \tag{6.9}$$

at $\{x, y, 0\}$, where $\mathbf{g}_x$ and $\mathbf{g}_y$ are the column vectors of the $2x2$ Green's function matrix. To model the distributed ring force, Kausel considers a differential element of the ring force,

$$d\mathbf{f}(x_s, y_s) = F_r \frac{d\phi}{2\pi} \{\cos\phi, \sin\phi\}^T \delta(x - x_s)\, \delta(y - y_s),$$

as a unidirectional force, which produces the differential response

$$d\mathbf{u}(x,y) = \left[\mathbf{g}_x(x-x_s, y-y_s), \mathbf{g}_y(x-x_s, y-y_s)\right] F_r \frac{d\phi}{2\pi} \{\cos\phi, \sin\phi\}^T.$$

The Taylor series expansion in x and y of this response is

$$d\mathbf{u}(x,y) = F_r \frac{d\phi}{2\pi} \left\{ \begin{array}{c} \mathbf{g}_x(x,y)\cos\phi - \mathbf{g}_{x,x}(x,y)\, a_x \cos^2(\phi) - \mathbf{g}_{x,y}(x,y)\, a_x \cos\phi \sin\phi \\ +\mathbf{g}_y(x,y)\sin\phi - \mathbf{g}_{y,x}(x,y)\, a_x \cos\phi \sin\phi - \mathbf{g}_{y,y}(x,y)\, a_x \sin^2(\phi) + O\left(a_x^2\right) \end{array} \right\}.$$

For small radius a_x, the response is well approximated by the leading order terms. The total response to the ring force, found by integrating over the 2π radian angular extent of the ring, is

$$\mathbf{u}(x,y) = -\frac{a_x F_r}{2} \left\{\mathbf{g}_{x,x}(x,y) + \mathbf{g}_{y,y}(x,y)\right\}, \tag{6.10}$$

which (after considering the relationship between Eq.(6.9) and Eq.(6.8)) is due to the force distribution

$$\mathbf{f}(x,y) = -\frac{a_x F_r}{2} \left\{\delta_{,x}(x)\,\delta(y), \delta(x)\,\delta_{,y}(y)\right\}^T. \tag{6.11}$$

Eq.(6.11) represents an orthogonally oriented pair of force-dipoles of equal dipole strength.

To express Eq.(6.11) in terms of point forces, I consider the function

$$f(x) = \delta(x - a_x) - \delta(x + a_x), \tag{6.12}$$

which represents two opposing concentrated forces with unit magnitude separated by distance $2a_x$. I expand the delta functions in Eq.(6.12) in a Taylor series about x as

$$\delta(x \pm a_x) = \delta(x) \pm \delta_{,x}(x)\, a_x + O\left(a_x^2\right)$$

and then substitute them back into Eq.(6.12) to approximate

$$f(x) = \delta_{,x}(x)\, 2a_x + O\left(a_x^2\right).$$

Using this result, I recast Eq.(6.11) as

$$\mathbf{f}(x,y) = \frac{F_r}{4} \left\{\delta(y)\left[\delta(x-a_x) - \delta(x+a_x)\right], \delta(x)\left[\delta(y-a_x) - \delta(y+a_x)\right]\right\}^T. \tag{6.13}$$

The distributed ring force is therefore replaced by four point forces applied to the plate.

Plate with hole

In this section, I calculate the correction factor to account for the hole in the plate. For an infinite plate without a hole, the displacment response to a uniform ring force (as described in the previous section) concentrated at $r = a_x$ is inversely proportional to the sum of the stiffness of a circular plate of radius a_x and the stiffness of an infinite plate with a hole of radius a_x. The displacment response for a plate with a hole is inversely proportional to the stiffness of an infinite plate with a hole of radius a_x. Therefore, if K_p is the stiffness of an infinite plate with a hole and K_p' is the stiffness of the circular plate, then the correction factor between the solution for the plate without the hole and a plate with the hole is equal to

$$\gamma_p = \frac{K_p + K_p'}{K_p}. \tag{6.14}$$

I have derived both K_p and K_p' in Appendix C. When a_x is small compared to a wavelength, their ratio is given by

$$\gamma_p = \frac{2}{(1-\nu)}, \tag{6.15}$$

which is frequency independent. If I express γ_p in terms of the plate and shear speeds as

$$\gamma_p = \left(\frac{c_p}{c_s}\right)^2,$$

then γ_p is consistent with Kausel's correction factor for a two-dimensional volume source in an infinite medium given by

$$\gamma_d = \left(\frac{c_d}{c_s}\right)^2,$$

where c_d is the dilational wave speed.

By multiplying Eq.(6.10) by the correction factor in Eq.(6.15), the corrected response of the plate is

$$\mathbf{u}(x,y) = -\frac{a_x F_r}{(1-\nu)} \left[\mathbf{g}_{x,x}(x,y) + \mathbf{g}_{y,y}(x,y)\right]. \tag{6.16}$$

Also, by multiplying Eq.(6.13) by the correction factor, the equivalent ring forcing is

$$\mathbf{f}(x,y) = F_o \left\{\delta(y)\left[\delta(x-a_x) - \delta(x+a_x)\right],\ \delta(x)\left[\delta(y-a_x) - \delta(y+a_x)\right]\right\}^T. \tag{6.17}$$

where the magnitude of the point forces are

$$F_o = \frac{F_r}{2(1-\nu)}.$$

Lin selected F_o based on the projection of the pressure on half of the source-shell contact area along either the x or ϕ coordinate direction, that is,

$$F_o = \frac{F_r}{2\pi a_x h} \int_{\phi=0}^{\pi} \cos(\phi)\, d\phi = \frac{F_r}{\pi},$$

which is about one half the proper value.

6.4 Shell model

In this section, I use the shell WFEM model formulated in terms of axial waves as described in Chapter 2. This model is an improvement over the flat plate model in a number of ways. It includes the effects of shell curvature, it predicts out-of-plane radial displacements, it includes all the significant wave types supported by the shell, and provides an accurate model of wave coupling and reflection off the free-ends.

The issue not addressed in Chapter 2 is how to model the source-shell interaction. The interaction is greatly simplfied by making the following assumptions:

- The source is compact and there is no mutual interaction between sources.
- The source dimensions are small compared to the shell radius.
- The shell excitation is only through the hoop mode of the source.
- The forces exerted by the source on the shell are the equivalent set of point forces as calculated in Section 6.3.4.

I'll discuss discuss the validity of the first three assumptions at the end of this chapter.

The WFEM model used in this section is that described in Chapter 2. There are two reason why I need to make the last assumption. The first is that the shell model is formulated such that the input is one or more point forces (or sums of ring forces). Another problem is that the stiffness of the shell to an applied point force goes to zero, which makes it impossible to determine how the source and shell interact.

The equivalent point forcing for a plate with a hole is derived in Section 6.3.4. The extension to the shell model is obvious. The appropriate forcing on the shell (when a hole is drilled in the shell to embed the source) is

$$\mathbf{f}(x,\theta) = \{f_x, f_\theta, f_r, m_x, m_\theta\} = \frac{F_r}{2(1-\nu)} \{\delta(x-a_x) - \delta(x+a_x), \delta(\theta - a_x/a) - \delta(\theta + a_x/a), 0, 0, 0\},$$

Figure 6-6: Schematic of 4xN WFEM shell model with embedded ring source.

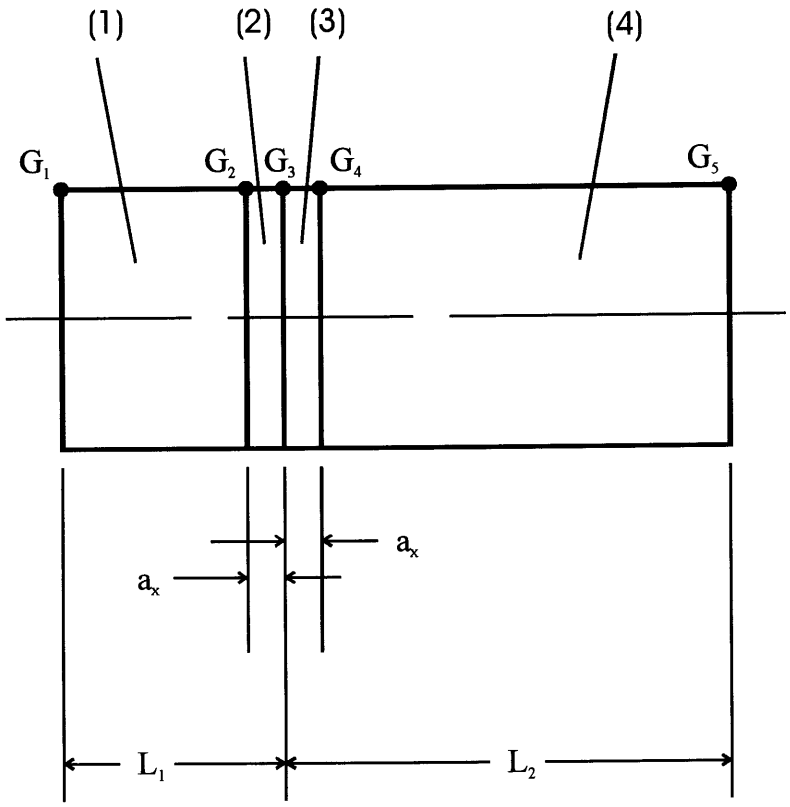

where the magnitude of the force is

$$F_r = K_p \left(\frac{U_R(a_x)}{V_o} \right)$$

given by the product of Eq.(C.12) and Eq.(6.3).

To find the response of the shell, I first decompose $\mathbf{f}(x, \theta)$ by its' n'th mode components using the spatial transform defined in Chapter 2. I then assemble a four element model, as shown in Figure 6.6, to analyze the shell response to each force component up to mode $n = 30$. The elements are welded together at nodes G_2 through G_4, while the boundary conditions at G_1 and G_5 are force and moment free. The shell and source material properties are those given in Table 2.

6.5 Comparison with experimental data

In this section, I compare the plate and shell models with the data collected by Lin on the 16 inch PVC shell.

6.5.1 Comparison of data with the plate model

To determine what size virtual source grid is required to accurately model an individual source, I compared the results using two grid sizes. The first grid has 7 rows and 5 columns, while the second grid had 13 rows and 9 columns or double the number of rows and columns not located at either $x = 0$ or $\theta = 0$. I compared the predicted axial response of the shell excited by a 12 element, in-phase, source array from $50Hz$ to $20kHz$. The differences in the results due to grid size at the receiver closest to the source at $x = .008m$ and at the receiver furthest away from the source at $x = 3.5m$ are negligible. Very slight differences at low frequency were just beginning to appear for the $x = 3.5m$ receiver. This is expected because the low frequency waves suffer the least attenuation assuming constant loss factor.

The plate model was initially run using the material and geometric properties of the source and shell as given by Lin. Because the exact material properties of PVC are not known, I tune the compressional sound speed c_p, the loss factor η, and the piezoelectric constant d_{31} to get the best agreement between the model and data for the axial velocity at $x = 3.5m$. The final values are those given in Table I.

The comparison between the measured axial velocity magnitude per unit input voltage in decibels at $x = .008m$ and the plate model prediction is plotted in Figure 6.7. This receiver is about two source radii from the center of the source. I'll show presently, as one might expect, that this is the near-field response dominated by the direct wave of the source. The agreement between the model and the data in the near-field is excellent at all frequencies. The same input parameters, tuned as described above, are used to make both of these predictions. The good agreement at both locations indicates that the tuning of the material parameters as described above is justified.

The comparison between the magnitude of the axial velocity at $x = 3.5m$ is plotted in Figure 6.8. I'll also show presently that this receiver is in the far-field of the source. The agreement between the data and the plate model is excellent above the ring frequency but suffers increasing degradation near the ring frequency. This is expected because the plate model is only valid at high frequency.

I may exercise the plate model to help explain the interference pattern of the data. I do this by comparing the receiver response at the $x = 3.5m$ using three different virtual source grid sizes: $7x1$, $7x2$, and $7x3$. The $7x1$ grid gives the direct wave response. The $7x2$ grid, where the second column is the virtual source array image off the right end of the shell, gives the sum of the direct wave and the first reflected wave off the right end. The $7x3$ grid, where the third column is the virtual source

Figure 6-7: Comparison between the measured axial velocity magnitude per unit input voltage in decibels at $x = .008m$ and the plate model prediction.

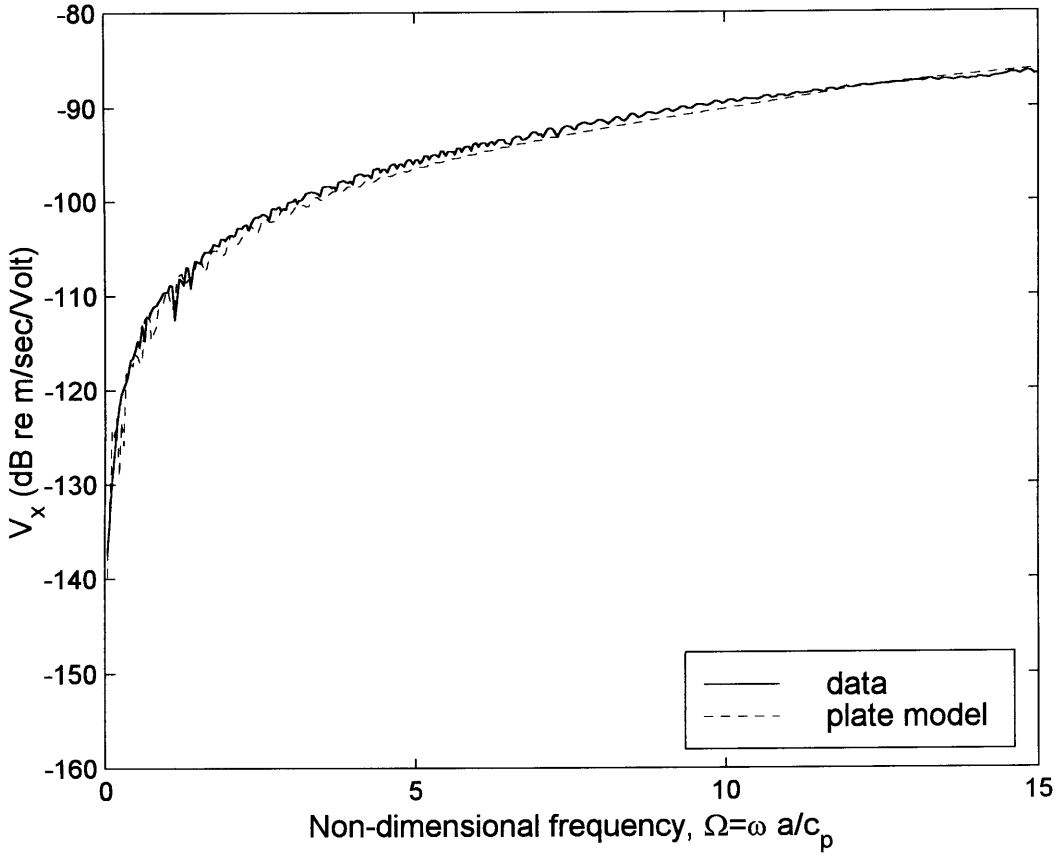

array imaged off the left end of the shell, gives the sum of the direct wave, the reflected wave off the right end, and the reflected wave off the left end. The results are shown in Figure 6.9. The figure shows that it is not enough to include just the direct field contribution, which, by itself, does not have much character but dominates the reciever response. By including only the direct wave and the first reflection off the right end, an interference pattern is developed that is superimposed on the direct field contribution. By including the left end reflected wave, a second interference pattern is developed that is due to the interference of the right and left end reflected waves. This second interference pattern is superimposed on the first interference pattern. The peaks and valleys of the second interference pattern have a more rapid variation due to a longer associated length scale. The length scale associated with the first pattern is $2L_2$ (the difference between the axial locations of the sources at the origin and right end virtual sources), while the length associated with the second interference pattern is $2(L_1 + L_2)$. The

Figure 6-8: Comparison between the measured axial velocity magnitude per unit input voltage in decibels at $x = 3.5m$ and the plate model prediction.

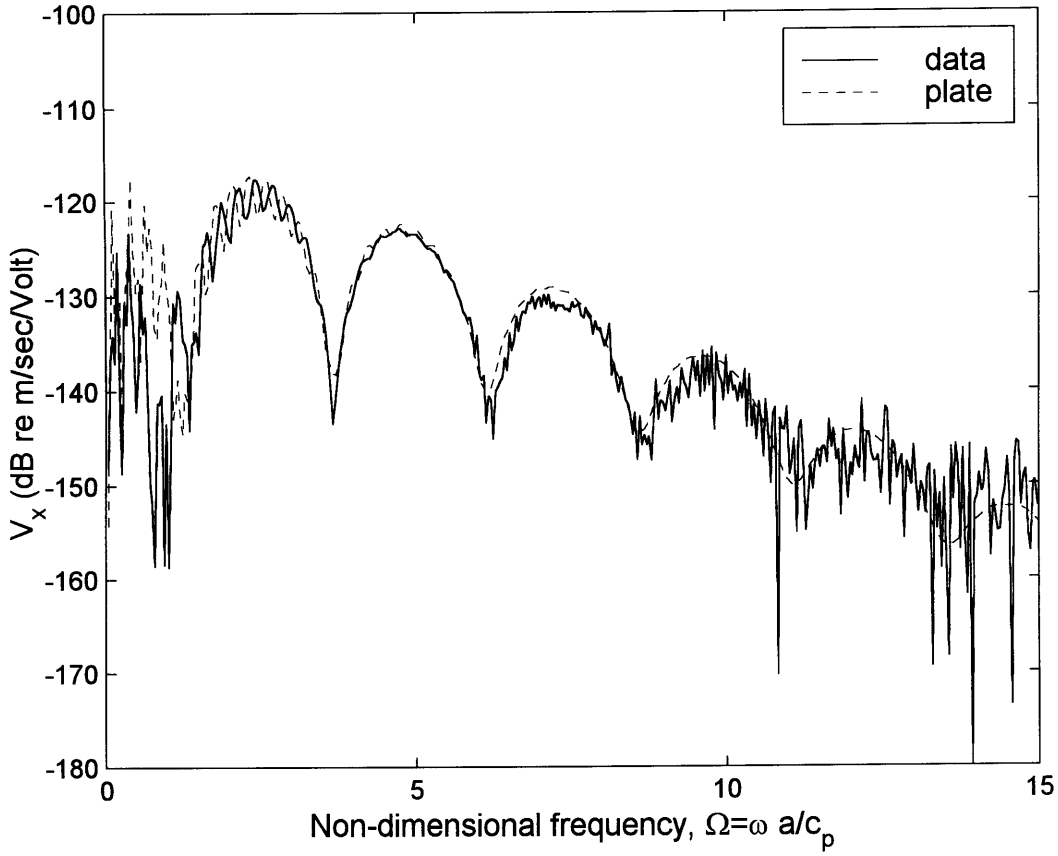

variation of the second interference pattern is smaller than the first because the interfering waves suffer greater attenuation travelling over the longer associated length. The effect of the left end reflected waves diminishes with increasing frequency, also due to damping.

I may also use the flat plate model to indicate the importance of mutual interaction between neighboring sources. In Figure 6.10, I plot the ratio of the plate displacement at $R_2 = R = 2\pi a/12$ compared to the displacement at the $R = R_1 = a_x$ versus frequency. This ratio is the displacement imposed by each source on its' nearest neighbor compared to its' own displacement. The plot shows that at the highest frequency considered this ratio is $-20dB$ and indicates that the assumption of no source interaction is reasonable.

Figure 6-9: Plate model predictions of axial velocity magnitude per unit input voltage in decibels at $x = 3.5m$ for three different virtual grid sizes.

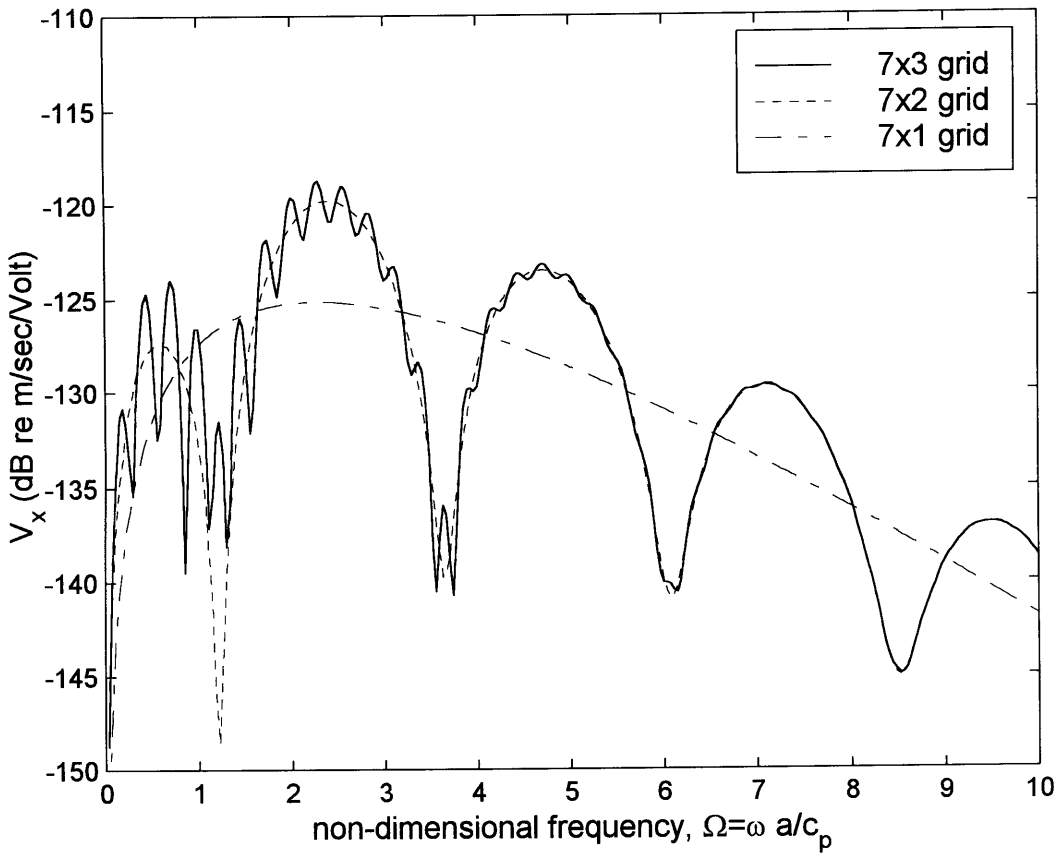

6.5.2 Comparison of data and shell model

The input material parameters for the shell model are exactly the same as the plate model. The model is run as described earlier in Section tbd.

The comparison of the axial velocity measurements and the shell model predictions in the near-field and far-field are plotted in Figure 6.11 and Figure 6.12, respectively. These figures may also be compared with the plate model predictions in Figure 6.7 and Figure 6.8. The agreement between the shell model and data in the near-field is excellent at all frequencies. The agreement in the far-field above the ring frequency is excellent but suffers some degradation near the ring frequency, although not as much as the plate model. To make a better comparison with data, I replot Figure 6.12 in Figure 6.13 in a limited frequency range about the ring frequency. The figure shows that the shell model does captures much of

Figure 6-10: Relative displacement due to a single source at $R = a_x$ and $R = 2\pi a/12$ as predicted by plate model.

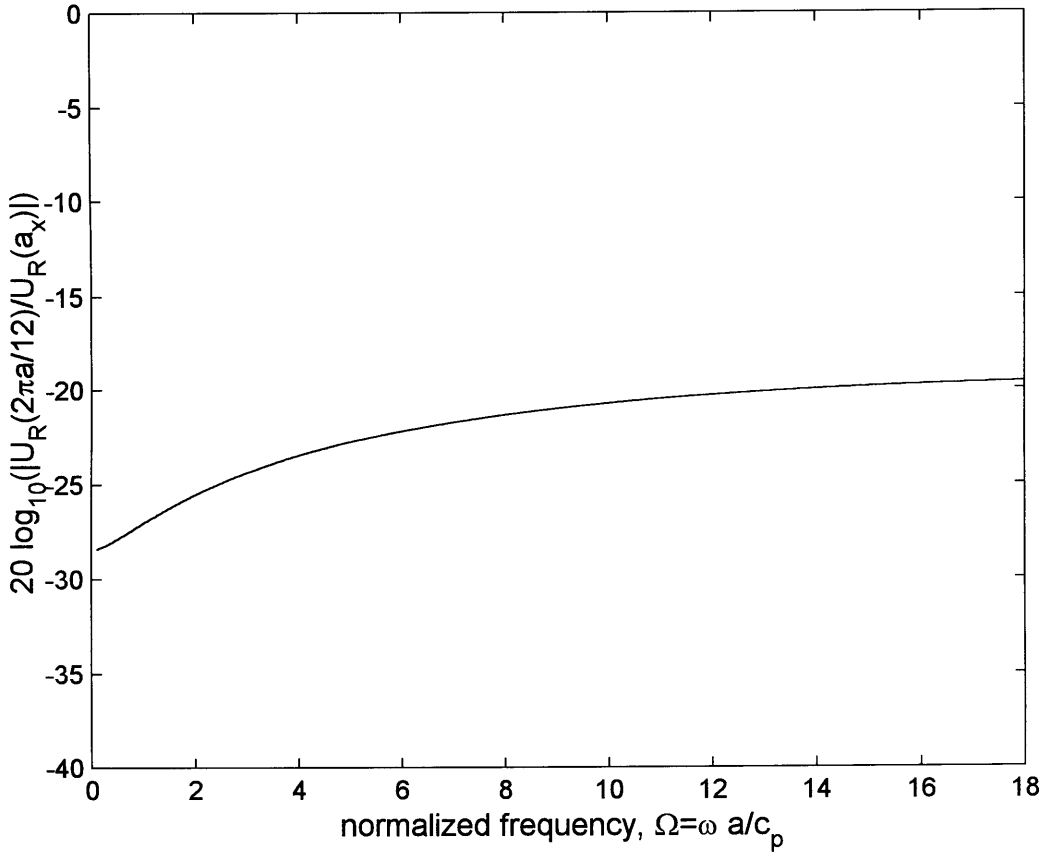

the character of the data near the ring frequency.

I can think of two possible reasons for the error near the ring frequency. The first is the keel attached on the left end of the shell. The keel is an asymmetric discontinuity that couples all circumferential modes of the shell. The shell and plate model do not include the effects of the keel. As discussed above, the ends of the shell are not isolated from each other especially at the low frequencies. The second reason is that the shell is anisotropic as discussed in Chapter 2, yet the equivalent forcing applied to the shell is based on the analysis of a plate, which is isotropic. The anisotropy of the shell is due to shell curvature, which is most pronounced at the lower frequencies. The source-shell interaction model could be improved by adjusting the relative strengths of the dipole pairs to compensate for the anisotropy.

A comparison of the radial velocity measurement in the far-field and the shell model predictions is shown in Figure 6.14. One of the benefits of the shell model is that the radial velocity may be predicted.

Figure 6-11: Comparison between the measured axial velocity magnitude per unit input voltage in decibels at $x = .008m$ and the shell model prediction.

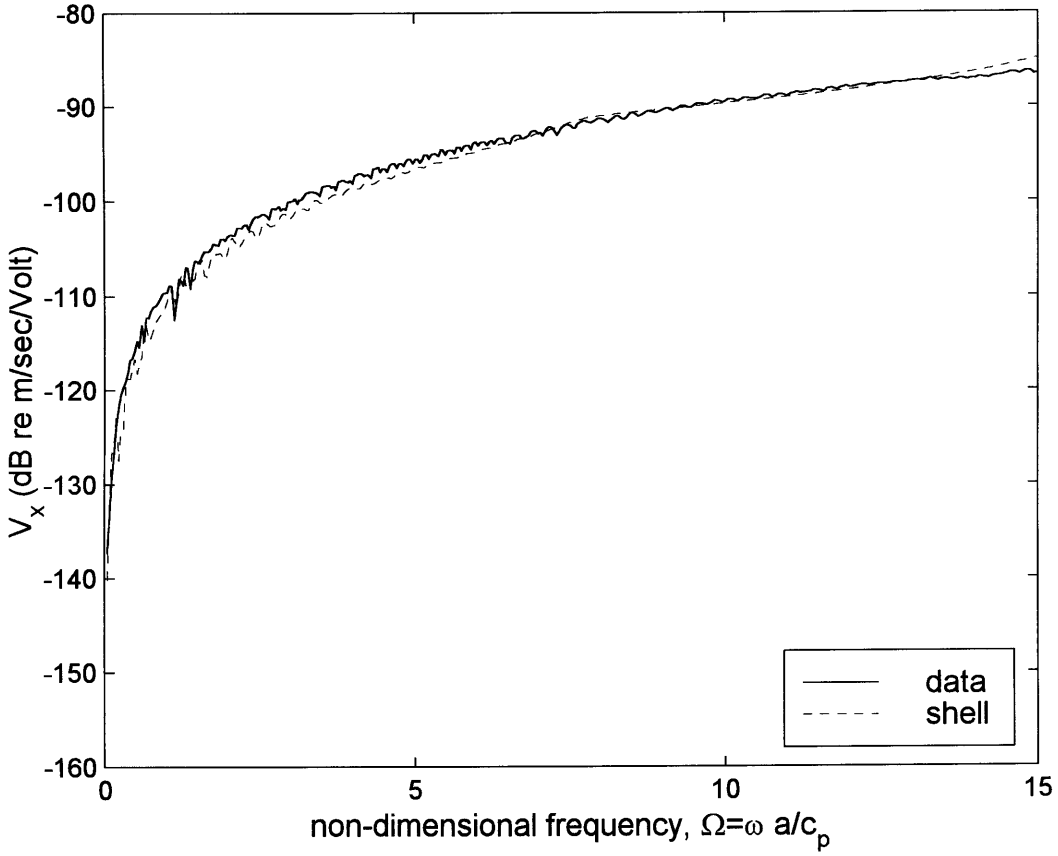

There is reasonable agreement in terms of the direct field and the two interference patterns below $\Omega = 6$. The misalignment of the nulls in the interference pattern of the direct field and the right end indicates that the shell may be thicker than that used as input to the model. To check this, I measured the shell thickness at one end. It did measure .200 inches rather than the vendor catalogue value of 3/16 inches(.186 inches) but this may be due to a build up of material when the shell is cut to length. The flexural wave speed is, of course, much more sensitive to changes in thickness than the shear or the compressional wave speed. I could, therefore, change the thickness without affecting the good agreement between model and data for the axial velocity measurements. Above $\Omega = 6$, the model and the data show very little agreement in terms of either the direct field response or the interference patterns. The keel is of course a possible source of error. Another source of error may be that the piezoelectric sources are not perfectly aligned in the plane of the shell. Therefore, when the source expands, there is an

Figure 6-12: Comparison between the measured axial velocity magnitude per unit input voltage in decibels at $x = 3.5m$ and the shell model prediction.

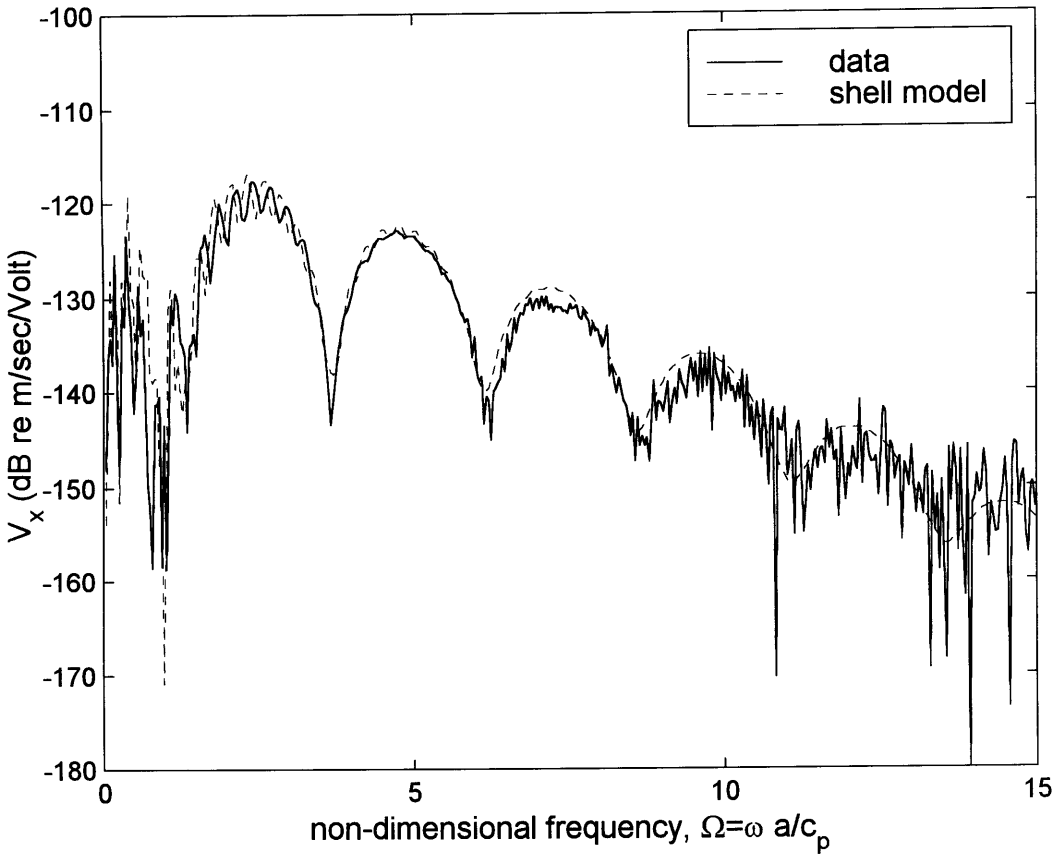

out-of-plane component that excites the low-impedance flexural waves.

6.6 Summary

I assumed that the source-shell interation is only through the breathing mode of the source. As shown in Chapter 2, however, the shell is anisotropic with respect to in-plane forces in the axial and circumferential directions. The degradation of the model prediction below the shell ring frequency indicates that this anisotropy is important. Another effect of anisotropy is that the shell begins to interact with the $n = 1$ source mode because it is primarily a low impedence flexural model. The use of the circular source needlessly complicates the shell-source interaction. The circular cross-section source was selected only because it is easy to install (I know because I selected these sources and conducted the initial tests on

Figure 6-13: Comparison between the measured axial velocity magnitude per unit input voltage in decibels at $x = 3.5m$ and the plate model prediction.

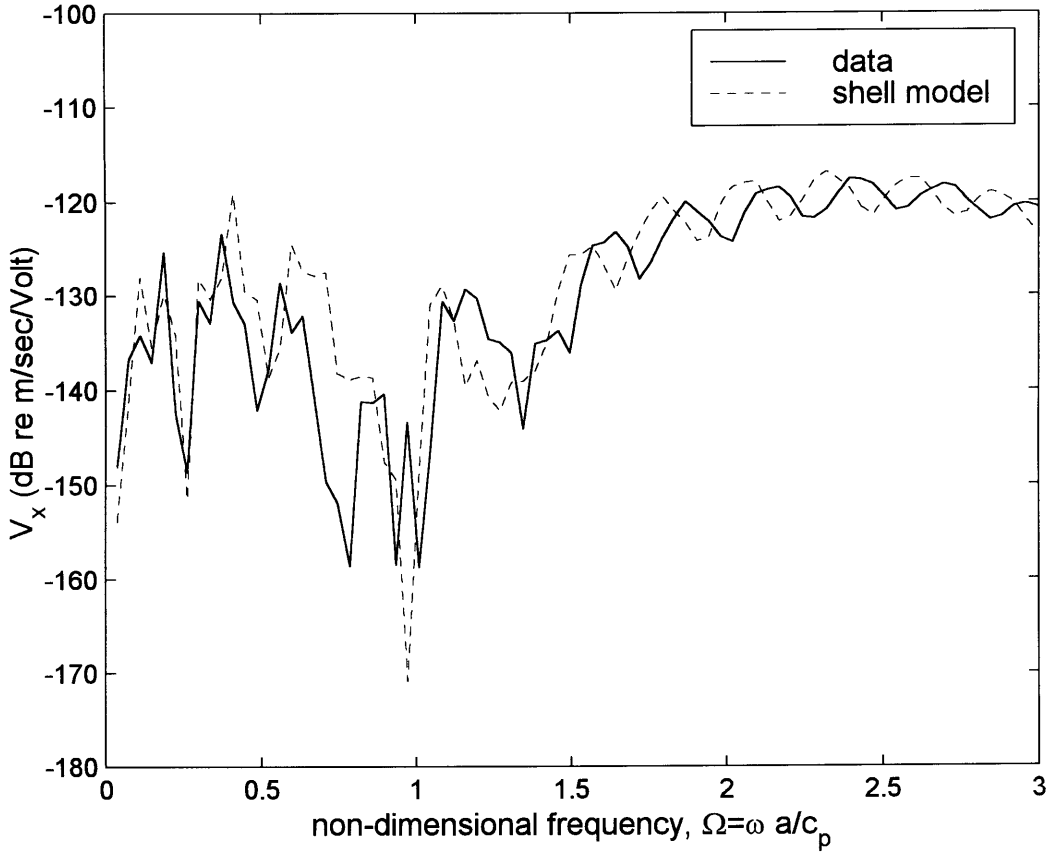

them on them in steel shells.). For future testing, I recommend a source design that acts more like a single force-dipole rather than a pair of orthogonally oriented force-dipoles. The source would also be embedded into the shell wall but would be long and slender rather than circular. It's orientation could be either axial or circumferential. This type of source would be much easier to model because it skirts the issue of shell anisotropy and I believe the shell model prediction below the ring frequency would be much improved.

Figure 6-14: Comparison between the measured radial velocity magnitude per unit input voltage in decibels at $x = 3.5m$ and the plate model prediction.

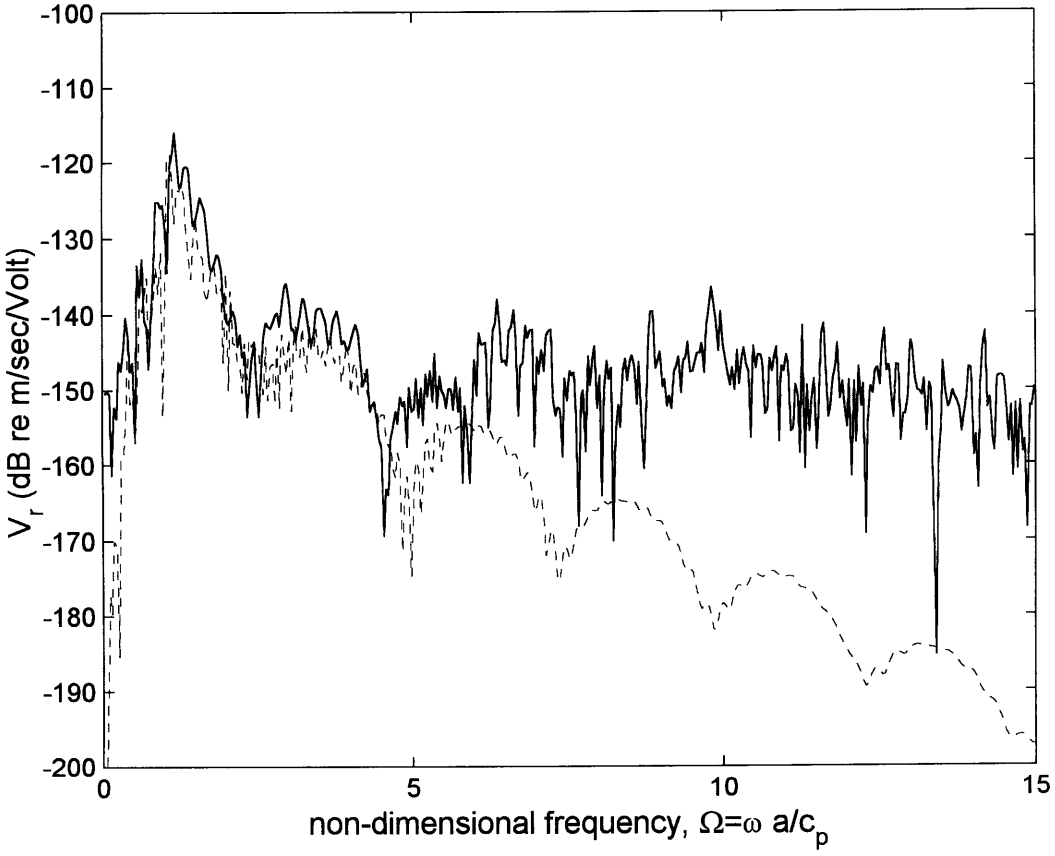

Chapter 7

Summary

7.1 Original contributions

Specifically, my contributions are:

- Formulated WFEM element for a thick, finite length, cylindrical shell in terms of axial wave amplitudes. The formulation is expressed in terms of a stiffness matrix, which relates ring forces applied to the ends of the shell element to their respective end displacements. The forces and displacements have an implied circumferential dependence of $e^{+in\theta}$ and a time dependence of $e^{-\imath\omega t}$.

- Formulated WFEM element for a thick, infinite length, cylindrical shell in terms of circumferential wave amplitudes. In contrast to the axial wave formulation, the circumferential length of the shell is finite. The formulation is expressed in terms of a stiffness matrix, which relates axial line forces applied to the ends of the shell element to their respective end displacements. The forces and displacements have an implied axial dependence of $e^{+ik_x x}$ and a time dependence of $e^{-\imath\omega t}$. This formulation is useful when analyzing shells with one or more discontinuities in the circumferential direction.

- Both shell models include wave sorting technique, which allows the motions of the shell to be first decomposed by wave direction and then also by wave type. The shell theory used includes five different wave types: compressional, shear, flexural, evanescent, and through thickness shear. There is no error associated with the wave decomposition from either wave amplitude decay caused by heavy viscoelastic dissipation or spatial sampling. Because the sorting includes the decaying waves (at most frequencies the evanescent and through-thickness shear are rapidly decaying waves),

the technique works in the near-field as well as the far-field.

- I demonstrated the use of the 2D shell model by comparing the predicted response of a cylindrical shell due to an array of piezoelectric volume sources embedded in the shell wall with available experimental data. I show that the agreement between the experimental data and the model is very good down to the ring frequency of the shell augmenting Lin's own analysis. I provided a detailed analysis of the source-shell interaction.

- Formulated full 3-D elastodynamic cylindrical shell model in terms WFEM stiffness matrix solution. The formulation serves as a very powerful analytic tool to study either very thick shells or shells with multiple layers. A compact Matlab code is included for public use.

- Formulated a beam/rigid link/beam element for both pinned and welded boundary conditions. I use the element to study how wave propagation past a rigid body is affected by flexural rigidity. The reflection and transmission are shown to be very sensitive to boundary conditions. I also show how the optimally designed fixed-end absorber performance degrads with increased flexural rigidity but may be re-optimized if the flexural rigidity is known.

7.2 Future work

- I have not fully exploited the use of the 2D shell models. The hybrid WFEM-FEM model may be used to analyze the wave scattering due to analyze wave scattering due to a conical end-cap or a neckdown section, where conventional FEM are applied to the end-cap and neckdown section.

- The computational cost of running the wavenumber integration model in Appendix H is high but not prohibitive. For a shell with a single bulkhead and a single deck attachment, the run time is on the order of 4 weeks for a few hundred frequencies on a typical PC using FORTRAN. Because each frequency is independent of all other frequencies, the program could be run on separate computers.

Bibliography

[1] K. J. Bathe. *Finite Element Procedures in Engineering Analysis.* Prentice-Hall, New Jersey, 1988.

[2] I. Dyer. Moment impedance of plates. J. Acoust. Soc. Am., Vol.32, 1290-1297, 1960.

[3] A. Leissa. *Vibration of Shells.* Acoustical Society of America, 1993.

[4] G. V. Borgiotti and E. M. Rosen. The state vector approach to the wave and power flow analysis of the forced vibrations of a cylindrical shell, Part I: Infinite cylinders in vacuum. J.Acoust. Soc. Am., 91 (2), February 1992.

[5] F. Hildebrand. *Advanced Calculus for Applications*, 2nd Ed. Prentice-Hall, New Jersey, 1976.

[6] M. Junger and D. Feit. *Sound, Structures, and their Interaction,* 2nd edition. MIT Press, Cambridge, Massachusetts, 1986.

[7] A. Harari. Wave propagation in cylindrical shells with finite regions of structural discontinuity. J. Acoust. Soc. Am., Vol. 62, No. 5, 1977.

[8] P. Morse and K. Ingard. *Theoretical Acoustics.* Princeton University Press, 1968.

[9] R. Woollett. *Sonar Transducer Fundamentals.* Naval Underwater Systems Center, Newport Rhode Island.

[10] D. Ricks. Elastodynamic Modeling of Fluid-Loaded Cylindrical Shells with Multiple Layers and Internal Attachments. PhD thesis, Massachusetts Institute of Technology, 1994.

[11] I. Mirsky and G. Herrmann. Nonaxially Symmetric Motions of Cylindrical Shells. J. Acoust. Soc. Am., Vol. 29, Number 10, 1957.

[12] H. He. Statistical model for the prediction of elastic wave scattering from finite complicated shells. Ph.D. thesis, Massachusetts Institute of Technology, February 1997.

[13] M. Rumerman. Contribution of membrane wave reradiation to scattering from finite cylindrical steel shells in water. J. Acoust. Soc. Am., **93** (1), January 1993.

[14] A. Klauson, G. Maze, and J. Metsaveer. Acoustic scattering by a submerged cylindrical shell stiffened by an internal lengthwise rib. J. Acoust. Soc. Am., **96** (3), September 1994.

[15] Y. P. Guo. Sound scattering by bulkheads in cylindrical shells. J. Acoust. Soc. Am., **95** (5), May 1994.

[16] Y. P. Guo. Normal mode propagation on conical shells. J. Acoust. Soc. Am., **96** (1), July 1994.

[17] Y. P. Guo. Fluid-loading effects on waves on conical shells. J. Acoust. Soc. Am., **97** (2), February 1995.

[18] Y. P. Guo. Acoustic scattering from cylindrical shells with deck-type internal plate at oblique incidence. J. Acoust. Soc. Am., **99** (5), May 1996.

[19] Y. P. Guo. Acoustic scattering from an internally loaded cylindrical shell. J. Acoust. Soc. Am., **96** (3), September 1994.

[20] Y. P. Guo. Diffraction of flexural waves at structural joints. J. Acoust. Soc. Am., **95** (3), March 1994.

[21] F. Jensen, W. Kuperman, M. Porter, and H. Schmidt. *Computational Ocean Acoustics.* A.I.P. Press, 1994.

[22] J. D. Achenbach. *Wave Propagation in Elastic Solids.* North-Holland and Elseview, 1975.

[23] A. Pathak and P. Stepanishen. Acoustic harmonic radiation from fluid-loaded infinite cylindrical elastic shells using elasticity theory. J. Acoust. Soc. Am., **96** (1), July 1994.

[24] Ching-Yu Lin. Pressure estimation of piezoelectric rings embedded orthogonally in cylindrical shells. S.M. thesis, Massachusetts Institute of Technology, January 1998.

[25] C. Corrado. Mid-frequency acoustic scattering from finite internally-loaded cylindrical shells and the influence of helical membrane waves. Ph.D. thesis, Massachusetts Institute of Technology, January 1993.

[26] M. Conti. Mid-frequency acoustic scattering from finite internally-loaded cylindrical shells near axial incidence. Ph.D. thesis, Massachusetts Institute of Technology, January 1993.

[27] M. Klausbruckner. Theoretical and experimental investigation of the acoustic behavior of viscoelastically damped cylindrical shells. S.M. thesis, Massachusetts Institute of Technology, June 1994.

[28] E. Kausel. Dynamic point sources in laminated media via the thin-layer method. Submitted to Bull. Seismo. Soc. Am. 1997

[29] E. Kausel. Blast loads versus point loads: the missing factor. J. Engr. Mech., ASCE, 1997

[30] J. Cushieri and D. Feit. A hybrid solution for the response Green's function of a fluid-loaded cylindrical shell J. Acoust. Soc. Am., **96** (5), November 1994.

[31] J. Cushieri and D. Feit. Acoustic scattering from a fluid-loaded cylindrical shell with discontinuities: double plate bulkhead. J. Acoust. Soc. Am., **98** (1), July 1995.

[32] L. Felson and Y. P. Guo. Hybrid ray-mode parametrization of acoustic scattering from submerged thin elastic shells with interior loading. J. Acoust. Soc. Am., **94** (2), August 1993.

[33] E. Kausel and J. Roesset. Stiffness matrices for layered soils. Bull. Seismo. Soc. Am., Vol. 71, No. 6, pp.1743-1761, December 1981

[34] H. Schmidt and F. Jensen. A full wave solution for propagation in multilayered viscoelastic media with application to Gaussian beam reflection at fluid-solid interfaces. J. Acoust. Soc. Am., **77**:813-825, March 1985.

[35] J. Tassoulas. Elements for the numerical analysis of wave motion in layered media. Research Report R81-2 National Science Foundation (1982)

[36] E. Kausel and R. Peek. Dynamic loads in the interior of a layered stratum: an explicit solution. Bull. Seismo. Soc. Am., Vol. 72, No. 5, pp.1459-1481, October 1982

[37] MSC/NASTRAN: *Static and normal mode analysis.* Wallace Press, Inc. Milford, N.H. c1979

[38] L. Li and J. K. Vandiver. Wave propagation in strings with rigid bodies. Journal of Sound and Vibration, Vol. 117, October 1995.

[39] J. K. Vandiver and L. Li. Vibration suppression of tension dominated slender structures by dynamic absorbers. Submitted to the Journal of Sound and Vibration

[40] L. Li. Dynamics of strings with rigid lumps. Ph.D. thesis, M.I.T, 1993.

[41] M. Reis. Wave propagation in elastic beams and rods. Ph.D. thesis, M.I.T, 1978.

[42] Y. P. Guo. Flexural wave transmission through angled structural joints. J. Acoust. Soc. Am. 97 (1), January 1995.

[43] D. G. Fertis. *Mechanical and Structural Vibrations.* J. Wiley & Sons, Inc., New York, c1995.

[44] J. Fricke and M. Hayner. Direct global stiffness matrix method for 3-D truss dynamics. ASME 15th Biennial Conference on Mechanical Vibration and Noise. Sept. 17-21, 1995.

[45] R. S. Langley. Elastic wave transmission coefficients and coupling loss factors for structural junctions between curved panels. Journal of Sound and Vibration 169(3), p.297-317, 1994.

[46] C. R. Fuller. The effects of wall discontinuities on the propagation of flexural waves in cylindrical shells. Journal of Sound and Vibration 75(2), p.207-228, 1980.

[47] Y. K. Tso and C. H. Hansen. Wave propagation through cylinder/plate junctions. Journal of Sound and Vibration 186(3), p.447-461, (1995).

[48] W. Press, S. Teukolsky, W. Vetterling, and B. Flannery. *Numerical Recipes in* FORTRAN. Cambridge University Press c1986

Appendix A

Stiffness matrix of a thick circular plate

In this appendix, I solve for the in-plane and out-of-plane motions of a thick circular plate. The in-plane motions are based on first order membrane wave theory. The out-of-plane motions are based on Mindlin's thick plate theory. The motions are formulated in terms of a $5x5$ stiffness matrix. I also discuss one method of attaching a circular plate to a cylindrical shell.

The plate is referred to the cylindrical coordinate system $\{r, \varphi, z\}$. The plate has radius a, thickness h, and is made from a linear elastic solid with Young's modulus E, density ρ, and Poisson's ratio ν. The motions are analyzed in terms of a stiffness matrix, which relates applied ring forces at the outer radius to the displacements at the outer radius. Both the applied force and the resulting displacements have an assumed circumferential dependence of $e^{+in\theta}$ and a time dependence of $e^{-\imath\omega t}$ (both of which are hereafter implied).

The relationship I derive is

$$\mathbf{K}(n)\,\mathbf{U}(n) = \mathbf{F}(n),$$

where $\mathbf{K}$ is the stiffness matrix,

$$\mathbf{F} = \{F_r(a), F_\varphi(a), F_z(a), M_r(a), M_\varphi(a)\}^T,$$

is a vector containing the applied forces and moments, and

$$\mathbf{U} = \{U_r(a), U_\varphi(a), U_z(a), \Psi_r(a), \Psi_\varphi(a)\}^T.$$

is a vector containing the resulting displacements and rotations. I use F and M for forces and moments, U and Ψ for displacements and rotations. Forces and displacements are in the same direction as their subscripts. Moments and rotations are *about* the same axis as their subscripts. The moment and rotation about the radial direction are in negative, while the moment and rotation about the circumferential direction are positive.

The method of analysis is the wave-based FEM method that is used throughout this thesis. It is therefore exact to within the assumptions of the governing differential equation. The stiffness matrix for a circular plate is also derived by Ricks [10]. However, the formulation for the stiffness matrix as presented here may also be used to derive the stiffness matrix for an annular plate using the same procedures as outlined in Chapter 4. The circular plate is used in the main text to model a bulkhead attachment.

The Mindlin plate theory assumes that the through-thickness fibers remain straight under loading but not necessarily normal to the mid-plane of the plate. I also assume that the only applied forces are those at the outer edges. If the stiffness matrix is formulated in a cylindrical coordinate system, then membrane waves are not coupled to the flexural waves in the plate even through the boundary conditions. For this reason, I formulate the stiffness matrix for the membrane waves, $\mathbf{K}_m$, and the flexural waves, $\mathbf{K}_f$, separately. The plate stiffness matrix is then simply given by

$$\mathbf{K} = \begin{bmatrix} \mathbf{K}_m & 0 \\ 0 & \mathbf{K}_f \end{bmatrix}. \tag{A.1}$$

At the end of this appendix, I discuss how to make the plate stiffness matrix compatible with the shell stiffness matrix, which is in a different coordinate system.

A.1 Membrane waves

The membrane wave motions are governed by two scalar wave equations, one governs compressional wave motion and the other shear wave motion [3]. The two equations are coupled only through the boundary conditions. The compressional waves are governed by

$$\left(\Phi_{,rr} + \frac{\Phi_{,r}}{r} + \frac{\Phi_{,\varphi\varphi}}{r^2}\right) + k_p^2\Phi = 0, \tag{A.2}$$

where $\Phi(r,\varphi)$ is the compressional wave potential and

$$k_p = \frac{\omega}{c_p} = \omega\left(\frac{E}{\rho(1-\nu^2)}\right)^{-1/2}$$

are various forms of the plate wavenumber. For the moment, I consider only the homogeneous equations. The ring forces are applied through the boundary conditions using the procedures described in Chapter 1.

Similarly, the shear waves are governed by

$$\left(\Psi_{,rr} + \frac{\Psi_{,r}}{r} + \frac{\Psi_{,\varphi\varphi}}{r^2}\right) + k_s^2 \Psi = 0, \tag{A.3}$$

where $\Psi(r, \varphi)$ is the shear wave potential (not to be confused with rotations, which have subscripts) and

$$k_s = \frac{\omega}{c_s} = k_p \left(\frac{1-\nu}{2}\right)^{-1/2} = \frac{k_p}{\sqrt{\sigma_m}}$$

are various forms of the shear wavenumber.

Eq.(A.2) and Eq.(A.3) are forms of Bessel's differential equation [6] and have Bessel function solutions, which may be written as

$$\Phi = A_1 \frac{J_n(k_p r)}{J_n(k_p a)} = A_1 F(r) \tag{A.4}$$

and

$$\Psi = A_2 \frac{J_n(k_s r)}{J_n(k_s a)} = A_2 G(r), \tag{A.5}$$

where A_1 and A_2 are unknown wave amplitudes that must be determined from the boundary conditions and J_n is the Bessel function of the first kind and order n.

In terms of the potential functions, the radial displacement is

$$U_r(r) = \Phi_{,r} + \frac{1}{r}\Psi_{,\varphi} \tag{A.6}$$

and the circumferential displacement is

$$U_\varphi(r) = \frac{1}{r}\Phi_{,\varphi} - \Psi_{,r} \tag{A.7}$$

The radial force per unit circumferential length is the radial stress times the plate thickness or

$$F_r(r) = \sigma_{rr}(r)\, h.$$

In terms of the displacements, the radial force is

$$F_r(r) = \gamma \left\{ U_{r,r} + \nu \left(\frac{1}{r} U_r + \frac{1}{r} U_{\varphi,\varphi}\right)\right\}, \tag{A.8}$$

where

$$\gamma = \rho c_p^2 h$$

The circumferential force per unit circumferential length is the shear stress times the plate thickness or

$$F_\varphi(r) = \sigma_{r\varphi}(r)\, h$$

($\sigma_{r\varphi}$ is the shear stress on the surface with surface normal r acting in the direction φ). In terms of the displacements, the circumferential force is

$$F_\varphi(r) = \gamma\sigma_m \left(\frac{1}{r}U_{r,\varphi} + U_{\varphi,r} - \frac{1}{r}U_\varphi\right). \tag{A.9}$$

The displacements given by Eq.(A.6) and Eq.(A.7) may be directly related to the unknown wave amplitudes using Eq.(A.4) and Eq.(A.5). The resulting relation is

$$\mathbf{D}_m(r) \left\{ \begin{array}{c} A_1 \\ A_2 \end{array} \right\} = \left\{ \begin{array}{c} U_r \\ U_\varphi \end{array} \right\}, \tag{A.10}$$

where

$$\mathbf{D}_m(r) = \left[\begin{array}{cc} F_{,r} & i\left(\frac{n}{r}\right) G \\ i\left(\frac{n}{r}\right) F & -G_{,r} \end{array} \right].$$

Formulas for the Bessel function derivatives may be found in Hildebrand [5].

Similarly, the forces given by Eq.(A.8) and Eq.(A.9) may be directly related to the wave amplitudes using Eq.(A.4) and Eq.(A.5). The resulting relation is

$$\mathbf{C}_m(r) \left\{ \begin{array}{c} A_1 \\ A_2 \end{array} \right\} = \left\{ \begin{array}{c} F_r \\ F_\varphi \end{array} \right\}, \tag{A.11}$$

where

$$\mathbf{C}_m(r) = \gamma \left[\begin{array}{cc} F_{,rr} + \frac{1}{r}\nu F_{,r} - \nu\left(\frac{n}{r}\right)^2 F & i2\sigma_m\left(\frac{n}{r}\right)\left(G_{,r} - \frac{1}{r}G\right) \\ i2\sigma_m\left(\frac{n}{r}\right)\left(F_{,r} - \frac{1}{r}F\right) & \sigma_m\left(-\left(\frac{n}{r}\right)^2 G - G_{,rr} + \frac{1}{r}G_{,r}\right) \end{array} \right].$$

The membrane wave stiffness matrix is then

$$\mathbf{K}_m = \mathbf{C}_m(a)\left[\mathbf{D}_m(a)\right]^{-1}, \tag{A.12}$$

where I have simply eliminated the wave amplitudes from Eq.(A.10) and Eq.(A.11) and evaluated the forces and displacements at the outer radius. This follows a similar procedure discussed in Chapter 4.

A.2 Out-of-plane waves

This section, presents the Mindlin thick plate equations as presented by Dyer [2] According to Mindlin, the dynamics of a thick plate are governed by three wave equations,

$$\left(\nabla^2 + k_1^2\right) w_1 = 0,$$

$$\left(\nabla^2 + k_2^2\right) w_2 = 0,$$

and

$$\left(\nabla^2 + k_3^2\right) T = 0,$$

expressed in terms of the three potential functions, $w_1(r,\varphi)$, $w_2(r,\varphi)$, and $T(r,\varphi)$. At high frequencies, w_1, w_2, and T characterize a surface wave, a compressional wave, and a through thickness shear wave, respectively. Their corresponding wavenumbers at infinite radius are given by

$$k_1^2,\ k_2^2 = \frac{1}{2}k_p^2\left[\left(1+\frac{1}{\kappa^2\sigma_m}\right) \pm \sqrt{\left(1-\frac{1}{\kappa^2\sigma_m}\right)^2 + \frac{4}{k_p^2 I}}\right]$$

and

$$k_3^2 = \frac{k_p^2}{\sigma_m} - \frac{\kappa^2}{I},$$

defined in terms a rotary inertia term

$$I = \frac{h^2}{12}$$

and the shear factor κ^2. The shear factor accounts for the fact that the shear stress is not really a constant through the plate thickness. By setting

$$\kappa = \frac{c_R}{c_s},$$

where c_R is the Rayleigh wave speed, then the k_1 wave speed asymptotes to the Rayleigh wave speed at high frequency. The Rayleigh wave speed may be approximated by letting

$$\kappa = \frac{\sqrt{\pi}}{12}.$$

In terms of the potential functions the radial displacement is

$$U_z = w_1 + w_2, \tag{A.13}$$

the twist rotation about the radial direction is

$$\Psi_r = \alpha_1 w_{1,r} + \alpha_2 w_{2,r} + \frac{1}{r} T_{,\varphi}, \tag{A.14}$$

and the bending rotation is

$$\Psi_\varphi = \alpha_1 \frac{1}{r} w_{1,\varphi} + \alpha_2 \frac{1}{r} w_{2,\varphi} - T_{,r}, \tag{A.15}$$

where

$$\alpha_1 = \frac{k_2^2}{\sigma_m k_3^2} - 1$$

and

$$\alpha_2 = \frac{k_1^2}{\sigma_m k_3^2} - 1.$$

Similarly, the radial force is

$$F_z = \gamma \kappa^2 \sigma_m \left[\Psi_r + U_{r,r}\right], \tag{A.16}$$

the twisting moment about the radial direction is

$$M_r = \gamma I \sigma_m \left[\frac{1}{r}\left(\Psi_{r,\varphi} - \Psi_\varphi\right) + \Psi_{\varphi,r}\right], \tag{A.17}$$

and the circumferential bending moment is

$$M_\varphi = \gamma I \left[\Psi_{r,r} + \nu\left(\frac{1}{r}\Psi_r + \Psi_\varphi\right)\right]. \tag{A.18}$$

The sign of the twist moment is reversed from that used by Dyer. This makes the direction of the twist moment agree with that of the twist rotation, both of which are now about the negative radial direction.

The solution to all three potential functions is

$$w_1 = A_3 \frac{J_n\left(k_1 r\right)}{J_n\left(k_1 a\right)} = A_3 Q\left(r\right), \tag{A.19}$$

$$w_2 = A_4 \frac{J_n\left(k_2 r\right)}{J_n\left(k_2 a\right)} = A_4 R\left(r\right), \tag{A.20}$$

and

$$T = A_5 \frac{J_n\left(k_3 r\right)}{J_n\left(k_3 a\right)} = A_5 S\left(r\right). \tag{A.21}$$

If I substitute Eq.(A.19), Eq.(A.20), and Eq.(A.21) into Eq.(A.13), Eq.(A.14), and Eq.(A.15) and carry out the spatial derivative, then I may directly relate the amplitudes of the three potential functions

to the plate displacements as

$$\mathbf{D}_f \begin{Bmatrix} A_4 \\ A_5 \\ A_6 \end{Bmatrix} = \begin{Bmatrix} U_z \\ \Psi_r \\ \Psi_\varphi \end{Bmatrix}, \tag{A.22}$$

where

$$\mathbf{D}_f(r) = \begin{bmatrix} Q & R & 0 \\ ia_1\left(\frac{n}{r}\right)Q & ia_2\left(\frac{n}{r}\right)R & -S_{,r} \\ \alpha_1 Q_{,r} & \alpha_2 R_{,r} & i\left(\frac{n}{r}\right)S \end{bmatrix}.$$

I may then substitute Eq.(A.22) into Eq.(A.16), Eq.(A.17), and Eq.(A.18) to express the axial force F_z, M_r, and M_φ in terms of the wave amplitudes by the matrix relation

$$\mathbf{C}_f \begin{Bmatrix} A_4 \\ A_5 \\ A_6 \end{Bmatrix} = \begin{Bmatrix} F_z \\ M_r \\ M_\varphi \end{Bmatrix}, \tag{A.23}$$

where

$$\mathbf{C}_f(r) = \gamma \begin{bmatrix} \kappa^2\sigma_m(\alpha_1+1)Q_{,r} & \kappa^2\sigma_m(\alpha_2+1)R_{,r} & i\kappa^2\sigma_m\left(\frac{n}{a}\right)S \\ i2I\sigma_m\alpha_1\left(\frac{n}{r}\right)\left(Q_{,r}-\frac{1}{r}Q\right) & i2I\sigma_m\alpha_2\left(\frac{n}{r}\right)\left(R_{,r}-\frac{1}{r}R\right) & I\sigma_m\left(-\left(\frac{n}{r}\right)^2 S+\frac{1}{r}S_{,r}-S_{,rr}\right) \\ \alpha_1 I\left(Q_{,rr}-\nu\left(\frac{n}{r}\right)^2 Q+\nu\frac{1}{r}Q_{,r}\right) & \alpha_2 I\left(-\nu\left(\frac{n}{r}\right)^2 R+\nu\frac{1}{r}R_{,r}+R_{,rr}\right) & i2I\sigma_m\left(\frac{n}{r}\right)\left(S_{,r}-\frac{1}{r}S\right) \end{bmatrix}$$

The flexural wave stiffness matrix is found by eliminating the wave amplitudes from Eq.(A.22) and Eq.(A.23). The resulting stiffness matrix is

$$\mathbf{K}_f = \mathbf{C}_f(a)\left[\mathbf{D}_f(a)\right]^{-1}. \tag{A.24}$$

Eq.(A.24) and Eq.(A.12) may be used in Eq.(A.1) and the stiffness matrix for the circular plate is now completely defined.

A.3 Attaching a circular plate to a cylindrical shell

In this section, I describe how to attach a circular plate to a cylindrical shell. The problem is that the forces and displacements of the plate are formulated in the cylindrical coordinate system $\{r, \varphi, z\}$, while the shell is formulated in the cylindrical coordinate system $\{x, \theta, r\}$. The following steps are required to make the plate stiffness matrix compatible with the shell stiffness matrix:

- I locate the plate in the shell coordinate system at $x = 0$, I let the origin of the plate coordinate system be coincident with the origin of the shell coordinate system and I align the positive r and z plate axes with the positive r and x shell axes, respectively. This means that the direction of φ axis is aligned with but in the opposite direction of the θ axis. It also means that a $+n$ helical shell wave corresponds to a $-n$ circumferential plate wave.

- The $5x5$ stiffness matrix for a circular plate is calculated as described above.

- I assume that the twisting moment $M_r(a)$ of the shell on the plate is zero. This allows me to eliminate both the twisting moment and the twisting rotation from the stiffness matrix relation and to reduce the dimension of the stiffness matrix from $5x5$ to $4x4$. I define the reduced plate displacement and force vectors as

$$\mathbf{U}^p = \left\{U_r^p, U_\varphi^p, U_z^p, \Psi_\varphi^p\right\}^T$$

and

$$\mathbf{F}^p = \left\{F_r^p, F_\varphi^p, F_z^p, M_\varphi^p\right\}^T,$$

where I have temporarily added the superscript p to refer to the plate coordinate system.

- If I define the plate displacements and forces (the forces of the shell on the plate) in the shell coordinate system as

$$\mathbf{U}^s = \left\{U^s, V^s, W^s, \Phi_x^s\right\}^T$$

and

$$\mathbf{F}^s = \left\{F_x^s, F_\theta^s, F_r^s, M_x^s\right\}^T,$$

where the superscript refers to the shell coordinate system, then the plate displacements and forces in the two coordinate systems are related as

$$\mathbf{T}_{p/s}\mathbf{U}^s = \mathbf{U}^p,$$

and

$$\mathbf{T}_{p/s}\mathbf{F}^s = \mathbf{F}^p,$$

by the coordinate transform matrix

$$\mathbf{T}_{p/s} = \begin{bmatrix} 0 & 0 & 1 & 0 \\ 0 & -1 & 0 & 0 \\ 1 & 0 & 0 & 0 \\ 0 & 0 & 0 & -1 \end{bmatrix}.$$

Using these relations, the plate stiffness matrix in the shell coordinate system is

$$\mathbf{K}^s = \mathbf{T}_{p/s}^{-1}\mathbf{K}^p\mathbf{T}_{p/s} = \mathbf{T}_{p/s}\mathbf{K}^p\mathbf{T}_{p/s}.$$

In the main text, I drop the superscript s because it is no longer needed.

Appendix B

Conventional FEM formulation of a 3D solid ring element

In this appendix, I formulate the stiffness and mass matrices for a solid ring element using a conventional FEM technique. The stiffness and mass matrix may be combined to form a dynamic stiffness matrix, which relates nodal forces to their resulting displacements. The forces and displacements have an assumed dependance in the circumferential direction of $e^{+in\theta}$ and a time dependence of $e^{-i\omega t}$, which effectively reduces a four dimensional problem to two dimensions. The formulation is non-isoparametric, which restricts the geometry of the element to be rectangular.

B.1 Dynamic stiffness matrix

Here I derive the stiffness matrix for a 3D solid ring element using conventional FEM procedures. The element is shown in Figure 1. The mean ring radius is $\bar{r}$, the total axial length $2L_x$, and the total radial thickness $2L_r$. The solid is assumed to be made from a linear elastic material with density ρ and Lame' constants λ and μ. The element is oriented in the cylindrical coordinate system $\{x, \theta, r\}$ with corresponding displacements

$$\mathbf{u}(x, r) = \{u, v, w\}^T.$$

The element has four nodes, G_1 through G_4, each with three displacement degrees of freedom. It is convenient to define the nodal displacement as

$$\mathbf{U} = \{u_1, v_1, w_1, u_2, v_2, w_2, u_3, v_3, w_3, u_4, v_4, w_4\}^T,$$

Figure B-1: Solid 3D ring element.

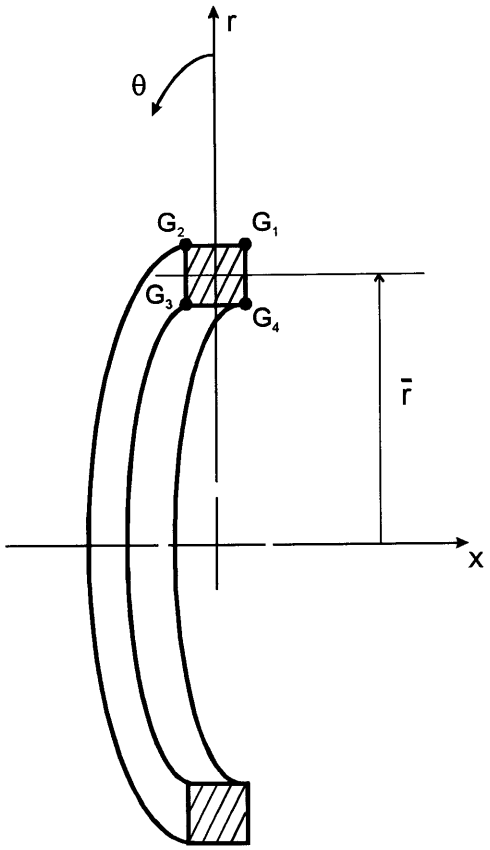

where the subscripts correspond to one of the four node numbers. The only external forces acting on the element are applied at the nodes. These forces are contained in $\mathbf{F}$ and are ordered in a manner consistent with $\mathbf{U}$.

My objective is to derive the dynamic stiffness matrix, which relates the externally applied forces to the resulting displacements. I do this in the usual fashion [1] by considering the scalar element potential given by

$$\Pi = \frac{1}{2}\int_{\mathcal{V}} \boldsymbol{\sigma}^{\dagger}\boldsymbol{\epsilon}\, d\mathcal{V} - \frac{1}{2}\rho\omega^2 \int_{\mathcal{V}} \mathbf{u}^{\dagger}\mathbf{u}\, d\mathcal{V} - \mathbf{U}^{\dagger}\mathbf{F}, \tag{B.1}$$

where $\boldsymbol{\sigma}$ and $\boldsymbol{\epsilon}$ are the stress and strain vectors (which I'll define shortly) and $\mathcal{V}$ is the element volume. The first integral in Eq.(B.1) represents the total elastic strain energy, the second integral is the total kinetic energy, and the last term is the work done by the external forces applied at the element nodes. Because the element displacements are assumed functions of the node displacements, the strain energy

and inertia terms are uncoupled and may be expressed by separate integrals.

The approach is to first assume that the displacements anywhere in the element may be written in terms of the element nodal displacement, then rewrite Π in terms of $\mathbf{U}$ only, and third consider the variation of Π with respect to each displacement in $\mathbf{U}$. This final step produces the dynamic stiffness matrix relation.

If I assume that the displacements internal to the element are linear interpolations of the nodal displacements, then I may write

$$\mathbf{u}(x,r) = \mathbf{H}(x,r)\,\mathbf{U}, \tag{B.2}$$

where

$$\mathbf{H}(x,r) = \left[\ \phi_1\mathbf{I},\quad \phi_2\mathbf{I},\quad \phi_3\mathbf{I},\quad \phi_4\mathbf{I}\ \right],$$

$\mathbf{I}$ is the $3x3$ identity matrix, and the ϕ_i's are the shape functions defined as:

$$\begin{aligned}
\phi_1 &= \frac{1}{4}\left(1+\frac{x}{L_x}\right)\left(1+\frac{r-\bar{r}}{L_r}\right)\\
\phi_2 &= \frac{1}{4}\left(1-\frac{x}{L_x}\right)\left(1+\frac{r-\bar{r}}{L_r}\right)\\
\phi_3 &= \frac{1}{4}\left(1+\frac{x}{L_x}\right)\left(1-\frac{r-\bar{r}}{L_r}\right)\\
\phi_4 &= \frac{1}{4}\left(1-\frac{x}{L_x}\right)\left(1-\frac{r-\bar{r}}{L_r}\right).
\end{aligned}$$

The strain-displacement relations in cylindrical coordinates [22] are:

$$\begin{aligned}
\epsilon_{xx} &= u_{,x}\\
\epsilon_{\theta\theta} &= \frac{1}{r}v_{,\theta}+\frac{1}{r}w\\
\epsilon_{rr} &= w_{,r}\\
2\epsilon_{x\theta} &= v_{,x}+\frac{1}{r}u_{,\theta}\\
2\epsilon_{xr} &= u_{,r}+w_{,x}\\
2\epsilon_{\theta r} &= \frac{1}{r}w_{,\theta}-\frac{1}{r}v+v_{,r}.
\end{aligned}$$

If I write the strains in vector form as

$$\boldsymbol{\epsilon} = \left\{\epsilon_{xx},\epsilon_{\theta\theta},\epsilon_{rr},2\epsilon_{x\theta},2\epsilon_{xr},2\epsilon_{\theta r}\right\}^T,$$

where the usual subscript notation is used to note the surface normal and direction, then I may relate

the strains to nodal displacements as

$$\boldsymbol{\epsilon}(x,r) = \mathbf{B}(x,r)\,\mathbf{U}, \tag{B.3}$$

where

$$\mathbf{B}(x,r) = \left[\begin{array}{cccc} \mathbf{B}_1, & \mathbf{B}_2, & \mathbf{B}_3, & \mathbf{B}_4 \end{array}\right]$$

defined in terms of

$$\mathbf{B}_i(x,r) = \left[\begin{array}{ccc} \phi_{i,x} & 0 & 0 \\ 0 & i\frac{n}{r}\phi_i & \frac{1}{r}\phi_i \\ 0 & 0 & \phi_{i,r} \\ i\frac{n}{r}\phi_i & \phi_{i,x} & 0 \\ \phi_{i,r} & 0 & \phi_{i,x} \\ 0 & \phi_{i,r} - \frac{1}{r}\phi_i & i\frac{n}{r}\phi_i \end{array}\right].$$

Note that the derivatives with respect to θ are carried out using the assumed wave dependence in the circumferential direction.

The stresses may also be written in vector form as

$$\boldsymbol{\sigma} = \{\sigma_{xx}, \sigma_{\theta\theta}, \sigma_{rr}, \sigma_{x\theta}, \sigma_{xr}, \sigma_{\theta r}\}^T,$$

where their order corresponds to those in $\boldsymbol{\epsilon}$. The stress and strain are related by the constitutive equation

$$\boldsymbol{\sigma} = \mathbf{C}\boldsymbol{\epsilon}, \tag{B.4}$$

where the constitutive matrix is

$$\mathbf{C} = \left[\begin{array}{cccccc} \lambda+2\mu & \lambda & \lambda & 0 & 0 & 0 \\ \lambda & \lambda+2\mu & \lambda & 0 & 0 & 0 \\ \lambda & \lambda & \lambda+2\mu & 0 & 0 & 0 \\ 0 & 0 & 0 & \mu & 0 & 0 \\ 0 & 0 & 0 & 0 & \mu & 0 \\ 0 & 0 & 0 & 0 & 0 & \mu \end{array}\right].$$

Using Eq.(B.2), Eq.(B.3), and Eq.(B.4), I may now rewrite Eq.(B.1) in terms of $\mathbf{U}$ only as

$$\Pi = \frac{1}{2}\mathbf{U}^\dagger\mathbf{K}_0\mathbf{U} - \frac{1}{2}\omega^2\mathbf{U}^\dagger\mathbf{M}_0\mathbf{U} - \mathbf{U}^\dagger\mathbf{F}, \tag{B.5}$$

where (anticipating the final result) the static stiffness matrix is

$$\mathbf{K}_0 = 2\pi \int_{x=-L_x}^{L_x} \int_{r=-L_r}^{L_r} \mathbf{B}^{\dagger}(x,r)\,\mathbf{CB}(x,r)\,r\,dr\,dx,$$

and the mass matrix is

$$\mathbf{M}_0 = 2\pi\rho \int_{x=-L_x}^{L_x} \int_{r=-L_r}^{L_r} \mathbf{H}^{T}(x,r)\,\mathbf{H}(x,r)\,r\,dr\,dx.$$

If I consider the variation of Π with respect to each nodal displacement in $\mathbf{U}$, that is,

$$\delta\Pi = 0,$$

then it must hold that

$$\mathbf{KU} = \left[\mathbf{K}_0 - \omega^2\mathbf{M}_0\right]\mathbf{U} = \mathbf{F}, \tag{B.6}$$

where $\mathbf{K}$ is the dynamic stiffness matrix. To evaluate $\mathbf{K}_0$ and $\mathbf{M}_0$, the integration is done numerically using Gauss quadrature as described in the following subsection. The dimensions of the nodal forces is force. Eq.(B.6) reveals that the static stiffness and mass matrix are not functions of frequency and need only be calculated once. The dynamic stiffness matrix is then formed simply by adding two matrices.

B.1.1 Gauss quadrature

The Gauss quadrature technique for integration in the x-coordinate direction using two point integration may be written as

$$f(x) = \int_{x=x_1}^{x_2} F(x)\,dx = \alpha_1 F(\beta_1) + \alpha_2 F(\beta_2),$$

where the Gauss points and weights are

$$\beta_1, \beta_2 = \frac{1}{2}\left(1 \pm \frac{1}{\sqrt{3}}\right)(x_2 - x_1) + x_1$$

and

$$\alpha_1, \alpha_2 = \frac{1}{2}(x_2 - x_1),$$

respectively. If $x_1 = -x_2$, then

$$\beta_1, \beta_2 = \pm\frac{x_2}{\sqrt{3}}$$

and

$$\alpha_1, \alpha_2 = x_2.$$

The same technique is used for integration in the radial direction.

B.1.2 Multi-point constraints

For reasons described in the main text, I need to constrain the relationship between various degrees of freedom of the global finite element assembly as if there were a (weightless) perfectly rigid body connecting them. In effect, the rigid body constrains the degree of freedom at one node to be dependent on one or more independent degrees of freedom. The relationship between the dependent and the independent degree of freedom must be linear and is usually based on geometry. The corresponding forces are also constrained, however, they are constrained based on force equilibrium. The following is an outline of a systematic procedure for handling multiple constraints.

I use the *multi-point constraint* method as described in reference [37]. I begin by partitioning the element displacements into two subvectors such that

$$\mathbf{U} = \left\{ \begin{array}{c} \mathbf{U}_m \\ \mathbf{U}_n \end{array} \right\}.$$

If the M dependent degrees of freedom are contained in $\mathbf{U}_m$ and the N independent degrees of freedom are contained in $\mathbf{U}_n$, then I may express their relationship as

$$\mathbf{R}_{mm}\mathbf{U}_m + \mathbf{R}_{mn}\mathbf{U}_n = 0, \tag{B.7}$$

where $\mathbf{R}_{mm}$ is an MxM matrix and $\mathbf{R}_{mn}$ is an MxN matrix. I may then use Eq.(B.7) to solve for

$$\mathbf{U}_m = -\mathbf{R}_{mm}^{-1}\mathbf{R}_{mn}\mathbf{U}_n.$$

and write the global displacement vector as

$$\mathbf{U} = \mathbf{T}_u\mathbf{U}_m, \tag{B.8}$$

where

$$\mathbf{T}_u = \left[\begin{array}{c} -\mathbf{R}_{mm}^{-1}\mathbf{R}_{mn} \\ \mathbf{I}_{nn} \end{array} \right]$$

has dimension $(M+N)\,xN$.

There is some similar transform for the force

$$\mathbf{T}_f\mathbf{F} = \mathbf{F}_m \tag{B.9}$$

based on force equilibrium on the rigid body. I may use Eq.(B.8) and Eq.(B.9) to write the reduced global stiffness matrix as

$$\mathbf{K}_{mm} = \mathbf{T}_f\mathbf{K}\mathbf{T}_u$$

written in terms of the original global stiffness matrix $\mathbf{K}$.

Appendix C

Response of an infinite flat plate to an embedded piezo-electric source

In this appendix, I consider the response of an infinite flat plate driven by a piezo-electric source. The source is a 31-mode piezoelectric ring. A hole is drilled in the plate and the source is centered in the hole and bonded into place as shown in Figure C-1. When a voltage is applied to the source, it expands uniformly in the radial direction, which excites compressional waves in the plate. My aim is to derive the transfer function between the input voltage and the plate response at a given radius.

To simplify the analysis, I assume:

- The ring behaves as if it were thin compared to its radius. This is exactly true for an infinite thickness to radius ratio. I expect that it is a reasonable assumption because the actual ratio thickness to radius ratio is about 1/6. Consistent with this assumption, I make no distinction between the mean radius and the outer radius of the ring.

- The motion of the ring and plate is symmetric with respect to the circumferential direction, that is, that the interaction of the ring with its surrounding is only through the hoop or $n = 0$ mode of the ring. Because the source is symmetric about its axis with respect to it both its' electrical and mechanical properties and the loading due to the plate is also symmetric, this assumption is justified.

- The frequency of operation is well below any electrical or mechanical resonances of the ring. Another way to say this is that wavelengths are long compared to the source dimensions. The ring then operates under quasi-static conditions and may be modeled by its' lumped equivalent circuit elements. A comparison of source wavelengths versus source dimensions is given in the main text.

Figure C-1: Piezoelectric source embedded in an infinite flat plate.

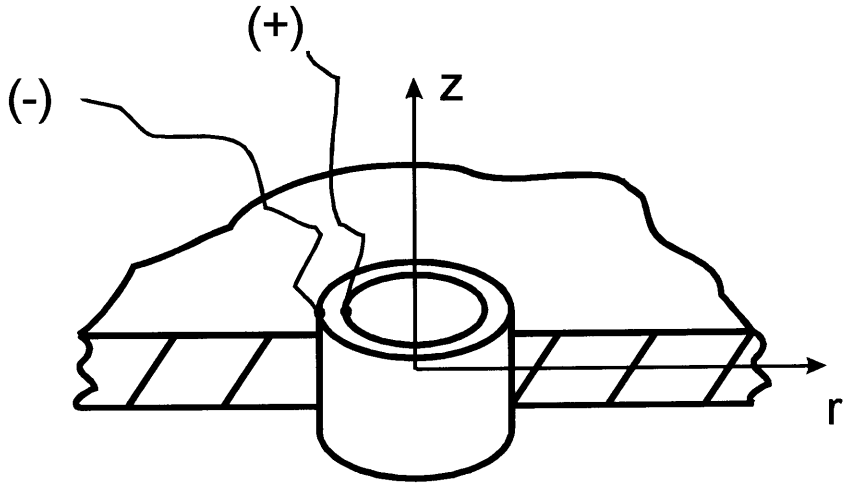

- I neglect the effects of thin bond joint between the plate and the source. In the main text, I consider a plate made from PVC material, which has properties that are close to that of the bond material. Therefore, the bond need not be distinguished from the plate.
- All time dependant quantities are proportional to $e^{-i\omega t}$.

My approach is to consider the source and the plate separately. The results from each are then combined to derive the expression for the desired transfer function.

C.1 Equivalent circuit model of the source

The source is a 31-mode ring poled in the "3" or radial direction, which produces a response in the "1" or circumferential direction. The particular ring being considered has outer radius a_x, thickness h_x

Figure C-2: Equivalent circuit model of piezoelectric source.

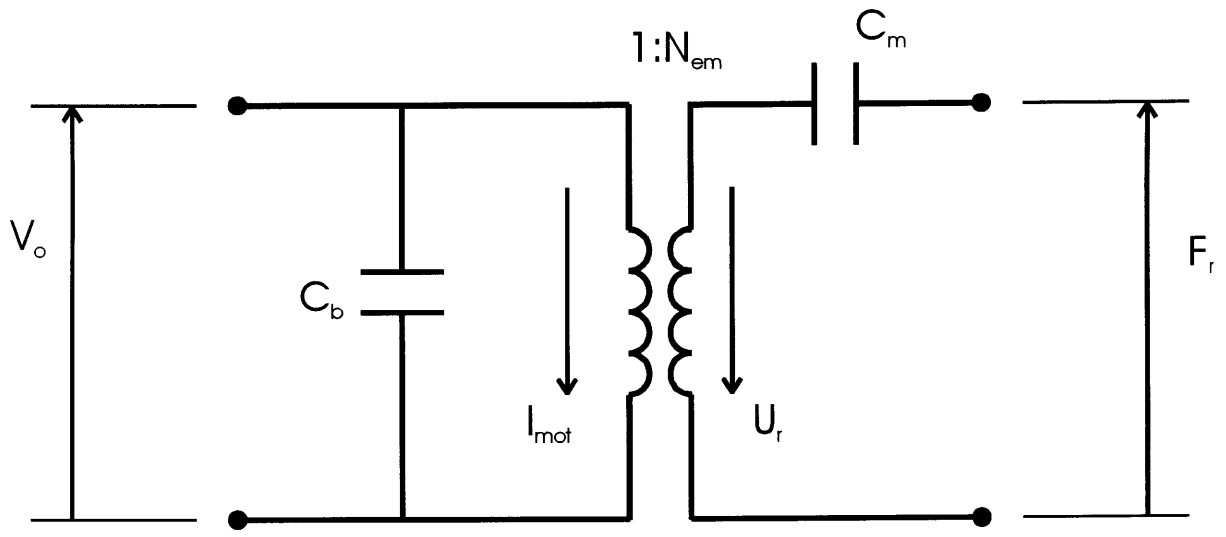

(I use a subscript x to distinguish ring properties from plate properties), height b. Such a source may be represented by the equivalent circuit shown in Figure C-2 [9]. Expressions for the circuit elements are found by considering the material constitutive relation in terms of the desired state variables (input voltage V_o, motional current I_{mot}, radial displacement U_r, and radial force F_r) subject to the assumptions listed above.

The constitutive relation, written in terms of the (undesired) state variables (dimensionless circumferential strain S_{11}, electric charge density D_{33} (C/m^2), circumferential stress T_{11} (N/m^2), and electric field E_{33} $(Volt/m)$ [9] is

$$\begin{Bmatrix} S_{11} \\ D_{33} \end{Bmatrix} = \begin{bmatrix} s_{11}^E & d_{31} \\ d_{31} & \varepsilon_{33}^T \end{bmatrix} \begin{Bmatrix} T_{11} \\ E_{33} \end{Bmatrix}, \tag{C.1}$$

where d_{31} is the piezoelectric constant, s_{11}^E is the inverse of Young's modulus in the circumferential

direction at zero electric field, and ε_{33}^T the dielectric constant at zero stress.

By consideration of geometry and the assumed symmetry of the problem, the radial displacement may be related to the circumferential strain as

$$U_r = a_x S_{11}. \tag{C.2}$$

A simple static force balance is used to relate the radial force of the plate on the ring to the circumferential stress as

$$F_r = T_{11} 2\pi b h_x. \tag{C.3}$$

The static balance is consistent with the assumption that the wavelengths are long compared to the source dimensions. I define the motional current in terms of the charge density as

$$I_{mot} = (-i\omega)\, 2\pi a_x b D_{33}. \tag{C.4}$$

Also, the applied voltage is defined in terms of the electric field as

$$V_o = E_{33} h_x. \tag{C.5}$$

I substitute Eq.(C.2)and Eq.(C.5) into Eq.(C.1) to replace the old state variables with these new defined state variables. Eq.(C.1) becomes

$$\begin{Bmatrix} U_r \\ I_{mot} \end{Bmatrix} = \begin{bmatrix} C_m & C_m N_{em} \\ -i\omega C_m N_{em} & -i\omega \left(C_b + C_m N_{em}^2\right) \end{bmatrix} \begin{Bmatrix} F_r \\ V_o \end{Bmatrix}, \tag{C.6}$$

where the coefficients of the constitutive matrix may be shown to represent the equivalent circuit elements in Figure C-2. The electrical side is represented by the blocked or zero displacement capacitance given by

$$C_b = \frac{2\pi a_x b \varepsilon_{33}^S}{h_x}, \tag{C.7}$$

which is defined in terms of the blocked dielectric strength

$$\varepsilon_{33}^S = \varepsilon_{33}^T \left(1 - \frac{d_{31}^2}{s_{11}^E \varepsilon_{33}^T}\right).$$

The electrical current is converted into mechanical current (radial velocity) by the transformer with electro-mechanical turns ratio

$$N_{em} = \frac{I_{mot}}{-i\omega U_r} = \frac{F_r}{V_o} = \frac{2\pi b d_{31}}{s_{11}^E}. \tag{C.8}$$

The mechanical side is represented by the internal mechanical compliance of the source given by

$$C_m = \frac{s_{11}^E a_x}{2\pi b h_x}. \tag{C.9}$$

I could include the effect of mass (electrical or mechanical) by letting C_b and C_m be complex quantities. This would capture the influence of the first one or two system resonances.

C.2 Plate equations

In this section, I consider the infinitely extended plate with a hole. My aim here is to calculate the load that the plate imparts on the source and also find the transfer function between the displacement at any position in the plate versus the displacment at the inside radius.

I put the plate in the same coordinate system as the source. I also use U_r and F_r for radial displacement and force. (If $r > a_x$, then U_r is the plate displacement. If $r = a_x$, then U_r is both the plate and source displacement.). The hole in the plate of radius a_x is centered at the origin. The plate has thickness h, density ρ, plate speed c_p, and Poisson's ratio ν.

From first order membrane theory, the motions of an infinite plate to axisymmetric motions are governed by the compressional wave potential

$$\Phi = AH_0(k_p r),$$

where H_0 is the Hankel function of the first kind,

$$k_p = \frac{\omega}{c_p}$$

is the compressional wavenumber, and A is some unknown wave amplitude that is determined by the boundary conditions. The Hankel function is used because it automatically satisfies the radiation boundary condition at infinite radius. In terms of this potential, the radial displacement is

$$U_r(r) = AH_0(k_p r)_{,r} = -Ak_p H_1(k_p r) \tag{C.10}$$

and the internal force in the radial direction is

$$F_r(r) = 2\pi r \rho c_p^2 h A \left(-k_p^2 H_0(k_p r) + (1-\nu)\frac{k_p}{r} H_1(k_p r) \right), \tag{C.11}$$

where the derivatives of the Bessel functions are given by Hildebrand [5].

I can combine Eq.(C.10) and Eq.(C.11) to calculate the plate stiffness as seen by the source as

$$K = \left(\frac{-F_r(r)}{U_r(r)}\right)\Big|_{r=a_x} = 2\pi h\rho c_p^2\left[(1-\nu) - k_p r\frac{H_0(k_p a_x)}{H_1(k_p a_x)}\right], \tag{C.12}$$

where the minus sign is required because the stiffness is defined in terms of a positive radial direction (The sign convention for F_r is the same as the radial stress.). As a check on K, I calculate its' low frequency limit as

$$K = 2\pi h\rho c_p^2(1-\nu), \tag{C.13}$$

where I have made use of the low frequency limits of the Hankel functions given by

$$\begin{aligned} H_0(k_p r) &= 1 + i\frac{2}{\pi}\ln(k_p r) \\ H_1(k_p r) &= \frac{1}{2}k_p r - i\frac{2}{\pi k_p r}. \end{aligned}$$

As expected, the stiffness to first order is a positive pure real number indicating the dominance of spring-like terms (as opposed to mass or dissipative terms).

I can also use Eq.(C.10) to find the transfer function between the displacement at any position and that at the inside radius as

$$\frac{U_r(r)}{U_r(a_x)} = \frac{H_1(k_p r)}{H_1(k_p a_x)}. \tag{C.14}$$

C.3 Transfer function

The table is set to find the transfer function between the input source voltage and the plate displacment. where I have assumed continuity of radial displacement and a dynamic force balance at the junction between the source and shell. The negative sign is needed because the shell resists the positive radial motions of the source. Using the top row of Eq.(C.6), I can find the relationship between the source voltage and the radial displacement as

$$U_r = \frac{N_{em}V_o}{K + \frac{1}{C_m}}.$$

This equation shows that the radial displacement is equal to the total force produced by the source (the numerator) divided by the serially connected mechanical stiffness of the source and shell (stiffness is inverse compliance). The force on the shell is therefore

$$F_r = \frac{K}{K + \frac{1}{C_m}}N_{em}V_o.$$

These last two equations are used to find the transfer function between the shell and the input source voltage.

C.4 Membrane stiffness of a circular plate

In the main text, I need to know the stiffness of a circular plate of radius a_x subject to a uniform radial force and it is convienient to do it here. This stiffness is given by Eq.(C.12) provided I replace the Hankel functions with Bessel functions with the same argument and order and also reverse the sign of the force (Because on the outer edge of a circular plate, the externally applied force is in the same direction as the internal plate force, which is opposite that for the inside edge of a plate with a hole). The resulting stiffness is

$$K = \left.\frac{F_r(r)}{U_r(r)}\right|_{r=a_x} = -2\pi h\rho c_p^2\left((1-\nu) - k_p R\frac{J_0(k_p r)}{J_1(k_p r)}\right).$$

In the low frequency limit, the stiffness approaches

$$K = 2\pi h\rho c_p^2(1+\nu), \tag{C.15}$$

where I have made use of the low frequency limits of the Bessel functions given by

$$\begin{aligned} J_0(k_p r) &= 1 \\ J_1(k_p r) &= \frac{1}{2}k_p r. \end{aligned}$$

For an elastic plate, the low frequency limit of the stiffness is a positive pure real number and there is no leading order dissipative term. A comparison of Eq.(C.15) and Eq.(C.13) shows that, as one might expect, the circular plate is stiffer than the plate with the hole at low frequencies.

Appendix D

Wave propagation on a tensioned beam with a rigid link attachment

This appendix presents the wave-based finite element method that I use to determine the stiffness matrix of a tensioned beam with a rigid body attachment. I derive two forms of the stiffness matrix. The first form is the stiffness matrix for a beam-link-beam assembly. The stiffness matrix is formulated for both pinned and welded connections between the beam and the link. It is useful in the main text for studying wave transmission and reflection coefficients through rigid bodies. The second form is the stiffness matrix for a *fixed-end* absorber, which is also discussed in the main text.

D.1 The tensioned Euler-Bernoulli beam element

Formulating the beam dynamics in terms of a stiffness matrix brings to bear well known finite element solution procedures [1] for solving the response of complicated assemblages of interconnected elements. However, unlike the better known conventional methods, the stiffness matrix given here is based on a wave solution rather than an approximate solution using polynomial interpolating functions. Two important advantages of the wave based approach are: first, the resulting stiffness matrix is exact to within the assumptions of the governing differential equations and second, both the input and the output may be expressed in terms of individual wave amplitudes. The stiffness matrix method is a generalization of the transfer matrix approach [43]. A tutorial on the use of the WFEM method applied to beams is given by Fricke and Hayner [44].

A typical beam element is shown in Figure D.1. The beam is made from a linear elastic solid with linear density ρ_c, longitudinal sound speed c_L, cross-sectional area S, and radius of gyration r_g. All

Figure D-1: Schematic of tensioned beam finite element.

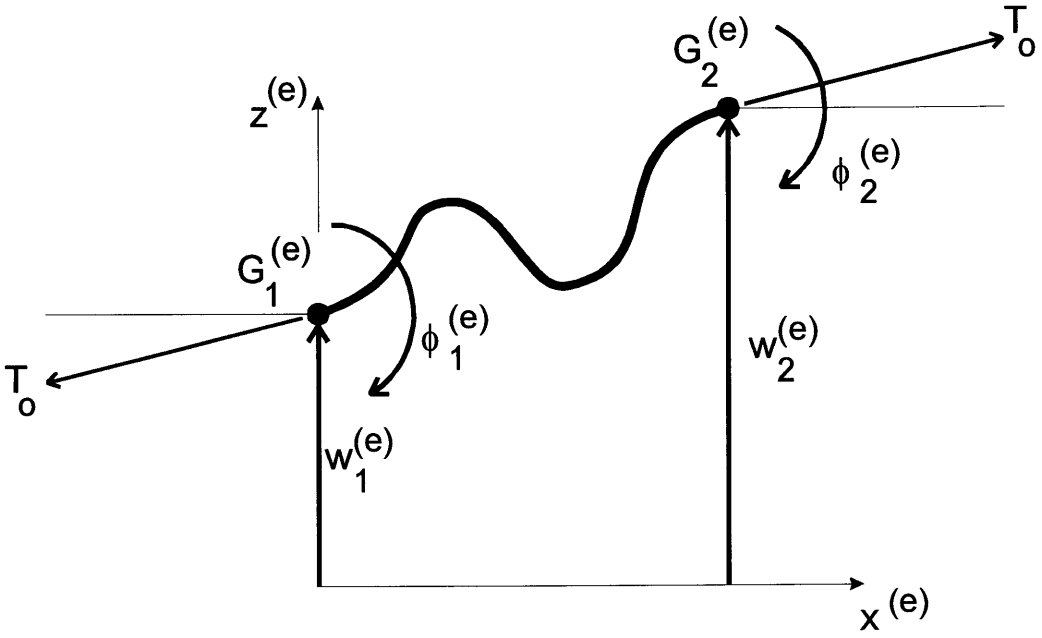

material and geometric properties are constant over the length of the beam. The beam is oriented in the local coordinate system $\{x, y, z\}$ and extends from node G_1 at $x = 0$ to node G_2 at $x = L$. The lateral and rotational displacements at G_1 and G_2 are $\{w_1, \phi_1\}$ and $\{w_2, \phi_2\}$, where w is in the z direction and the ϕ is about the y direction. There are no external forces acting between the nodes but forces f_1 and f_2 and moments m_1 and m_2 may be applied at the nodes. These forces may be due to either the reaction force of another element or a force external to all elements [1]. The sign conventions adopted for the end forces and displacements at both nodes are consistent with the positive directions of the local coordinate system. I assume that the beam displacements are sufficiently low that the tension in the beam, T_o, is a constant.

My goal is to find the dynamic stiffness matrix, which relates the nodal displacements to the externally

[1] I sometimes refer to both the lateral force and the moment as just the forces. The same goes for the lateral displacement and the rotation.

applied nodal forces. In deriving the stiffness matrix, two other matrices are derived, which I refer to as the displacement-amplitude matrix and the force-amplitude matrix (or just the displacement matrix and force matrix). The displacement matrix relates the beam wave amplitudes to the displacements at the nodes, while the force matrix relates the wave amplitudes to the forces.

D.1.1 Governing differential equations

The classical equations governing the dynamics of a zero tension beam and a string combine in a simple way to apply to a tensioned beam. Written in terms of the transverse displacement, the momentum equation for a tensioned beam is

$$-c_L^2 r_g^2 w\left(x,t\right)_{,xxxx} + c_o^2 w\left(x,t\right)_{,xx} - w\left(x,t\right)_{,tt} = 0, \tag{D.1}$$

where

$$c_o = \sqrt{\frac{T_o}{\varrho_c}}$$

is the string wave speed (the wave speed when the flexural rigidity is zero). Eq.(D.1) is homogeneous because there are no forces acting on the beam. Forces are introduced through the boundary conditions at the nodes in a subsequent section. In deriving Eq.(D.1), the assumed angle of rotation between a plane cross-section and the neutral axis of the beam is

$$\phi\left(x,t\right) = -w_{,x}. \tag{D.2}$$

Provided the beam is sufficiently thin so that rotary inertia and shear deformation can be neglected, the resultant moment and shear force expressed in terms of displacement are

$$m\left(x,t\right) = -\rho_c c_L^2 r_g^2 w_{,xx} \tag{D.3}$$

and

$$f\left(x,t\right) = -\rho_c c_L^2 r_g^2 w_{,xxx} + \rho_c c_o^2 w_{,x}, \tag{D.4}$$

respectively. Eq.(D.2) through Eq.(D.4) are needed to solve for boundary conditions when specified in terms other than the lateral displacement.

D.1.2 Wave dispersion

To solve Eq.(D.1), I assume a wave solution of the form

$$w(x) = Ae^{+ikx}e^{-\imath\omega t} \tag{D.5}$$

where ω is the real frequency, k is the possibly complex axial wavenumber, and A is the complex wave amplitude. The time dependence is hereafter implied. If I substitute Eq.(D.5) into Eq.(D.1), then the result is the dispersion relation

$$+c_L^2 r_g^2 k^4 + c_o^2 k^2 - \omega^2 = 0, \tag{D.6}$$

relating wavenumber and frequency in terms of the beam material properties and geometry. The dispersion relation has four wavenumber roots at each frequency. It is second order in k^2, which means the third and fourth roots are negative values of the first and second roots and that all may be solved for explicitly. For an elastic beam, there are two pure real roots, $\pm k_p$, corresponding to the propagating waves and two pure imaginary roots, $\pm ik_e$, corresponding to the evanescent waves. If I first define the *critical frequency* as

$$\omega_c = \frac{c_o^2}{r_g c_L} \tag{D.7}$$

and the *critical wavenumber* as

$$k_c = \frac{c_o}{r_g c_L},$$

then the propagating wavenumber is

$$k_p = k_c\sqrt{-\frac{1}{2} + \sqrt{\frac{1}{4} + \left(\frac{\omega}{\omega_c}\right)^2}},$$

and the evanescent wavenumber is

$$k_e = k_c\sqrt{+\frac{1}{2} + \sqrt{\frac{1}{4} + \left(\frac{\omega}{\omega_c}\right)^2}},$$

where I take the values of k_p and k_e that are positive. To interpret the critical frequency and wavenumber, I plot k_p and k_e versus frequency in Figure D.2. In the low frequency limit, the propagating wavenumber is equal to the string wavenumber

$$k_o = \frac{\omega}{c_o},$$

Figure D-2: Dispersion relation for tensioned beam.

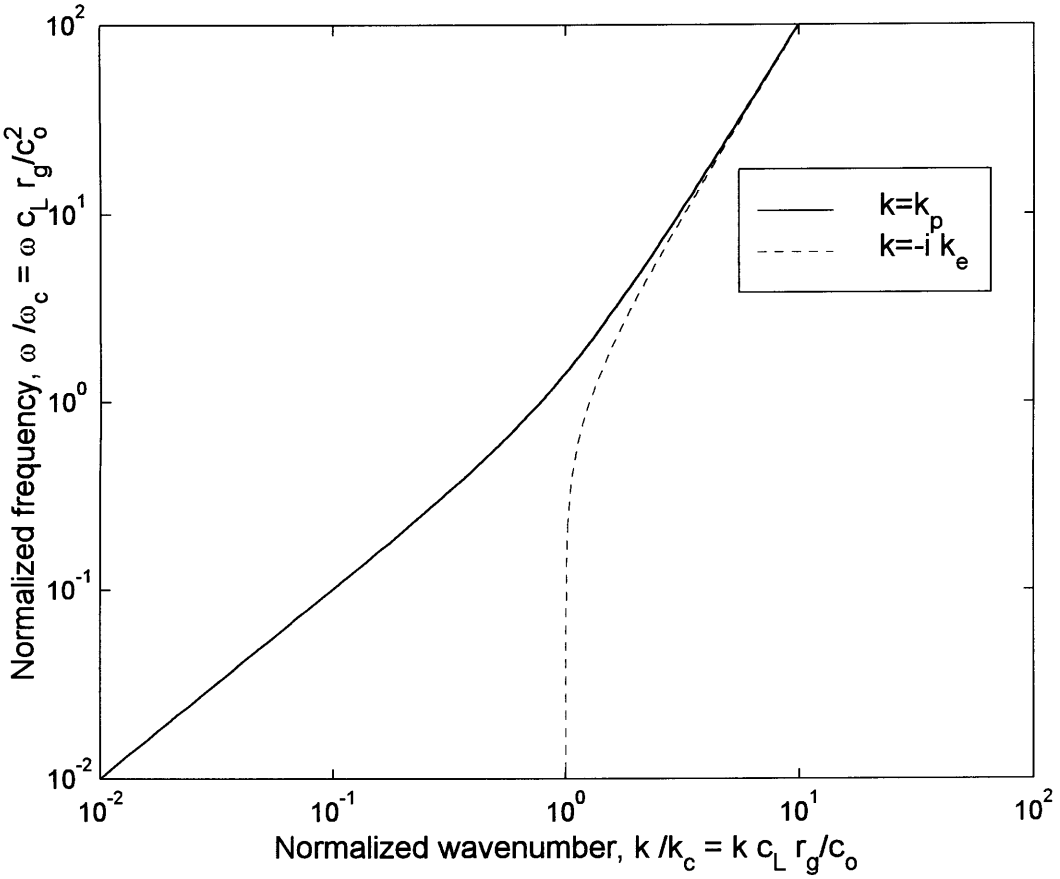

while, in the high frequency limit, the propagating wavenumber is equal to the flexural wavenumber

$$k_f = \sqrt{\frac{\omega}{c_L r_g}}.$$

As shown in the figure, the transition between these two asymptotic values is defined by the critical frequency. In other words, we know that tension effects always dominate at low enough frequency. The critical frequency defines the transition frequency at which tension effects *begin* to dominate. Beams with very high flexural rigidity have very low critical frequencies.

I can now express the general solution for the displacement at any position along the beam axis in terms of four waves as

$$w(x) = A_1 e^{+ik_p x} + A_2 e^{-k_e x} + A_3 e^{-ik_p x} + A_4 e^{+k_e x}. \tag{D.8}$$

The first and second terms in Eq.(D.8) represent a right-going and a right-decaying evanescent wave, while the third and fourth are left-going and left-decaying wave[2]. Therefore, at a given frequency, the displacement on the beam is known to within a set of four unknown complex wave amplitudes, which are determined from the boundary conditions.

D.1.3 Stiffness matrix

To determine the stiffness matrix, I first determine the *displacement* matrix and the *force* matrix. The displacement matrix, **D**, which relates the beam wave amplitudes to the displacements at the element nodes, is defined by the relation

$$\mathbf{DA} = \mathbf{U}, \tag{D.9}$$

where

$$\mathbf{A} = \{A_1, A_2, A_3, A_4\}^T \tag{D.10}$$

is a vector containing the four wave amplitudes (the superscript T denotes the transpose operator) and

$$\mathbf{U} = \{w_1, \phi_1, w_2, \phi_2\}^T$$

is a vector containing the four nodal displacements.

Before solving for the displacement matrix, I rewrite Eq.(D.8) as

$$w = A_1 e^{+ik_p x} + A_2 e^{-k_e x} + A_3 e^{-ik_p(x-L)} + A_4 e^{+k_e(x-L)}. \tag{D.11}$$

where I have referenced (or phase shifted) the left-going to the right side of the beam at $x = L$. This is valid because I have not yet specified the wave amplitudes. This phase shift improves the conditioning of the displacement and force matrix. The displacement matrix is inverted in the following section to calculate the stiffness matrix.

To determine the first and third rows of the displacement matrix, I evaluate Eq.(D.11) at $x = 0$ and $x = L$. The other two rows are found by substituting Eq.(D.11) into Eq.(D.2) and evaluating the resulting expression at $x = 0$ and $x = L$. After gathering these four equations into a form consistent

[2] I will refer to the right-propagating and right-decaying waves collectively as the right-going waves and like-wise for the left going waves.

with Eq.(D.9), the displacement matrix is

$$\mathbf{D} = \begin{bmatrix} +1 & +1 & +e^{+ik_pL} & +e^{-k_eL} \\ -ik_p & +k_e & +ik_pe^{+ik_pL} & -k_ee^{-k_eL} \\ +e^{+ik_pL} & +e^{-k_eL} & +1 & +1 \\ -ik_pe^{+ik_pL} & +k_ee^{-k_eL} & +ik_p & -k_e \end{bmatrix}. \tag{D.12}$$

The displacement matrix is a function of the beam material properties, the beam geometric properties, and frequency. By phase shifting the left-going waves as discussed earlier, I prevent very large terms proportional to e^{+k_eL} from appearing in $\mathbf{D}$, which greatly improves its' conditioning. This is important because I'll show presently that $\mathbf{D}$ must be inverted to calculate the stiffness matrix.

The force matrix $\mathbf{C}$ is defined by

$$\mathbf{CA} = \mathbf{F}, \tag{D.13}$$

where

$$\mathbf{F} = \{f_1, m_1, f_2, m_2\}^T.$$

I use Eq.(D.11), Eq.(D.3), and Eq.(D.4) to find the forces and moments at $x = 0$ and $x = L$. After gathering the resulting equations into a form consistent with Eq.(D.13), the force matrix is

$$\begin{aligned} \mathbf{C} = {} & \rho_c c_L^2 r_g^2 \begin{bmatrix} -ik_p^3 & -k_e^3 & +ik_p^3e^{+ik_pL} & +k_e^3e^{-k_eL} \\ -k_p^2 & +k_e^2 & -k_p^2e^{+ik_pL} & +k_e^2e^{-k_eL} \\ +ik_p^3e^{+ik_pL} & +k_e^3e^{-k_eL} & -ik_p^3 & -k_e^3 \\ +k_p^2e^{+ik_pL} & -k_e^2e^{-k_eL} & +k_p^2 & -k_e^2 \end{bmatrix} \\ & +\rho_c c_o^2 \begin{bmatrix} -ik_p & +k_e & +ik_pe^{+ik_pL} & -k_ee^{-k_eL} \\ 0 & 0 & 0 & 0 \\ +ik_pe^{+ik_pL} & -k_ee^{-k_eL} & -ik_p & +k_e \\ 0 & 0 & 0 & 0 \end{bmatrix}. \end{aligned} \tag{D.14}$$

In deriving $\mathbf{C}$, I reverse the sign of f and m evaluated at $x = 0$ to make them consistent with my convention for the direction of the externally applied forces at the element nodes, that is, $f_1 = -f|_{x=0}$ and $m_1 = -m|_{x=0}$. For a zero tension beam, the second matrix on the right side of Eq.(D.14) is zero. As expected, the force matrix is also a function of the beam material, geometric properties, and frequency. The force matrix is well conditioned for the same reasons as the displacement matrix.

I can now solve for the dynamic stiffness matrix, defined by the relation

$$\mathbf{KU} = \mathbf{F}, \tag{D.15}$$

by eliminating the wave amplitudes from Eq.(D.9) and Eq.(D.13). The stiffness matrix is given by

$$\mathbf{K} = \mathbf{C}\,[\mathbf{D}]^{-1}. \tag{D.16}$$

The stiffness matrix for a beam is always symmetric and for this particular beam element has only five unique elements due to its physical symmetry. For finite length beams, the stiffness matrix elements are pure real. Positive and negative real values denote spring-like and mass-like characteristics respectively. Dissipative effects may be included by letting the compressional sound speed be complex, which results in complex stiffness matrix elements with negative imaginary parts.

D.1.4 Semi-infinite length element

With some slight modifications of the finite length beam element equations, a semi-infinitely long beam that extends from G_1 at $x = 0$ to positive infinity may be formulated. For this single node element, I first redefine the displacement and force vectors as

$$\mathbf{U} = \{w_1, \phi_1\}^T$$

and

$$\mathbf{F} = \{f_1, m_1\}^T.$$

If I assume that only the right-going waves are present, then the displacement at any position along the beam is

$$w = A_1 e^{+ik_p x} + A_2 e^{-k_e x}$$

and the wave amplitude vector must also be redefined as

$$\mathbf{A} = \{A_1, A_2\}^T.$$

Following the same steps as for the finite length element, the resulting $(2x2)$ displacement matrix is

$$\mathbf{D} = \begin{bmatrix} +1 & +1 \\ -ik_p & +k_e \end{bmatrix}, \tag{D.17}$$

the force matrix is

$$\mathbf{C} = \rho_c c_L^2 r_g^2 \begin{bmatrix} -ik_p^3 & -k_e^3 \\ -k_p^2 & +k_e^2 \end{bmatrix} + \rho_c c_o^2 \begin{bmatrix} -ik_p & +k_e \\ 0 & 0 \end{bmatrix}, \tag{D.18}$$

and the stiffness matrix is

$$\mathbf{K} = \frac{\rho_c c_L^2 r_g^2}{k_p^2 + k_e^2} \begin{bmatrix} -(k_p^4 k_e + k_p^2 k_e^3) - i(k_p^3 k_e^2 + k_p k_e^4) & +i(k_p^3 k_e + k_p k_e^3) \\ +i(k_p^3 k_e + k_p k_e^3) & (k_p^2 k_e + k_e^3) - i(k_p^3 + k_p k_e^2) \end{bmatrix}. \tag{D.19}$$

Note that, even though the beam is elastic, the stiffness elements are complex indicating energy dissipation. This dissipation is now, however, due to radiation rather than conversion into heat. I use the semi-infinite length element to help calculate reflection and transmission coefficients.

D.2 The beam-link-beam element

I may now use the results of the previous section to formulate the *global* stiffness matrix of a beam-link-beam system, where the term global refers to the system or collection of elements. The global matrix is merely an ordered statement of dynamic equilibrium at each independent displacement degree of freedom. In this section, I derive the stiffness matrix for both pinned and welded beam-link connections.

D.2.1 Pinned beam-link connections

The global system of elements is shown in Figure D.3. The left beam extends from node G_1 to G_2, the link from G_2 to G_3, and the right beam from G_3 to G_4. I designate the left beam as element number one, the link as element number two, and the right beam as element number three. The stiffness matrix for the right or left beams is that derived in the previous section. The link is assumed to be perfectly rigid with length $L^{(2)}$, mass M, and moment of inertia I_0 about the center of mass located at a distance b from its' left end.

I begin by defining the global displacement vector of the beam-link-beam assembly as

$$\mathbf{U} = \left\{ w_1^{(1)},\ \phi_1^{(1)},\ w_2^{(1)},\ \phi_2^{(1)},\ \phi_1^{(2)},\ \phi_1^{(3)},\ w_2^{(3)},\ \phi_2^{(3)} \right\}^T,$$

where each superscript refers to the element number and the subscript refers to the local element node number. The vector $\mathbf{U}$ contains all four of the left beam displacements, one of the two link displacements (Note that only two are needed to fix the position of the link.), and three of the four right beam displacements. The missing displacements may be written in terms of those in $\mathbf{U}$. The missing link

Figure D-3: Beam-link-beam system of finite elements.

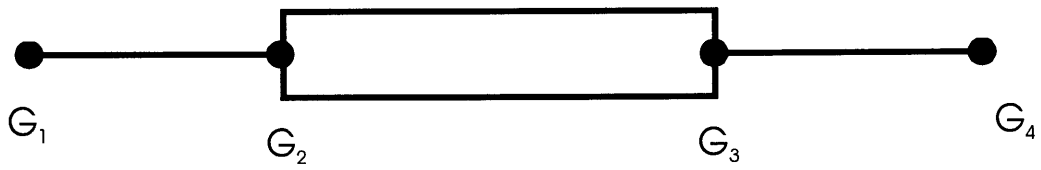

displacement is

$$w_1^{(2)} = w_2^{(1)}$$

from continuity of vertical displacement at G_2. The missing right beam displacement is

$$w_1^{(3)} = w_2^{(1)} - L^{(2)}\phi_1^{(2)} \tag{D.20}$$

from continuity of vertical displacement at both G_2 and G_3 and because the link is perfectly rigid.

The external forces applied to the system are contained in the global force vector

$$\mathbf{F} = \left\{ f_1, \quad m_1, \quad f_2, \quad m_2^-, \quad m_2^+, \quad m_3^+, \quad f_4, \quad m_4 \right\}^T, \tag{D.21}$$

where the ordering of $\mathbf{F}$ corresponds to $\mathbf{U}$. The notation convention is to use subscripts without super-

scripts in braces to refer to the global node number. The $\pm$ superscripts refer to moments applied just the right or left of the global node. For example, m_2^+ is the externally moment at G_2 applied to the link element.

My objective now is to solve

$$\mathbf{KU} = \mathbf{F}, \tag{D.22}$$

where $\mathbf{K}$ is the global assembly stiffness matrix. Because all but two of the forces (f_2 and m_2^+) are directly applied to the beam elements, I may set

$$\mathbf{F} = \left\{ \begin{array}{cccccccc} f_1^{(1)}, & m_1^{(1)}, & f_2, & m_2^{(1)}, & m_2^+, & m_1^{(3)}, & f_2^{(3)}, & m_2^{(3)} \end{array} \right\}^T,$$

where the forces are now expressed in the local beam element notation. I then use Eq.(D.15) derived in the previous section to write the forces applied to the beams in terms of the displacements in $\mathbf{U}$. For the right beam element, I need Eq.(D.20) to do this. This procedure determines the stiffness matrix coefficients in all rows except the third and fifth.

To solve for the relationship between f_2, m_2^+ and $\mathbf{U}$ (and for the coefficients in the third and fifth row of the stiffness matrix), I consider the linear and angular momentum balance of the link in detail. I do this carefully because there is some subtlety in the way that tension acts on the link.

A free-body diagram of the link is shown in Figure D.4. The linear momentum balance in the z direction is

$$f_2 - f_2^{(1)} - f_1^{(3)} = -\omega^2 M w_0, \tag{D.23}$$

and the angular momentum balance about its' center of mass is

$$\begin{aligned} & \underbrace{-\left(f_2^{(1)} + T_o\phi_2^{(1)}\right)b}_{1} + \underbrace{T_o\left(\phi_2^{(1)} - \phi_1^{(2)}\right)b}_{2} \\ & \underbrace{-\left(f_1^{(3)} + T_o\phi_1^{(3)}\right)\left(L^{(2)} - b\right)}_{3} + \underbrace{T_o\left(\phi_1^{(3)} - \phi_1^{(2)}\right)\left(L^{(2)} - b\right)}_{4} \\ & \underbrace{+m_2^+}_{5} + \underbrace{f_2 b}_{6} \\ = \; & -\omega^2 I_0 \phi_0, \end{aligned} \tag{D.24}$$

where the link center of mass displacements are w_0 and ϕ_0 and I've labeled the moment terms so I can refer to them individually.

Let's consider the first and second terms, which together represent the total moment imposed by the left beam element. The first term is due to the flexural shear force acting in the vertical direction with

Figure D-4: Free-body diagram of rigid link element.

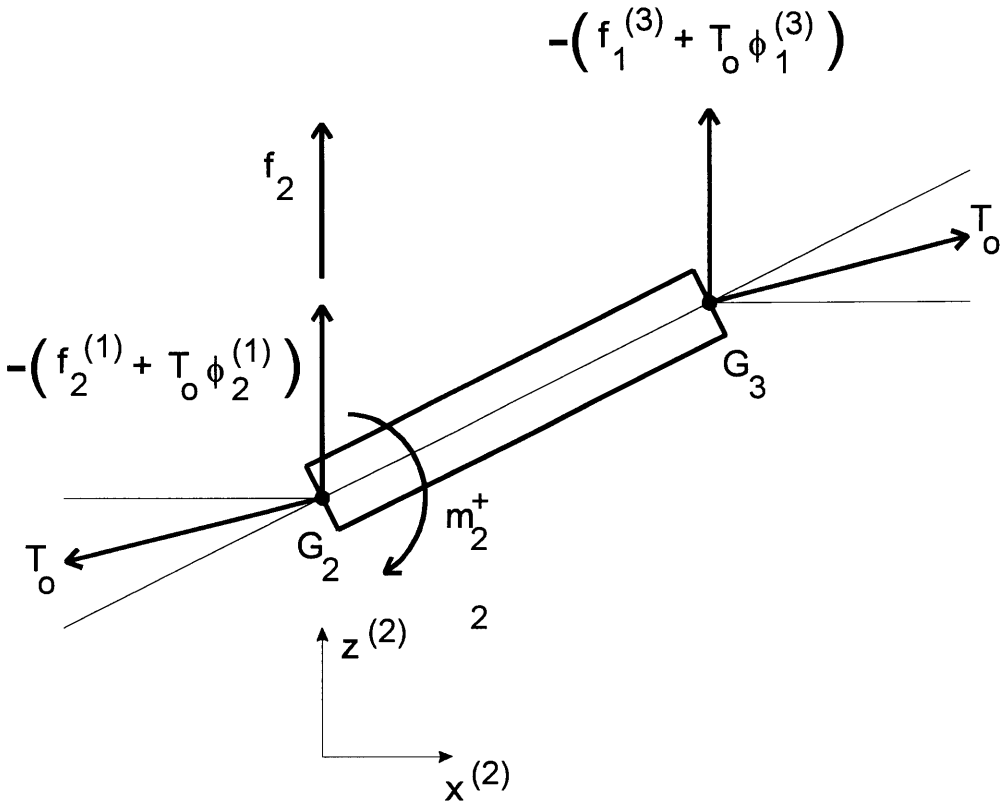

the vertical component of tension removed. The second term is due to both the vertical and horizontal component of tension acting at an angle of $\phi_2^{(1)}$ (see the free-body diagram in Figure D.4). For the pinned beam-link connection, $\phi_2^{(1)}$ is not generally equal to the link angle $\phi_1^{(2)}$ and the component of the tension normal to the link (the component that rotates the link) is proportional to the difference between these two angles. One might be tempted to say that the moment due to the left beam element is simply

$$-f_2^{(1)} b$$

but this does not consider the horizontal component of tension and is therefore not correct. The third and fourth terms are the corresponding moments due to the right beam element and are calculated in the same manner the first and second terms. The remaining fifth and sixth terms in Eq.(D.24) are self-evident.

To complete the assembly of the global matrix, I write Eq.(D.23) and Eq.(D.24) in terms of the global displacements contained in $\mathbf{U}$ and solve for f_2 and m_2^+. To do this I express the center of mass displacements as

$$w_0 = w_2 - b\phi_1^{(2)}$$

and

$$\phi_0 = \phi_1^{(2)},$$

assuming the link is perfectly rigid. Following these steps, the stiffness matrix for the pinned beam-link-beam element is

$$\mathbf{K} = \begin{bmatrix}
\mathbf{K}^{(1)}_{(1,1)} & \mathbf{K}^{(1)}_{(1,2)} & \mathbf{K}^{(1)}_{(1,3)} & \mathbf{K}^{(1)}_{(1,4)} & 0 & 0 & 0 & 0 \\
\mathbf{K}^{(1)}_{(1,2)} & \mathbf{K}^{(1)}_{(2,2)} & \mathbf{K}^{(1)}_{(2,3)} & \mathbf{K}^{(1)}_{(2,4)} & 0 & 0 & 0 & 0 \\
\mathbf{K}^{(1)}_{(1,3)} & \mathbf{K}^{(1)}_{(2,3)} & \mathbf{K}_{(3,3)} & \mathbf{K}^{(1)}_{(3,4)} & \mathbf{K}_{(3,5)} & \mathbf{K}^{(3)}_{(1,2)} & \mathbf{K}^{(3)}_{(1,3)} & \mathbf{K}^{(3)}_{(1,4)} \\
\mathbf{K}^{(1)}_{(1,4)} & \mathbf{K}^{(1)}_{(2,4)} & \mathbf{K}^{(1)}_{(3,4)} & \mathbf{K}^{(1)}_{(4,4)} & 0 & 0 & 0 & 0 \\
0 & 0 & \mathbf{K}_{(3,5)} & 0 & \mathbf{K}_{(5,5)} & -L^{(2)}\mathbf{K}^{(3)}_{(1,2)} & -L^{(2)}\mathbf{K}^{(3)}_{(1,3)} & -L^{(2)}\mathbf{K}^{(3)}_{(1,4)} \\
0 & 0 & \mathbf{K}^{(3)}_{(1,2)} & 0 & -L^{(2)}\mathbf{K}^{(3)}_{(1,2)} & \mathbf{K}^{(3)}_{(2,2)} & \mathbf{K}^{(3)}_{(2,3)} & \mathbf{K}^{(3)}_{(2,4)} \\
0 & 0 & \mathbf{K}^{(3)}_{(1,3)} & 0 & -L^{(2)}\mathbf{K}^{(3)}_{(1,3)} & \mathbf{K}^{(3)}_{(2,3)} & \mathbf{K}^{(3)}_{(3,3)} & \mathbf{K}^{(3)}_{(3,4)} \\
0 & 0 & \mathbf{K}^{(3)}_{(1,4)} & 0 & -L^{(2)}\mathbf{K}^{(3)}_{(1,4)} & \mathbf{K}^{(3)}_{(2,4)} & \mathbf{K}^{(3)}_{(3,4)} & \mathbf{K}^{(3)}_{(4,4)}
\end{bmatrix} \tag{D.25}$$

where

$$\mathbf{K}_{(3,3)} = \mathbf{K}^{(1)}_{(3,3)} + \mathbf{K}^{(3)}_{(1,1)} - \omega^2 M,$$

$$\mathbf{K}_{(3,5)} = +\omega^2 Mb - L^{(2)}\mathbf{K}^{(3)}_{(1,1)},$$

and

$$\mathbf{K}_{(5,5)} = -\omega^2\left(I_0 + Mb^2\right) + T_o L^{(2)} + \left(L^{(2)}\right)^2 \mathbf{K}^{(3)}_{(1,1)}.$$

The stiffness matrix has the same symmetry properties as the individual beam stiffness matrix.

D.2.2 Welded beam-link connections

The stiffness matrix for the welded beam-link-beam assembly is found directly from the results for the pinned boundary condition. I begin by imposing continuity of rotation at G_2 and G_3,which is equivalent to setting

$$\phi_2^{(1)} = \phi_1^{(2)}$$

and

$$\phi_2^{(2)} = \phi_1^{(3)}.$$

I then redefine the global displacement vector as

$$\mathbf{U} = \left\{ \begin{array}{cccccc} w_1^{(1)}, & \phi_1^{(1)}, & w_2^{(1)}, & \phi_2^{(1)}, & w_2^{(3)}, & \phi_2^{(3)} \end{array} \right\}^T \tag{D.26}$$

and global force vector as

$$\mathbf{F} = \left\{ \begin{array}{cccccc} f_1, & m_1, & f_2, & m_2, & f_4, & m_4 \end{array} \right\}^T. \tag{D.27}$$

The global stiffness matrix for the welded boundary conditions is derived from Eq.(D.25) by adding the stiffness matrix elements in columns adding (column-wise) columns four, five and six and then adding (row-wise) rows four, five, and six. This operation reduces the $8x8$ stiffness matrix for the pinned connections to a $6x6$ stiffness matrix for the welded connections. Consistent with the $\mathbf{U}$ and $\mathbf{F}$ in Eq.(D.26) and Eq.(D.27), the welded stiffness matrix is

$$\mathbf{K} = \begin{bmatrix} \mathbf{K}_{[1,1]}^{(1)} & \mathbf{K}_{[1,2]}^{(1)} & 0 \\ \left[\mathbf{K}_{[1,2]}^{(1)}\right]^T & \mathbf{K}_{[2,2]}^{(1)} + \mathbf{K}^{(2)} + \mathbf{T}^T\mathbf{K}_{[1,1]}^{(3)}\mathbf{T} & \mathbf{T}^T\mathbf{K}_{[1,2]}^{(3)} \\ 0 & \left[\mathbf{T}^T\mathbf{K}_{[1,2]}^{(3)}\right]^T & \mathbf{K}_{[2,2]}^{(3)} \end{bmatrix}, \tag{D.28}$$

where the rigid link stiffness matrix is

$$\mathbf{K}^{(2)} = \begin{bmatrix} -\omega^2 M & +\omega^2 Mb \\ +\omega^2 Mb & -\omega^2\left(I_0 + Mb^2\right) \end{bmatrix} + \begin{bmatrix} 0 & 0 \\ 0 & +T_o L \end{bmatrix}, \tag{D.29}$$

the transform matrix is

$$\mathbf{T} = \begin{bmatrix} 1 & -L^{(2)} \\ 0 & 1 \end{bmatrix}, \tag{D.30}$$

and I use subscripts in brackets to refer the $2x2$ submatrices of the beam element stiffness matrix.

D.3 The fixed-end absorber

A fixed-end absorber is a spring-mass-dashpot system used to dissipate vibrational energy of a beam or cable. Rather than attaching the end of the beam to a fixed inertial reference frame, the beam is attached to the absorber and the absorber is fixed to the inertial reference frame. The idea is to design the absorber such that it's impedance matches the beam impedance over some frequency band. If a perfect match is achieved then all incident wave energy is absorbed.

Figure D-5: Schematic of fixed-end absorber.

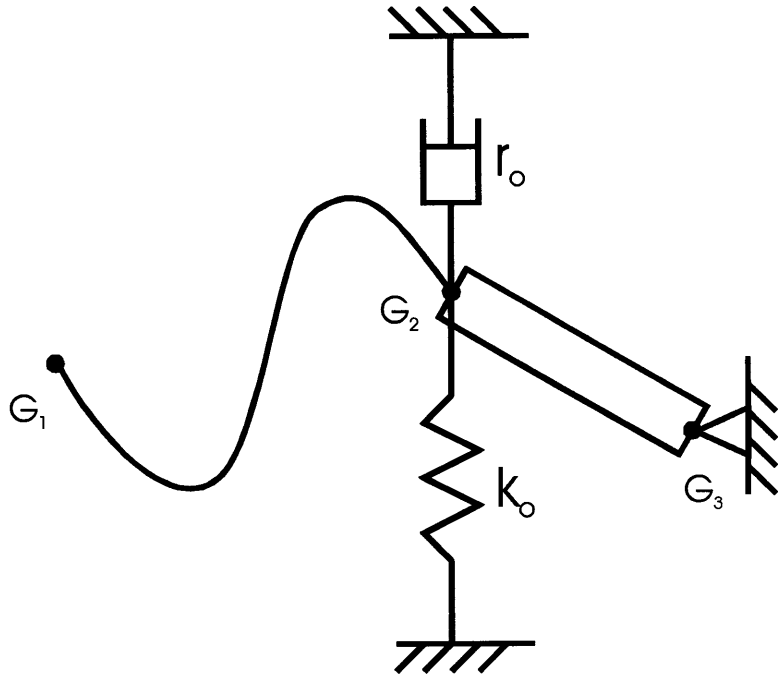

A schematic of a fixed end absorber is shown in Figure D.5. It is comprised of a beam that extends from G_1 to G_2 and a rigid link that extends from G_2 to G_3. The link is welded or pinned to the beam at G_2 and pinned to the inertial reference frame at G_3. In addition, a spring with spring constant k_o and a dashpot with damping constant r_o are attached to G_2 and the inertial reference frame. The absorber system is similar to the beam-link-beam system in the previous section and I use the same notation used for the beam-link-beam.

My objective in this section is to calculate the boundary conditions that the link imposes on the beam at G_2. I use these results in the following section to calculate reflection coefficients. I consider both the pinned and welded beam-link connection. The subtle factor is again how the tension acts on the link and it is addressed in the same manner as the previous section.

D.3.1 Pinned beam-link connection

Two conditions are needed to specify the boundary conditions at the end of a beam. By definition a pinned connection does not transmit moment and I may immediately specify one boundary condition as

$$m_2^{(1)} = 0. \tag{D.31}$$

The second boundary condition is found by considering the momentum balance of the link. The rotational momentum balance for the link about the fixed point G_3 is

$$\begin{aligned} & -\left(f_2^{(1)} + T_o\phi_2^{(1)}\right) L^{(2)} + T_o\left(\phi_2^{(1)} - \phi_1^{(2)}\right) L^{(2)} \\ & -\left(k_o - i\omega r_o\right) w_2^{(1)} L^{(2)} \\ = \; & -\omega^2\left(I_0 + M\left(L^{(2)} - b\right)^2\right)\phi_1^{(2)}, \end{aligned} \tag{D.32}$$

where I use the same notation as in the previous section. By using G_3 as the fixed point, then the reaction forces at G_3 do not enter the equations. Eq.(D.32) has terms that are similar to those in Eq.(D.24). Note that I have set the applied moment $m_2^+ = 0$, because it may be specified as an equivalent force and included in f_2. Also note that the applied force f_2 is replaced by the force due to the spring and dashpot. Because the link is fixed at G_3 and there is continuity of displacement at G_2, I can equate

$$w_1^{(2)} = w_2^{(1)} = \phi_1^{(2)} L^{(2)}.$$

These may be used to simplify the Eq.(D.32) and I may express the second boundary condition as

$$\mathbf{K}^{(2)} = \frac{-f_2^{(1)}}{w_2^{(1)}} \tag{D.33}$$

where I define the link stiffness as

$$\mathbf{K}^{(2)} = \frac{-f_2^{(1)}}{w_2^{(1)}} = \frac{T_o}{L^{(2)}} + k_o - i\omega r_o - \omega^2 m_o, \tag{D.34}$$

and the effective mass as

$$m_o = \frac{I_0 + M\left(L^{(2)} - b\right)^2}{\left(L^{(2)}\right)^2}.$$

The tension in the beam provides an additional stiffness term. The absorber parameters,k_o r_o, and m_o may be adjusted to any impedance at a single frequency.

D.3.2 Welded beam-link connection

The first boundary condition for a welded connection, by definition, is

$$\phi_2^{(1)} = \phi_1^{(2)} = \frac{w_2^{(1)}}{L^{(2)}}. \tag{D.35}$$

The second boundary condition is found by reconsidering the momentum balance of the link. Because the welded connection is able to transmit a moment between the beam and the link, Eq.(D.32) must be modified to include the additional moment $-m_2^{(1)}$ on the link due to the beam. The beam force and moment are then related to the link stiffness by

$$\mathbf{K}^{(2)} = -\left(\frac{m_2^{(1)}}{L^{(2)}} + f_2^{(1)}\right)\frac{1}{w_2^{(1)}}, \tag{D.36}$$

where $\mathbf{K}^{(2)}$ is still given by Eq.(D.34).

D.4 Reflection coefficients

To close this appendix, I now consider how to calculate the wave power reflection coefficient of the propagating wave on an infinitely long beam that encounters a discontinuity. The discontinuity may be either the rigid-link discussed in Section D.2 or the fixed-end absorber discussed in Section D.3. The procedure as outlined below applies to either case.

Let's consider a finite length beam element, which I'll designate as element one. On the right end of the beam is some type of attachment with a known impedance, which is given by two equations expressed in terms of some combination of the right end displacements and the right end forces. For the moment, I won't specify the left end boundary conditions. As derived earlier, the beam supports a right-going propagating wave with amplitude $A_1^{(1)}$, a right-decaying evanescent wave with amplitude $A_2^{(1)}$, a left-going propagating wave with amplitude $A_3^{(1)}$, and a right-decaying evanescent wave with amplitude $A_4^{(1)}$. The amplitudes of these waves are related to the force, moment, displacement, and rotation at the right end of the beam by

$$w_2^{(1)} = \mathbf{D}_{(3,1)}^{(1)}A_1^{(1)} + \mathbf{D}_{(3,2)}^{(1)}A_2^{(1)} + \mathbf{D}_{(3,3)}^{(1)}A_3^{(1)} + \mathbf{D}_{(3,4)}^{(1)}A_4^{(1)}, \tag{D.37}$$

$$\phi_2^{(1)} = \mathbf{D}_{(4,1)}^{(1)}A_1^{(1)} + \mathbf{D}_{(4,2)}^{(1)}A_2^{(1)} + \mathbf{D}_{(4,3)}^{(1)}A_3^{(1)} + \mathbf{D}_{(4,4)}^{(1)}A_4^{(1)}, \tag{D.38}$$

$$f_2^{(1)} = \mathbf{C}_{(3,1)}^{(1)}A_1^{(1)} + \mathbf{C}_{(3,2)}^{(1)}A_2^{(1)} + \mathbf{C}_{(3,3)}^{(1)}A_3^{(1)} + \mathbf{C}_{(3,4)}^{(1)}A_4^{(1)}, \tag{D.39}$$

and

$$m_2^{(1)} = \mathbf{C}_{(4,1)}^{(1)} A_1^{(1)} + \mathbf{C}_{(4,2)}^{(1)} A_2^{(1)} + \mathbf{C}_{(4,3)}^{(1)} A_3^{(1)} + \mathbf{C}_{(4,4)}^{(1)} A_4^{(1)}. \tag{D.40}$$

These relationships are given by the last two rows of Eq.(D.9) and Eq.(D.13). If I substitute these four equations into the right boundary condition equations, then I am left with two equations expressed in terms of the four unknown wave amplitudes. If I specify $A_1^{(1)} = 1$ and $A_2^{(1)} = 0$, then I simulate a source at negative infinity with no effect due to the right decaying evanescent wave. This allows me to solve for the remaining unknowns, $A_3^{(1)}$ and $A_4^{(1)}$. Finally, I may calculate the power reflection coefficient defined as

$$\gamma = \left| A_3^{(1)} \right|^2.$$

I may use the above approach to calculate the wave reflection characteristics of the fixed end absorber. The pinned boundary conditions are Eq.(D.31) and Eq.(D.31). The welded boundary conditions are Eq.(D.35) and Eq.(D.36). Because power is conserved, the power absorption coefficient of the absorber is

$$\alpha = 1 - \gamma.$$

I would also like to calculate the reflection due to a rigid link attached to an infinite beam. To do this, I need to modify the stiffness matrix of the beam-link-beam element. The first thing I do is attach a semi-infinite beam element to the G_4 node. I simulate this by adding the semi-infinite beam stiffness matrix given by Eq.(D.19) to the beam-link-beam stiffness matrix as calculated by either Eq.(D.25) or Eq.(D.28). If I assume that there are no external forces applied to G_2, G_3, and G_4, then the stiffness matrix may be reduced using the standard *condensation* procedure as described by Bathe [1]. The resulting $2x2$ condensed stiffness matrix is in a form that is suitable for using the procedure described above. If there is no viscous dissipation in the beam-link system and because power is conserved, the power transmission coefficient is

$$\beta = 1 - \gamma.$$

The reflection coefficients for the absorber and the beam-link system are calculated for both pinned and welded boundary conditions. The results are presented in the main text.

Appendix E

Dynamics of a beam with a rigid body attachment

In this appendix, I study wave propagation on tensioned-beams with a rigid body attachment (I also refer to the rigid body attachment as the link). The study is motivated by vortex induced vibration problems arising in cable suspension systems, such as the one shown schematically in Figure E-1. I analyze the beam-link system in terms of wave reflection coefficients using the methods developed in Appendix D. In this appendix, I use power reflection coefficients to analyze two different systems. The first is an infinite length beam with a single rigid body attachment. The second is a semi-infinite beam terminated with a rigid link attachment that is configured to absorb incident wave energy. I refer to the termination as the *fixed-end absorber*.

E.1 Contributions

Original contributions in this appendix and Appendix D include:

- Formulated WFEM stiffness matrix for a tensioned beam-link-beam system for both pinned and welded boundary conditions. Derived equations for calculating wave power coefficients for beam-link-beam system and the fixed-end absorber.
- Analyzed effect of boundary condition, link mass, flexural rigidity on beam wave transmission past a rigid link.
- Analyzed effect of boundary condition and flexural rigidity on performance (wave power absorption) of fixed-end absorber.

Figure E-1: Schematic of votex induced cable vibration due to fluid flow across instrumented cable mooring system.

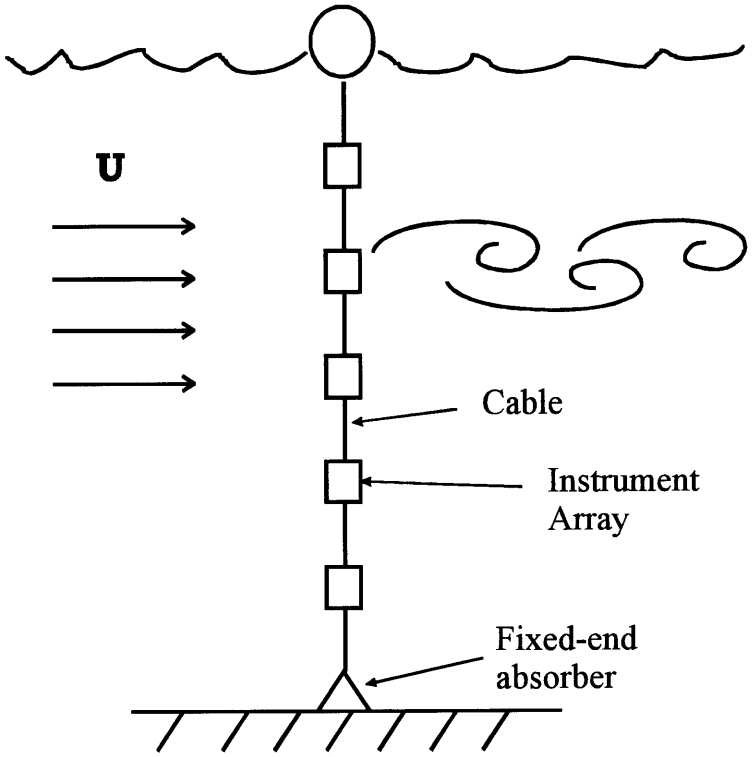

E.2 Wave transmission on an infinite beam with a single rigid body attachment

In this section, I study the behavior of waves on an infinitely long beam with a single rigid link attached as shown in Figure E-2. The beam properties and geometry are the same on both sides of the link. The beam has linear density ρ_c, longitudinal wave speed c_L, and radius of gyration r_g. The link is assumed to be a uniform slender rod of length L, mass M, and moment of inertia $I_o = ML^2/12$ about its' center of mass. The system supports an axial tension T_o and exists in a vacuum.

In Appendix D, I derive the equations governing such a system. In that analysis I make several assumptions. The system exists in a vacuum. The beam is modeled using classical theory with the usual modifications to include the effects of tension. The rigid link is perfectly rigid. All displacments are

Figure E-2: Infinite beam with single rigid link attachment.

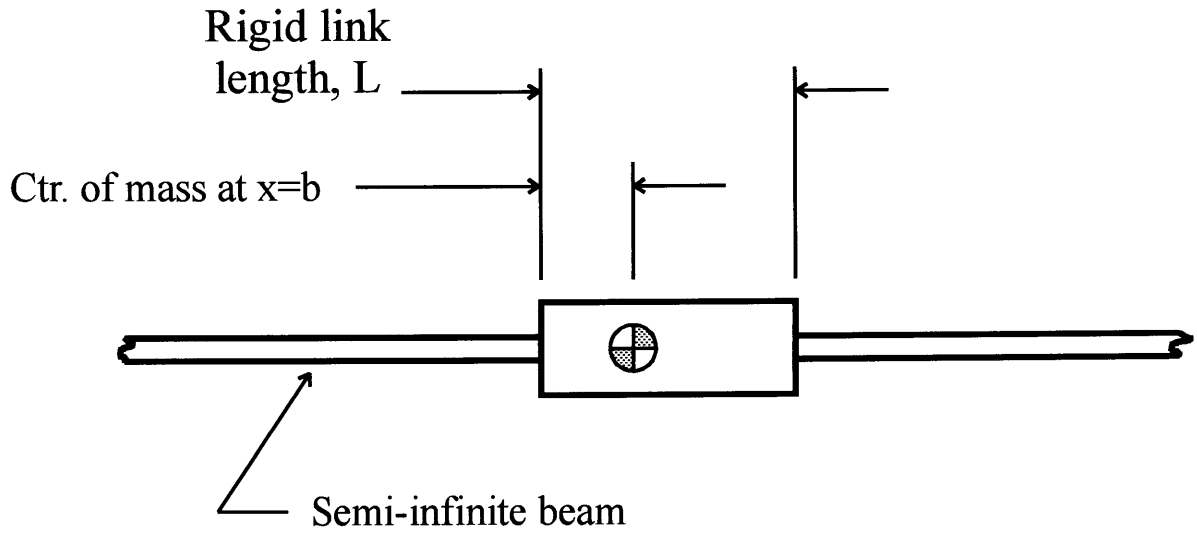

assumed small so that the tension remains constant at all times and the system is linear.

Also in Appendix D, I show that the tensioned beam supports two wave types, which I'll refer to as the propagating wave with wavenumber k_p and the evanescent wave with wavenumber k_e. I discussed how in the low frequency limit, the propagating wavenumber is equal to the string wavenumber

$$k_o = \frac{\omega}{c_o} = \frac{\omega}{\sqrt{\frac{T_o}{\rho_c}}},$$

while, in the high frequency limit, the propagating wavenumber is equal to the flexural wavenumber

$$k_f = \sqrt{\frac{\omega}{c_L r_g}}.$$

The transition between these two asymptotic values is defined by the critical frequency

$$\omega_c = c_o^2/c_L/r_g.$$

In other words, we know that tension effects always dominate at low enough frequency. The critical frequency defines that transition frequency at which tension effects begin to dominate. Beams with very high flexural rigidity have very low critical frequencies.

The cable system has three fundamental dimensions: length, time, and mass and six independent parameters: ω, ρ_c, c_o, ω_c, M, and L. According to the Buckingham Pi theorem, there are only three dimensionless parameters needed to completely describe the system. I find them by letting ρ_c, c_o, and L be the characteristic values and choose my system parameters to be the non-dimensional frequency

$$\Omega = \frac{\omega L}{c_o}, \tag{E.1}$$

the non-dimensional critical frequency

$$\Omega_c = \frac{\omega_c L}{c_o}, \tag{E.2}$$

and non-dimensional rigid body mass

$$M_o = \frac{M}{\rho_c L}. \tag{E.3}$$

I choose L rather than r_g as my characteristic length because I am looking at the problem from the perspective of how does flexural rigidity alter or perturb the performance of cables. The unperturbed system has a value of $r_g = 0$ and I therefore do not want to use it to normalize anything.

In physical terms, when Ω approaches unity (I hereafter refer to the non-dimensional frequency as just the frequency and likewise for the critical frequency and the link mass) the wavelength as predicted by string-theory is about the length of the link. As discussed earlier, the critical frequency Ω_c is the frequency at which the sound speed of the beam transitions from being tension dominated to flexure dominated (only now it is expressed relative to the non-dimensional frequency). The link mass, M_o, is the ratio of the rigid body mass to the length of cable it replaces, which is greater than one under ordinary circumstances.

I can now use the equations derived in Appendix D to calculate wave transmission for the cable system by analyzing the full range of the three parameters for this system. I do this by calculating the transmission for four different beams with critical frequencies $\Omega_c = .1$, 1, 10, and 100, attached to three different links with $M_o = 1$, 10, and 100. Because I consider both a welded and pinned connection for each beam-link combination, there are a total of 24 cases. I analyze each case over a wide frequency range within which all variations in the transmission are observed.

The range of parameters are carefully selected. It will be seen that the $\Omega_c = 100$ beam exhibits stringlike behavior and represents one extreme. The beam with $\Omega_c = .1$ represents the other extreme of a cable with an extremely high flexural rigidity. It does not represent a beam with essentially zero tension, although, the equations derived in the previous appendix are valid up to $\Omega_c = \infty$. I am interested in this problem from the perspective of cable design and therefore limit the critical frequency to practical levels.

The link masses are also chosen to encompass the full range of practical cable designs. The link mass of $M_o = 1$ represents the lower bound because it is unlikely that the link mass would be less than the mass of the cable it replaces. A link mass of $M_o = 100$ represents the upper bound that is possible due to heavy fluid loading. In a typical scenario, the rigid body represents an instrument of some sort attached to the cable.

E.2.1 Nominal link mass

Let's consider the "nominal" link mass of $M_o = 10$ first. The power transmission curves for the welded beams are plotted in Figure E-3a. The figure has four plots corresponding to the four critical frequencies. The curves show a convergence in the transmission for increasing critical frequency. Because the difference between the $\Omega_c = 10$ and $\Omega_c = 100$ beams is negligible, the effect of flexural rigidity is negligible and the $\Omega_c = 100$ beam is essentially a string.

Let's consider the $\Omega_c = 100$ beam curve more closely. At low frequency, there is perfect transmission. The beam does not sense the attached mass until it reaches a frequency at which the mass of a wavelength of cable is on the order of the mass of the link, which is mathematically expressed as

$$\Omega = O\left(M_o^{-1}\right). \tag{E.4}$$

Near this frequency the mass begins to impede the displacement of the beam and a portion of the incident wave is reflected. At a somewhat higher frequency, the impedance looking into the left end of the link matches the impedance of the incidence wave and there is perfect transmission. Li and Vandiver ?? identified this as a *rocking resonance* and showed that for a string it occurs at

$$\Omega_{r,string} = \frac{\sqrt{12(M_o - 1)}}{M_o}. \tag{E.5}$$

Beyond the rocking resonance, at even higher frequency, the impedance of the mass is large and there is perfect reflection of the incident wave.

In comparison to $\Omega_c = 100$, increased flexural rigidity has several effects. It dramatically increases the

Figure E-3: Power transmission coefficient versus frequency for nominal link mass.

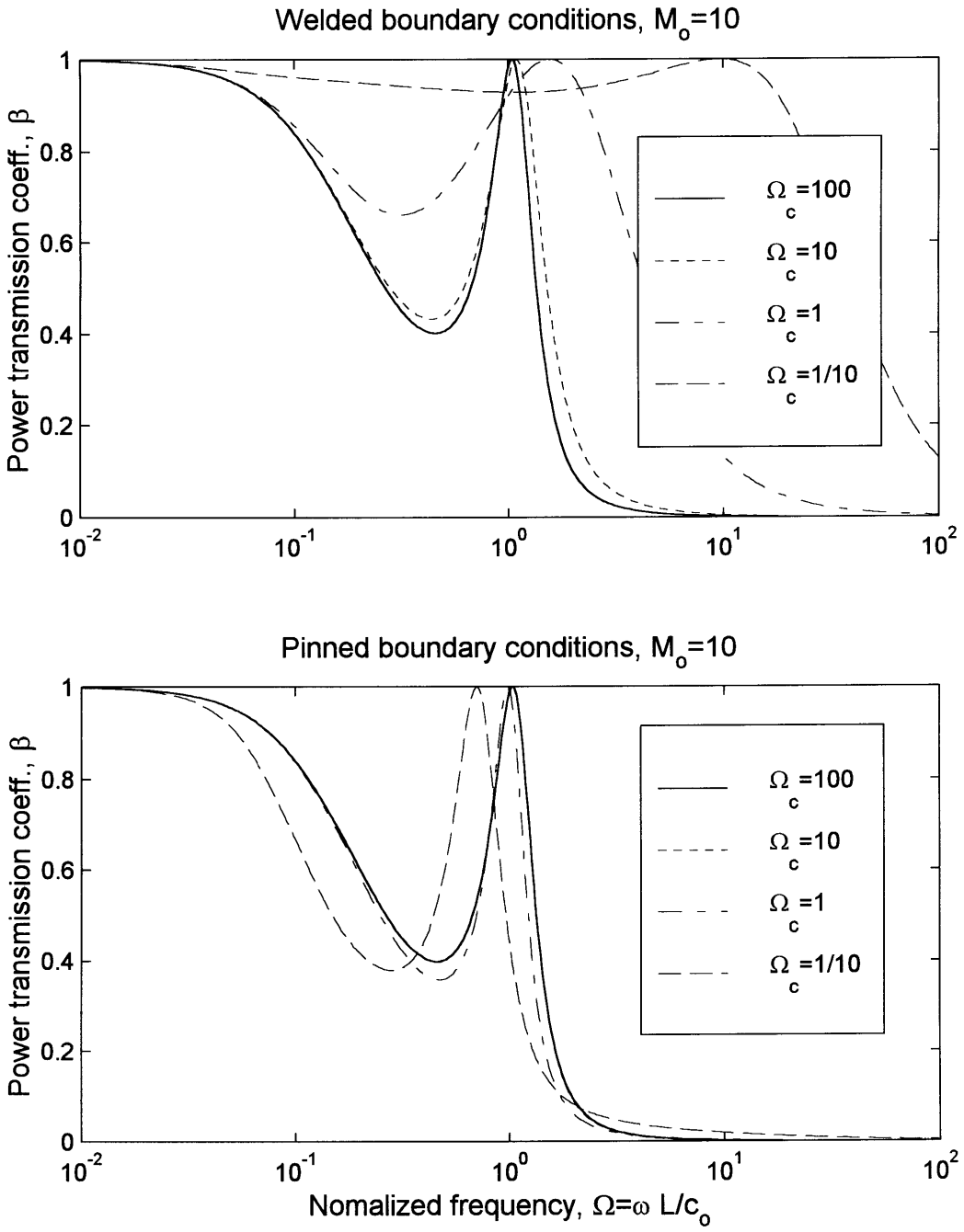

total integrated transmission by increasing both the rocking frequency and the minimum transmission below the rocking frequency. For the $\Omega_c = .1$ beam, the beam with highest flexural stiffness, the rocking resonance is roughly a decade above the string rocking frequency and the transmission coefficient is nearly unity at all frequencies below the rocking frequency. It is evident that the string model breaks down at a frequency beginning at $\Omega > \Omega_c/10$ for $\Omega_c \leq 1$.

The transmission curves for the pinned boundary condition are plotted in Figure E-3b. A comparison of the $\Omega_c = 100$ beam both the welded and pinned connection shows that they are both essentially the same. This convergence to the string case with increasing critical frequency provides a check that the model is correctly implemented. Figure E-3b shows that the effect of increased flexural stiffness for a pinned connection is much less than that for the welded connection. The rocking resonance is shifted downward slightly compared to the upward shift for the welded case. It is clear that the beam presents a spring-like stiffness for the welded connection and a mass-like stiffness for the pinned connection. Also, the minimum transmission frequency below the rocking frequency is not increased significantly in contrast to the welded beam. The string model breaks down for $\Omega_c \leq .1$, an order of magnitude lower than that for the welded beam.

The boundary condition effects may be understood by looking at the stiffness matrix, $\mathbf{K}$, of a semi-infinite length beam (see Eq.(D.19) in Appendix D). The imaginary part of the stiffness matrix represents a dissipative mechanism, the positive real part represents a spring-like character, and the negative real part represents a mass-like character. Looking at Eq.(D.19), it is clear that the only spring-like element is $\mathbf{K}_{(2,2)}$. Because the welded boundary condition,

$$\phi = -\frac{w}{L},$$

requires that the beam rotate as it displaces, the beam stiffness is dominated by the $\mathbf{K}_{(2,2)}$ term and the resonance of the beam-link system increases. For the pinned boundary condition, the beam may displace without rotation, the beam stiffness is dominated by the mass-like $\mathbf{K}_{(1,1)}$ term and the resonance is shifted downward. It may be intuitive that a semi-infinite beam is mass-like to a point load and spring-like to a point moment. We shall see shortly that the trend of lower transmission for the pinned connection and higher transmission for the welded connection compared to the string model holds for the entire range of link mass and critical frequencies explored in the present analysis.

E.2.2 Low link mass

Now, let's consider the low link mass of $M_o = 1$. The power transmission curves for the welded boundary condition are plotted in Figure E-4a. The convergence in the transmission with increasing critical

frequency to the string model is again evident. Eq.(E.5) correctly predicts that there is no rocking resonance for the string when $M_o \leq 1$. But there is still perfect transmission at low frequency and perfect reflection at high frequency for the same reasons stated above. Li [tbd] showed that the string model predicts that the power transmission is exactly one half at

$$\Omega\left(\beta = .5\right) = \Omega_{1/2} = \frac{6}{M_o}.$$

The transmission increases for beams with higher flexural stiffness because the wavelengths are longer. Therefore, $\Omega_{1/2}$ is also higher. The string model breaks down at $\Omega_c \leq 1$.

The power transmission for the pinned boundary condition are plotted in Figure E-4b. As we now expect, the total transmission is decreased and $\Omega_{1/2}$ occurs at a lower frequency. The effect of the added mass of the beam is now more pronounced because it is a larger percentage of the link mass. The string model breaks down at $\Omega_c \leq 1$. The rocking resonance reappears for both the $\Omega_c = 1$ and the $\Omega_c = .1$ beams. Also, there is second peak occurring near $\Omega = 100$ for the $\Omega_c = .1$ beam.

E.2.3 High Link Mass

The final link mass I consider is $M_o = 100$. The power transmission curves for the welded boundary and pinned boundary conditions are plotted in Figure E-5a and Figure E-5b, respectively. The same trends observed for the $M_o = 10$ case are evident. The welded beams exhibit higher rocking frequencies and greater transmission than the string model, while the pinned beams have lower rocking frequencies and lower transmission. For the pinned beams, the added beam mass is negligible compared to the large link mass and the effect of increased flexural stiffness is negligible even at $\Omega_c = .1$.

E.3 The Fixed End Absorber

In many marine applications, extremely long cables are used. This may be due to the desire to extend the resolution of a sensor array or the need to reach the ocean floor for mooring purposes. In any case, the use of long cables is not often limited by the great expanse of the ocean. The vibration modes for long cables are very closely spaced and generally the response to vortex induced vibration is wave dominated. Attempts to move modes out band by modifying the boundary conditions at the ends of the cable are futile either because the boundary conditions have little effect on the resonance location or by moving one mode out of band, another mode moves into band. An alternative approach to reduce vibration is to attach an absorber to one or both ends of the cable. If the absorber impedance is perfectly matched to the cable impedance at the center or strumming frequency of the VIV, then all incident wave energy at

Figure E-4: Power transmission coefficient versus frequency for low link mass.

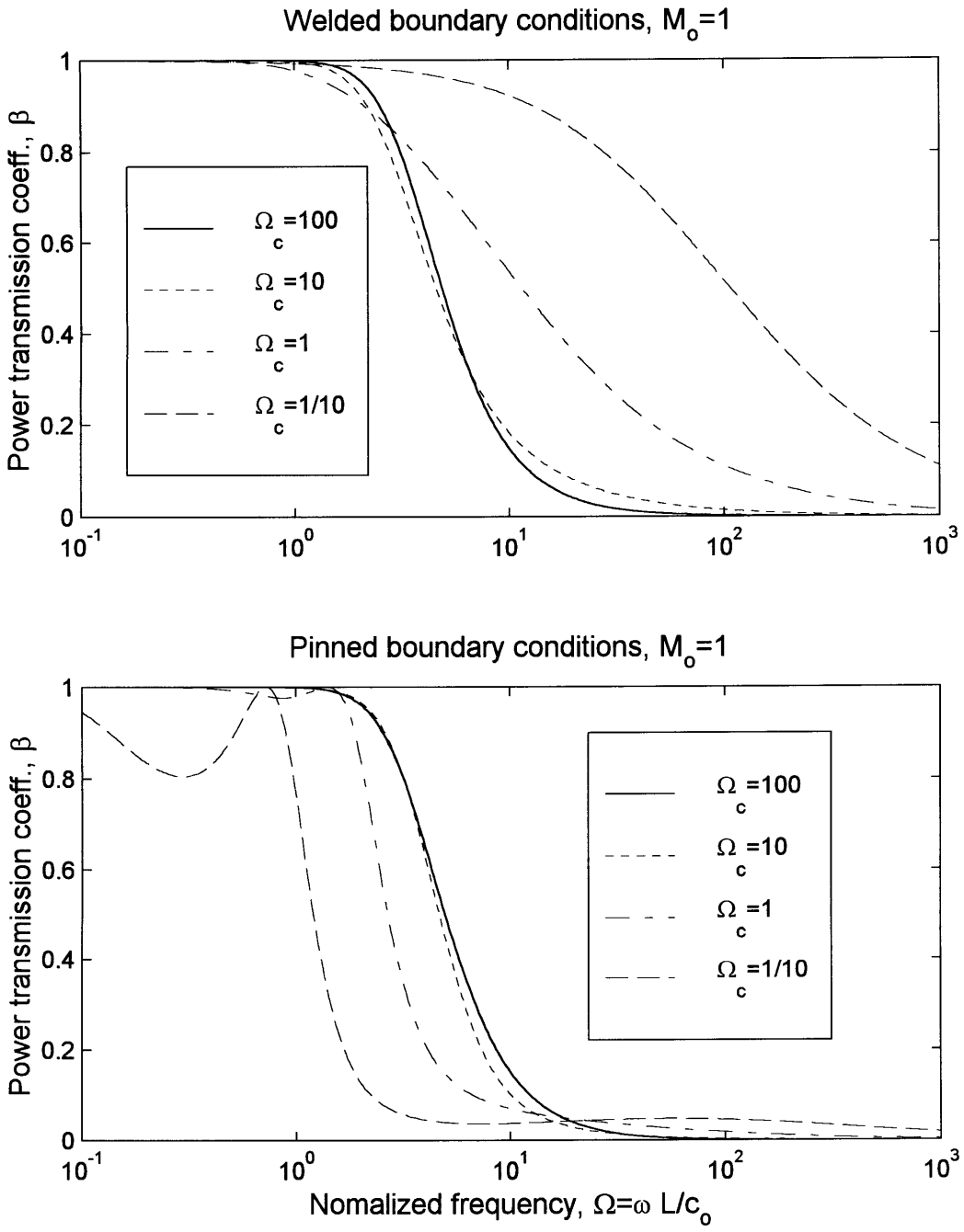

Figure E-5: Power transmission coefficient versus frequency for high link mass.

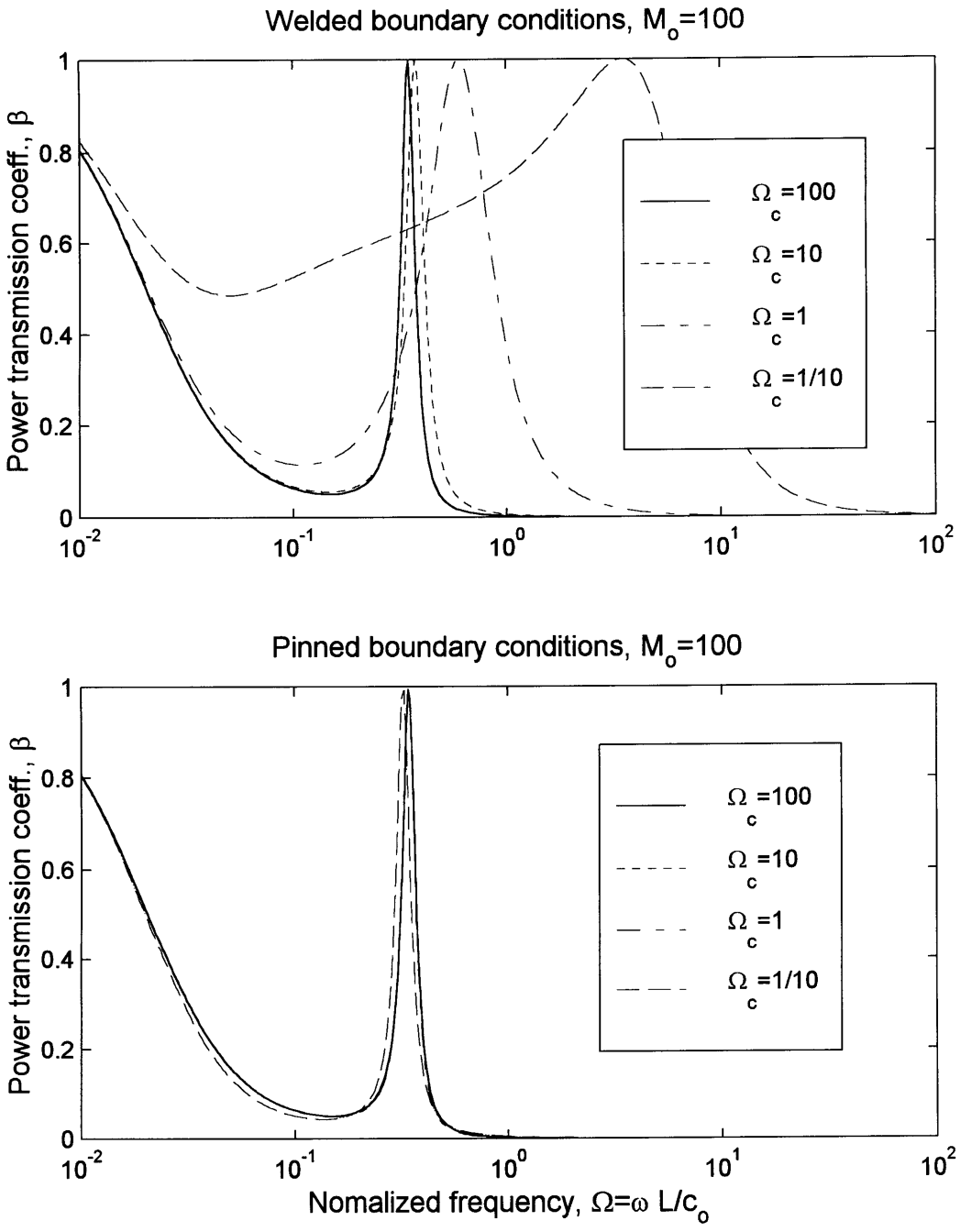

that frequency is absorbed. When the absorber is attached to fixed inertial reference frame, it is referred to as a *fixed end absorber*, which is the focus of the present section.

In a series of papers, Li and Vandiver studied the behavior of the fixed end absorber. A figure of the absorber is shown back in Appendix D-5. As shown in the figure, the cable is attached to a slender rigid link of uniform density, which is either welded or pinned to the cable-link connection and pinned to ground at the other end. A parallel combination of a mechanical spring having spring constant k_o and a dashpot having resistance r_o are also attached. The link provides mass so that the absorber is a spring-mass-dashpot combination, whose parameters may be varied to provide a generally specified impedance at a particular frequency.

The performance of the absorber was analyzed in detail by Li and Vandiver. They derived closed form solutions for optimum performance. My work is an extension of theirs with several objectives best defined by posing the following questions:

- How does the flexural stiffness in the cable degrade the performance of the optimized absorber? The scenario being that the ocean engineer is optimizing the absorber performance based on the string model with no knowledge of the flexural stiffness. When does he or she get into trouble?
- How do the boundary conditions effect the performance? By using the tensioned beam model for the cable I am also able to study the effect of the boundary condition at the beam-link connection. I choose to limit this to the usual pinned (moment free) and welded (continuous displacement and rotation) cases.
- If the flexural stiffness is known, is it possible to reoptimize the absorber parameters? Is the performance of the reoptimized absorber improved?
- Since it is always true that at low enough tension, flexural effects are important, and it is most likely that we are interested in this problem because of VIV, then at what tension are flexural effects important?

To answer these questions I use peak power absorption and bandwidth as my performance metrics, which are the same metrics used by Li and Vandiver. The derived equations, however, may be used to find the optimum performance in terms of peak stress or displacement.

Before looking at some results, I need to define two new parameters. They are the dimensionless absorber stiffness

$$K_o = \left(\frac{k_o L}{\varrho_c c_o^2} \right)$$

and the dimensionless dashpot constant

$$R_o = \left(\frac{r_o}{\varrho_c c_o} \right)$$

which are normalized by the same characteristic values used in the infinite beam study.

E.3.1 String Model Results

Here I present a summary of Li and Vandiver's results, which forms a the basis of my own analysis. I present their results using my own notation. When the cable is modeled as a string the power absorption coefficient, defined as the powered absorbed divided by the incident power, is

$$\alpha = \frac{4R_o}{(R_o+1)^2 + \left(\frac{\Omega_o M_o}{3}\right)^2 \left(\frac{\Omega_o}{\Omega} - \frac{\Omega}{\Omega_o}\right)^2}, \tag{E.6}$$

where

$$\Omega_o = \left[\frac{1+K_o}{\left(\frac{M_o}{3}\right)}\right]^{\frac{1}{2}} \tag{E.7}$$

is the absorber resonance frequency. Eq.(E.6) and Eq.(E.7) apply for a slender rigid link with uniform density, which has an effective mass (normalized by the left end link displacement) of $M_o/3$. At $\Omega = \Omega_o$, the power absorption has a peak value of

$$\alpha_p = \frac{4R_o}{(R_o+1)^2}. \tag{E.8}$$

It is clear that the peak absorption is maximum when $R_o = 1$. Li defines the loss factor as

$$\eta = \frac{\Omega_2 - \Omega_1}{\Omega_o}, \tag{E.9}$$

where

$$\Omega_1 = \Omega\left(\alpha = \frac{1}{2},\ \Omega < \Omega_o\right)$$

and

$$\Omega_2 = \Omega\left(\alpha = \frac{1}{2},\ \Omega > \Omega_o\right).$$

This definition erroneously leads to the conclusion that increased damping is not beneficial and that the optimum absorber design based on peak power absorption is when $R_o = 1$. A more accepted definition of loss factor is defined by letting

$$\Omega_1 = \Omega\left(\alpha = \frac{\alpha_p}{2},\ \Omega < \Omega_o\right) \tag{E.10}$$

and

$$\Omega_2 = \Omega\left(\alpha = \frac{\alpha_p}{2},\ \Omega > \Omega_o\right). \tag{E.11}$$

I will use this general definition of loss factor not only for the analysis of the string but also for beams as well. Using Eq.(E.11) and Eq.(E.10), the redefined loss factor for the string is

$$\eta = \frac{R_o + 1}{\Omega_o \left(\frac{M_o}{3}\right)}. \tag{E.12}$$

To measure absorber performance, I may define a total power absorption (or total absorption) in a general way as

$$\Pi_t = \int_{\Omega=0}^{\Omega=\infty} \alpha \, d\Omega,$$

which for the string model is approximately

$$\Pi_t = \eta \cdot \alpha_p = \frac{4R_o}{\Omega_r \left(\frac{M_o}{3}\right)(R_o + 1)}.$$

The total absorption increases with increased damping but with diminishing returns for large R_o. It is also clear that lower link masses also increases the total absorption.

E.3.2 Optimally designed absorber

The criteria for an optimum absorber, therefore, depends on the problem at hand. If the excitation is narrowband about some center frequency, then the optimum absorber would be designed to resonant at that frequency and to maximize the peak absorption. As shown by Li and Vandiver, the maximum peak absorption for a string occurs when $R_o = 1$. However, if the excitation is broadband or if it is narrowband whose center is not well known (known only to within a wideband due to either variable environmental conditions or unknown variations in the performance of the absorber itself), then it may be better to let $R_o > 1$ to increase the total absorption at the cost of lower maximum peak absorption. In either case, the optimum damping is always greater or equal to unity. Having said all this, I hereafter will consider only the narrowband case with $R_o = 1$ and refer to it as *the* optimized absorber.

E.3.3 An example

To improve our understanding of the string model results, let's look at a specific example. Consider an absorber that has $M_o = 10$, $K_o = 7/3$, and $R_o = 1$. Using Eq.(E.7), this absorber resonates at $\Omega_o = 1$.

To see how the absorber performance depends on damping, I plot the absorption versus frequency for the nominal $R_o = 1$ damping constant and two additional damping constants, $R_o = 1/2$ and $R_o = 2$, in Figure E-6a. It is clear that the maximum peak absorption occurs for $R_o = 1$. Decreased damping lowers the peak absorption and lowers the bandwidth, while increased damping lowers the peak absorption and

increases the bandwidth.

To see how the performance depends on the link mass, I plot the absorption for the nominal $M_o = 10$ link mass and two additional link masses, $M_o = 5$ and $M_o = 20$, in Figure E-6b. Clearly, greater bandwidth is inversely related to link mass. These relationships are the same as a simple single degree of freedom oscillator. The only difference being that the stiffness of the cable-link system has an additional term $T_o/L = 1$ appearing in Eq.(E.7). This term is due to tension and the discontinuity in slope between the link and the cable.

E.3.4 Degradation of the optimally designed absorber

What errors are incurred by ignoring the effects of flexural rigidity and using the string model rather than the beam model? How do they depend on the boundary conditions? I can use the equations derived in the Appendix D to answer these questions using the example just considered.

In Figures E-7a, E-7b, and E-7c, I plot the absorption versus frequency for welded and pinned beams with successively decreasing critical frequencies of $\Omega_c = 10$, 1, and .1 (or successively increasing flexural stiffness). In each figure there are three curves representing the absorption for the string model and the absorption using the beam model with both the welded and pinned beam-link connections. Let's consider them one at a time.

In Figure E-7a, the critical frequency for both beams is $\Omega_c = 10$, which is a decade above the absorber resonance (as calculated using the string model) and well outside the absorber bandwidth. The absorption for all three cables are essentially the same. Clearly, the effect of both the boundary conditions and flexural rigidity is negligible under these conditions.

In Figure E-7b, the critical frequency for both beams is $\Omega_c = 1$, which is now equal to the absorber resonance. The resonance for the welded beam (defined as the peak in the absorption curve) is shifted upward and its peak level is less than unity. The pinned beam absorption is, however, essentially the same as the string model. Its resonance is shifted slightly downward and its peak level is also decreased slightly.

In Figure E-7c, the critical frequency for both beams is $\Omega_c = .1$, which is a decade below the absorber resonance. The trends established in Figure E-7b continue for both the welded and pinned beams. For the welded beam, there is a significant shift in the resonance and the peak absorption is nearly zero. For the pinned beam, the shift in the resonance is significant but the peak absorption is only slightly changed.

The observed trends in these figures are consistent with those observed in the transmission curves for the infinite beam system presented earlier. The upward shift in the resonance frequency for the welded beam and the downward shift for the pinned beam are due to the fact that the input impedance is stiffness

Figure E-6: Absorber performance for a.) fixed R_o and varied M_o and b.) fixed M_o and varied R_o. All cases shown are a string.

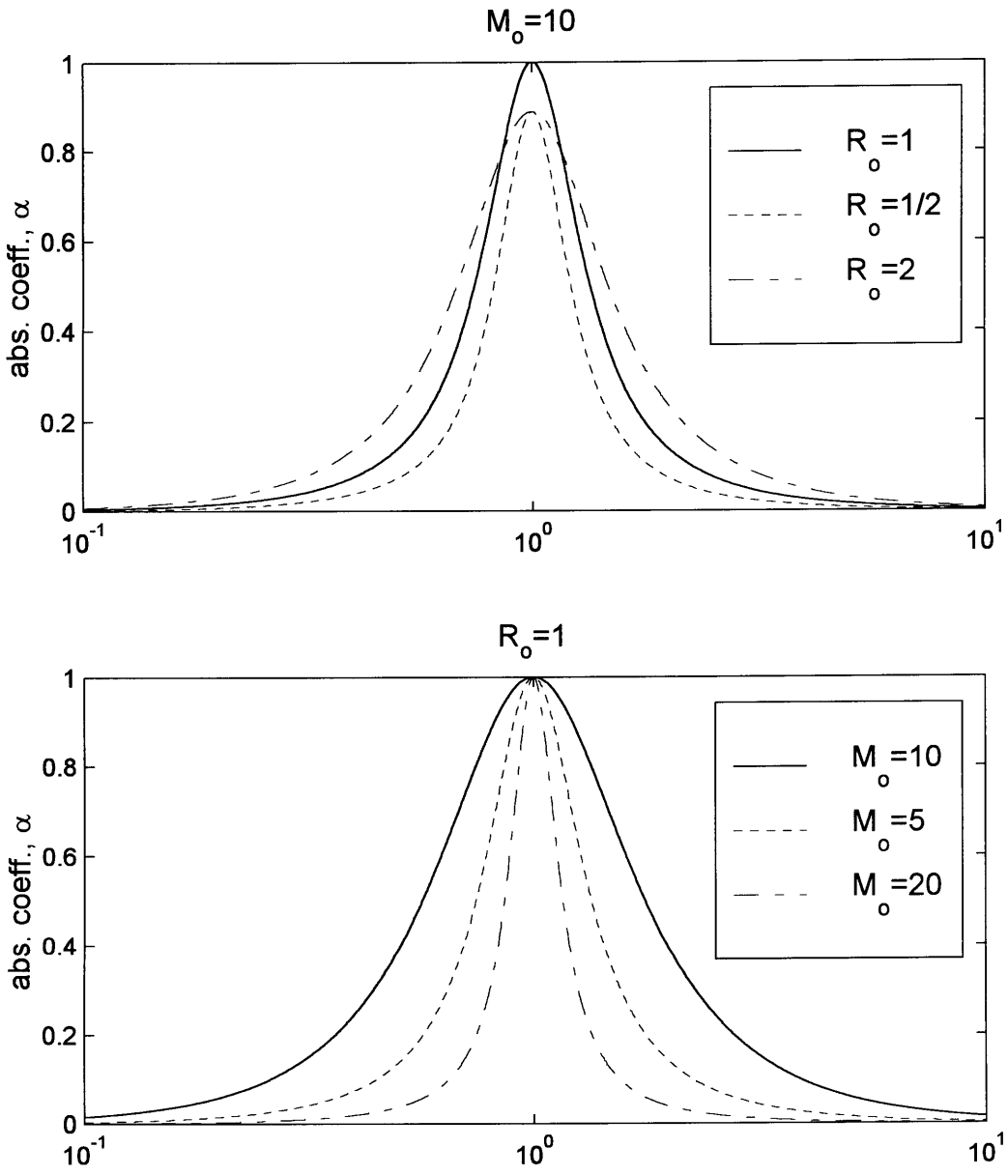

Figure E-7: Degradation of absorber performance for a.) $\Omega_c = 10$, b.) $\Omega_c = 1$, b.) $\Omega_c = 1/10$ and for both welded and pinned boundary conditions.

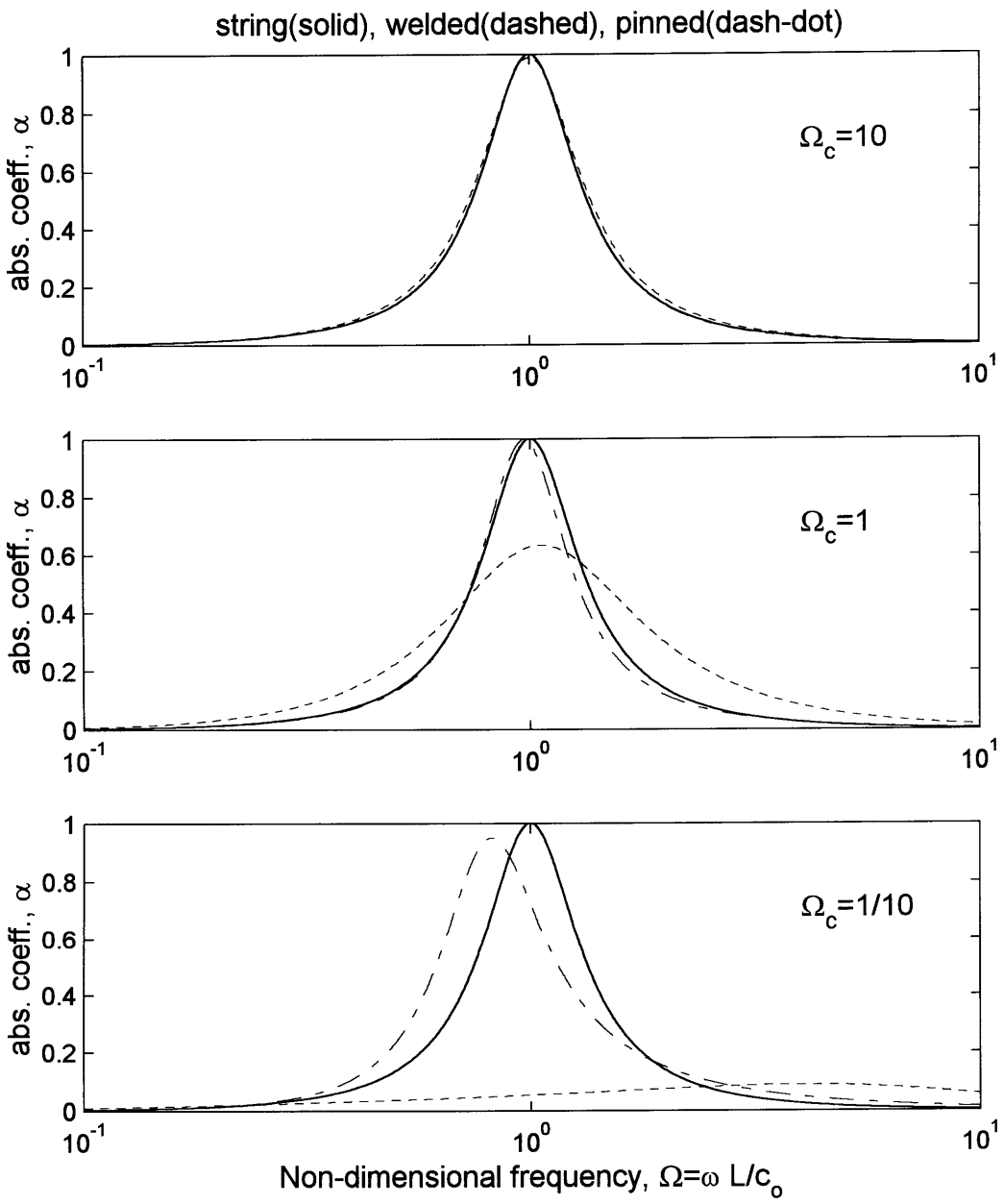

dominated in the former case and mass dominated in the latter case. I expect the peak absorption to be less than one because the cable and absorber impedances are no longer perfectly matched. From these results, I conclude that provided the critical frequency is a decade above the resonance frequency and not within the upper bandwidth of the absorber, then the effects of both flexural rigidity and the type of boundary condition at the cable-link connection is negligible.

E.3.5 Reoptimized absorber

If the critical frequency of the cable is known, then the absorber can be reoptimized, that is, the absorber can be designed to achieve perfect absorption at a desired frequency. This is simply because an the absorber can match the beam impedance at any single frequency. It is not immediately clear, however, how the absorber parameters must be varied to achieve a reoptimized design and what is the reoptimized bandwidth. I address these questions here.

Let's first consider the sample problem of an absorber with a given link mass of $M_o = 10$ and a cable with a known critical frequency of $\Omega_c = 1$. I would like to know the *reoptimized* spring and damping constants such that the absorber resonates at $\Omega_o = 1$ and has $\alpha_p = 1$. I may use the equations derived in Appendix D to find that $R_o = 4.05$ and $K_o = 1.85$ compensate for the effects of flexural rigidity. In comparison, $R_o = 1$ and $K_o = 7/3$ for a cable with an infinite critical frequency (a string). The absorptions for these two cases are plotted in Figure 6.8. The reoptimized resistance is higher because the cable resistance is higher and the reoptimized spring constant is lower because the cable reactance is lower. The bandwidth for the two cases is $\eta = .60$ to $\eta = 2.20$. This is an increase by a factor of 3.7, which is roughly the increase in the ratio of the damping constants.

In practice, reoptimization might be difficult. While it is possible to back out the critical frequency by measuring the cable tension, linear density, and sound speed from impact tests, the critical frequency is most likely is a complex function of the tension in the cable and environmental factors, such as temperature and the viscosity of the surrounding fluid. Another unknown is the boundary condition at the cable-link connection. Rarely is a connection either a perfect pinned or welded connection. Based on the results of this section, however, if it is suspected that flexural rigidity is important and the absorber has been designed based on a string model, then the cable-link connection should be designed to be as close as possible to a pinned connection.

Figure E-8: Comparison of optimized absorber attached to a string, unoptimized absorber attached to a beam with significant flexural rigidity, and reoptimized absorber attached to that same beam.

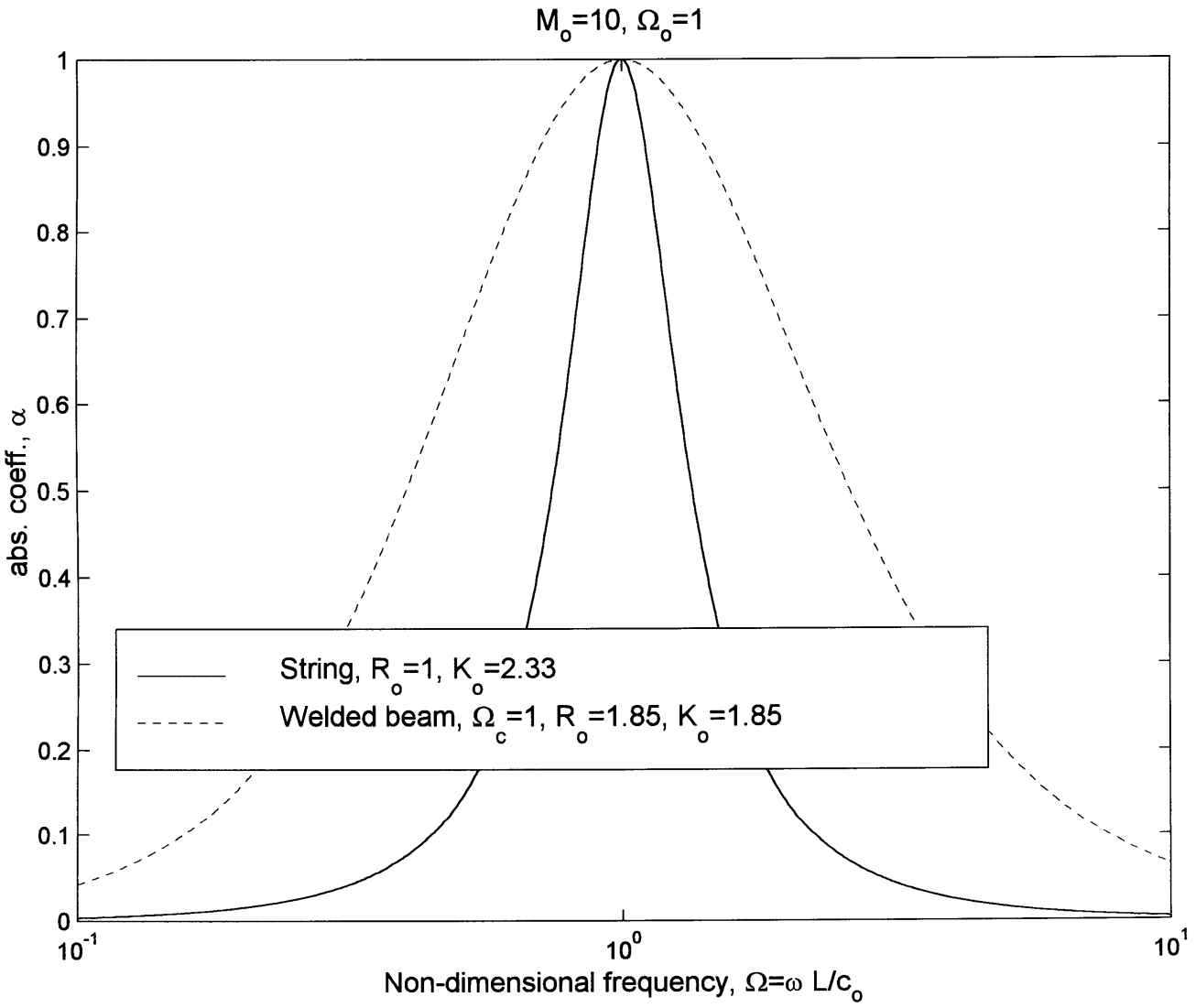

Appendix F

Acoustic scattering from an infinitely long cylindrical shell with bulkhead and deck attachments

F.1 Introduction

In this appendix, I consider a cylinder with an infinitely extended, heavy fluid surrounding the shell exterior. Any such problem connot be solved using the WFEM method without some type of approximation. The reason is that the infinite fluid introduces a branch point in the complex wavenumber plane at the fluid wavenumber. The contribution of the branch cut in the wavenumber integration is not negligible. Because it is not possible to include the branch cut contribution in the WFEM method, one has to resort to the straightfoward wavenumber integration.

F.2 Method of solution

The problem I consider is the steady-state scattering from an infinitely long cylinder due to an acoustic plane wave with radial frequency ω. The exterior of the cylinder is loaded by a heavy fluid medium, while the interior is a vacuum. The new aspect of this analysis is that the cylinder has structural discontinuity in both the axial and circumferential directions. These discontinuities are produced by two wave bearing plate attachments as shown in Figure F-1. The first is a circular plate, which I will refer to as the bulkhead. The second is a rectangular plate, which I refer to as the deck. The bulkhead and deck

Figure F-1: Geometry and coordinate system of the shell scattering problem.

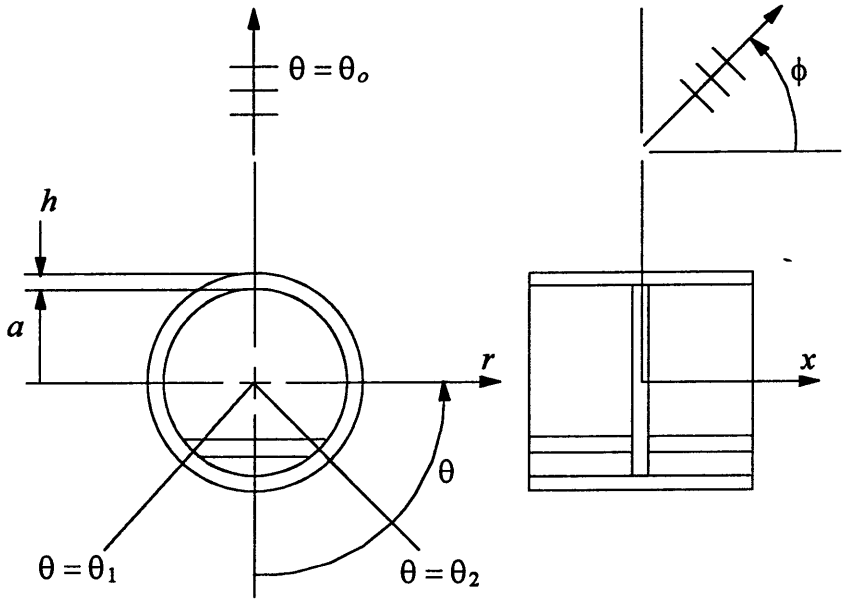

are not attached to each other and (miraculously) do not interfere with each other. Their only path of communication is through the shell.

The cylinder, shown in coordinate system $\{x, \theta, r\}$, has radius a, thickness h, and is made from a linear elastic solid with Young's modulus E, density ρ, and Poisson's ratio ν. Both the bulkhead and the deck have the same properties and thickness as the shell. The sides of the deck are welded to the shell at θ_1 and θ_2. The bulkhead is welded to the shell at $x = 0$. The exterior fluid has sound speed c_o and density ρ_o. The incident plane wave is travelling in the θ_o direction and inclined at an angle of incidence ϕ from the cylinder axis. If I let $\theta_o = 0$, then $\theta = \pi$ is the backscatter direction. If I let $\phi = \pi/2$, then the plane wave is at beam incidence with the cylinder.

The frequency range of interest is the mid-frequency range at which the acoustic wavelengths are on the order of the shell perimeter (This definition of the mid-frequency range is about 3.5 times lower

than that defined in the previous chapters). If k_o is the acoustic wavenumber, then the mid-frequency range is about $k_o a = 1$. The mid-frequencies are high enough that shell resonances are numerous and low enough that shell curvature effects are still important. These frequencies are particularly difficult to model. Conventional FEM elements are not efficient due to wavelength sampling requirements and high frequency ray methods approximate important shell curvature effects.

I use the wavenumber integration approach to analyze the scattering from the shell following a similar procedure used by Guo, who analyzed the scattering from a shell with a single bulkhead and no deck and also from a shell with a single deck but no bulkhead [18][19][15]. The double bulkhead problem was analyzed by Cushieri and Feit [30][31]. The WI may be used when the shell system is linear and that its response may be constructed in terms of helical waves that travel up and down the shell axis. The approach is numerically efficient even at the mid-frequency range and suitable for application to this problem. The thickness of the plate at the mid-frequency range is such that Mindlin thick plate theory may be used for the bulkhead and deck and that the Hermann-Mirsky thick shell theory may be used for the shell.

F.2.1 Transforms

If the system is linear than it may be analyzed in terms of its Fourier components. To solve for the shell displacements, I need to define two spatial transforms. The first is the discrete Fourier transform pair defined as

$$f(\theta) = \frac{1}{2\pi} \sum_{n=-\infty}^{\infty} F(n)\, e^{+in\theta} \quad \Leftrightarrow \quad F(n) = \int_{\theta=0}^{2\pi} f(\theta)\, e^{-in\theta} d\theta, \tag{F.1}$$

where f is some variable decomposed by circumferential modes of integer order n due to the finite angular extent of the shell. The second is the continuous wave transform in the axial direction using the integral Fourier transform pair defined as

$$f(x) = \frac{1}{2\pi} \int_{k=-\infty}^{\infty} F(k)\, e^{+ikx} dk \quad \Leftrightarrow \quad F(k) = \int_{x=-\infty}^{\infty} f(x)\, e^{-ikx} dx, \tag{F.2}$$

where, in this case, f is some variable decomposed by axial waves of wavenumber k. All wavenumbers are present due to the infinite extent of the shell in the axial direction. Hereafter, the limits on the sums and integrals are understood. In this chapter, my convention is to use capital letter for transformed variables.

I will often need to transform a variable that is a function of both x and θ. This two dimensional

transform is defined as

$$f(x,\theta) = \frac{1}{(2\pi)^2} \sum_n \int F(k,n)\, e^{+ikx} e^{+in\theta} dk \quad \Leftrightarrow \quad F(k,n) = \int\int f(x,\theta)\, e^{-ikx} e^{-in\theta} dx d\theta$$

consistent with the two one-dimensional transforms. Because a transformed variable may be a function of n only, k only, or both n and k, I will write the dependance explicitly to avoid confusion and be consistent with all three of the transforms defined above. This means that $F(k,n)$ is not generally equal to $F(n)$.

F.2.2 Fluid Equations

A source-free, linear, elastic fluid is governed by the scalar wave equation, which, written in terms of the fluid potential function $\Phi(x,\theta,r)$, is

$$c_o^2 \nabla^2 \Phi - \Phi_{,tt} = 0 \tag{F.3}$$

where

$$\nabla^2 (\,) = (\,)_{,rr} + \frac{1}{r}(\,)_{,r} + \frac{1}{r^2}(\,)_{,\theta\theta} + (\,)_{,xx}$$

is the Laplacian operator in the cylindrical coordinate system $\{x,\theta,r\}$. The fluid displacements are related to the potential function as

$$\{u_o, v_o, w_o\} = \left\{ \; \Phi_{,x}, \quad \tfrac{1}{r}\Phi_{,\theta}, \quad \Phi_{,r} \; \right\},$$

where $\{u_o, v_o, w_o\}$ are the axial, circumferential, and radial displacements, respectively. I use subscripts for the fluid displacements to distinguish them from the shell displacements $\{u,v,w\}$. The fluid pressure is related to the radial displacement by

$$p_{o,r} = -\rho_o w_{o,tt},$$

which is a statement of conservation of radial momentum. For the scattering problem considered here the fluid pressure may be written as the sum of the incident pressure field, p_i, and the scattered pressure field, p_s, or simply

$$p_o = p_i + p_s.$$

Eq.(F.3) is separable with the general solution

$$\Phi(x,\theta,r) = \frac{1}{(2\pi)^2} \int \sum_n \left[A(k,n)\, J_n(k_r(k)\, r) + B(k,n)\, H_n^{(1)}(k_r(k)\, r) \right] e^{+in\theta} e^{+ikx} e^{-i\omega t} dx,$$

where A and B are arbitrary amplitudes determined from the boundary conditions, J_n is the Bessel function of order n, H_n is the Hankel function of the first kind and order n, and

$$k_r(k) = \sqrt{\frac{\omega^2}{c_o^2} - k^2} = \sqrt{k_o^2 - k^2} \tag{F.4}$$

is the radial wavenumber at infinite radius. I have also assumed a time dependance of $e^{-\imath\omega t}$, which is hereafter suppressed. Since the fluid pressure and displacements are related to the potential function through spatial and time derivatives, they also have the same functional dependance as the potential function. The square root function appearing in Eq.(F.4) identifies $\pm k_o$ as branch points in the complex wavenumber plane. The corresponding branch cuts are discussed in a subsequent section.

It is instructive to look at the limiting values of the Bessel and Hankel functions as their arguments go to infinity to see what type of solution they represent. The limiting values are given by Hildebrand [5] as

$$\lim_{k_r r \to \infty} J_n(k_r(k) r) \to \sqrt{\frac{2}{\pi k_r(k) r}} \left(\frac{1}{2} e^{+\imath k_r(k) r} + \frac{1}{2} e^{-\imath k_r(k) r} \right) e^{-\imath\pi/4} e^{-\imath n\pi/2} \tag{F.5}$$

and

$$\lim_{k_r r \to \infty} H_n^{(1)}(k_r(k) r) \to \sqrt{\frac{2}{\pi k_r(k) r}} e^{+\imath k_r(k) r} e^{-\imath\pi/4} e^{-\imath n\pi/2}. \tag{F.6}$$

The Bessel function wave is the superposition of an incoming and outgoing wave of equal amplitudes. The wave with the Hankel function dependance is an outgoing wave. It is clear from this that the incident plane wave that ensonifies the shell should be represented by the Bessel function and the scattered field from the shell is represented by the Hankel function.

I can express the incident plane wave in the cylindrical coordinate system $\{x, \theta, r\}$ as

$$p_i(x, \theta, r) = P_o \exp(+ik_o \sin(\phi) r \cos(\theta - \theta_o) + isx), \tag{F.7}$$

where the axial wavenumber component is

$$s = k_o \cos(\phi).$$

Morse and Ingard [8] give an equivalent series summation over the circumferential index n for

$$p_i(x, \theta, r) = \sum_n P_o \imath^{|n|} J_{|n|}(k_o \sin(\phi) a) e^{-in\theta_o} e^{+in\theta} e^{+isx}.$$

This expansion is valid for pure real radial wavenumber. For integer n the absolute value operators may

be dropped and I may express the incident pressure in a more convenient form as

$$p_i(x,\theta,r) = \frac{1}{(2\pi)^2}\int\sum_n P_i(k,n)\frac{J_n(k_r r)}{J_n(k_r a)}e^{+in\theta}e^{+\imath kx}dk, \tag{F.8}$$

where

$$P_i(k,n) = \delta(k-s)(2\pi)^2 P_o i^n J_n(k_r a)\, e^{-in\theta_o}. \tag{F.9}$$

To find an expression for the scattered field, I must consider the boundary conditions at the shell surface. Because I am ignoring viscous effects, the fluid interacts with the shell through the radial displacement and the fluid pressure. The boundary conditions at the shell surface are continuity of radial displacement, which may be expressed as

$$w(x,\theta) = w_o(x,\theta,a),$$

and conservation of momentum in the radial direction, which may be expressed as

$$[p_{o,r}]_{@r=a} = -\rho_o [w_{o,tt}]_{@r=a} = -\rho_o w_{,tt}. \tag{F.10}$$

By ignoring viscous effects, the no-slip condition at the shell surface is violated and u_o and v_o are not generally equal to u and v. If I write the scattered pressure field in the fluid, and the shell radial displacement, generally, in terms of the Fourier transforms defined earlier, as

$$p_s(x,\theta,r) = \frac{1}{(2\pi)^2}\int\sum_n \left(P_s(k,n)\frac{H_n^{(1)}(k_r r)}{H_n^{(1)}(k_r a)}\right)e^{+in\theta}e^{+\imath kx}dk, \tag{F.11}$$

and

$$w(x,\theta) = \frac{1}{(2\pi)^2}\int\sum_n W(k,n)\, e^{+in\theta}e^{+ikx}dk, \tag{F.12}$$

then using Eq.(F.10), I can relate the scattered pressure to the incident pressure and the shell radial displacement by

$$P_s(k,n) = \alpha(k,n)W(k,n) + \beta(k,n)P_i(k,n), \tag{F.13}$$

where

$$\alpha(k,n) = \rho_o\omega^2\frac{H_n^{(1)}(k_r(k)a)}{H_n^{(1)}(k_r(k)a)_{,a}} \tag{F.14}$$

and

$$\beta(k,n) = -\frac{H_n^{(1)}(k_r(k)a)}{H_n^{(1)}(k_r(k)a)_{,a}}\frac{J_n(k_r(k)a)_{,a}}{J_n(k_r(k)a)}. \tag{F.15}$$

If I can find an expression that relates the incident pressure amplitude to the shell radial displacement, then I know the scattered field through Eq.(F.11).

F.2.3 Scattering form function

The scattered field is usually presented in terms of the form function, which is defined as

$$f_f(x,\theta,\omega) = P_o\sqrt{\frac{2r}{a}}e^{-ik_r(s)r}\lim_{k_r r\to\infty} p_s(x,\theta,r).$$

The limiting value of the scattered field given Eq.(F.11) is found by taking the limiting value of the Hankel function given by Eq.(F.6). In terms of the scattered pressure helical wave amplitudes on the shell surface, the form function is then given as

$$f_f(x,\theta,\omega) = \frac{e^{-i\pi/4}e^{-ik_r(s)r}}{2\pi^{5/2}P_o}\int\sum_n\left(\frac{P_s(k,n)\,e^{-in\pi/2}e^{ik_r r}}{H_n^{(1)}(k_r a)\sqrt{k_r a}}\right)e^{+in\theta}e^{+\imath kx}dk \tag{F.16}$$

In most cases the magnitude of the form function is of chief interest. As a check on Eq.(F.16), the form function magnitude for perfectly rigid and perfectly soft (pressure release) shells approaches unity at high frequency.

F.2.4 Calculating shell displacements

The momentum equations using the Hermann-Mirsky thick shell theory (refer to Chapter 3) takes the form

$$\mathbf{k}^{(s)}\,\mathbf{u}^{(s)}(x,\theta) = \mathbf{f}^{(s)}(x,\theta), \tag{F.17}$$

where $\mathbf{k}^{(s)}$ is a linear differential matrix operator,

$$\mathbf{u}^{(s)}(x,\theta) = \left\{\begin{array}{ccccc} u, & v, & w, & \phi_\theta, & \phi_x \end{array}\right\}^T \tag{F.18}$$

is the shell mid-surface displacement vector, and

$$\mathbf{f}^{(s)}(x,\theta) = \left\{\begin{array}{ccccc} f_x, & f_\theta, & f_r, & m_\theta, & m_x \end{array}\right\}^T \tag{F.19}$$

is the surface force vector. I use bold face fonts to denote either vector or matrix variables. The superscript (s) is used to refer to variables associated with the shell. The forces and moments are the forces and moments per unit mid-plane surface area. Note that the direction of both ϕ_θ and m_θ are in

the *negative* x direction. If I define the transformed displacement vector as

$$\mathbf{U}^{(s)}(k,n) = \left\{ \begin{array}{ccccc} U, & V, & W, & \Phi_\theta, & \Phi_x \end{array} \right\}^T.$$

and the transformed force vector as

$$\mathbf{F}^{(s)}(k,n) = \left\{ \begin{array}{ccccc} F_x, & F_\theta, & F_r, & M_\theta, & M_x \end{array} \right\}^T$$

then I may write the shell displacements as

$$\mathbf{u}^{(s)}(x,\theta) = \frac{1}{(2\pi)^2} \int \sum_n \mathbf{U}^{(s)}(k,n)\, e^{+ikx} e^{+in\theta} dk$$

or alternatively as

$$\mathbf{u}^{(s)}(x,\theta) = \frac{1}{(2\pi)^2} \int \sum_n \mathbf{C}^{(s)}(k,n)\, \mathbf{F}^{(s)}(k,n)\, e^{+ikx} e^{+in\theta} dk \tag{F.20}$$

where

$$\mathbf{C}^{(s)}(k,n) = \left[\mathbf{K}^{(s)}(k,n)\right]^{-1}.$$

The various forces on the shell are considered in the following sections.

F.2.5 Empty shell solution

When the shell is empty with no attached plates the only forces on the shell are the pressure forces due to the fluid. The shell displacements are related to these forces by

$$\mathbf{K}^{(s)}(k,n)\,\mathbf{U}^{(s)}(k,n) = -\left\{ \begin{array}{ccccc} 0, & 0, & P_i(k,n) + P_s(k,n), & 0, & 0 \end{array} \right\}^T = -\mathbf{F}^{(f)}(k,n),$$

where $\mathbf{K}^{(s)}(k,n)$ is the shell stiffness matrix equal to the inverse of the compliance matrix and $\mathbf{F}^{(f)}(k,n)$ is the force of the shell on the fluid (the superscript (f) is used to refer to fluid variables). Using Eq.(F.13) and Eq.(F.9), I can define the fluid force as

$$\mathbf{F}^{(f)}(k,n) = \left\{ \begin{array}{ccccc} 0, & 0, & P_i(k,n)\,(1+\beta(k,n)), & 0, & 0 \end{array} \right\}^T \tag{F.21}$$

and absorb the term proportional to the radial displacement into the stiffness matrix simply by adding $\alpha(k,n)$ to $\mathbf{K}^{(s)}_{(3,3)}$. Using the Wronskian relation for Bessel functions,

$$J_n(k_r a) H_n(k_r a)_{,a} - H_n(k_r a) J_n(k_r a)_{,a} = \frac{2i}{\pi a},$$

the non-zero forcing term may be more simply expressed as

$$P_i(k,n)(1+\beta(k,n)) = \delta(k-s) G(k,n) = \delta(k-s) \frac{8\pi P_o i^{n+1} e^{-in\theta_o}}{a H_n(k_r(s)a)_{,a}}.$$

The empty shell displacement is then given by

$$\mathbf{u}^{(s)}(x,\theta) = -\frac{1}{(2\pi)^2} \int \sum_n \mathbf{C}^{(s)}(k,n) \mathbf{F}^{(f)}(k,n) e^{+in\theta} e^{+ikx} dk, \tag{F.22}$$

where $\mathbf{C}^{(s)}(k,n)$ is the inverse of $\mathbf{K}^{(s)}(k,n)$ after it has been modified. The integral over wavenumber may be eliminated by evaluating the delta function, which leads to

$$\mathbf{u}^{(s)}(x,\theta) = -\sum_n \mathbf{C}^{(s)}_{(3,1..5)}(s,n) G(s,n) e^{+in\theta} e^{+isx}.$$

F.2.6 Bulkhead compliance matrix

The shell displacement and force as defined by Eq.(F.18) and Eq.(F.19) both have dimension $5x1$, yet the bulkhead displacement and force as derived in Appendix-A (after the twist rotation and moment have been eliminated) both have dimension $4x1$. The unmatched shell displacement is $\phi^{(s)}_\theta$ and the unmatched force is $m^{(s)}_\theta$. The corresponding bulkhead force is zero, while the corresponding bulkhead displacement is not defined. I am free to define the bulkhead displacement provided I maintain the physics of the shell-bulkhead interaction.

It is convenient to define the bulkhead $\phi^{(b)}_\theta(\theta)$ to be equal the shell $\phi^{(s)}_\theta(0,\theta)$. I also define the bulkhead compliance to $M^{(b)}_\theta(n)$ as

$$c_\infty = \frac{\Phi^{(b)}_\theta(n)}{M^{(b)}_\theta(n)}.$$

This compliance is infinite but for now I will consider it to be a very large but finite constant. This does nothing more than allow me to equate the bulkhead displacements to the total shell displacements as

$$\mathbf{u}^{(b)}(\theta) = \mathbf{u}^{(s)}(0,\theta). \tag{F.23}$$

The bulkhead displacements may then be expressed as

$$\mathbf{u}^{(b)}(\theta) = \frac{1}{2\pi} \sum_{n} \mathbf{C}^{(b)}(n)\, \mathbf{F}^{(b)}(n)\, e^{+in\theta}, \tag{F.24}$$

provided I redefine

$$\mathbf{F}^{(b)}(n) = \left\{ \; F_x^{(b)}(n), \quad F_\theta^{(b)}(n), \quad F_r^{(b)}(n), \quad M_\theta^{(b)}(n), \quad M_x^{(b)}(n) \; \right\}^T$$

and the bulkhead compliance matrix as

$$\mathbf{C}_e^{(b)}(n) = \begin{bmatrix} \mathbf{C}_{(1,1)}^{(b)}(n) & \mathbf{C}_{(1,2)}^{(b)}(n) & \mathbf{C}_{(1,3)}^{(b)}(n) & 0 & \mathbf{C}_{(1,4)}^{(b)}(n) \\ \mathbf{C}_{(2,1)}^{(b)}(n) & \mathbf{C}_{(2,2)}^{(b)}(n) & \mathbf{C}_{(2,3)}^{(b)}(n) & 0 & \mathbf{C}_{(2,4)}^{(b)}(n) \\ \mathbf{C}_{(3,1)}^{(b)}(n) & \mathbf{C}_{(3,2)}^{(b)}(n) & \mathbf{C}_{(3,3)}^{(b)}(n) & 0 & \mathbf{C}_{(3,4)}^{(b)}(n) \\ 0 & 0 & 0 & c_\infty & 0 \\ \mathbf{C}_{(4,1)}^{(b)}(n) & \mathbf{C}_{(4,2)}^{(b)}(n) & \mathbf{C}_{(4,3)}^{(b)}(n) & 0 & \mathbf{C}_{(4,4)}^{(b)}(n) \end{bmatrix},$$

where I use subscripts in braces to refer to the particular ij'th entry of the $4x4$ compliance matrix. The zeros that fill the empty column and row merely mean that there is no coupling between $\Phi_\theta^{(b)}(n)$ and the remaining displacements. I also use the subscript e to refer to the *expanded* deck compliance matrix, which is hereafter understood.

In a later section I need to add the bulkhead compliance to a shell compliance and invert it. This operation may be symbolically written as

$$\lim_{c_\infty \to \infty} \left[\begin{bmatrix} \mathbf{a} & \mathbf{b} \\ \mathbf{c} & \mathbf{d} \end{bmatrix} + \begin{bmatrix} \mathbf{e} & 0 \\ 0 & c_\infty \end{bmatrix} \right]^{-1} = \begin{bmatrix} [\mathbf{a}+\mathbf{e}]^{-1} & 0 \\ 0 & \frac{1}{c_\infty} \end{bmatrix},$$

where $\mathbf{a}$, $\mathbf{b}$, $\mathbf{c}$, $\mathbf{d}$, and $\mathbf{e}$ are submatrices. The effect of c_∞ is therefore to decouple the degree of freedom associated with c_∞ from all other degrees of freedom and to insure that the force associated with c_∞ is equal to zero.

F.2.7 Deck compliance matrix

The deck stiffness matrix may be easily found by considering the WFEM 2D shell stiffness matrix at infinite radius after terms involving n/a have been set equal to k_θ. The deck compliance matrix (inverse stiffness matrix) is also incompatible with the shell formulation. In this case, there are two unmatched shell displacements, $\phi_x^{(s)}(x,\theta_1)$ and $\phi_x^{(s)}(x,\theta_2)$, and two unmatched forces, $m_x^{(s)}(x,\theta_1)$ and $m_x^{(s)}(x,\theta_2)$.

It is convenient to redefine

$$\mathbf{u}^{(d)}(x) = \left\{ \begin{array}{c} \mathbf{u}_1^{(d)}(x) \\ \mathbf{u}_2^{(d)}(x) \end{array} \right\} = \left\{ \begin{array}{c} \mathbf{u}^{(s)}(x,\theta_1) \\ \mathbf{u}^{(s)}(x,\theta_2) \end{array} \right\}. \tag{F.25}$$

The deck displacements may then be expressed as

$$\mathbf{u}^{(d)}(x) = \frac{1}{2\pi} \int \mathbf{C}^{(d)}(k)\, \mathbf{F}^{(d)}(k)\, e^{+ikx} dk \tag{F.26}$$

provided I redefine

$$\mathbf{F}^{(d)}(k) = \left\{ \begin{array}{c} \mathbf{F}_1^{(d)}(k) \\ \mathbf{F}_2^{(d)}(k) \end{array} \right\} = \left\{ \begin{array}{ccccc} F_{x_1}^{(d)}(k), & F_{\theta_1}^{(d)}(k), & F_{r_1}^{(d)}(k), & M_{\theta_1}^{(d)}(k), & M_{x_1}^{(d)}(k), \quad \ldots \\ F_{x_2}^{(d)}(k), & F_{\theta_2}^{(d)}(k), & F_{r_2}^{(d)}(k), & M_{\theta_2}^{(d)}(k), & M_{x_2}^{(d)}(k) \end{array} \right\}^T,$$

and the deck compliance matrix as

$$\mathbf{C}_e^{(d)}(k) = \left[\begin{array}{cccc} \mathbf{C}_{[1,1]}^{(d)}(k) & \left\{ 0, \; 0, \; 0, \; 0 \right\}^T & \mathbf{C}_{[1,2]}^{(d)}(k) & \left\{ 0, \; 0, \; 0, \; 0 \right\}^T \\ \left\{ 0, \; 0, \; 0, \; 0 \right\} & c_\infty & \left\{ 0, \; 0, \; 0, \; 0 \right\} & c_\infty \\ \mathbf{C}_{[2,1]}^{(d)}(k) & \left\{ 0, \; 0, \; 0, \; 0 \right\}^T & \mathbf{C}_{[2,2]}^{(d)}(k) & \left\{ 0, \; 0, \; 0, \; 0 \right\}^T \\ \left\{ 0, \; 0, \; 0, \; 0 \right\} & c_\infty & \left\{ 0, \; 0, \; 0, \; 0 \right\} & c_\infty \end{array} \right],$$

where I use subscripts in square braces to refer to the submatrices of the compliance matrix and I again use c_∞ to ensure the force associated with this degree of freedom is zero. I also, for the moment, use the subscript e to refer to the *expanded* deck compliance matrix, which is hereafter understood.

F.2.8 Interaction forces

The total force on the shell is the sum of forces due to the surrounding fluid, the deck along constant θ_1 and θ_2 positions, and the bulkhead attached along constant x_1. The total force may, therefore, be written as

$$\mathbf{f}^{(s)}(x,\theta) = -\mathbf{f}^{(f)}(x,\theta) - \mathbf{f}^{(b)}(\theta)\, \delta(x - x_1) - \mathbf{f}_1^{(d)}(x)\, \delta(\theta - \theta_1) - \mathbf{f}_2^{(d)}(x)\, \delta(\theta - \theta_2)$$

or in terms of its transform as

$$\mathbf{F}^{(s)}(k,n) = -\mathbf{F}^{(f)}(k,n) - \mathbf{F}^{(b)}(n)\, e^{-ikx_1} - \mathbf{F}_1^{(d)}(k)\, e^{-in\theta_1} - \mathbf{F}_2^{(d)}(k)\, e^{-in\theta_2}, \tag{F.27}$$

where I have used superscripts to refer to the fluid, bulkhead, and deck contributions. The fluid force is already known through Eq.(F.21) but I need to solve for the unknown interaction forces between the shell and the deck and between the shell and the bulkhead. I do this by solving the left side of Eq.(F.23) using Eq.(F.24) and the right side of Eq.(F.23) using Eq.(F.27) and Eq.(F.20). Furthermore, I solve for the left side of Eq.(F.25) using Eq.(F.26) and the right side of Eq.(F.25) using Eq.(F.27) and Eq.(F.20). This yields two sets of matrix equations that may be rearranged as

$$\mathbf{\Theta}(k)\,\mathbf{F}^{(d)}(k) = -\frac{1}{2\pi}\sum_{n}\mathbf{\Lambda}^{*T}(n)\,\mathbf{C}^{(s)}(k,n)\left[\mathbf{F}^{(f)}(k,n) + \mathbf{F}^{(b)}(n)\right] \tag{F.28}$$

and

$$\mathbf{\Xi}(n)\,\mathbf{F}^{(b)}(n) = -\frac{1}{2\pi}\int \mathbf{C}^{(s)}(k,n)\left[\mathbf{F}^{(f)}(k,n) + \mathbf{\Lambda}(n)\,\mathbf{F}^{(d)}(k)\right]dk, \tag{F.29}$$

where, to save writing, I have defined the $10x10$ auxiliary matrix

$$\mathbf{\Theta}(k) = \mathbf{C}^{(d)}(k) + \frac{1}{2\pi}\sum_{n}\mathbf{\Lambda}^{*T}(n)\,\mathbf{C}^{(s)}(k,n)\,\mathbf{\Lambda}(n), \tag{F.30}$$

the $5x5$ auxiliary matrix

$$\mathbf{\Xi}(n) = \mathbf{C}^{(b)}(n) + \frac{1}{2\pi}\int \mathbf{C}^{(s)}(k,n)\,dk, \tag{F.31}$$

and the $5x10$ auxiliary matrix

$$\mathbf{\Lambda}(n) = \begin{bmatrix} e^{-in\theta_1} & 0 & 0 & 0 & 0 & e^{-in\theta_2} & 0 & 0 & 0 & 0 \\ 0 & e^{-in\theta_1} & 0 & 0 & 0 & 0 & e^{-in\theta_2} & 0 & 0 & 0 \\ 0 & 0 & e^{-in\theta_1} & 0 & 0 & 0 & 0 & e^{-in\theta_2} & 0 & 0 \\ 0 & 0 & 0 & e^{-in\theta_1} & 0 & 0 & 0 & 0 & e^{-in\theta_2} & 0 \\ 0 & 0 & 0 & 0 & e^{-in\theta_1} & 0 & 0 & 0 & 0 & e^{-in\theta_2} \end{bmatrix}. \tag{F.32}$$

I can eliminate the unknown bulkhead forces from the two equations to arrive at

$$\begin{aligned} &\sum_{n}\left[\delta_{mn}\mathbf{\Xi}(m) - \frac{1}{(2\pi)^2}\int \mathbf{\Gamma}(k,m,n)\,dk\right]\mathbf{F}^{(b)}(n) \\ &= \sum_{n}\left[-\delta_{mn}\frac{1}{2\pi}\int \mathbf{C}^{(s)}(k,m)\,\mathbf{F}^{(f)}(k,m)\,dk + \frac{1}{(2\pi)^2}\int \mathbf{\Gamma}(k,m,n)\,\mathbf{F}^{(f)}(k,n)\,dk\right], \end{aligned} \tag{F.33}$$

defined in terms of the Kronecker delta function

$$\delta_{mn} = \left\{ \begin{array}{l} 1,\ m = n \\ 0,\ m \neq n \end{array} \right\}$$

and the additional $5x5$ auxiliary matrix

$$\mathbf{\Gamma}(k,m,n) = \mathbf{C}^{(s)}(k,m)\,\mathbf{\Lambda}(m)\,\mathbf{\Theta}^{-1}(k)\,\mathbf{\Lambda}^{*T}(n)\,\mathbf{C}^{(s)}(k,n).$$

If I choose an upper limit of N for the total number of circumferential modes, then Eq.(F.33) is a system of $10N$ equations.

When there is no bulkhead, Eq.(F.28) may be solved directly for the deck forces as

$$\mathbf{F}^{(d)}(k) = -\frac{1}{2\pi}\mathbf{\Theta}^{-1}(k)\sum_{n}\mathbf{\Lambda}^{*T}(n)\,\mathbf{C}^{(s)}(k,n)\,\mathbf{F}^{(f)}(k,n)$$

and when there is no deck, Eq.(F.29) may be solved directly for

$$\mathbf{F}^{(b)}(n) = -\frac{1}{2\pi}\mathbf{\Xi}^{-1}(n)\int \mathbf{C}^{(s)}(k,n)\,\mathbf{F}^{(f)}(k,n)\,dk.$$

I use these equations to verify the model against previous analyses.

In all of the above cases, having solved for the unknown interaction forces, I may then calculate in turn: the shell displacements using Eq.(F.20); the scattered field pressure amplitude using Eq.(F.13); and the form function using Eq.(F.16) and Eq.(F.11).